Working Towards a Compact Cold Ion Source

Dominic Reed

Abstract

This thesis presents work on creating a cold atomic ion source based on a diffraction grating magneto-optical trap using caesium. Due to this technique, the source profile has been minimised in terms of both spatial extent and production cost - characteristics that have been emphasised throughout this work so as to be more applicable to both industrial applications and further research.

To ionise the Cs, a novel excitation scheme has been designed involving three low energy transitions from the ground state of $6S_{1/2}$, to the Rydberg state $21P_{1/2}$, from which the atoms can be field ionised. In order to maximise the efficiency of the Rydberg state coupling, a new offset frequency reference based on Zeeman detuned ground state spectroscopy of rubidium was devised.

Only a weak caesium trap using a grating was observed in this work, however discussion as to the reasons for this are presented. Despite this, full schematics and engineering diagrams for the proposed integrated ion source are presented with the hope of construction once a viable trap is demonstrated as there are no fundamental reasons hindering success.

Working Towards a Compact Cold Ion Source

Dominic Reed

A thesis submitted in partial fulfilment
of the requirements for the degree
of Doctor of Philosophy

Quantum Light and Matter
Department of Physics
University of Durham
England

October 2019

Contents

List of Figures

List of Tables

Declaration

I confirm that no part of the material offered has previously been submitted by myself for a degree in this or any other University. Where material has been generated through joint work, the work of others has been indicated.

Dominic Reed
Durham, 2019

To the all that was none.
To the none that was all.
To the shadows that crept.
To the lights that crawled.
To the one that was.
To the one that is.
To the one that fell,
Toward that letter in the dark.

To these words of meaning I know,
But do dearly hope,
To forget.

Truthfully, from very early on, I didn't think that I'd get very far with this. Every moment has been a constant struggle. From the empty days in the lab, to the spirals that lead me down the garden path. The highs and lows of life, love, and this experiment, have become all too familiar bedfellows over the years. But I was never alone in this endeavour. When I needed to surface for air there were always those that I could talk to (be they a sympathetic ear or someone with all the answers) and for this I am sincerely grateful. Thus, this thesis represents a sum of work for not just myself, but for all those who have helped me along the way, be it professionally, personally, familial, or even fanciful in form. You likely know who you are, but if you don't, just remember: *Even the smallest of smiles can soothe a soul lost in the storm.*

To think that for one glorious moment I believed that I had seen the light.

For this mistake, I blame myself, for in fact; I had.

Chapter 1

Introduction

The technique of laser cooling has had a profound impact on the field of atomic physics research but this thesis though will focus on another field where laser cooling is in the process of causing a revolution: bright focused ion beams (FIBs). To begin, I will give an overview of the developmental history of FIBs, from the mid 1970s, wherein they were generated by liquid metal sources, to the most state-of-the-art cold atom-electron-ion sources (CAEIS) currently in development hoping to shatter the limitations imposed by rapidly ageing technologies such as the liquid metal ion source (LMIS).

1.1 The Tipping Point

The forms of the first FIBs evolved from devices used for field ion microscopy (FIM), in conjunction with the development of the LMIS [1]. FIM devices were first invented in 1951 by Erwin Müller and in 1955 were used to obtain the first images of individual atoms [2, 3]. Their principle of operation is that a sharp, cryogenically cooled metal tip is placed in a vacuum that has been filled with an inert gas. The tip is then given a strongly positive potential such that gas moving near the tip is ionised. These free ions are repelled by the tip and can be collected to form an image of the tip. This design of microscope began the paradigm of using sharp tip-based technologies as ion sources.

V. E. Krohn and G. R. Ringo were the first to suggest the use of an electrohy-

drodynamic (EHD) ion source [4] and in 1975 published their work on developing a source that used liquid metal [5]. Their paper described the successes that they had had as part of their efforts to create an ion-microprobe analyser, chiefly information on their EHD ion source. It used gallium to wet a sharp tip in a region of strong electric fields and was shown to produce ions with a brightness of 0.9×10^5 A cm^{-2} sr^{-1} and an energy spread of 12 eV with a current of 10 μA at an ion energy of 21 kV. While they tested three liquids - gallium, caesium, and mercury, the best results were found with gallium, which produced a spot size of 15 μm in diameter. In this paper they also posited that greater performance could be achieved with more appropriate lenses than they had used.

The development of the LMIS continued for many years with leap-frogging performance enhancements [6–8] and by the 1980s had been fully adopted by the semiconductor industry and become ubiquitous for the purposes of mask and circuit repair [9]. It took longer for the LMIS to become popular in research communities but by the 1990s they too had embraced this ion source. To this day there are still many groups utilising an LMIS for their individual purposes and a thriving ecosystem of manufacturers willing to produce such devices: Zeiss Int., Orsay Physics, and Hitachi Inc. to name a small number.

By 1983 though, the limitations of the LMIS were already well known [10–12]. The fundamental design of the LMIS sharp tip in a strong electric field means that all LMIS have an imposed energy spread of 5 eV and thus an ultimate limit to both their resolution and brightness. Efforts were made to nurture a similar technology, the gas field ion source (GFIS) [13]. However, while this source could better both the brightness and achievable spot sizes of the LMIS, it could not replicate the peak currents of the LMIS, making it nonviable for the large volume circuit and mask edits required by industry.

1.2 To a Colder Future

Fortunately by this stage, there was another rapidly progressing field of study, that of cold atom science. The theoretical predictions of neutral atom and ionic cooling were

made as early as 1975 [14–16] with realisations taking place soon thereafter [17, 18].

From this point the developments can be broadly split into two areas relevant to this work: 3D traps and collimated beams of particles. The former evolved from experiments first performed in 1985 [19] involving 6 laser beams acting in 3 pairs of perpendicular beams to produce 'viscous confinement'. More effective confinement was later achieved by utilising magnetic fields to generate a spatially dependent trapping force in 1987 [20]. The latter used the same principles of viscous cooling and trapping, but in a 2D geometry, presenting its own issues to overcome [21–25]. Key developments included the earliest collimated metastable beams from 1996 [26, 27] and the first 2D+- magneto optical trap configuration in 1998 [28] with a novel method of atomic deposition in 1993 [29]. It was from these 2D and 3D designs that the ideas of cold ion sources arose.

The first proposition of such an idea was by Freinkman *et al.* in 2003 [30]. It was based on the principle of a transversely cooled beam of atoms that could then be ionised by additional lasers at the end of a collimating beam line. In their paper they predicted a number of advantages of such a system, including ion currents of up to 1 μA and transverse energy spreads as low as 0.035 eV - far below the limitations imposed on an LMIS. While not the subject of this thesis, it is also interesting to note some proposals and development articles of cold electron sources around this time as they are very similar in working principles to cold ion sources [31–33].

A collaboration in 2006 [34, 35] took a different approach with their cold ion source, opting instead for a full 3D trap to create the first device of its category, dubbed the magneto-optical trap ion source (MOTIS). Variations on this theme included work in the Netherlands on a trap that used Rydberg excitation to produce a plasma from which to extract ions [36]. A chromium based source with similar characteristics was also demonstrated around this time [37, 38].

From 2010, advancements and implementations have steadily continued with both varieties of source. In 2011, NIST demonstrated the first instance of MOTIS utilising lithium as a species, with subsequent work performed in 2014 and 2019 to build a cold Li ion microscope and Li FIB, thus adding to the growing number of atoms shown to be exploitable [39–41]. Later, in 2013, there was the proposal of a

European collaboration to build a CAEIS for low energy ions, with its completion in 2016 [42,43]. With acceleration voltages below 300 V, this system is able to produce ion bunches with a relative energy spread of 0.032 and 10 nm spot sizes. Both of these latest designs from NIST and the European collaboration could be considered hybrid systems with atoms being fed from a 3D trap into a transversely cooled beam for ionisation, or vice versa.

Other work in this decade, based around either a 3D trap or hybrid systems, includes efforts by an Australian led collaboration, based in Melbourne, to study topics such as: the effects of space-charge dynamics on a source [44], whether source brightness can be increased using Rydberg blockade [45], if better source efficiency can be achieved using stimulated Raman adiabatic passage [46], and whether the emittance of a source can be suppressed by shaping the outputted ion bunches [47]. Their most recently published works relate to a CAEIS based on ionising Rydberg atoms proposed in 2017 [48] and completed in 2018 [49]. This system has allowed them to produce heralded ions via ionisation coincidence and may lead to new means of optimising the brightness of ion beams.

Back in Europe, a French-Italian collaboration was also studying the dynamics of cold Rydberg gases [50] and later the ionisation of Cs Rydberg states as a source of high brightness ion beams [51]. This research has culminated in the first installation of a Cs cold ion beam system onto an SEM-FIB TESCAN microscope in 2018 [52] as well as a deterministic single ion source with controllable trajectories [53]. Elsewhere in Europe, at the University of Manchester, an AC driven MOTIS utilising potassium was also demonstrated [54].

Concurrent with work regarding 3D source technology, efforts were also made to develop purely 2D MOT based devices. Essentially this was due to knowledge of the limiting factors of the current output of a MOTIS. Despite the relative ease in their construction, their maximum current is principally determined by the density of the atom trap; a 2D device, however, is only limited by the rate at which atoms can be pushed along its beam line and ionised. One significant paper published in 2013 [55] details the modelling of a Cs low temperature ion source (LoTIS) being developed in a partnership between NIST and ZeroKnanotech. A follow-up article

was then published in 2014, elaborating upon its possible performance and including highly favourable comparisons to competing sources such as the LMIS [56]. When constructed, the LoTIS performed as expected with brightness in excess of the LMIS and 2 nm spot sizes [57]. Similar work was also being done in the Netherlands to produce a LoTIS using rubidium. [58].

1.3 In A Smaller Space

While the question of ultimate performance may be answered by a LoTIS, there are still innovations that can be made upon designs of the MOTIS. A weakness of 2D based apparatus is its propensity to be naturally cumbersome. This is mainly due to requiring the necessary length to collimate the atoms. Within this extended section, the necessary magnetic field gradients must remain consistent as well as have laser beams of sufficient width in order to efficiently, transversely cool the atoms. A 'standard' MOTIS, meanwhile, is far less complex, requiring just a single pair of easily constructed magnetic coils and a clear intersection of 6 beams into which to either aim the ionisation lasers or generate your ionising field.

The goal of this work is to simplify this paradigm even further while also minimising the size of the source as a whole. To achieve this, the MOT would be generated using a surface-patterned diffraction grating chip with a hole at its centre. The grating is able to generate upward trapping beams from a single cooling beam directed towards its surface in a perpendicular direction. The advantage of this geometry is that the trap is fully exposed on all sides for further ionisation via laser beams with the chip hole allowing free passage of ions. In theory this would provide the same possible performance as a MOTIS but in a more compact form factor with economic savings.

Multiple grating-based traps have been demonstrated, most notably by the photonics group at the University of Strathclyde using Rb [59] - the source of the grating chip used in this work, but also at the Eindhoven Institute of Technology (also using Strathclyde gratings) used to make a cold electron source [60]. Others include the University of Maryland [61], the Air Force Institute of Technology in Ohio [62], and

at NIST (using Li) [63]. While there is ongoing work at the Universities of Hannover, Birmingham, and Chicago. None of these groups aimed to create a MOTIS using their gratings and at time of writing, no one has produced an ion source based on a grating magneto-optical trap (GMOT). The aim of this work was to be the first do so by cooling Cs in such a trap using a grating initially intended for use with Rb and the methods outlined in figure 1.1. The promising results of chapter 5 and the predictions of chapter 2 give hope that no fundamental issues are inhibiting the creation of such a trap and that it can be integrated into the proposed compact cold ion source; an explanation as to how this might be realised forms the remaining body of this thesis.

Motivations

The purpose of the work described in this thesis was to create a relatively inexpensive and compact caesium ion source for a FIB system, to be used in further research and industrial applications. These include: nano-fabrication (the process of removing from, or adding to, nano-scale structures), microscopy (using ions to image with nanometre resolutions), and sample analysis (gaining insight into material properties on a nano-scale). The advantages of using a cold atom based source for these processes are numerous and so I will only give a few notable examples which will be expanded upon in chapter 3. For nano-fabrication, while my source is designed to use Cs, laser cooling allows ∼27 species to be used and thus a greater number of properties can be exploited than traditional tip-based sources. In the case of Cs, the ion is far more massive than an electron and so gives a greater rate of removal when nano-fabricating. For microscopy, the use of a cold atom source allows new beam energies to be used at smaller focal spot sizes and generally offers greater contrast versus an electron based alternative. Similarly, sample analysis options are improved by a cold atom source due to the range of species available to use as well as new beam energies.

Thesis Structure

This thesis details the experimental and theoretical work towards a functioning compact cold atom ion source; complete with initial designs, use of a testing chamber, construction of an in-vacuum atom trap harness, and the challenges encountered. The specifics of each chapter are as follows:

- Chapter 2 begins by outlining the theory of laser cooling and trapping in order to build towards describing the interactions within a grating MOT. These interactions are then analysed to determine how this paradigm differs from a more standard 6-beam MOT and how this affects the system performance as an ion source.

- Chapter 3 deals with ions and begins with a brief introduction to them followed by the outlining of the measurements used to characterise ion sources. Using this context, the ion sources themselves are introduced, from the oldest liquid metal, to the newest cold atom sources.

- Chapter 4 begins the description of experimental work by noting the lasers used for cooling, trapping, and further excitation as well as their locking methods. This chapter also includes details on atomic spectroscopy and optical diagrams.

- Chapter 5 gives details on the progress of experimental work and current results including work with the test vacuum chamber and its magnetic coils. The control mechanisms of the experiment are also described, both in terms of hardware and software.

- Chapter 6 is the beginning of the outlook part of the thesis and gives full details of the proposed cold ion source hardware construction and execution.

- Finally, Chapter 7 brings the thesis to a close with discussions and overall conclusions of the project.

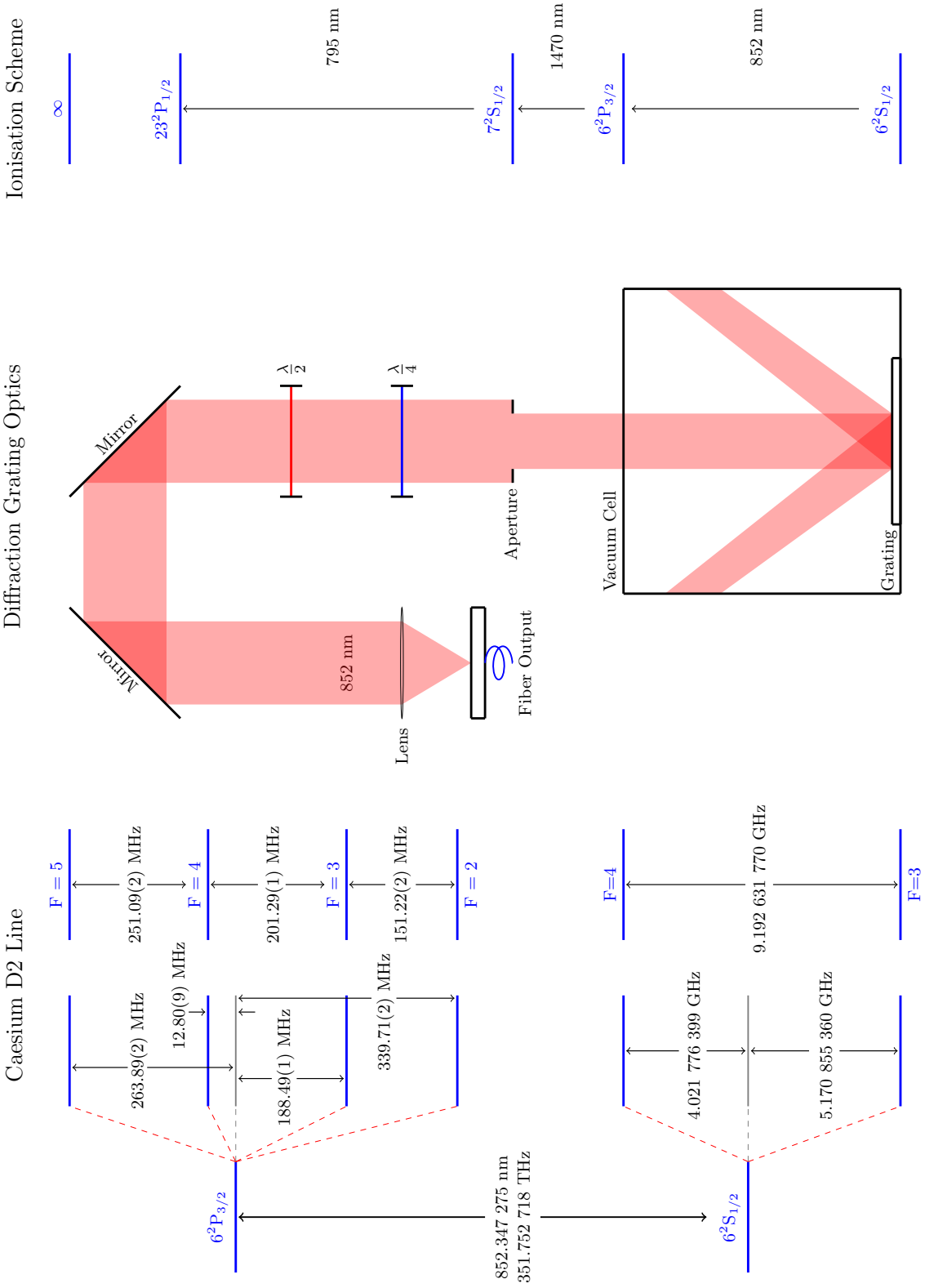

Figure 1.1: A summation of the main methods of this work. (Left) The caesium D2 line with all hyperfine transitions used to cool the atoms. (Middle) An illustration of a single beam GMOT apparatus (minus the magnetic coils around the chamber). The light is circularly polarised by the half and quarter wave plates after rebounding from two mirrors. This assures uniformity in radial illumination for the GMOT. (Right) The Cs ionisation scheme.

Publications Arising from this Work

[64] D. J. Reed, N. Šibalić, D. J. Whiting, J. M. Kondo, C. S. Adams, K. J. Weatherill., "Low-drift Zeeman shifted atomic frequency reference," OSA Continuum **1**, 4-12 (2018).

Chapter 2

Optical Cooling and Trapping

2.1 Laser Cooling

In this chapter, I will discuss the theory behind the project's primary aim: to create a magneto-optical trap using a surface-patterned grating chip (GMOT) with a single cooling beam and an inhomogeneous magnetic field. To this end, over several subsections, I will build from the basics of Doppler cooling in the low intensity limit and how this technique can be combined with magnetically based, spatially dependent forces to construct the most simple version of a 6 beam MOT. I will then use this basis to explain, contrast and analyse the resulting subtleties that arise because of the less symmetrical geometry present in a GMOT.

2.1.1 Doppler Cooling

2.1.1.1 Basics of Atom Deceleration

Radiation has an associated pressure force due to the momentum of a photon $\hbar\vec{\mathbf{k}}$, therefore if a photon were to interact with an atom it would exert a force on said atom. If the atom were to be moving with a velocity $\vec{\mathbf{v}}$ in an atomic beam towards the laser, it would experience a kick in the opposite direction, slowing it. Finally, when the atom de-excites, the spontaneous emission would be in a random direction, which over many cycles gives an average slowing, or 'cooling', effect in that direction. Due to the random nature of the spontaneous emission it does not itself contribute

to the cooling effect. As the strength of this interaction is dependent on the effective detuning of the atoms versus the incident photon frequency: $\Delta \pm \vec{\mathbf{k}} \cdot \vec{\mathbf{v}}$, where $\vec{\mathbf{k}}$ is the wavevector of the photons which for opposing directions is either positive or negative, $\vec{\mathbf{v}}$ is the velocity of the atom, and Δ is the detuning of the laser photons - it is known as Doppler cooling [14, 15, 65].

More formally, the force associated with Doppler cooling can be thought of as a scattering force as it is also dependent on the photon scattering rate and atom de-excitation times as well as the photon momenta [66, 67]:

$$F_{\text{scatt}} = \frac{\hbar k \Gamma}{2} \frac{I/I_{\text{sat}}}{1 + I/I_{\text{sat}} + 4\Delta^2/\Gamma^2}, \tag{2.1.1}$$

where k is the photon wavenumber, Γ is the natural linewidth of the atom transition, I_{sat} is the saturation intensity of the transition, I is the photon beam intensity, and Δ is the detuning of the photon frequency relative to the transition frequency whilst taking into account the Doppler shift ($\Delta = \omega - \omega_0 - \vec{\mathbf{k}} \cdot \vec{\mathbf{v}}$). This is the case when considering a plane wave in the low intensity limit [68–71].

From equation 2.1.1 we can extract several useful metrics for future analysis of the experiment. To begin, as the intensity of the photon beam $I \to \infty$, we reach the maximum force experienced by the atoms:

$$F_{\text{max}} = \frac{\hbar k \Gamma}{2}, \tag{2.1.2}$$

which in turn can be used to identify the maximum acceleration (due to the relationship of $F_{\text{max}} = m a_{\text{max}}$) and interesting parameters associated with it:

$$a_{\text{max}} = \frac{\hbar k}{m} \frac{\Gamma}{2} = \frac{v_r}{2\tau}, \tag{2.1.3}$$

where m is the mass of the atom, v_r is the recoil velocity of the atom for each photon absorption, and τ is the lifetime of the excited state before de-excitation.

Finally, using equation 2.1.3 we can establish a length scale of a 'stopping distance' from which an atom can be slowed to rest:

$$L_0 = \frac{{v_0}^2}{a_{\max}}, \tag{2.1.4}$$

where v_0 is an arbitrary initial atom velocity in the direction of the beam.

In the case of a gas, however, the atoms can have any random components of velocity in 3D space and so require cooling beams in all 3 axes, a technique known as an optical molasses. For the purposes of this discussion, I am going to leave aside the fact that this technique can be used to cool to sub-Doppler temperatures and will not address this process as optimal parameters for a MOT do not fall within the low intensity limit that is required for sub-Doppler cooling. In this instance, the forces experienced by the atoms do not balance until the atom has zero velocity for anti-parallel cooling beams due to the Doppler effect. One can derive the general behaviour of the force by the sum of opposite instances of equation 2.1.1, giving the molasses force F_{mol}:

$$\begin{aligned} F_{\text{mol}} &= F_{\text{scatt}}(\Delta - kv) - F_{\text{scatt}}(\Delta + kv) \\ &\approx -2\frac{\partial F}{\partial \Delta} kv \\ &= -\alpha v. \end{aligned} \tag{2.1.5}$$

A low velocity range has been assumed in this relation for the case that $|\,\vec{\mathbf{k}} \cdot \vec{\mathbf{v}}\,| \ll \Gamma$. The cooling beams therefore, exert a force that is proportional to the velocity of the atom, not dissimilar to a treacle or molasses [19, 72].

Assuming the photon beam is monochromatic, the maximum velocity range of interactions is also very small, on the order of Γ/k, or $\approx 9\ \mathrm{m\,s^{-1}}$ for caesium. Figure 2.1 shows the effect that varying the ratio of the photon detuning with regards to the transition linewidth can have on the force experienced by atoms travelling at various velocities when two opposing beams of photons are incident upon them. The maximum decelerating force for caesium is shown to be experienced by atoms travelling at $8.9\ \mathrm{m\,s^{-1}}$, with a detuning factor of -2.

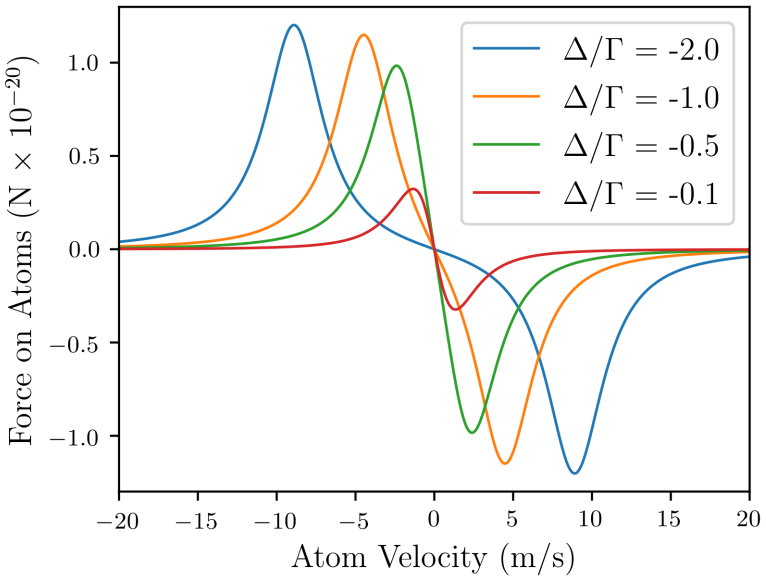

Figure 2.1: The relationship between resultant forces (F_{mol}) on caesium atoms with two anti-parallel molasses beams incident on them, and their velocity, for a range of detuning factors. Atoms experience a maximum force at $\Delta/\Gamma = -2$. For a given detuning, the velocity distribution within the peaks is the capture velocity range described by equation 2.1.14.

2.1.1.2 The Limits of Doppler Cooling

As the atoms' velocities are decreased, the laser detuning factor Δ tends to zero meaning that they experience a smaller retarding force. There are two main methods to combat this effect: chirp cooling [73] and Zeeman slowing [70].

The former involves a detuning sweep of the laser frequency in order to stay resonant with the atoms as the Doppler shift changes [74]. The resultant profile of which is a narrow band of colder atom velocities from which to measure the temperature, but still an overall large average velocity because of the larger proportion of atoms that were not cooled. The latter uses an inhomogeneous magnetic field such that as atoms travel through it, the Zeeman effect causes them to remain resonant to the slowing beam. A more esoteric method of compensating for the Doppler shift involves using curved wavefronts generated by continually reflecting a laser beam between pairs of near-parallel mirrors for a transverse cooling effect of a particle beam [75].

To understand the order of minimum temperatures achievable using Doppler cooling, we begin by considering a single cooling beam and how the force from that

beam on the atoms is composed: absorption and spontaneous emission and how these can have a heating effect. Thus we set the relationship as follows:

$$F = F_{\text{abs}} + \delta F_{\text{abs}} + F_{\text{spont}} + \delta F_{\text{spont}}, \tag{2.1.6}$$

where on average, $\bar{F}_{\text{abs}}$ is in fact equation 2.1.1 while $\bar{F}_{\text{spont}} = 0$ as the emission direction profile is entirely isotropic. The remaining variables are due to the fluctuations in the previous processes. Spontaneous emission always follows a scattering event and gives a recoil in a random direction, leading to random walk in the velocity of the atom. If there are n scattering events in a time t then we can write the following relation:

$$n = R_{\text{scatt}} t, \tag{2.1.7}$$

where R_{scatt} is the latter part of equation 2.1.1 (neglecting the photon momentum term $\hbar k$). This emission causes the overall mean squared velocity to increase as $\bar{v^2} = v_r^2 R_{\text{scatt}} t$, or with regard to a single axis:

$$[\bar{v_z^2}]_{\text{spont}} = \eta v_r^2 R_{\text{scatt}} t. \tag{2.1.8}$$

Each photon emission gives a kick in the z-axis of $\hbar k \cos\theta$ and so the factor of η is added to represent the angular average direction $\langle \cos^2 \theta \rangle$ which for an isotropic emission is $1/3$.

Finally, the variations in $\delta \bar{F}_{\text{abs}}$ are due to the atoms not always absorbing the same number of photons in time t. This heating is very similar in form to equation 2.1.8 but neglects the η term as all the absorption happens in one direction:

$$[\bar{v_z^2}]_{\text{abs}} = v_r^2 R_{\text{scatt}} t. \tag{2.1.9}$$

To account for a corresponding anti-parallel cooling beam we simply double the scattering term R_{scatt}. From here, we can insert equations 2.1.9 and 2.1.8 into equation 2.1.5 which, when stated in terms of Newton's second law, reveals links to the atom temperature limits:

$$\frac{1}{2}m\frac{d\bar{v_z^2}}{dt} = (1+\eta)E_r(2R_{\text{scatt}}) - \alpha\bar{v_z^2}, \tag{2.1.10}$$

where $E_r = \frac{1}{2}mv_r^2$. To estimate this relationship in the case of six beam orthogonal overlap and the low intensity limit, we assume that the scattering rate is $6\times R_{\text{scatt}}$ and that the factor η must be $3\times$ greater than the case of 2 overlapping beams. At the point of minimal average velocity, the time derivative in equation 2.1.10 must be 0 and so we can rearrange for the average square velocity:

$$\bar{v_z^2} = 2E_r\frac{2R_{\text{scatt}}}{\alpha}. \tag{2.1.11}$$

This kinetic energy can be related to the temperature of the atoms by the equipartition theorem: $\frac{1}{2}m\bar{v_z^2} = \frac{1}{2}k_{\text{B}}T$. Substituting α and R_{scatt} into equation 2.1.11 gives a general expression of temperature with regards to the transition linewidth and cooling beam detuning:

$$k_{\text{B}}T = \frac{\hbar\Gamma}{4}\frac{1+(2\Delta/\Gamma)^2}{-2\Delta/\Gamma}, \tag{2.1.12}$$

which has a minimum value when $\Delta = -\Gamma/2$ of:

$$T_{\text{D}} = \frac{\hbar\Gamma}{2k_{\text{B}}}. \tag{2.1.13}$$

This is the Doppler cooling limit relation and is the expected minimum temperature of atoms cooled by the optical molasses technique. For comparison, the predicted Doppler temperature for the Cs D2 cooling transition is 126 μK whereas for Rb it is 146 μK. By rearranging for the 'Doppler velocity limit' we can find two other interesting characteristic values:

$$v_{\text{D}} \approx \sqrt{\frac{\hbar\Gamma}{M}} = \sqrt{\frac{\hbar k}{M}\frac{\Gamma}{k}} = \sqrt{v_r v_c}, \tag{2.1.14}$$

where v_r is the recoil velocity, as described above, while v_c is approximately the capture velocity of the optical molasses technique.

While this theory does not take into account the subtleties of the degenerate

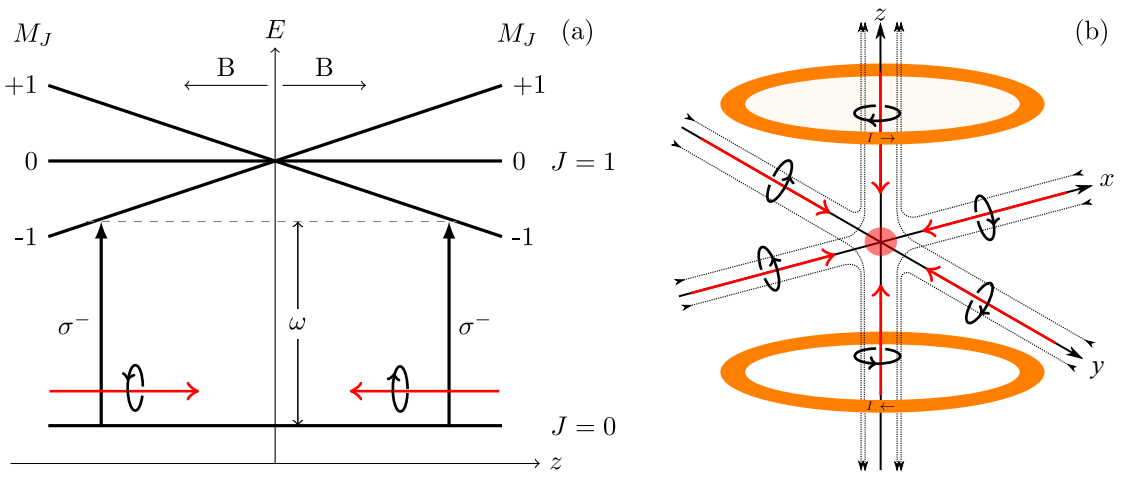

Figure 2.2: (a) The MOT mechanism for a $J = 0 \rightarrow J = 1$ transition. The B field gradient causes spatially dependent Zeeman splitting of the $J = 1$ state. Two anti-parallel beams with opposite circular polarisation are incident on an atom. Incoming beams drive σ^- transitions while outgoing beams drive σ^+ transitions. (b) A representation of a MOT showing the 3 orthogonal pairs of anti-parallel cooling beams with dashed lines to represent the B field. The helicity of the light necessary for trapping is dependent upon the relative directions of the E and B field vectors. When the field vectors are parallel, left-hand circular polarisation is required to excite a σ^- transition, whereas right-hand circular polarisation is required when the field vectors are anti-parallel.

energy levels of atoms, it still gives a reasonable approximation for the general results of laser cooling and a basis from which to analyse cooling in a GMOT [76].

2.1.2 Magneto-Optical Trap

The MOT can be thought of as a combination of the optical molasses (with careful choice of beam polarisations) and Zeeman slowing techniques wherein the orthogonal cooling beams provide a velocity dependent force and the magnetic field gradient provides a force that is spatially dependent for a more effective trap. Typically, a weak magnetic quadrupole field is generated using coils of opposing current direction for a B field minimum halfway between the coils [20, 77].

The basics of a MOT can be readily explained in the simple case of a $J = 0 \rightarrow J = 1$ transition. Close to the B field zero, between the magnetic coils, there is a region of uniform field gradient that perturbs the atomic energy levels through the Zeeman effect. It causes the sub-levels of the $J = 1$ ($M_J = 0, \pm 1$) state to become

non-degenerate and vary linearly with the position of the atom from the B field zero.

As in the case of optical molasses, the cooling beams are red-detuned from resonance but they are also circularly polarised. The effect of this is that, in the case of an atom travelling in the z-axis towards the centre of the field, the $M = -1$ level is shifted closer to resonance which can, due to selection rules, be excited in a σ^- transition by an incoming circularly polarised cooling beam. Due to the changing direction of the B field vector, once the beam passes through the centre of the field it is then considered a σ^+ beam. Both beams thus act in unison to trap atoms within the region. This is illustrated in figures 2.2(a) and (b).

We can mathematically describe this process of trapping by taking the optical molasses force from equation 2.1.5 and inserting new terms to take into account this spatial dependence of the Zeeman effect that brings the atoms into resonance:

$$\begin{aligned} F_{\text{mol}} &= F^{\sigma^+}_{\text{scatt}}(\omega - kv - (\omega_0 + \beta z)) - F^{\sigma^-}_{\text{scatt}}(\omega + kv - (\omega_0 - \beta z)) \\ &\approx -2\frac{\partial F}{\partial \omega} kv + 2\frac{\partial F}{\partial \omega_0}\beta z \\ &= -2\frac{\partial F}{\partial \omega}(kv + \beta z) \\ &= -\alpha v - \frac{\alpha\beta}{k} z. \end{aligned} \tag{2.1.15}$$

The new terms, $\omega_0 + \beta z$ and $\omega_0 - \beta z$, are the resonant frequencies for the $\Delta M_J = \pm 1$ levels at a displacement z while the Zeeman shift at z is given by:

$$\beta z = \frac{g\mu_{\text{B}}}{\hbar}\frac{dB}{dz} z, \tag{2.1.16}$$

where g is the Landau g factor and μ_B is the Bohr magneton. Unlike equation 2.1.5 which is purely a velocity dependent 'cooling' force, equation 2.1.15 describes a cooling force with an additional term that provides a spatially dependent 'trapping' force.

Compared to the more simplistic analysis given above which was assumed to be operating in the low intensity and therefore limited by potential stopping distance, MOTs generally have a greater capture velocity range v_c [77] due to their larger

beam widths [78] and so can be easily loaded from a background vapour of Rb or Cs. This allows two-step experiments wherein atoms are first captured in a MOT and then further cooled by disengaging the magnetic field for an optical molasses in the low intensity limit. A process such as this counteracts the fact that the lowest achievable temperatures in a MOT are much higher than that of an optical molasses as it requires beam intensities of the order $I >> I_{\text{sat}}$ and large detunings of $\Delta \approx -2\Gamma$. This muddies the analysis and leads to the conclusion that simple Doppler theory is an adequate description of the system. The standard result then, for the temperature of an isotropically illuminated region of atoms by 6 orthonormal cooling beams is [79]:

$$T_6 = T_{\text{D}} \frac{1 + s_{\text{T}} + 4\Delta^2/\Gamma^2}{-4\Delta/\Gamma}, \tag{2.1.17}$$

where s_{T} is the saturation parameter of the total intensity $\frac{I_{\text{T}}}{I_{\text{S}}}$ and T_{D} is the Doppler temperature as defined in equation 2.1.13. One can also calculate the size of a MOT from the temperature because the constants α and β are proportional to each other. This is due to the equipartition of energy theorem [80] which requires that the MOT temperature, velocity spread, and position spread are related by:

$$k_{\text{B}} T = m v_{\text{rms}}^2 = \frac{\alpha\beta}{k} z_{\text{rms}}^2. \tag{2.1.18}$$

Assuming that the MOT has not reached its density limit in which radiation pressure from spontaneous emissions within the trap becomes greater than the inward restoring force causing the trap size to increase with increased atom number [81].

A final consideration for this brief introduction on magneto-optical traps is the loading rate of the trap. For general circumstances the rate of population increase in a MOT can be modelled using the following simple rate equation

$$\frac{dN}{dt} = R - \frac{N}{\tau}, \tag{2.1.19}$$

where R is the loading rate, which is dependent upon the supply of atoms from the background gas of the chamber that meet the requirements for trapping, and τ is the MOT lifetime. This is determined by factors such as the collision rate of trapped

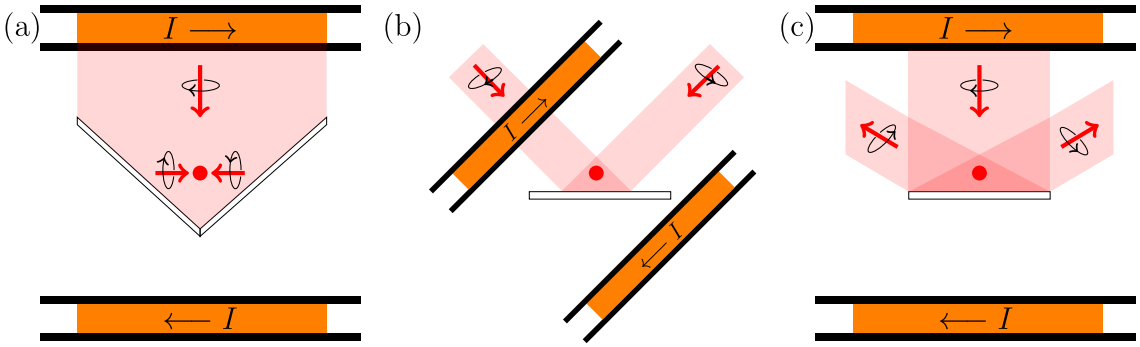

Figure 2.3: 2D representations of various MOT geometries including; (a) a pyramid MOT consisting of a single circularly polarised beam rebounded within a pyramid structure. (b) a planar mirror MOT where 2 of the 4 input beams are represented and (c) a GMOT, showing 2 of the possible diffracted beams (of 3, +1 order beams in my geometry). I in these diagrams denotes the current used in the coils to generate the B field for trapping.

atoms with the background gas. It is important to note that Equation 2.1.19 is only valid during initial formation of the trap as the population will soon reach a steady state value which is also dependent upon other factors such as trapping beam width and detuning [81].

2.2 Grating Magneto-Optical Trap

As previously illustrated in figure 2.2, a typical MOT uses 6 circularly polarised beams to confine a cloud of atoms - either individually controlled or retro reflected in pairs; the grating magneto-optical trap or 'GMOT' is a single beam atom trap that utilises a planar diffractor to split the incoming beam into additional, upward directed confinement beams. It could be thought of as an evolution on the principle of a pyramid MOT wherein an incident beam is split at 90° by mirrors in an internal pyramid structure to give the correct polarisation and beam balance [82, 83] or a planar mirror MOT that requires more input beams but allows greater access to the atomic cloud [84–86]. The key advantage of a GMOT is in its geometry which allows greater access to the atom cloud as well as having only a single input beam. It is because of this, as well as its small size, that we have used it to design a compact ion source. These designs are illustrated in figure 2.3.

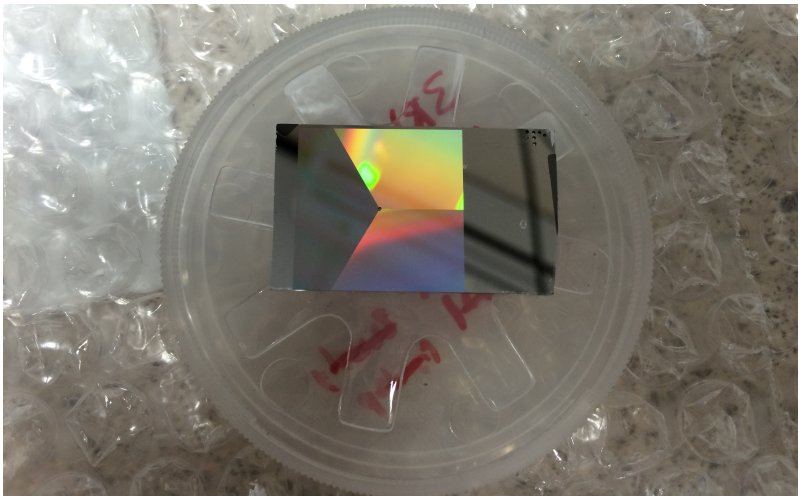

Figure 2.4: The triad diffraction grating chip as it arrived in Durham. This chip has an active grating area of approximately 400 mm^2 split into three subsections with points at 120° to each other. Each subsection has a grating pitch of 1500 nm, an etch depth of 195 nm, and a duty cycle of 50:50. They are not blazed and therefore diffract into both the ±1 orders while all other orders are minimised by design. The input beam power is split evenly between the ±1 orders but the intensity of the resultant beams is increased due to their geometric constriction. At the centre of the diffraction subsections is a hole of radius of 250 µm which is designed to allow the passage of ions.

2.2.1 Grating Design

The grating chip that we have used (Figure 2.4) was designed and graciously provided by the Experimental Quantum Optics and Photonics group of Strathclyde University. In this subsection, I will focus on the properties of our chip, but more information on the history of the Strathclyde development process, prior designs and in-depth discussions can be found in the noted papers and thesis, from which I draw the following technical explanations and derivations for the predicted GMOT radiation balance and temperature estimates - leading to the analysis thereof: [59, 87–93].

The active area of the chip measures approximately 400 mm^2 split between three separate diffraction grating sections. Each of these sections is a periodic linear grating with a duty cycle of 50:50, an etch depth of 195 nm and periodicity of 1500 nm. The principle of its operation is the Bragg condition:

$$m\lambda = d \sin\theta, \tag{2.2.1}$$

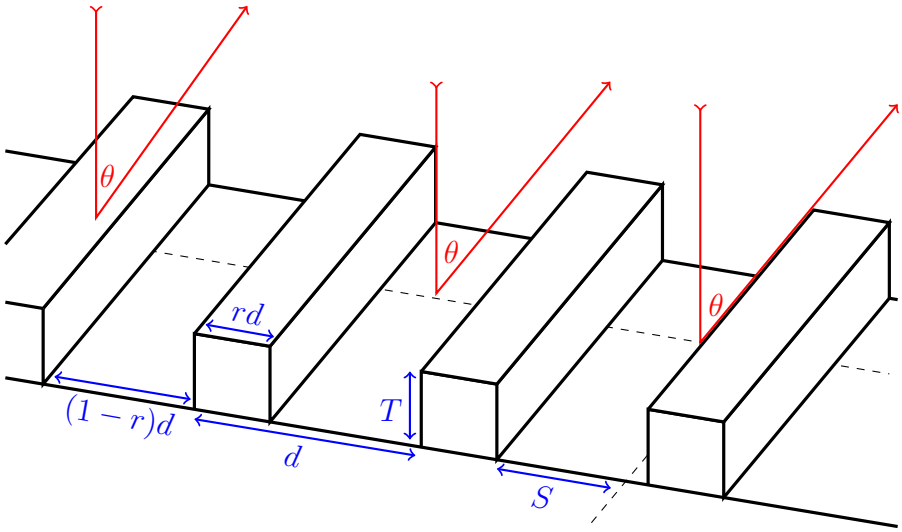

Figure 2.5: Idealised diagram of the grating design where θ is the Bragg diffraction angle, r is the duty cycle of the grating, d is the grating period, T is the etch depth, and S is the effective trough width given the shadowing from the peaks.

where m is the order of diffraction, λ the wavelength of the incoming beam perpendicular to the grating, d the grating periodicity, and θ the 1$^{\text{st}}$ order diffraction angle relative to the normal. Using the known characteristics of the chip and equation 2.2.1, one can calculate θ to be 35°; resulting in a possible trapping volume of approximately 0.46 cm^3 (the geometry of this will be discussed in section 2.3.4 with figure 2.12).

The characteristics of the chip allow for a negligible 0^{th} order diffraction (m = 0) while prioritising the 1$^{\text{st}}$ order (m = 1) resulting in a trapping region composed of 4 beams. The grating is not blazed and so gives equal diffraction efficiency in the m = $\pm$1 orders.

Figure 2.5 shows the idealised nanoscale structure of the diffraction grating where d and θ are described by equation 2.2.1, T is the etch depth of the grating, r is the duty cycle, and S is the effective etched width. Originally this grating was designed for cooling and trapping Rb, and so these factors are optimised for this purpose. Despite this, there is evidence to suggest that this grating design is widely applicable and can give the necessary ingredients for trapping of a number of alkali metals [91]. For this analysis I will focus on Cs and break down the differences in performance versus Rb to be expected over the following subsections. It should also be noted that

prior to section 2.3.5, the grating is assumed to be perfectly uniform and therefore give a uniform diffraction efficiency.

2.2.1.1 Phasor Diffraction Model and Balancing Radiation Pressure

Fortuitously, the diffraction from the grating can be modelled using a simple phasor diagram approach that considers the grating to be a series of periodically placed, reflective elements with a variable depth component which can be seen on figure 2.6 [94] while assuming an input beam perpendicular to the grating. (This is as opposed to a more complex treatment of the grating using Maxwell's equations.) A discussion on the necessity of a perpendicular input beam can be found in reference [91]. This approach also shows how, on a nano scale, the final beam, and thus electric field, is formed of many diffracted orders from both the peaks and troughs of the grating. They are weighted by their duty cycles, r and $r_t = (1 - r)$ with phase shifts determined by the path difference between AB $= \frac{d}{2}\sin(\theta)$ and CDE $= T(1 + \cos\ \theta)$:

$$E_{\text{tot}} \propto \sqrt{\rho}(r + r_t e^{i\phi}), \tag{2.2.2}$$

where $\phi = \frac{2\pi}{\lambda}(m\lambda/2 - T(1 + \cos\ \theta))$, ρ is the surface reflectivity, and T is the etch depth of the grating. In the case of a 50:50 duty cycle (which our chip has) a first order diffraction efficiency can be calculated:

$$\eta_1 = \rho\frac{|1 + \exp[i\pi(1 - 2T(1 + \cos\ \theta)/\lambda)]|^2}{8}. \tag{2.2.3}$$

From equation 2.2.3 we have relationships between the diffraction efficiency in the first order to both the input wavelength and grating period. In the simplest, assuming that there are no orders of diffraction for $|m| \geq 1$ and that the process is lossless:

$$2\eta_1 + \eta_0 = \rho. \tag{2.2.4}$$

Back in equation 2.2.3 we can also manufacture a more simple relationship by defining an optimal etch depth T as $\lambda_{\text{d}}/4$, where λ_{d} is the wavelength for which the

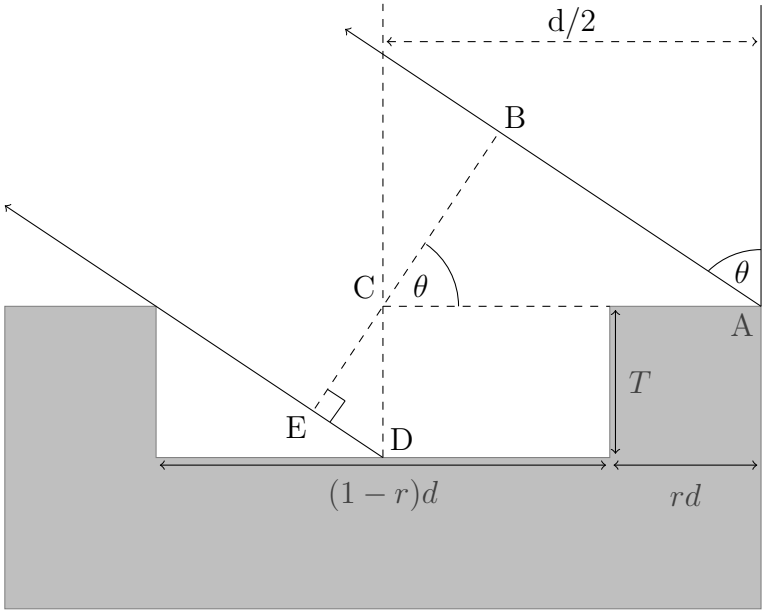

Figure 2.6: Diagram of the simplified phasor grating model where T is the etch depth, θ is the Bragg diffraction angle, d is the grating period, and r is the duty cycle.

grating has been designed to cool at (this will be further explained in the following subsection) - in this case 780 nm to target the Rb D2 transition. Finally, using the small angle approximation $\cos\ \theta \approx 1$, we arrive at:

$$\eta_1 = \rho \frac{[1 + \exp(i\frac{\pi\lambda_\mathrm{d}}{2\lambda})]^2}{8}. \tag{2.2.5}$$

To achieve radiative balance in the z axis, the incoming intensity I, and the components of the diffracted intensities I_d, anti-parallel to I, must be equal: $\frac{I_{dy}}{I} = \eta_1 \frac{\omega}{\omega_d} = \frac{\eta_1}{\cos\ \theta} = 1$, where ω and ω_d are the incident and diffracted beams' respective widths. The balance then, is between the net incident intensity: $I(1 - \eta_0)$ and $NI_d \cos\ \theta \rightarrow NI\eta_1$ where N is the number of diffracted beams. Finally, this gives:

$$\eta_\mathrm{B} = \frac{N\eta_1}{1 - \eta_0}, \tag{2.2.6}$$

which can be used to assess a large input wavelength and grating period range, given a fixed manufactured value of T. The radial power balance does not need to be addressed as there is radial symmetry in the case of a Gaussian input beam centred on the grating with circular polarisation and balanced efficiency of the grating sections.

2.2.1.2 Avoiding a Strong Back-Reflection

It is optimal for T to be $\lambda_d/4$ as this minimises the back-reflection of the incident beam. To explain this, we start by refining the analysis derived from figure 2.6 and introducing S from figure 2.5. This is the effective trough area from which light can be diffracted due to the shadowing effect of the peaks on the troughs. By combining the two figures, it can be seen that: $S = (1-r)d - T\tan\theta$, which can be used to define the path difference between the rays coming from the centre of a peak and this reduced trough centre:

$$\Phi = k\left[\frac{(d - T\tan\theta)\sin\theta}{2} - T(1+\cos\theta)\right], \tag{2.2.7}$$

where $k = 2\pi/\lambda$. By again taking the grating reflectivity to be ρ and assuming a relatively large propagation distance of the electric field from the grating surface, the field can be approximated using the Fraunhofer integral:

$$\frac{E(\theta)}{E_{\text{in}}} = \sqrt{\frac{\rho}{R\lambda}}\left(\int_{-rd/2}^{rd/2} e^{ikx\sin\theta}dx + e^{i\Phi}\int_{-S/2}^{S/2} e^{ikx\sin\theta}dx\right)\left(\sum_{n=1}^{N} e^{iknd\sin\theta}\right), \tag{2.2.8}$$

where R is a propagation distance. The square of equation 2.2.8 is the intensity distribution of the field which has maxima at the Bragg angles from equation 2.2.1. Due to the constant grating period d and a large number of grating lines illuminated, the single-period factor is essentially constant over the relatively small angular spread of the Bragg peaks. One can therefore integrate over an m^{th} order to find the total power in that order:

$$\frac{P_m}{P_{\text{in}}} = \frac{\rho}{d^2}\left|\int_{-rd/2}^{rd/2} e^{2\pi imx/d}dx + e^{i\Phi}\int_{-S/2}^{S/2} e^{2\pi imx/d}dx\right|^2, \tag{2.2.9}$$

where P_{in} is the incident power on N illuminated grating lines, which, when evaluated, gives:

$$\frac{P_m}{P_{\text{in}}} = \frac{\rho}{m^2\pi^2}[\sin^2(m\pi r) + \sin^2(m\pi S/d) + 2\cos(\Phi)\sin(m\pi r)\sin(m\pi S/d)]. \tag{2.2.10}$$

In order to achieve the greatest efficiency for cooling, the 0^{th} order diffraction (retro-reflection) has to be eliminated because it will imbalance the trapping beams as described above. This must be achieved through choice of grating design parameters which can be deduced with the following logic: first, Φ is eliminated by subbing equation 2.2.7 into equation 2.2.10 and taking the limit as $m \to 0$ to reach:

$$\frac{P_0}{P_{\text{in}}} = \rho \left[1 + 2r(r-1) \left(1 - \cos \left(\frac{4\pi T}{\lambda} \right) \right) \right], \tag{2.2.11}$$

which tends to 0 when $r = \frac{1}{2}\left(1 + \frac{i}{\tan(2\pi T/\lambda)}\right)$. Given that the duty cycle must be a real value, an infinite divisor must be devised by manufacturing the etch depth to be $\frac{\lambda}{4}$, which for our grating is the target design wavelength λ_{d} of 780 nm. To ensure this effect, the input beam must be perpendicular to the grating surface [91]. Later in this chapter I will analyse what difference my use of 852 nm makes on the grating effectiveness as well as present an efficiency map of the grating.

2.2.1.3 GMOT Temperatures

Next we can consider how the temperature of the trapped atoms is affected by the unconventional geometry of the GMOT and how this compares to the standard 6 beam setup described by equation 2.1.17. In order to stay consistent with this equation throughout, I have assumed the parameters of $I_t >> I_{\text{sat}}$ and $\Delta \approx -2\Gamma$ as well as the polarisation of the diffracted beams of intensity I_i, being consistent with the spatially uniform incoming beam of intensity I_0. The following is essentially an expansion of the theory in section 2.1.1.2 into 3D.

First, we define the wave vector of the incoming beam onto the grating as $\vec{\mathbf{k}}_0 = k\{0, 0, -1\}$, where k is $\frac{2\pi}{\lambda}$, which will be diffracted into N orders from the grating with intensities of $I_i = I_0/N \cos\theta$ where $i = 1, 2, ..., N-1, N$ and wavevectors: $\vec{\mathbf{k}}_i = k\{\sin\theta \sin\frac{2\pi i}{N}, \sin\theta \cos\frac{2\pi i}{N}, \cos\theta\}$. θ here is consistent with equation 2.2.1 which in this setting is the angle from the vector {0,0,1}. The total intensity of the diffracted beams is thus: $I_t = \sum_{i=0}^{N} I_i = (1 + \sec\theta) I_0$ from which the heating due to spontaneous emission and absorption can be calculated.

As above, the spontaneous emission is assumed to be isotropic which gives a

heating rate for a beam with a wavevector of the form $\vec{\mathbf{k}}_i = \{k_{ix}, k_{iy}, k_{iz}\}$ proportional to $\hbar^2 R_i k^2 \{\frac{1}{3}, \frac{1}{3}, \frac{1}{3}\}$, where R_i is the scattering rate:

$$R_i(\vec{\mathbf{v}}) = \frac{\Gamma}{2} \frac{s_i}{1 + s_\mathrm{T} + 4(\Delta - \vec{\mathbf{k}} \cdot \vec{\mathbf{v}})^2/\Gamma^2}, \tag{2.2.12}$$

which for simplicity can be taken in the low velocity limit of capture range as: $R_i(0) = \frac{I_i}{I_\mathrm{sat}} R = s_i R$.

The heating caused by absorption in 3D is $\hbar^2 R_i \{k_{ix}^2, k_{iy}^2, k_{iz}^2\}$ and so the total heating effect on the atoms near zero velocity is the sum of these contributions:

$$\vec{\mathbf{H}} = \hbar^2 k^2 \frac{I_0}{6 I_\mathrm{sat}} R(\{2, 2, 8\} + \sec\theta\{3\sin^2\theta + 2, 3\sin^2\theta + 2, 6\cos^2\theta + 2\}). \tag{2.2.13}$$

As I have assumed the low velocity limit and balanced beam intensity, I can use a Maclaurin series to determine the total force about $\vec{\mathbf{v}} = 0$: $\vec{\mathbf{F}} = \sum_{i=0}^{N} \hbar \vec{\mathbf{k}} R_i(\vec{\mathbf{v}})$ which leads to dissimilar damping coefficients parallel ($\beta_\parallel$) and perpendicular ($\beta_\perp$) to the grating:

$$\vec{\mathbf{F}}(\vec{\mathbf{v}}) \approx -\vec{\boldsymbol{\beta}} \cdot \vec{\mathbf{v}} = -\{\beta_\parallel v_x, \beta_\parallel v_y, \beta_\perp v_z\}, \tag{2.2.14}$$

for:

$$\{\beta_\parallel, \beta_\perp\} = \beta_6 \left\{ \frac{\sin\theta \tan\theta}{4}, \frac{1 + \cos\theta}{2} \right\}, \text{where } \beta_6 = \frac{-16\hbar I_0 k^2 R \Delta}{I_\mathrm{sat} \Gamma^2 (1 + s_\mathrm{T} + 4\Delta^2/\Gamma^2)}$$

is the damping force in the case of a standard 6 beam MOT as described in the latter part of section 2.1.2. The final expected MOT temperature in each dimension is then the steady state ratio of the damping forces (equation 2.2.14) and atom heating (equation 2.2.13) which can be given in a form only dependent on the grating diffraction angle θ:

$$(T_\parallel, T_\perp) = \frac{T_6}{6} \left\{ 3 + \csc^2 \frac{\theta}{2}, 3 + \sec\theta \right\} \tag{2.2.15}$$

This however, does not entirely agree with experimental findings [59, 89] as it

only takes into account effects due to the direct absorption of light from the trapping beams and so neglects inter-atomic forces and spacing effects within the dense MOT region [95–98]. These processes slightly homogenise the temperatures between both dimensions to give the following relationship:

$$T = \frac{2}{3}T_{\parallel} + \frac{1}{3}T_{\perp}, \tag{2.2.16}$$

which agrees with experimental findings of the Strathclyde Photonics group [59].

2.3 GMOT Modelling

2.3.1 Introduction

The motivation of this section is to explain the disparity seen between the successful implementation of surface patterned grating chips using rubidium, in experiments such as those based at the University of Strathclyde and the Eindhoven University of Technology, and the so far unsuccessful Durham implementation using caesium.

The main finding of the modelling is that caesium traps may be less viable than rubidium traps using similar parameters and grating chips. This can be seen at all intensity and detuning factors and is largely due to the differences in the fundamental properties of caesium compared to rubidium (see table 2.1) and the compromises one must make in the generation of a GMOT. Throughout the modelling, the B field gradient is consistently 15 G/cm to reflect the maximum current the experimental coils can maintain. The base parameters include (unless stated otherwise): an input power of 89 mW, a beam waist of 2.2 cm, a beam truncation width of 1.2 cm and a detuning factor of -1.8 for both atomic species. These parameters are consistent with the experimental work.

In this section, I will expand upon this finding and the reasoning behind my conclusions with comparisons made between modelling of the Strathclyde traps and my own attempts at a caesium trap.

2.3.2 Model and Implementation

The modelling program that I have modified for use in this section was originally written with Mathematica and used by Aidan Arnold in a number of his publications on grating MOTs and diffraction chip properties. The program takes an incoming Gaussian beam of a given power and $1/e^2$ width then truncates it through a virtual aperture. The calculated intensity of this truncated beam is then incident on a triangular grating held within a region of a magnetic field with a defined linear gradient and zero point. The beam is then diffracted into the three upwardly projecting trapping beams with an angle to the normal θ as defined by the Bragg condition in equation 2.2.1. By taking into account the natural properties of the atoms such as their excitation wavelengths, transition saturation intensities, etc. as well as the polarisations and detuning of the trapping beams; the trap behaviour is calculated. The polarisation of the input beam is assumed to be circular and have uniformity in radial illumination. An illustration of this is shown in figure 2.7. Unless otherwise stated, all simulations were carried out using experimentally determined parameters [59, 87–92].

2.3.3 Power, Collimation, and Beam Radii

To begin the analysis, I will consider the interplay between the input beam power P_0, beam collimation $1/e^2$ radius w, and truncation aperture radius rA. As with a standard MOT, it is shown through the modelling that the curvature of the beam wavefront in a GMOT affects trap generation but to a much greater degree than the standard case. Figure 2.7 demonstrates the difference in trapping effect for caesium in the case of (a), $w = 1.2$ cm and, (b) $w = 3.0$ cm, with $rA = 1.2$ cm in both cases. For (a), it is unclear whether trapping could be achieved as the trap region can be seen to 'leak' into the outer circulation regions without additional shim fields to compensate for the reduced B field gradient in the x and y axes, whereas (b) shows a clear region of trapping, far from this same boundary. Early attempts at creating a caesium GMOT may have failed for this reason as beams with $w = 1.2$ cm were used.

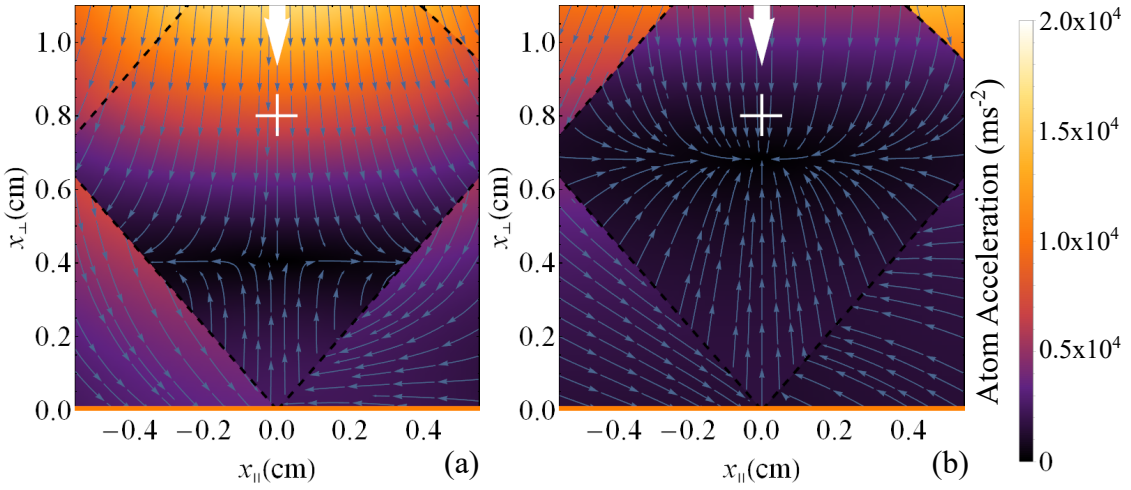

Figure 2.7: A comparison of caesium atom acceleration and trap region shape with varying gaussian beam $1/e^2$ radius for (a) $w = 1.2$ cm and (b) $w = 3.0$ cm. Both cases are with $rA = 1.2$ cm. The white arrow in both subfigures represents the incoming beam direction, while the cross indicates the B field zero position with no additional bias fields.

The effect that w has on the localisation of the trap can be explained through the first column of figure 2.8 which shows a series of intensity profiles in a cross section of the diffraction chip in the Z direction. As w is increased, the intensity profile has a smaller gradient for each section of summed illumination for a more 'top hat-like' trapping beam, and therefore, a more localised trap. This effect can be explained by considering the overlap of two wavefronts: the first, a heavily curved Gaussian front, and the other, a top hat function. In the case of the Gaussian, the intensity of the light is far smaller at the edges of the distribution than at the centre; resulting in very low intensities at the extremities of the final overlap region. The flat top function does not have this issue and so it provides even trapping beams over the entire overlap region. Thus, the largest possible waist is desirable.

The downside of increasing w can first be seen in figure 2.7 where the more localised trap shows a 54% decrease in peak acceleration despite all other variables being consistent. This is due to the decrease in intensity caused by increasing the beam width, as illustrated in column 2 of figure 2.8. The $w = 1.2$ cm case in column 2 of figure 2.8 shows a β_0 value (the ratio of input intensity to the transition saturation intensity) of approximately 14 whereas, after increasing to $w = 3.0$ cm, β_0 has fallen to approximately 4. Because of this interplay, the experimental value

of w has been set to 2.2 cm for a 'happy medium' scenario in which there is clearly a localised region predicted and the β_0 value is near the local maximum of the trapping coefficient.

Using these parameters, we can calculate useful metrics to describe the trapping behaviour for a range of intensities and detuning factors. Figure 2.9 shows the maximum acceleration that a caesium atom would experience in the region of the trap with reference to the aforementioned factors. The calculated accelerations are all negative as the atoms experience a retarding force. Crudely, by using known relations between the maximum acceleration, the intended stopping distance, and transition excitation time, one can then convert this plot to show the maximum expected capture velocity from the background gas, as shown in figure 2.10 using equation 2.1.4. Using this metric, we can begin to compare the differences between caesium and rubidium traps.

Figure 2.11 showcases the expected differences in maximum trapping velocity for caesium and rubidium for like parameters (aside from $w_{\mathrm{Rb}} = 2.0$ cm to reflect the Strathclyde experimental parameters). The leftmost colour plot 2.11(a) shows the maximum capture velocity for caesium as calculated from the maximum acceleration experienced by the atoms in relation to the distance they have in which to be cooled in the chamber. Figure 2.11(b) shows the same relationship for rubidium referenced to the Strathclyde experimental values. Both plots use the same colour ranges and share an x and y axis. The '$\times$' on figure 2.11(a) indicates the beam intensity and detuning factors used for the Durham experiment whereas the '$\triangle$' on figure 2.11(b) denotes the parameters of the Strathclyde experiment. Despite the disparity in beam intensities, it is clear that even if parity were achieved, the Cs GMOT would have approximately two thirds the capture velocity range or 59% of the maximum acceleration.

This means that the properties of Rb and Cs cause them to behave differently in a GMOT. These properties and their effects on maximum acceleration magnitude are given in table 2.1.

To begin, the wavelengths of the respective D2 transitions mean that rubidium cooling is 9.2% more efficient than caesium cooling due to the higher momentum

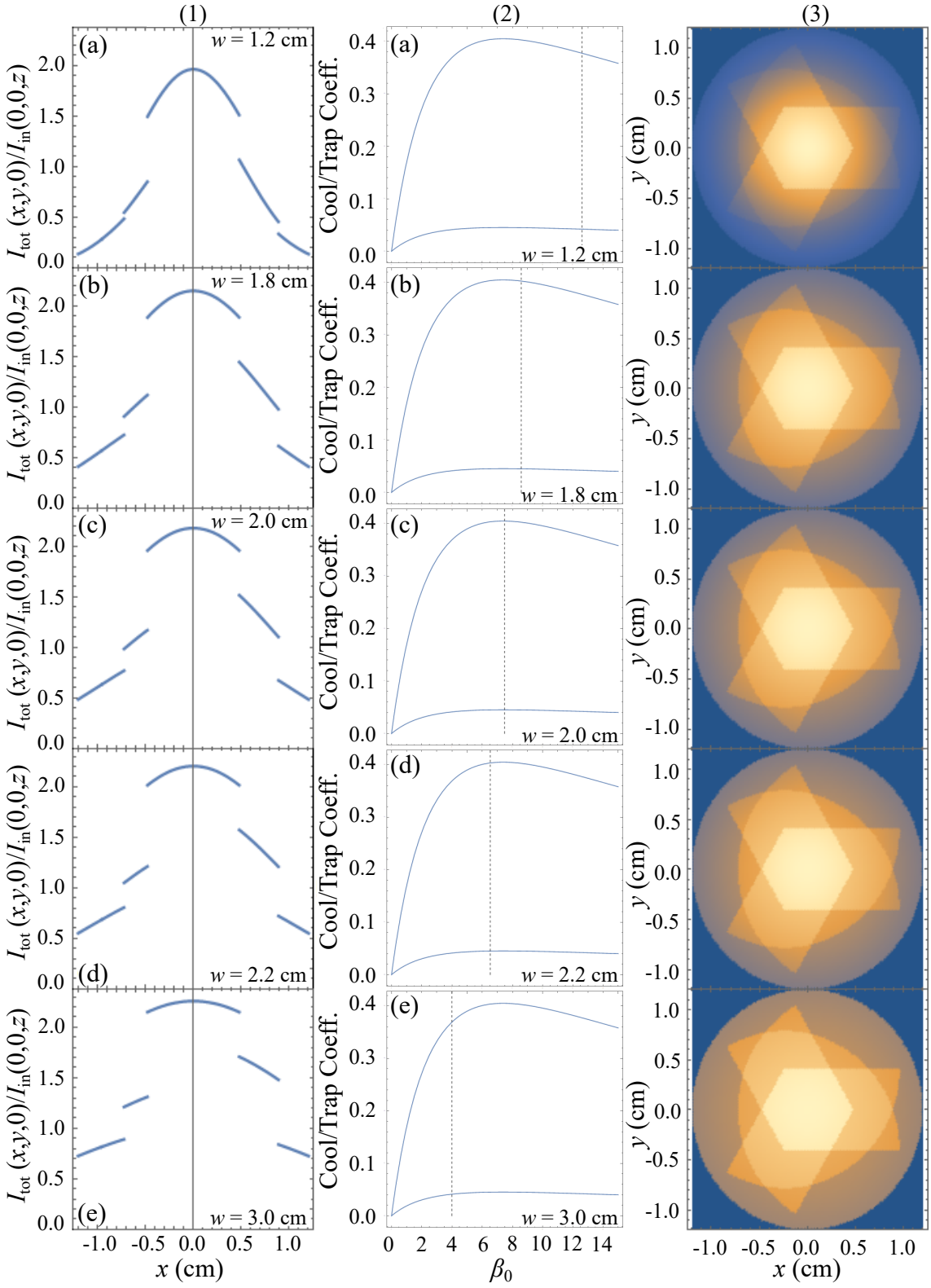

Figure 2.8: 2D projections of beam overlap (1), trapping coefficients (2), and top-down intensity profiles (3). The rows vary from a $1/e^2$ beam radius of $w = 1.2$ cm to 3.0 cm. Plots in column (1) correspond to a plot in column (3) as they represent a slice in the z axis across the y = 0 line. The dotted lines in column (2) indicate the β_0 value for each w with a constant power of 100 mW.

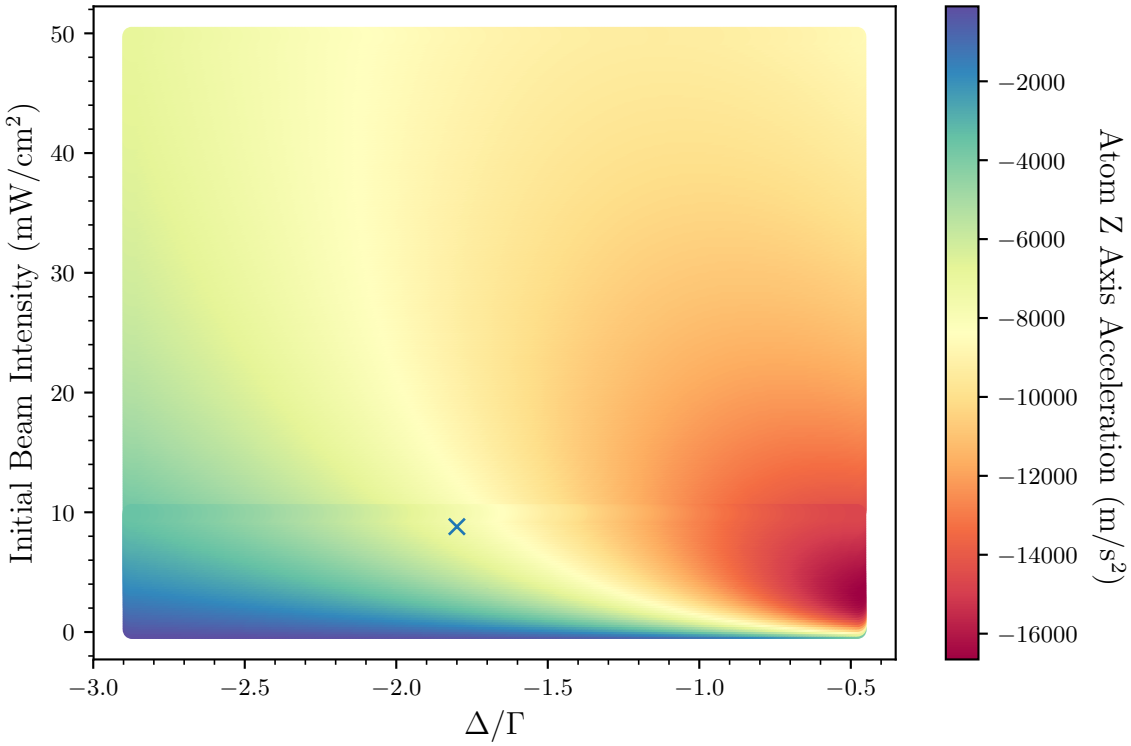

Figure 2.9: Colour plot of caesium atom acceleration in the z axis for a range of initial beam intensities and detuning factors where the '×' denotes the Durham experiment parameters.

per photon of the 780 nm wavelength. The incident wavelength on the grating also influences its diffraction angle which, as previously stated, can be determined by the Bragg relation: equation 2.2.1. A longer wavelength in this case gives a larger diffraction angle relative to the perpendicular and therefore a smaller overlapping region with a maximum height closer to the grating surface making the already difficult process of localising a magnetic field minimum to a small region more difficult.

The saturation intensity of caesium is the only advantageous property in table 2.1 with a marked decrease in efficiency of 12% when substituting the rubidium value. The I_{sat} value is a simple expression of how much intensity is required to saturate the respective transitions, but unfortunately, despite caesium having a I_{sat} value 66% of the Rb saturation intensity, its effect on acceleration magnitude is non-linear and so only accounts for a 12.3% reduction.

The natural linewidths of the transitions Γ are one of the larger contributors in the acceleration calculation. Physically, this is because it is also the decay rate of

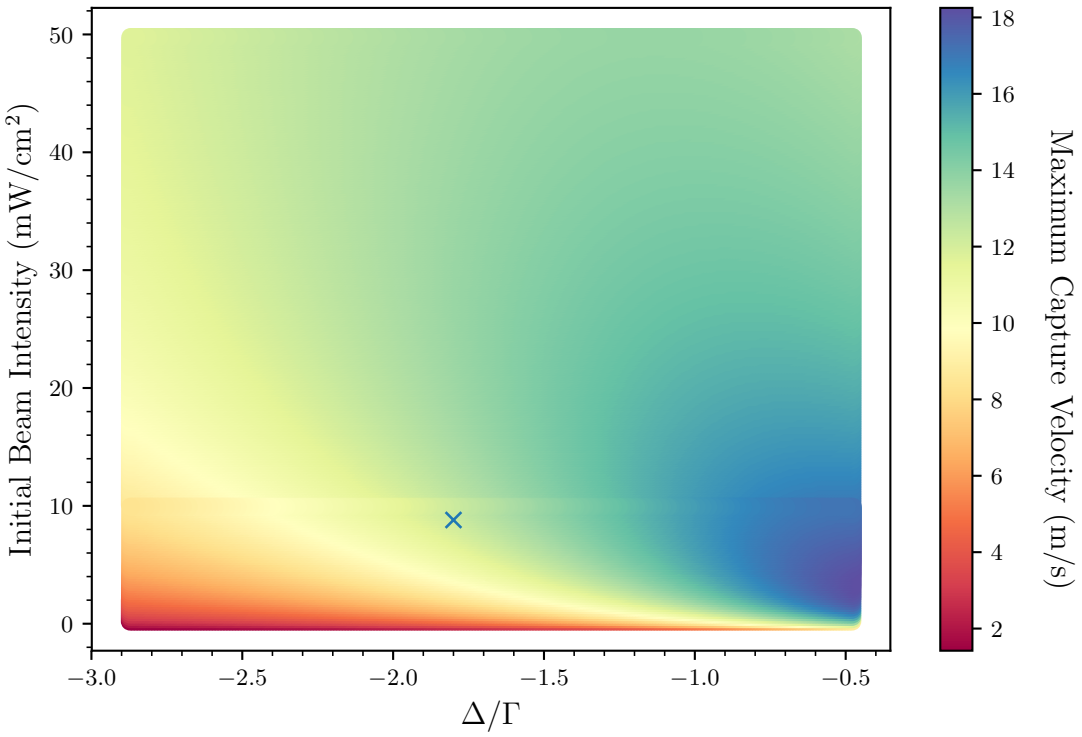

Figure 2.10: Colour plot of caesium atom capture velocity in the z axis for a range of initial beam intensities and detuning factors where the '×' denotes the Durham experiment parameters.

the transition. A higher decay rate necessarily means that, for a given time, more excitations and decays can take place for a more efficient cooling process. This factor is linear as a 16% difference in linewidth induces a nearly 16% change in acceleration magnitude which can, in part, be traced back to the initial descriptions of the scattering force and recognising it as a product of two elements: photon momenta and the scattering rate, which is linearly dependent on Γ.

Finally, the mass differential, which is the largest factor of acceleration magnitude difference in these calculations. As one would expect with Newton's second law, rubidium has 35% less mass and therefore has 52.9% greater maximum acceleration than caesium with the same force. Despite these factors, all but the saturation intensity of the atoms should make a difference as although the mass of the rubidium is lower, it has a corresponding drop in fraction of atoms within the capture velocity due to its increase in mean thermal velocity.

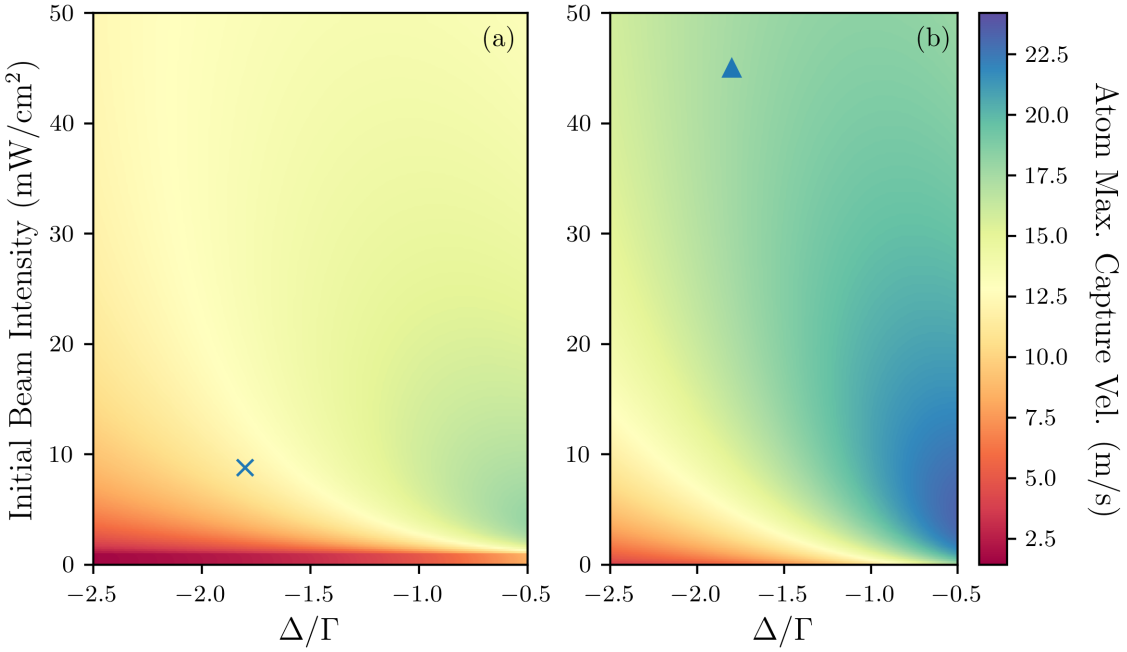

Figure 2.11: Comparison of (a) Cs where the 'X' denotes the Durham experiment parameters and (b) Rb maximum atom capture velocities in the z axis plotted on the same colour scale where the blue '△' denotes the Strathclyde experiment parameters.

2.3.4 Effects of λ and d

Next we can consider how the input wavelength λ, and grating period d, affect trap characteristics with comparisons of Cs and Rb.

First, the volume of the trap can be calculated using only these variables and simple geometric principles. From equation 2.2.1, we can determine the angle of diffraction perpendicular to the grating surface θ, and therefore its inner counterpart angle, ϕ. The general geometry is shown in figure 2.12, which includes the case of a diffraction chip with a central hole of radius B and grating major axis length of A. The shape of the GMOT volume formed by the trapping beams is non-trivial and can be thought of in terms of two connected pyramidal structures of differing bases. The bottom pyramid of volume V_H is hexagonally based with (due to the central hole in the chip) its point situated a distance $h_1 = B\cot\theta$ above the chip, and terminus, a distance $h_1 + h_2 = B\cot\theta + \frac{A\cot\theta}{2}$ above the chip.

Figures 2.12(a) and (b) illustrate how the trapping beam overlap region evolves from $z = 0$ (on the chip surface) to a point one quarter of the total trap height at

	Cs (18089 $\mathrm{m\,s^{-2}}$)	Rb (30776 $\mathrm{m\,s^{-2}}$)	Acc. Mag. ($\mathrm{m\,s^{-2}}$)	Diff. (%)
λ:	852 nm	780 nm	19761	9.2
I_{sat}:	1.10 $\mathrm{mWcm^{-2}}$	1.67 $\mathrm{mWcm^{-2}}$	15859	-12.3
Γ:	2π x 5.2227 MHz	2π x 6.067 MHz	21012	16.2
Mass:	2.2069 x 10^{-25} kg	1.443 x 10^{-25} kg	27665	52.9

Table 2.1: Properties of Cs and Rb and their effect on acceleration magnitude relative to each other while keeping all other experimental parameters e.g input power, magnetic field gradient, beam and aperture width, detuning factor, etc. consistent with values stated in section 2.3.1.

$z = h_1 + \frac{h_2}{2}$. These figures also show the source of the hexagonal cross section being the overlap of three triangles at 120° to each other. The third of the smaller plots figure 2.12(c), shows how the final base shape is formed as the beams progress: a Reuleux triangle-based pyramid of volume $\mathrm{V_{Re}}$, composed of three intersecting arcs. All the relevant measurements for calculation of the total volume have been marked on figure 2.12. Combining the two sections gives the total volume V, as:

$$\mathrm{V} = \mathrm{V_H} + \mathrm{V_{Re}} = \frac{\sqrt{3}\mathrm{A}^3}{16}\cot(\theta) + \frac{\mathrm{A}^3(\pi - \sqrt{3})}{16}\cot(\theta) = \frac{\mathrm{A}^3\pi}{16}\cot(\theta) \tag{2.3.1}$$

Thus, by varying λ and d, we can generate the expected GMOT volume for a number of prevalent cooling wavelengths and draw comparisons between Cs and Rb. An interesting side note from equation 2.3.1 is that it predicts that 55% of the volume of the trap is concentrated in its lower half. Thus, when designing trapping apparatus, this lower half should be prioritised. The temperature of the trap can also be predicted using equation 2.2.16 and how this varies for a range of λ and d.

Figures 2.13(a) and (b) show the variation of GMOT volume in the case of λ and d. In (a) we can see a clear advantage of Rb when using a grating chip where $d = 1500$ nm - or indeed any element with a cooling transition of a shorter wavelength than Cs. Specifically for Rb, this amounts to an 12% increase in possible trapping volume versus using Cs. In (b) the advantage is illustrated for lines of constant λ which shows how, due to the $\sin^{-1}$ relationship of equation 2.2.1 for θ, the 852 nm line becomes undefined at this longer wavelength, thus curtailing its efficiency.

Interestingly though, an advantage for Cs may arise from this smaller volume in

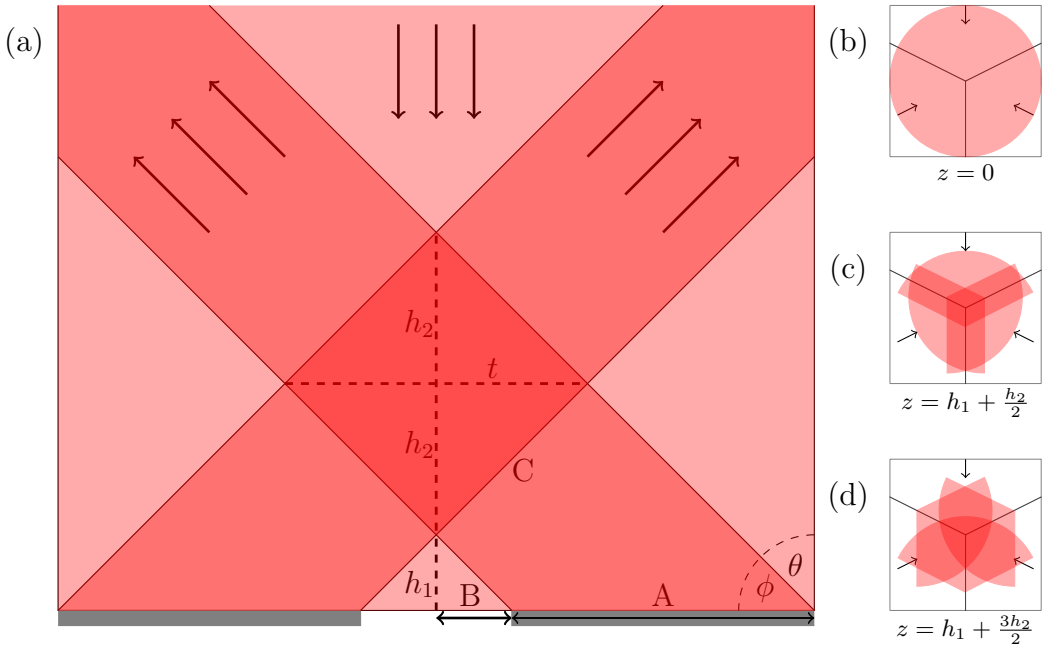

Figure 2.12: 2D profile of GMOT geometry where all dimensions can be derived from the Bragg diffraction angle θ, grating period d, and input beam radius rA which in this diagram is the sum of the grating radius A and hole radius, B. The three additional plots show the intensity overlaps at defined heights and the evolution of the tetrahedron base from hexagonal to a Reuleux triangle.

the form of decreased trap temperatures. The predicted temperature of the GMOT, calculated using equation 2.2.16, is shown in figures 2.14(a) and (b) for varying λ and d. While the relationships of figures 2.13(a) and 2.14(a) appear to be equivalent, the opposite conclusion can be drawn in that a Cs trap will reach a temperature 12.5% lower than the Rb equivalent. This may be due to the general nature of a MOT in that its spatial extent is proportional to its temperature, thus by limiting the possible volume, we are limiting its maximum possible temperature. As for figure 2.14(b), it demonstrates that for equivalent grating periods, the Rb trap will always be at a higher temperature. This behaviour is predicted in equation 2.1.18. Given the goal of creating a compact ion source this is a good finding as it implies a lower emittance (see chapter 3) from the source and is therefore less likely to require additional large and especially costly magneto-optical lenses.

One final matter, relating to the input beam wavelength and period of the diffraction grating, is the balance of radiation pressure. Section 2.2.1.1 introduced the method by which the diffraction grating can be considered as a series of periodically

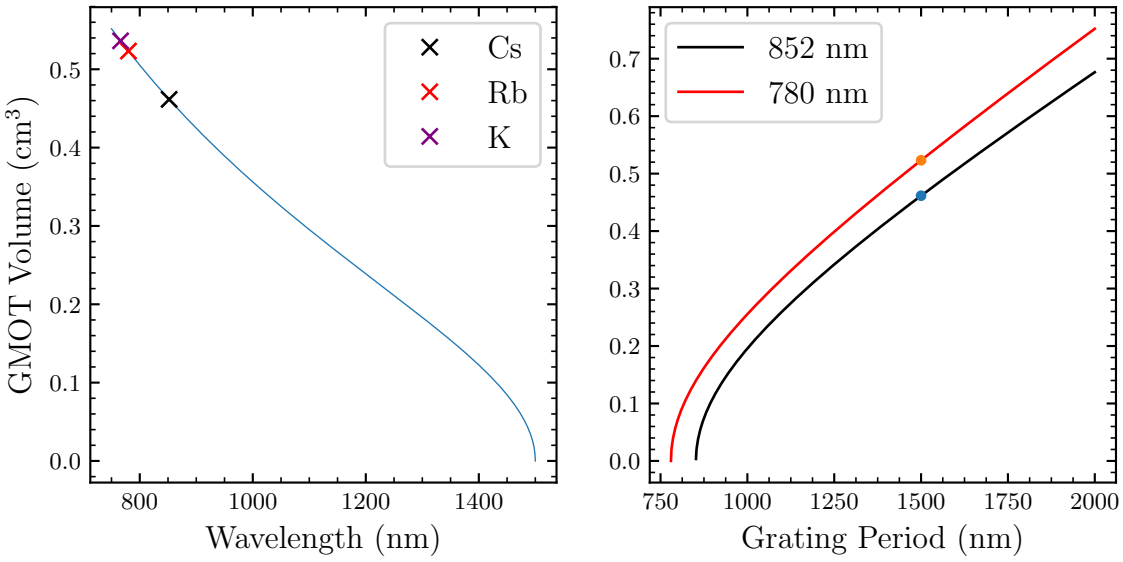

Figure 2.13: (a) GMOT volumes as calculated with equation 2.3.1 using a constant grating period of 1500 nm and several alkali metal D2 cooling transitions noted. (b) Volumes calculated with a constant wavelength for the Cs and Rb cooling transitions and varying grating period.

placed reflective elements with a variable depth component in order to derive its diffraction order efficiencies. A consequence of this analysis was that, for maximum efficiency at the intended input wavelength, the etch depth of the grating T, must be one quarter of that wavelength. This was taken into account in the chip fabrication, but as this series of chip was initially designed for cooling Rb at 780 nm, not Cs at 852 nm, there is a question as to how well the chip will perform.

Using equations 2.2.4, 2.2.5, and 2.2.6 one can compute the effect that using a non-intended wavelength will have, for a given etch depth, on the zeroth and first order diffraction efficiencies (η_0 and η_1) and thus the overall light balance, η_B. The three relations are plotted in figure 2.15, assuming a design wavelength of 780 nm and therefore an etch depth of 195 nm with a grating period d, of 1500 nm. The model predicts that between ~(670 nm-940 nm) a chip of these characteristics should produce only up to a 3% loss of first order beam efficiency and almost balanced light pressure for ±200 nm. For these calculations, the reflectivity ρ of the aluminium grating surface was taken to be 0.868 and then decreased by 15% so as to be consistent with the findings in reference: [91].

The red line on figure 2.15 essentially illustrates the back-reflection that one

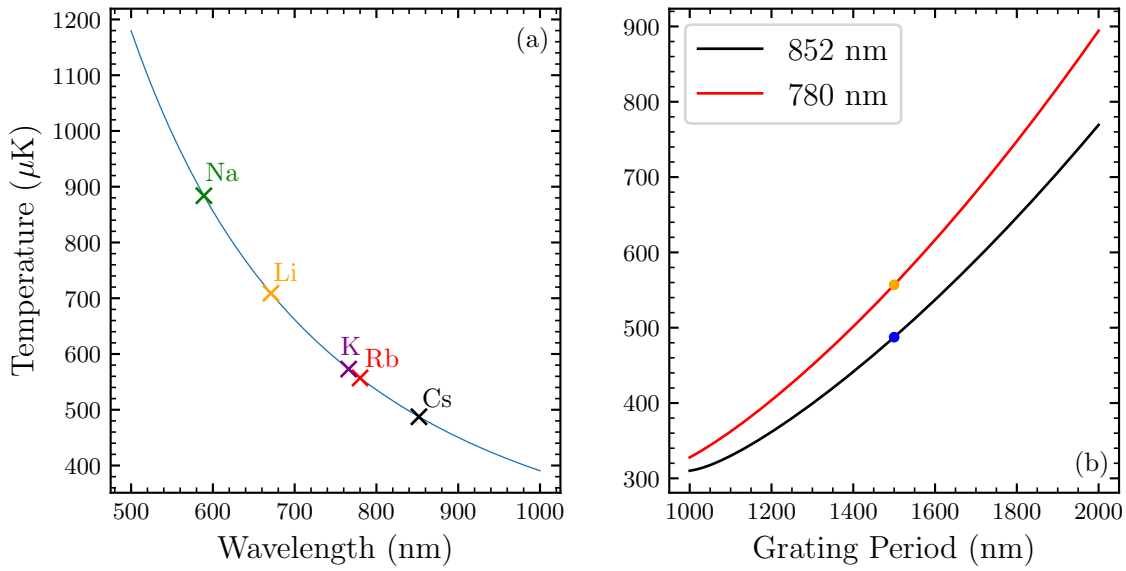

Figure 2.14: (a) GMOT temperatures as calculated using equation 2.2.16 with constant grating period of 1500 nm and several alkali metal D2 cooling transitions noted. (b) Temperatures calculated with a constant wavelength for the Cs and Rb cooling transitions with varying grating period.

should expect from the chip as the wavelength is changed. Meanwhile, the blue line indicates efficiency of the first order diffraction while also taking into account the extra $m = -1$ orders. With this in mind, the black line shows the beam balance perpendicular to the grating surface considering only the $m = 1$ order beams (N in equation 2.2.6 is therefore 3). The dashed violet lines approximately centred on the figure mark the cooling transitions of Rb and Cs at 780 nm and 852 nm, respectively.

The measurements of back-reflection were made using a fibre output from a Ti-Sapphire laser that was collimated to a $1/e^2$ width such that it covered the grating surface. The light was first horizontally polarised for maximum transmission through a polarising beam splitter to then be circularly polarised before impacting the grating surface. At the noted cooling transitions, the back-reflection collected at the exit face of the PBS (after considering the small losses to the optical elements) was 2% and 3% - a discrepancy from the model of 2% and 1.7% (these points are noted on figure 2.15 as red dots). While this is not within experimental error, it may be explained by considering the construction of the grating and how its characteristics may not be as perfectly defined as intended; or perhaps that the grating stage was not as perpendicular to the input beam as initially thought. Despite this, these

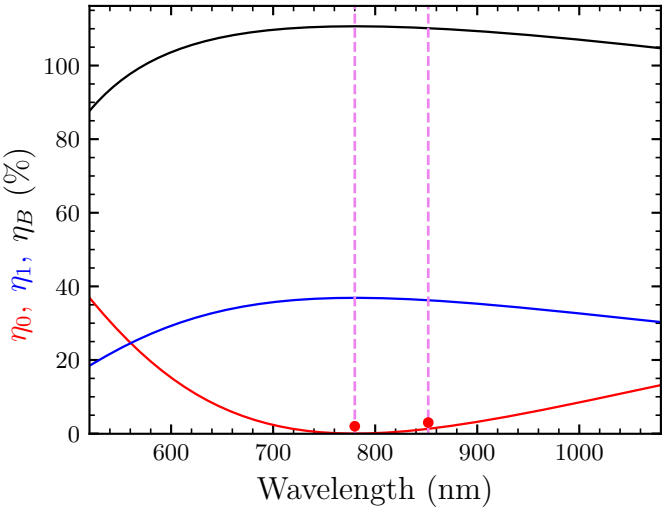

Figure 2.15: For a 1D diffraction grating with etch depth, $T = 195$ nm and design wavelength, $\lambda_d = 780$ nm: (Red) The expected back-reflection from a diffraction grating stated as a percentage of the input power for a range of wavelengths (equation 2.2.4) with experimental measurements noted as points with errors too small to see at this scale. (Blue) The expected first order diffraction efficiency when considering both the $m = \pm 1$ orders (equation 2.2.5). (Black) The overall perpendicular radiative balance when noting the 3 $m = 1$ beams (equation 2.2.6). Dashed violet lines indicate the cooling transitions of Rb and Cs at 780 nm and 852 nm, respectively.

findings indicate that using an 852 nm input beam with a chip intended for use with 780 nm light should not greatly affect the grating performance.

2.3.5 Small Scale Diffraction Grating Efficiency

Another point to consider in this analysis is the efficiency of the diffraction grating on a smaller scale. In all prior calculations this was assumed to be 33% with each grating section evenly creating upward trapping beams; this is however not the case. During the process of shortening the wafer of the diffraction grating, the grating itself was damaged in the form of visible scuffs and scratches across the surface of the grating. The effect of this can be seen in figure 2.16 wherein the three sections of the diffraction grating are mapped out in terms of their efficiency of diffracting a beam of power, $P = 1$ mW and $1/e^2$ radius, $w = 0.5$ mm into a first order beam. The profile closely matches what can be seen with the naked eye in that the top-most section is heavily scuffed and so exhibits a much lower average efficiency than the

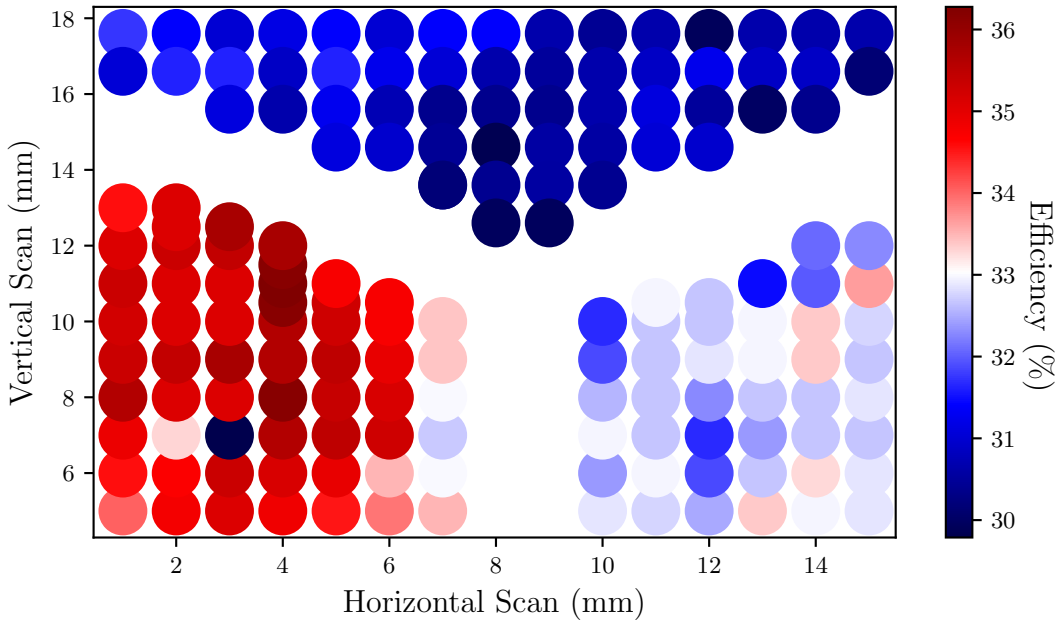

Figure 2.16: Colour profile of the grating chip diffraction efficiency in spots of ∼500 µm $1/e^2$ beam radius. The 'gap' between the different grating sections is due to not measuring the power efficiency at the interfaces between sections.

others as well as a deep scratch on the bottom left section being clearly apparent on the colour map. Curiously though, it also highlights inconsistencies with the maximum efficiency reaching as high as 36% on the bottom left section.

The question as to how this variation in efficiency will affect GMOT performance for a caesium trap is an open question at this stage, however there is evidence that even heavily scratched chips can indeed be used for rubidium trapping, but with a smaller trap being formed than would be standard, as has been achieved in Strathclyde experiments. This may be explained by the overall average η_1 grating efficiency of the chips in question, with a threshold value still being achieved despite the damage and therefore still being able to form a GMOT. For reference, the average η_1 value of this grating is 32.8%, which according to equation 2.2.5 would be reached at approximately 640 nm or 1000 nm. If the back-reflectance is equally affected, this may be why trapping is possible with damaged gratings. Thus, while scratched chips may be viable, this implies an ever lower trapping efficiency and possible 'dead-spots' within the desired trapping region due to the imbalance of upward diffracted beams.

2.3.6 Magnetic Field Modelling

Before moving on further towards concluding remarks, it should be noted how the on axis field calculations were made. In the Mathematica code, the B field was approximated linearly as a quadrupole field by a defined gradient which, as stated above, was kept at 15 G/cm throughout all calculations. Due to concerns about accuracy when considering more possible parameters, the true magnetic coils were modelled as the combination of fields generated by two opposing coils of wire with radius, R, using Python. In the code, each coil is itself composed of many individual loops of wire with increasing radius, r per layer and relative shifting of position, z per turn, with current, I. From the Biot-Savart law, the on axis magnetic field of a current loop is given by [99]:

$$B_z = \frac{\mu_0}{2} \frac{r^2 I}{(z^2 + r^2)^{3/2}}. \tag{2.3.2}$$

The relative distance between each coil was defined as $2R$ and their fields summed to achieve an anti-Helmholtz field with a zero crossing at a distance R from either coil. Modelling this way allows for errors in construction such as miscounting a few loops or shifts in individual wire positions as the coil is constructed. The process of construction and calibration of the magnetic coils will be expanded upon in section 5.2.3.

The modelling of shim coils and their effect on the main field zero was modelled in a similar way, with the shims again composed of many divisible loops of wire but with aligned currents for a Helmholtz configuration. This field was then superimposed onto the main field to show the shift in zero position. Due to the known property of a magnetic field having zero divergence, the radial fields are necessarily half the magnitude of the axial ones and thus the shim fields in the x and y axes can be used to compensate.

2.3.7 Concluding Remarks

To summarise the above sections; the largest possible beam waist w is desirable as this provides the most localised region in which to form the GMOT. The limiting

factor on this value is the input power P_0 as this determines the final beam intensity. This is an issue that affects both Cs and Rb equally but considering the role that the saturation intensity of the cooling transitions play, as well as the increased thermal velocity of Rb, there should be little difference in necessary power for cooling Cs in a GMOT.

Geometric analysis does show a bias towards Rb in terms of possible overlap volume within which to form the GMOT. A larger volume would give an easier job of localising a magnetic field within the trapping region. Conversely though, this means a higher inherent temperature of the cloud. For the purposes of an ion source, the possibility of not requiring bulky and expensive magneto-optical lenses depends on reaching the lowest possible temperatures to reduce beam emittance, and so Cs is better than Rb in this regard. It is not however, the ultimate limiter of potential source performance as there are many, often conflicting, characteristics of focused ion beams (including disorder induced heating) - concepts that will be expanded upon in chapter 3.

Finally, the diffraction grating itself may be damaged, but according to team members at Strathclyde University, they have not had issues with generating a MOT from a scratched grating.

From these factors I conclude that a GMOT with Cs is entirely possible and, once achieved, will make a superior cold ion source.

Chapter 3

Cold Atoms as an Ion Beam Source

3.1 Introduction

In this chapter, I will first elaborate upon the applications of FIBs to give context for their development, and then go on to define the principal characteristics on which they are compared: namely, their emittance and brightness, and what determines possible spot size. I will then give greater detail on the conventional ion sources, which will lead to a comparison with CAEIS and their current and proposed implementations.

3.1.1 Focused Ion Beams

The growth of the nanotechnology industry has made the development of ever more precise and versatile nanoscale techniques a necessity for continuing technological progression. A set of instruments that have provided techniques central to this progress are the focused ion beam (FIB) systems. These allow the generation of a beam of ions that can be focused down to the nanoscale and have been used across many diverse fields. These systems typically consist of a vacuum chamber, an ion source, an ion column, a sample stage, detectors, a gas delivery system, and a computer with which to control the instrument.

The key component of a FIB is its source as it determines the maximum current of the beam as well as how tightly the beam can be focused. The first source that was suitably realised for generating a FIB was the liquid metal ion source (LMIS) in 1970 [5,6,10], which soon became the standard source due to its highly advantageous characteristics for its contemporary use cases.

Another source realised later was the gas field ionisation source (GFIS) which allowed for smaller spot sizes to be achieved as well as the use of naturally gaseous elements such as He and Ne when it became commercially available in 2005 [13]. This lifted some of the restrictions in place when using a LMIS, which could only utilise Ga and some metal alloys of highly specific characteristics.

In a similar vein, plasma based sources were also developed that allowed the use of many more elements. These sources cannot match the spot sizes of the LMIS or GFIS but have become prevalent in other fields of research and industry, such as those that require dense plasmas [100–102].

By comparison, the field of cold atom electron/ion sources (CAEIS) is in its infancy but has the potential to offer far more versatility than previous sources; this is due to a fundamental change in technological approach. Prior to this, all sources relied on minimising the effective size of their emitter in order to achieve small spot sizes. The CAEIS however, achieves small spot sizes by cooling the emitter, or the beam, to micro kelvin temperatures [55]. This means that beams of any atom that can be cooled are available as an ion species ($\sim$27) as well as many other advantages over the more conventional sources.

3.2 Applications

This section will cover some broad application examples from the plethora of use cases in the literature [103–113] with a focus on techniques and processes that could be improved by using a CAEIS in the future.

3.2.1 Fabrication

The most prominent application for FIBs has been the removal or addition of a substance to a nano structure. This is because they offer appropriately small spot sizes and a variety of characteristics to suit the task.

Milling is the removal of material from a target sample by the process of firing ions at its surface to dislodge or 'sputter' material from the sample [107]. Sputtering yields depend greatly on the mass of the ion species employed as well as the energy used for the beam, thus the ratios of these factors can be tuned for the desired sputtering rate. Incorrect control of these factors could result in more surface damage than was intended or indeed unwanted surface contamination through implantation. A third factor determining the milling effectiveness of a FIB is its beam current. This is largely dependent on the source and greatly influences the overall rate of milling with pico amperes generally considered to give sufficient processing rates.

In addition to milling, FIBs can also aid in the deposition of another material when used in conjunction with a gas that is reactive with a milled surface. This is useful for applications such as mask repair and integrated circuit editing. In a similar vein, doping is also an option with ion beams and can be used to create various nanoscale structures such as quantum dots [114], semiconductor junctions [115], and quantum wells [116]. This can also be leveraged for resist patterning in which the ion beam renders sections of a resist vulnerable to dissolution by a solvent [117].

Presently, conventional ion sources are reaching the limits of their usefulness to the field of nano-fabrication. This is due to the ever increasing need for smaller spot sizes with high beam currents and new varieties of ion species - issues that could be solved with CAEIS technology.

3.2.2 Microscopy

Despite fabrication being the majority of use cases for FIBs, there have been advancements in the field that have enabled ion beam systems to rival and even exceed their electron based counterparts in terms of resolution and certainly in terms of versatility.

Used in much the the same way as a scanning electron microscope (SEM), the beam is rastered across a sample and the backscattered particles are captured to form an image. This has the potential to give the same readings as a SEM by reading the released electrons from the sample but the process is more efficient as there are multiple electrons released per ion, resulting in a brighter image. Ions also inherently follow a given trajectory better than electrons and so the image is more likely to be formed by particles from the intended target region. Ion beams have a further advantage over a SEM in that, because of their inherent charges, they are more efficient at creating charge contrast images. Backscattered ions themselves can also be detected to map the relative atomic masses of regions of a sample against the mass of the impinging ions.

However, an issue to take note of with ion microscopy, is the probability of sample damage or contamination; while this was an advantage for fabrication, for microscopy the implantation of ions during imaging is a process that must be carefully monitored. It can be reduced by lowering the beam energy but this places a limiting factor on achievable resolutions.

Possible advantages offered by CAEIS technology include new ranges of beam energies and ion species. For each sample, the least damaging ion could be used while also having the possibility of lower beam energies [40].

3.2.3 Analysis

FIBs can also be advantageous for analytical purposes. Secondary ion mass spectroscopy (SIMS) is a technique that can provide parts per million to parts per billion sensitivity when used over large areas of a sample and is comparable to Auger electron analysis when used in a small area. The technique involves firing a beam at a sample to sputter its surface and analysing the resultant particulates. The beam energy, angle of incidence, and ion species can all be considered for the desired analytical effects [118, 119].

Another possibility for compositional analysis is Rutherford backscattering - this is the process of firing a high energy beam at a sample and detecting the backscattered ions within a small solid angle. By collecting in a small window the mass of the

target atoms can be deduced. This is because during the recoil process between the target atoms and the backscattered ions, the ions will experience some energy loss that depends on their relative masses and the scattering angle. Recent implementations of a GFIS based ORION FIB microscope has allowed nanoscale resolutions for mapping [120].

Rather than using high beam energies, low energy ion scattering (LEIS) can also be used to analyse a sample surface [121]. This is because at low energies, ions are far less likely to penetrate into the bulk of the sample and thus will only give surface-based readings.

CAEIS technology can offer advantages to analysis for similar reasons as to microscopy. A greater choice of ion species would enable new samples to be analysed, especially with the beam energies that a CAEIS could offer.

3.3 Characteristics

Before introducing and contrasting the conventional and cold atom ion sources, it is important to define the characteristics on which they are judged. The main requirements for the source of a FIB are for it to produce ions with a maximally useful amount of current that can be focused into the smallest possible spot size. Secondarily, it should be able to operate at a number of beam energies and with multiple ionic species in order to broaden its applicability. While some of these properties are determined by the interplay of source and focusing column, the following discussion of beam quality parameters and aberrations gives the basic principles on which to judge both conventional and cold ion sources.

3.3.1 Emittance

The emittance is a property of all charged particle beams and gives a quantitative understanding of the quality of a beam [122]. It does this by considering the ion beam as a statistical ensemble of particles whose trajectories can be described in terms of transverse positions and angles, x_i and Θ_i, respectively. From these variables, a phase space can be defined along the beam propagation axis, z. Assuming that

the beam is neither strongly convergent or divergent, the angle Θ_i can be related to the momentum of the particle p_i as $\Theta_i \approx v_i/v_z = p_i/\sqrt{2mU_i}$; where v_i and v_z are transverse and longitudinal velocities, m is the mass of the particle, and U_i is its kinetic energy. Using Liouville's theorem [123], which states that the volume of phase space that an ensemble of particles inhabits within a conservative potential is conserved; the normalised emittance can be defined as

$$\epsilon_x = \sqrt{m/2}(\bar{x^2}\bar{v_x^2} - \overline{xv_x}^2)^{1/2}, \tag{3.3.1}$$

where the bars indicate an averaged value over the ensemble. Due to the above relationship between the Θ and v, we can restate equation 3.3.1 for the emittance of a beam propagating in the z direction

$$\epsilon_x = \sqrt{U}(\bar{x^2}\bar{\Theta_x^2} - \overline{x\Theta_x}^2)^{1/2}. \tag{3.3.2}$$

Mathematically, equation 3.3.2 now relates the moments of the beam distribution in x-Θ_x trace space to define a RMS (root mean square) emittance which is normalised by the factor $\sqrt{U}$. The first term within the bracket gives the product of spatial and angular spreads (which itself relates to the thermal velocity spread) within the beam while the second term gives the correlation between particle position and trajectory when the beam is either diverging or converging. In the case of an ideal beam (with an absence of Coulomb interactions and focusing aberrations), this factor is zero at its waist.

This definition of the emittance avoids measuring beam quality in terms of its trace-space area which, despite being a conserved quantity, can be misleading when used as a measure of quality as is illustrated in figure 3.1.

While during beam propagation it must be assumed that there is a correlation between the position and trajectory of the ions, this is not the case at the ion source itself. The RMS emittance at this point can thus be simplified to

$$\epsilon_x = \sigma_x \sigma_\Theta \sqrt{U}, \tag{3.3.3}$$

where σ_x is the RMS deviation in positions, σ_Θ is the RMS deviation in trajectory

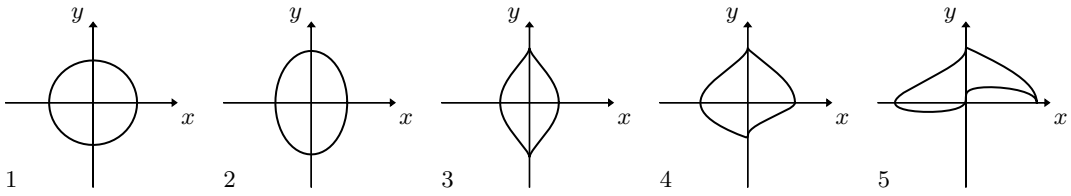

Figure 3.1: An illustration of the issue with trace-space area emittance defining beam quality. Sub-figures 1-5 show a cross section of a hypothetical ion beam as it evolves through a series of lenses with spherical aberrations whilst propagating in the z direction. The trace-space area remains constant throughout but is clearly not a well-behaved beam in a linear focusing system.

angles, and U is the average beam energy. For sources where the temperature is the dominant factor determining the transverse motion of its ions, the emittance can be restated as

$$\epsilon_x = \sigma_x \sqrt{k_B T/2}, \tag{3.3.4}$$

where k_B is Boltzmann's constant and T is the source temperature.

Equations 3.3.2 and 3.3.4 can be understood as separate points on the timeline of the evolution of an ion beam. Initially, equation 3.3.4 describes the beam behaviour at the source where there is no correlation between ion position and trajectory. As the beam propagates, however, equation 3.3.2 becomes relevant as the correlation of position and trajectory grows. If this beam were to pass through a lens, its correlation factor would reverse and be focused down to a point similar to its initial state at the source.

3.3.2 Spot Size

The next step is to consider the limits imposed on spot size by the source emittance. Given a system where this quantity is conserved, equation 3.3.3 is a valid approximation for any focused point in the beam path and thus can be used to estimate the focal spot size using only properties of the source. Therefore from equation 3.3.3 we have

$$\sigma_x^{'} = \frac{\epsilon_x}{\sigma_\Theta^{'}\sqrt{U}}, \tag{3.3.5}$$

where the factors of $\sigma_x^{'}$ and $\sigma_\Theta^{'}$ now describe the RMS deviations of position and trajectory at the focal point. However, this neglects any possible contributions from aberrations which can increase both the emittance and RMS trajectory values. By including a description of the effects of aberrations, a more complete theory can be established.

The main sources of aberration in an ion beam system are chromatic and spherical in nature. The former arises from the differing kinetic energies of the ions in the beam; higher energy ions are more difficult to focus, leading to a smearing of the focal plane. The latter depends on the positional distribution of the ions; the further they are from the focusing axis and the greater the deviation, the greater the smearing of the focal plane [124].

For simplicity we can assume the case of an ion beam nearly parallel to its propagation axis z, which can be focused to a spot for which the aberration contributions to the beam diameter can be written as [125]:

$$d_{\text{circ}} = \xi C_{\text{circ}} \Delta\Theta (\Delta U/U) \tag{3.3.6}$$

$$d_{\text{sph}} = \eta C_{\text{sph}} \Delta\Theta^3 \tag{3.3.7}$$

where C_{circ} and C_{sph} are the chromatic and spherical coefficients of aberration, $\Delta\Theta$ is the trajectory angle spread, and $\Delta U/U$ is energy spread in the beam. ξ and η are numerical constants that depend on each of the other definitions used, as well as the distributions of angular trajectory and beam energy.

In order to standardise with the literature, I will use a measurement of the beam diameter that contains 50% of the overall current, d_{50}. The most simple case for d_{circ} and d_{sph} consists of a uniform circular distribution and a Gaussian distribution in beam energy with a FWHM of $\Delta U_{1/2}$. Using these parameters gives the aberration factors in the following form [126]:

$$d_{\text{circ}} = 0.34 C_{\text{circ}} \Theta_0 \frac{\Delta U_{1/2}}{U}, \tag{3.3.8}$$

$$d_{\text{sph}} = 2^{-5/2} C_{\text{sph}} \Theta_0^3. \tag{3.3.9}$$

Assuming that the spot size resulting from the emittance also has a Gaussian distribution we know that the diameter at which the beam has 50% of the current is at $d_\epsilon = 2\sqrt{2\ln 2}\sigma_x'$ and $\sigma_\Theta' = \Theta_0/\sqrt{2}$, giving

$$d_\epsilon = \frac{4\sqrt{\ln 2}\epsilon_x}{\Theta_0\sqrt{U}}. \tag{3.3.10}$$

These equations 3.3.8, 3.3.9, and 3.3.10 all relate to ion beam technologies based on point sources such as the LMIS or GFIS and so are useful to compare to CAEIS that have different operating parameters.

It can be shown that in the case of a uniform distribution in angular trajectory Θ, and Gaussian distribution in U, the combined spot size is represented by the following [11, 125]

$$d_{50} = [(d_\epsilon^{1.3} + d_{\text{sph}}^{1.3})^{2/1.3} + d_{\text{circ}}^2]^{1/2}. \tag{3.3.11}$$

Using equation 3.3.11, we can compare and contrast older technologies with the CAEIS systems; it also provides insight into the various factors of aberration that can be seen in figure 3.2, which models a hypothetical cold ion source.

3.3.3 Brightness

Emittance is an incomplete description of beam quality. This is firstly because it depends on the kinetic energy of the ions. This is an issue because equation 3.3.2 shows that the trajectory angle Θ_x, decreases as the longitudinal momentum increases, meaning that the emittance must be normalised in order to compare beams of varying energy. There is also a further issue of specifying what fraction of the beam ions lay within a given cross section, as the distribution of ions is rarely uniform. For example, the emittance can be easily reduced by using a small aperture

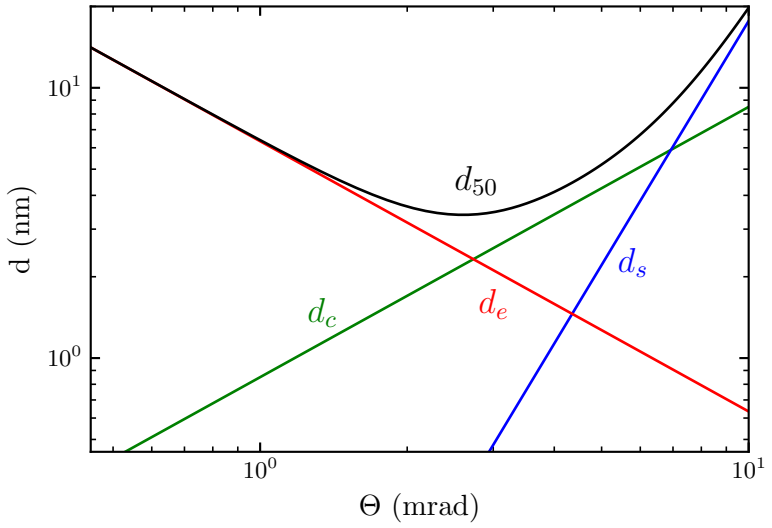

Figure 3.2: The contributions of aberration components to the effective source size on a log scale as a function of convergence angle Θ. The components noted, d_c (chromatic aberration), d_e (emittance), and d_s (spherical aberration) sum according to equation 3.3.11 to give d_{50}, the size of the spot containing 50% of the total beam current. The figure values are for a hypothetical cold ion beam with $\epsilon_x = 3.3{\times}10^{-10}$ mrad $\sqrt{\text{eV}}$, $U = 3 \times 10^4$ eV, $\Delta U_{1/2}/U = 3 \times 10^{-4}$, $C_c = 25$ mm, and $C_s = 100$ mm.

to remove high-emittance trajectory ions but this does nothing to guarantee a greater flux of ions onto a focal spot and decreases the overall beam current.

What is clearly important then, is a metric for the useful beam current with respect to a given emittance. This metric is the normalised brightness of the beam, which is the ion current density per unit solid angle per beam energy:

$$B = \frac{1}{U}\frac{\partial^2 I}{\partial A \partial \Omega}, \tag{3.3.12}$$

where I is the beam current, A is the cross-sectional area of the ion beam, Ω is the solid angle, and U is the beam energy. In the case of thermal sources with temperature T, a uniform angular distribution in the forward z direction of solid angle 2π, and a beam energy of $k_B T/2$; the normalised brightness can be reduced to

$$B(x, y) = \frac{J(x, y)}{\pi k_B T}, \tag{3.3.13}$$

where $J(x, y)$ is the current density in the plane of emission. While the brightness can be written in terms of its dependence on the transverse positions x and y, as is the case in equation 3.3.13, it is useful to have a general comparative figure due to current density generally varying across a source. This is often the peak brightness, normally referred to as *the* brightness of the source, taken at the point $B(0, 0)$ (assuming that the brightness has a Gaussian distribution) or a spatially averaged brightness.

Using this assumption we can combine equations 3.3.4 and 3.3.13 to give the peak normalised brightness in terms of the normalised emittance in the axes perpendicular to the beam direction

$$B_{\text{peak}} = \frac{I_0}{4\pi^2 \epsilon_x \epsilon_y}, \tag{3.3.14}$$

where I_0 is the total current of the beam.

Further, assuming that this quantity is conserved, the expected beam current at the focus can be derived by combining equations 3.3.13 and 3.3.14

$$I_0 = 4\pi \frac{\epsilon_x \epsilon_y J_0}{k_B T}, \tag{3.3.15}$$

where ϵ_x and ϵ_y are the final emittance values and J_0 is the peak current density at the centre of the beam.

The final important consideration for an ion beam is its Coulomb interactions. These principally affect the beam in two ways; the first is a stochastic effect caused by random inter-ionic collisions, and the second is because of the space charge of the ions themselves. The former causes an exchange in temperature between the transverse and longitudinal directions leading to heating of the beam and a possible reduction in both emittance and brightness. The latter also causes defocusing, aberrations, and reduction in beam brightness; this is because ions propagating in the beam experience the charge of ions in front of them as a small potential barrier as well repulsive charges in the transverse directions.

3.4 Ion Sources

Now that the judging criteria have been established, we can move onto the available ion sources; the first of which have enabled the steady progression of nanotechnology until the present day but are beginning to show limitations in their modern use. The latter sources are based on cold atom technology and have the possibility of replacing their ageing counterparts. For reference, a summary table is included after the relevant technologies have been introduced in section 3.4.5.

3.4.1 LMIS

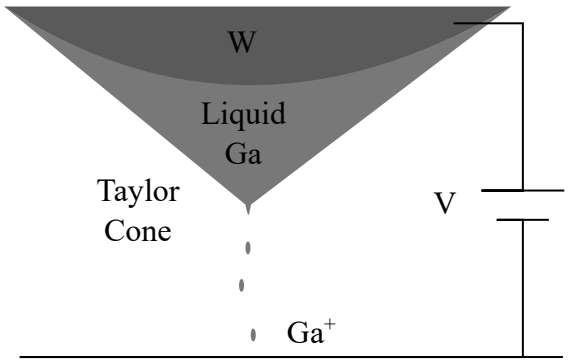

Figure 3.3: Schematic of a LMIS using gallium. The tungsten tip is wetted by Ga as it seeps from a heated reservoir to cover the needle. When a strong electric field is formed between the tip and conducting plate a Taylor cone is formed from which a jet of ions can be extracted at the apex.

Though not the first proposed of the ion sources, the LMIS was the first realised and has the capability of producing spot sizes on the order of 5 nm in diameter. Figure 3.3 shows a simplified diagram of a LMIS, noting the Taylor cone that is formed by, in this case, liquid gallium at the end of a tungsten needle that is itself attached to a reservoir of Ga. While there are a number of metals that can be used in a LMIS, the most common metal is Ga due to, amongst other things, its low melting temperature and low volatility. This means that very little heat is required to operate a FIB using a LMIS and it is stable for long periods.

The source emits ions via the following process. First, the Ga is heated in order that it be allowed to flow down and wet a tungsten needle which has been machined to a point on the order of 2.5 µm. Once wetted, an electric field is then applied to

the tungsten tip - this is typically around 10^8 V/cm - that causes a Taylor cone to form. This cone acts as a point source and has a diameter of 2-5 nm. It is formed when there is a balance between the electrostatic force due to the applied electric field and the surface tension of the Ga. Once balance has been reached, the small size of the Taylor cone tip means that a voltage can be applied to an accelerator plate which strips Ga from the tungsten needle and field ionises it [113].

In terms of other capabilities, the LMIS has the highest general beam current at (2-10)$\times 10^3$ nA of any FIB source in general use. Some typical emittance and brightness values are 1.0×10^{-9} mrad $\sqrt{\text{eV}}$ and 1.0×10^6 A/m^2 sr eV. Fundamentally, the LMIS is limited in two ways that make it unsuitable in some circumstances. The first is in its available species - because reservoir metal requires very specific characteristics there are few species to choose from. The second is due to its nature as a source of ions from a high density region at the tip of a Taylor cone. At this point there is a high charge density which inherently leads to a large energy spread in the ions that are produced, this process is known as the Boersch effect [127]. This causes an increase in the chromatic aberration of the source when used at lower beam energies, which also causes an increase in emittance, thus widening its smallest achievable spot sizes.

3.4.2 GFIS

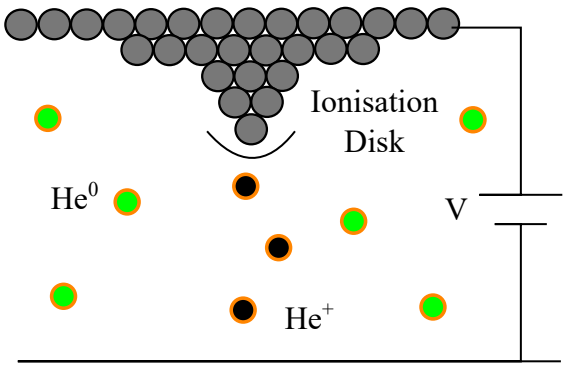

Figure 3.4: Schematic of a GFIS using helium. This source uses a trimer as a tip to create a strong electric field region and thus ionise gas incident within this ionisation disk.

The GFIS was proposed earlier than the LMIS [128] but has only recently become

a viable technology - primarily as a microscope due to its ability to produce spot sizes in the sub-nm range [13]. Figure 3.4 shows a simplified diagram of a GFIS in which the ionisation disk region is noted. This is where the free gas of the system is ionised. Much like how the LMIS is driven by the effects of strong electric fields, this disk arises due to a high voltage applied to the tip which produces an extremely strong ionising field at the apex of the tip. This tip however, is machined such that it is composed of a single trimer of atoms. Thus, when the voltage is calibrated correctly, the ionisation disk only appears around these atoms, making the source region effectively a single atom in size.

This source has become prominent in the field of microscopy for a number of reasons, first of all, the effective source size means an extremely high brightness compared to the LMIS on the order of 1×10^9 A/m^2 sr eV and an achievable spot size as low as 0.35 nm with a 30 keV beam energy. Second, the most commonly used gas in the GFIS is He; this is a relatively light element and so when using it to image there is less chance of damage to the structure being imaged.

The GFIS also has its issues. Much like the LMIS, it is limited in its species choice, although in this case it is constrained to elements with very high ionisation potentials; these are the lightest of the noble gases such as He [129] or Ne [130]. Also, due to the ionisation method, it is difficult to create low energy ion beams or implement a mode with higher current output than the standard 0.01 nA and a larger focal spot for large scale milling exercises.

3.4.3 Inductively Coupled Plasma

The ICP departs from the paradigm of generating ions by ionisation in the region of a sharp tip. It instead relies on electron currents within a plasma. Generally, this plasma is created within a chamber that has a gas inlet, highlighted in figure 3.5 by the sample flow and plasma labels. The output of the source is via a small exit aperture, typically under a millimetre in diameter. The plasma itself is generated by antennae that are outside of the chamber using RF waves. These waves are high enough frequency such that they strip electrons from the atoms without imparting much energy to the ion cores. Freed electrons can then further ionise other atoms

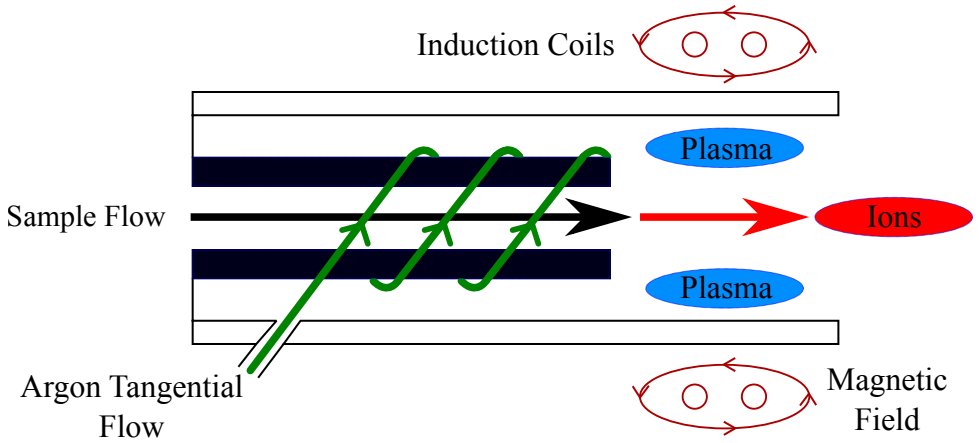

Figure 3.5: A schematic of an inductively coupled plasma generation assembly. The plasma is first generated within the assembly by the induction coils, with the sample gas then flowing through the chamber and being ionised by the plasma.

in a cascade effect. The ions can then be extracted from the chamber via the exit aperture using a potential of a few keV.

The brightness of this source is determined by its current and small angular spread rather than its effective size and varies depending on the ion species - the brightness of the ICP source is also much lower than the LMIS or GFIS values with O^- measuring at $4{\times}10^2$ A/m^2 sr eV or Xe^+ giving 1×10^4 A/m^2 sr eV. While these do not match the previous source examples, the ICP has found its own niche applications where its available ion species and high densities are advantageous [100–102].

3.4.4 Cold Atom Sources

The point of divergence between the traditional and the cold ion sources can be traced to equation 3.3.4 in which the emittance of the source is shown to be determined by a combination of its size and temperature. The previous iterations of sources predominantly minimised the effective source size σ_x, by generating ions at some variation of sharp tip - while this can enable sub nm spot sizes and high ion currents, it cannot provide both simultaneously due to Coulomb interactions. As per their namesake, in a CAEIS, the temperature of the source is minimised in order to lower the emittance. This was never a reasonable proposition before laser cooling techniques as the emittance is proportional to the square root of the temperature;

meaning that only with micro kelvin temperatures do sources of this nature become viable alternatives. Due to the change in priority, the effective source density is reduced. This means that, among other things, a CAEIS has the potential to provide both a high current and sub nm spot sizes because they do not suffer as greatly with either Coulomb or the Boersch effects.

Aside from this, a CAEIS has many other advantages over the traditional ion sources. Through a combination of the source itself being larger than an atomic tip, and the small angular deviation of the source due to its inherently small energy spread, a CAEIS has a large demagnification factor and is therefore more stable in the face of vibration than a traditional source. This also means that a source of this nature has a very low chromatic aberration when compared to a LMIS for a tighter possible focus at lower beam energies. These factors are also achievable with many more ionic species than is possible with any traditional ion source. While these different species will produce slightly incongruous characteristics in their final ion beams, the ~ 27 atoms allow for differing modes of operation including continuous ionisation for higher currents or Rydberg field excitation for finer control of ion numbers. Fundamentally though, current cold ion sources can be broadly categorised in terms of three approaches: the source of ions can be from a full 3D trap with ionisation taking place within the atomic cloud, a beam of atoms cooled in a 2D fashion to be ionised at the end of a column, or a combination thereof.

3.4.4.1 MOTIS

A sub-category of CAEIS is the magneto-optical trap ion source (MOTIS) is the most easily realised of the cold ion source designs in terms of experimental complexity. From its first incarnations, it essentially consists of a magneto-optical trap, one or more lasers with which to ionise the trapped atoms, and extraction electrodes. There have been modifications to this initial design as first demonstrated in these works [35, 36] but the basics have remained consistent. This is because the characteristics inherent to even the most mundane of MOTs are a suitable basis for a cold ion source as a typical MOT can have a temperature of the order of $\sim$100 μK.

In this configuration, the ionisation region is defined by the either the cross

section of the cloud exposed to the ionisation laser (in the case of a two photon excitation scheme), or the overlap of two or more lasers (in the case of a greater number of excitation steps). While both ionisation methods rely on the diffusion rate of cold atoms into the ionisation region, thus limiting the possible ion current by the trap density, there are three possible configurations within these options. Figure 3.6 shows 2D representations of these trap ionisation approaches subdivided into the categories of 2 and 3 photon processes.

The first noted technique is the axial mode of ionisation, which involves generating a flux of ions via an ionisation beam that is coaxial with the resultant beam trajectory. This method produces the highest possible ion current, as the trap is ionised across its entire diameter, but also the largest energy distribution due to the potential gradient across the trap and the self-induced barrier of the ion charges themselves. The second method is via transverse ionisation, which can lower the energy spread of the ions. This can be achieved by reducing the ionisation beam width and therefore the charge density for fewer Coulomb effects. Fundamentally though, this method also reduces the useful ion current as a smaller beam width necessarily means fewer ions and only a small virtual aperture region will supply useful ions (noted on figure 3.6 as the region between the dashed lines) while ions from outside of this space must be rejected by additional optics, thus increasing the necessary bulk of the source. Finally, a 3 photon ionisation scheme utilises two ionising laser beams, the crossover of which forms the true ion source. This method is superior to transverse ionisation in that it maintains ion current while precluding unnecessary depletion of the MOT by unwanted ionisation. The true source of ions can also be pared down to the smallest focal point of the final ionising beam, rather than a single collimated line, thus reducing ion beam emittance, energy spread, and negating the need to filter unwanted ions.

The final consideration for a MOTIS is the extraction of the ions. This can be performed by electrodes with planes perpendicular to the desired beam direction. Traditionally the arrangement of these electrodes was greatly difficult as a standard MOT would require trapping in all dimensions which may be blocked by such extraction optics. Recent advances in transparent electrodes however, such as ITO

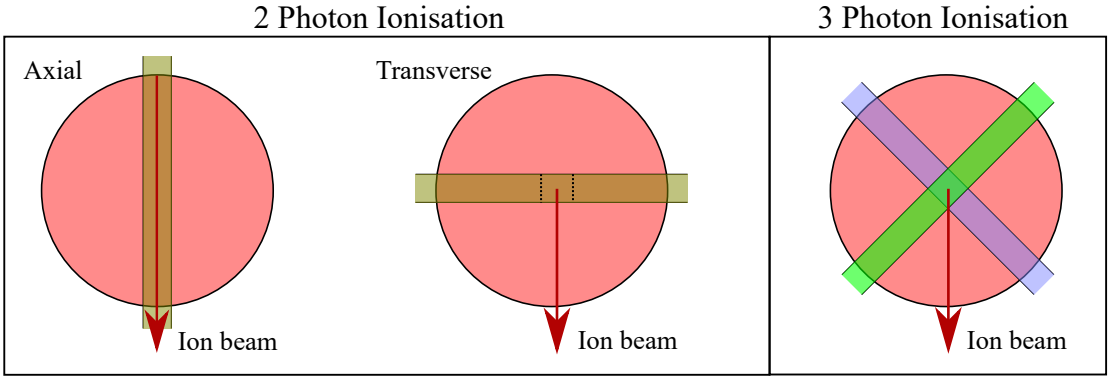

Figure 3.6: The three main modes of ionisation within a MOTIS requiring either one, or two ionising lasers. The axial mode follows the resulting ion beam direction and produces the highest possible current but also the greatest energy distribution. Transverse ionisation enables control over energy distribution through tapering of the beam width but also unnecessary depletion of the MOT, as only a virtual aperture (noted by dashed lines) produces useful ions for the beam. 3 photon ionisation meanwhile, uses crossed ionising beams and so does not cause extraneous ions to be produced outside of the desired aperture region and can be pared down to reduce Coulomb effects.

coated glass [131], have allowed the formulation of ever more succinctly engineered ion sources.

Across the literature there are many examples where the theoretical limits of such sources and their varying modes of operation have been calculated [30,31,34,35,132] as well as true experimental realisations of such systems [43,44,53,54,133–138]. Due to the wealth of work in this area, I will not delve into derivations here but will instead summarise the best of their performance examples in table 3.1. This will later provide an estimate of performance of the proposed 3 photon ionisation source in this work (see chapter 6).

In these papers it is found that the maximal brightness of the source is proportional to the MOT density and its loading rate. Given this known limitation, it is down to the discretion of the user as to whether this will be an issue for their usage case as, despite this limit, a MOTIS offers the most easily realised route to engineer for a compact cold ion source.

3.4.4.2 LoTIS

A low temperature ion source (LoTIS) meanwhile, is a device more heavily influenced in terms of design by 2D MOTs that can break through the limits of current imposed on a MOTIS [42, 58, 139]. These essentially comprise of a beam of neutral atoms emanating from an effusive source whereby the atoms are then cooled transversely by a 2D MOT as they travel along a beam column. At the end of the cooling process, they are photoionised which allows further ion optics to be employed.

There have been several realisations of sources of this nature with some taking a more hybrid approach, combining the virtues of both the LoTIS and MOTIS configurations [28,41,53,57,58,140]. Each of these are able to provide ion currents far in excess of those possible using a MOTIS as the maximum current is now dependent upon the initial neutral atom beam flux and the efficiency of ionisation. Sources of this nature carry the potential of replacing the LMIS as the most ubiquitous of ion sources because they can compete with and exceed them in terms of normalised brightness and achievable spot sizes.

3.4.4.3 Grating MOTIS

The ion source proposed in this work is a magneto-optical trap based on a single input beam split into 3 additional cooling beams by a diffraction grating. These beams balance in intensity as described in chapter 2 to form a trapping volume. Due to the geometry of the trap, the atomic cloud is exposed on all sides and thus can be ionised transversely by additional lasers, or elevated to a Rydberg state and ionised via extraction electrodes. This geometry is the main strength of the system as, while it may fall short in terms of peak brightness or current compared to beam based sources like its fellow MOTIS, it allows a far more compact ion source to be designed around it just as GMOTs have been used for other purposes [61, 63]. Further details on the proposed apparatus are given in chapter 6.

3.4.4.4 Disorder-Induced Heating

A common issue of all ion source technology, cold or otherwise, are the Coulomb interactions between the ions which cause heating of the beam. For the LMIS, these

interactions mean a fundamental limit to the energy spread of the beam, also known as the Boersch effect. This arises from the nature of the LMIS tip being an area of very high charge density and thus extremely strong Coulomb forces which influence the beam spread. Cold sources do not approach the charge densities present in tip-based technologies, however disorder-induced heating (DIH) can still play a role with sufficient charge density. The advantageous characteristics of cold ion sources stem from equation 3.3.4 in that a lower source temperature means a lower average transverse velocity of the ions, which is defined by the temperature of the MOT. If, after ionisation, the heating of the beam is such that the ions are raised above this MOT temperature, the effective emittance will be much higher thus degrading the usefulness of the source. Modelling and measurement of DIH in a MOTIS can be found in a number of publications [55, 141–145] as well as methods to combat it, ranging from paired down virtual apertures for a 'pencil beam' regime [146] to the use of Rydberg blockade [45, 147] both of which could be used in my MOTIS design to maintain low emittance values.

3.4.5 Summary

Source	ϵ_x (mrad mm $\sqrt{\text{eV}}$)	B_{peak} $(\frac{A}{m^2\, sr^{-1}\, eV^{-1}})$	ΔU (eV)	U (keV)	I (nA)	d_{50} (nm)
LMIS	1×10^{-9}	1×10^{6}	5	30	$1{\times}10^{4}$	5
GFIS	1×10^{-11}	1×10^{11}	1	30	0.01	0.35
ICP	1×10^{-5}	1×10^{4}	3.5-5	30	0.1	50
CAEIS	3.6×10^{-10}	2.4×10^{7}	0.205	15-30	> 1	2.1

Table 3.1: Characteristics of both conventional and cold ion sources. Stated values are in best case scenarios of experimental realisations where possible, e.g the CAEIS peak brightness and spot size values are taken from [57] while others include: [41, 58, 131, 132, 148, 149].

To summarise the above sources, both classical and contemporary, I have compiled table 3.1 detailing examples of their best known characteristic values from a number of references of the most recent CAEIS and older ion sources. It must be remembered though, that realised cold atom based source technology is in its relative infancy compared to prior techniques such as the LMIS, and so while in some cases better standards have already been achieved, there are still improvements that can

be made. Even neglecting purely numerical advances, the true versatility of cold ion sources has yet to be tapped as very few of the possible trappable atoms have been exploited as an ion source.

Chapter 4

Ionisation Scheme

4.1 Introduction

4.1.1 Project Goals

The primary objectives of this project are to design and create a Cs ion source that is both compact and reasonably priced compared to existing systems, with secondary objectives being to ensure that the resulting system has long term stability and is easy to use with limited need for specialised maintenance. These objectives have informed the decisions made with regards to the use of lasers for the cooling, trapping, and ionisation of Cs. In this chapter I will elaborate upon each step towards ionisation, explaining how and why it is attained, with reference to the lasers used and how each laser is stabilised.

4.1.2 Cooling and Trapping Cs

As explained in chapter 2, the cooling and trapping of Cs will be performed using a grating magneto-optical trap (GMOT) as this will allow the system to be compact compared to the standard 6-beam trapping geometries or a conventional 2D MOT configuration. The requirements for this are lasers that can excite the cooling and repumping transitions of the D2 line of Cs ($6S_{1/2} \longrightarrow 6P_{3/2}$) at approximately 852 nm, with intensities greater than the saturation intensity of 1.10 mW/cm^2 [150]. Both transitions are marked on figure 4.1. The cooling transition of Cs is noted in

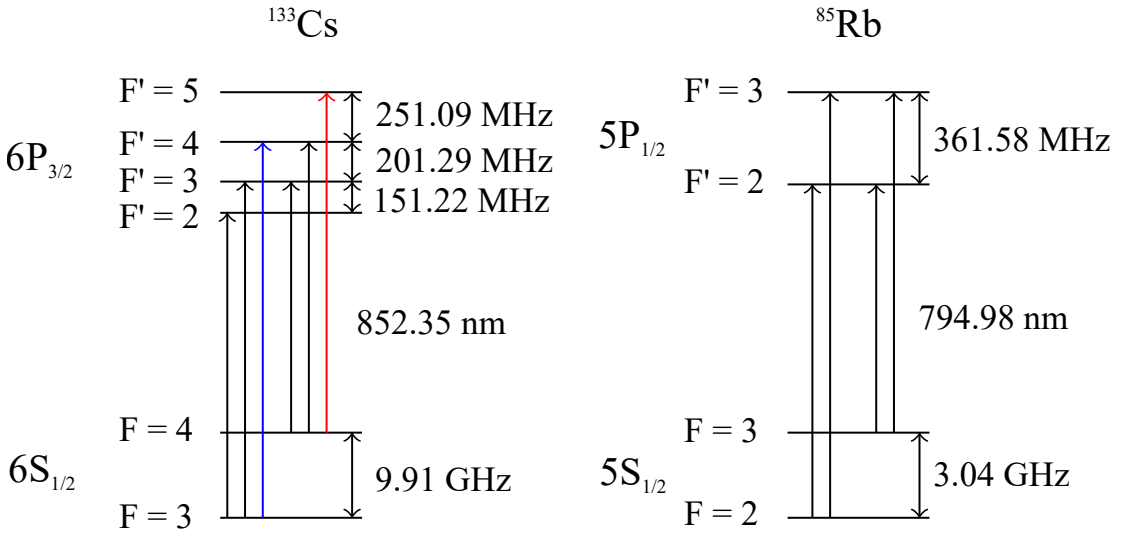

Figure 4.1: ^{133}Cs D2 and ^{85}Rb D1 energy level diagrams. All allowed transitions are marked between the ground and excited states while the cooling and repumping transitions are noted in red and blue, respectively. While non-Zeeman shifted spectroscopy of Rb is not present in this thesis, the D1 level diagram can be used to give more context in section 4.5. The transition frequencies and spacings are taken from references [151, 152].

red and is between the F=4 and F'=5 hyperfine states. Selection rules for F quantum numbers (ΔF=0,$\pm$1) mean that this is a closed loop and so the temperature of the Cs atoms can be slowly reduced by a continuous process of excitation and decay. This requires a small red shift of the cooling light from the transition, so as to take advantage of the Doppler effect - which can be achieved by using acousto-optic modulators (AOM). Additionally, in practice, there is a small chance that an atom will be excited to the F'=4 state and decay to the ground level F=3 state; this atom would then be lost to the cooling process in a dark state as it would no longer follow the closed loop. To remedy this, a repumping laser is introduced to pump the transition F=3$\longrightarrow$F'=4, noted in blue on figure 4.1, which ensures that all atoms remain in the cooling loop. As the chance of losing an atom to the dark state is low; the repumping laser does not require as much power as the cooling laser. The repumping process also does not depend on the Doppler effect and therefore does not require any red shifting. It is however still useful to include an AOM in the repumping setup as it can be used as a fast light switch to turn the trapping effect on and off for analysis purposes.

While there are many laser system combinations that could achieve the cooling and trapping of Cs, the choices of lasers for this process are restricted by the project objectives. For example, a Ti:Sapphire laser system is widely tunable and offers multiple watts of output power and thus could act as a cooling laser, but it is expensive and requires a large ring pumping system - characteristics that make it unsuitable for this project.

The repumping laser, meanwhile, has other considerations and as the maximum power output is less important; this means that laser technology can be explored in more detail. As an example, an external cavity diode laser rated at 80 mW could be sufficient as a repumping laser, however these devices can be prone to mode hops and need some maintenance to keep at the desired wavelength. Other laser technologies can be superior in this regard as well as more compact, but may be more expensive as a result of these advantages. Thus these factors must be considered with regards to the stated project goals for an optimal solution.

4.1.3 Ionising Cs

As explained in chapter 3, the ionisation of cold atoms has the potential to revolutionise sectors of industry and research that rely on nano-scale processes and processing, due the inherent and advantageous properties of a CAEIS. In this work, the ion source is cold Cs that, at this stage, is assumed to have been cooled and trapped in a GMOT. Thus, the question is, how best to ionise the trapped Cs in line with the stated project goals. Figure 4.2 illustrates some potential ionisation schemes from which to begin the evaluation.

The first ionisation method to recognise, and immediately reject, is to ionise the Cs from the ground state of $6^2S_{1/2}$ up to the ionisation limit using a laser running at approximately 318 nm. This is impractical for several reasons including, but not limited to, requiring an extremely powerful UV laser to excite this weakly coupled transition, thus presenting a hazard to a user. Such a laser would also be prohibitively expensive. Crucially though, this method would not allow the cooling of the atoms and would potentially cause a large amount of heating of the resulting ions.

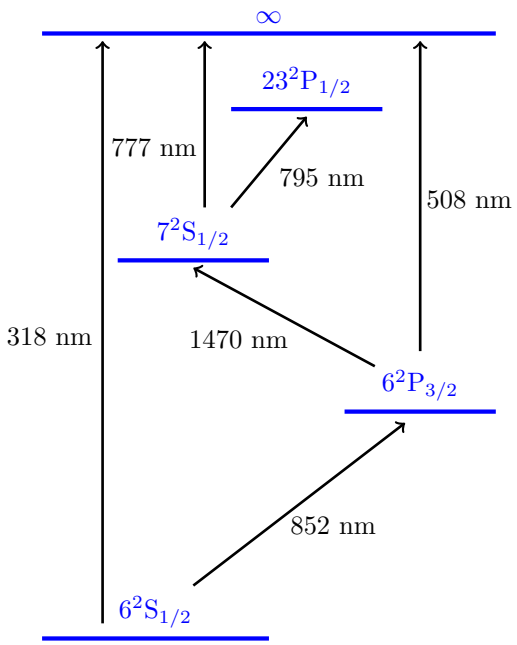

Figure 4.2: Possible routes to ionisation for Cs from its ground state. The route following $6^2S_{1/2} \longrightarrow 6^2P_{3/2} \longrightarrow 7^2S_{1/2}$ and then either to ionisation via a 777 nm laser or to $21^2P_{1/2}$ with a 795 nm laser; can be entirely excited using inexpensive semiconductor diode lasers.

The second method uses two transition steps, the first from $6^2S_{1/2} \longrightarrow 6^2P_{3/2}$ and then from this excited state to the ionisation limit. The first step is the laser cooling process using two 852 nm lasers, as noted earlier to be the cooling and repumping lasers respectively, while the second step to ionisation requires a 508 nm laser. The first step is non-negotiable but the 508 nm transition presents issues that do not fit with the project objectives because of the necessity of a dye laser. These lasers; while they can output less harmful light in the visible spectrum, use highly toxic dyes that must be replaced by specially trained individuals, which explicitly violates a secondary objective of the system design: for it to have long term stability with limited need for specialised maintenance. Finally, this approach can also be discounted due to the weaker coupling of the transition (and therefore less power efficient nature) as compared to an alternative in table 4.1.

The final noted method includes three transition steps. It retains the cooling step $6^2S_{1/2} \longrightarrow 6^2P_{3/2}$ but from here it branches to the $7^2S_{1/2}$ state via 1470 nm light. This level is special in that it offers two distinct routes to ionisation; the first

using 777 nm light to reach the ionisation limit, while the second uses 795 nm light to reach an intermediary state: $23^2P_{1/2}$ that can be easily field ionised. The specific advantages and reasoning behind each approach will be elaborated upon in section 4.5, while this subsection will concentrate on analysing the overall ionisation scheme with regards to the project objectives.

The first crucial aspect of this three state excitation scheme is that all the transitions are now within reach of existing solid state laser diodes. These devices are invariably cheaper and more compact than the laser systems required in the previous excitation schemes, while having long operational lifetimes with little need for specialised maintenance after initial setup, and thus meet all requirements of the project goals. Splitting the ionisation into more gradual steps also reduces the laser power required for each transition due to increased coupling strength, which translates to lower operating costs as well as less hazardous operation for the end user. A further point to consider is that the ionisation region within the MOT will only consist of the overlap region of all three beams, thus minimising the effective source size and therefore, its emittance. For these reasons, this is the preferred ionisation scheme and thus is employed in this project.

Throughout this subsection I have mentioned the term 'coupling strength' and noted whether a transition was 'weak'; this is a an indication of the dipole transition strength which is essentially a measure of how easy it is to excite between two atomic states. For completeness, table 4.1 shows the complete list of the radial part of the coupling between the noted states in atomic units, either from the literature [151–153] or calculated by the Alkali Rydberg Calculator [154], for each stated transition and the energy required to ionise it from the resultant state.

4.1.4 Laser Stabilisation

Now that the transition route from cooling to ionisation has been defined to use three excitation steps and semiconductor diode lasers, an important concept to introduce is laser stabilisation or 'locking' of a laser to an atomic transition, as this will enable the smooth climb up the transition ladder and informs the decisions that are described in section 4.5.

Transition	$6^2S_{1/2} \longrightarrow 6^2P_{3/2}$	$6^2P_{3/2} \longrightarrow 7^2S_{1/2}$	$7^2S_{1/2} \longrightarrow 23^2P_{1/2}$
λ (nm)	852.347	1469.892	794.98
Binding Energy (eV)	2.439	1.596	0.036
Coupling Strength (a_0e)	5.477	5.611	0.025
Transition	$7^2S_{1/2} \longrightarrow \infty$	$6^2S_{1/2} \longrightarrow \infty$	$6^2P_{3/2} \longrightarrow \infty$
λ (nm)	777.433	318.488	508.490
Binding Energy (eV)	-	-	-
Coupling Strength (a_0e)	0.003	0.001	0.004

Table 4.1: Properties of each transition noted on figure 4.2. The wavelength noted in nm is that of each transition, while the binding energy in eV is the energy required to singly ionise the atom from the resulting state. Meanwhile coupling strength indicates the radial part of the dipole matrix element in atomic units of a_0e. These values are either calculated using the Alkali Rydberg Calculator Python module [154] or from the literature [151–153].

The locking of narrow linewidth lasers to atomic transitions is common practice in atomic and molecular physics experiments [155–157]. There are many well-established techniques for locking a laser on, or close to, resonance including saturated absorption spectroscopy [158,159], polarisation spectroscopy [160,161], dichroic atomic vapour level lock (DAVLL) [162–164], modulation transfer spectroscopy [165, 166], frequency modulation spectroscopy [167–169], two or three-photon EIT setup [170–172] etc. All of these techniques essentially boil down to different methods of producing an error signal, typically in the form of a sloped feature that can be manipulated, either electronically or physically, to have a zero voltage crossing. This feature can then be fed into any variation of proportional, integrator, differential (PID) feedback loop circuitry to stabilise the laser frequency such that it remains coincident with the chosen feature, thus ensuring efficient use of laser power. For ECDL semiconductor lasers this is typically achieved by varying the voltage to its piezoelectric crystal or for a DFB laser, varying its input current.

Each method of generating an error signal has distinct advantages and disadvantages which, for the methods used in this work, will be elaborated upon in later subsections. A further point to mention is that all referenced techniques thus far allow for very small frequency ranges of resonant locking; techniques that allow stable off, or indeed, far-off resonant locking are more difficult to achieve. The creation of one such method, using a frequency reference, is the subject of section 4.5,

with the goal of generating an error signal for the transition $7^2S_{1/2} \longrightarrow 23^2P_{1/2}$, which is far more power efficient and easier to maintain than the traditional locking method [171].

4.2 Cooling Transition

4.2.1 Requirements

As has been previously discussed, in order to meet the given project goals, the cooling laser must meet a number of criteria - the most pressing of which is its output power at 852 nm for the cooling transition $6^2S_{1/2} \longrightarrow 6^2P_{3/2}$. The minimum requirement for cooling in a MOT can be considered to be the saturation intensity of the cooling transition 1.10 mW/cm^2, but far greater intensities than this are used in general practice. For this work, as explained in chapter 2, laser beams with a $1/e^2$ radius of at least 2.2 cm must be used in order to ensure adequate trapping in the GMOT which necessarily increases the laser power required. By recognising the successful experiments at the University of Strathclyde in creating a rubidium GMOT we can assume an optimal cooling laser intensity of 45 mW which for a beam of 2.2 cm $1/e^2$ radius requires a fibred laser power of 230 mW. However, there is no basis in theory to suggest that lower laser intensities will not work; thus the test in this project is aimed at generating an intensity of 25 mW/cm^2 with 130 mW of fibred laser power. This means that a semiconductor diode can be used as a seed laser to a tapered amplifier rated at 500 mW rather than one of a higher output and thus of greater expense.

4.2.2 Laser

The laser system that meets the requirements and reasoning of the above is the Toptica TA 100 tapered amplifier (TA). It is a system rated at 500 mW maximum output from the amplifier section and therefore meets the power requirements laid out previously. The amplifier is seeded by a semiconductor diode rated at 90 mW (LD-0860-0080-AR-1) with a central wavelength at the Cs cooling transition and kHz

linewidths once paired with an external grating on the DL 100 laser head. Due to the nature of the amplifier, it mimics all properties displayed by the seed diode and thus acts as a higher output semiconductor laser with all the advantages already mentioned concerning lasers of this kind.

4.2.3 Stabilisation

4.2.3.1 Test Beam

For the locking of the seed laser, and thus, the TA; the original design of the system allows a weak leakage 'test' beam to escape from the casing by way of an internal partially transmitting mirror that works as one of a pair of mirrors used to seed the TA. Because of the power of the diode, this test beam is enough to perform spectroscopy and generate error signals for locking. Using this test beam one can also introduce the first half of an arbitrary red-shift of the output light to enable the Doppler cooling effect. This is achieved by using an AOM in a double pass configuration to increase the frequency of the test beam by 400 MHz before performing any spectroscopy, thus shifting the seed beam by -400 MHz to be resonant with any atomic transition that can be seen in figure 4.4. When an AOM is used in this manner, the deflection of the beam that occurs within the device is counteracted such that the frequency of the effect can be adjusted once aligned. How the TA is seeded with light of merely -(10-15) MHz rather than -400 MHz will be explained in section 4.2.4 as I will now concentrate on the spectroscopy generated after this first 400 MHz shift as well as its theoretical basis.

4.2.3.2 Saturated Absorption Spectroscopy

Conventionally during laser spectroscopy, the narrow, closely spaced, spectral lines that are characteristic of the hyperfine structure cannot be resolved due to Doppler broadening. This arises from the Maxwellian distribution of velocities within an atomic vapour, which causes some of the atoms to experience the laser light as shifted away from resonance in much the same way as described in chapter 2 with the (1D) detuning relationship: $\Delta - \omega_0 - kv$. The result is a broad transmission

profile reflecting the range of velocities relative to the probing beam.

In order to produce spectra with less Doppler broadening, Schawlow and Hänsch [173] developed the saturated absorption method of spectroscopy (SAS), which is based on the fundamentals of non-linear optical effects [174]. This method of spectroscopy requires shining two counter-propagating laser beams through an atomic vapour: one 'weak' probe beam, and one 'strong' pump beam [175–177]. The probe beam transmission is recorded and details how the vapour is affected by the pump beam.

In the case of a two level atom, the probe beam absorption by the vapour is proportional to the population difference between the upper and lower states. If the atoms have a normalised velocity distribution concurrent with the probe beam direction then the standard result is a steady state solution proportional to the initial population difference [155]. For a probe beam of intensity $I < I_{\text{sat}}$ there is a linear increase in population of the excited state, but as I becomes much greater than I_{sat}, this population tends to equal that of the ground state. This results in the transmission lineshape of a power-broadened Lorentzian where the low intensity limit reveals the transition linewidth Γ as the FWHM of the Lorentzian.

Three of the six smaller sub-Doppler features seen in the top spectra of figure 4.3 can be explained by considering the velocity profile of the vapour and how the pump beam burns a hole in this distribution with a Lorentzian shape and FWHM, Γ'. The hole is located at a position $v_z = -\Delta/k$, where Δ is the detuning of the laser from resonance and k is the laser light wavevector. Defining the pump propagation direction as positive in z means that it interacts with atoms of velocity $v_z = -(\Delta \pm \Gamma')/k$ while the probe selects the velocities: $v_z = (\Delta \pm \Gamma')/k$. The only time that both beams interact with the same atoms, thus changing the absorption of the probe beam, is when they have a velocity centred about $v_z = 0$. This change in absorption can be seen in figure 4.3 as half of the smaller sub-Doppler features. The other half of the features are crossover resonances which occur when the laser is tuned halfway between two hyperfine transitions [178].

While not used for locking in this project, SAS is useful for determining crude frequency scales and giving a more widely recognised idea of the resonance your

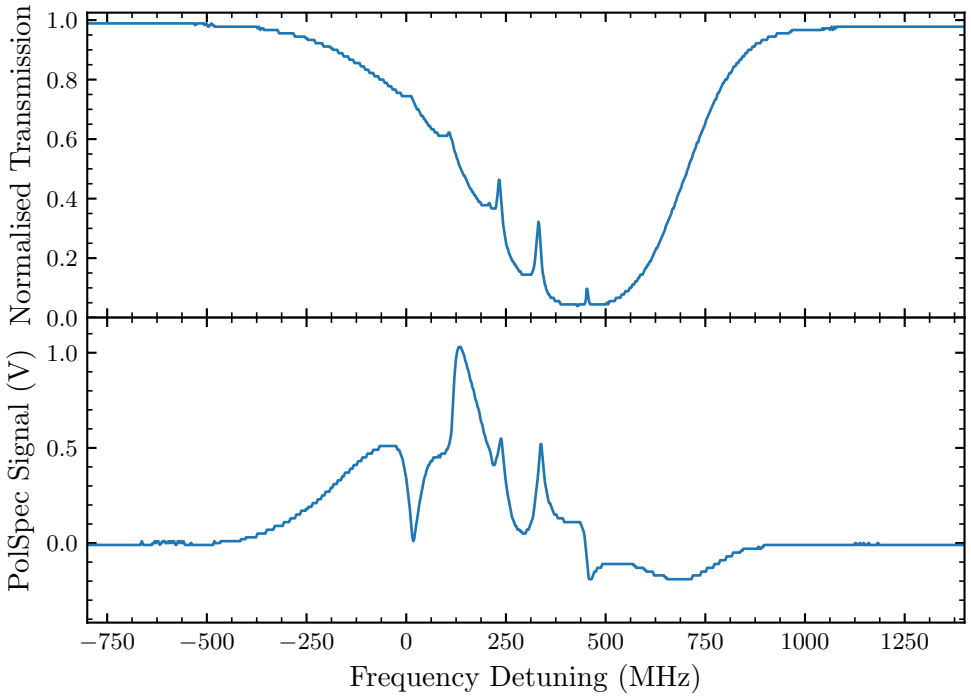

Figure 4.3: (Top) Normalised saturated absorption signal of the $6^2S_{1/2} \longrightarrow 6^2P_{3/2}$ transition showcasing the F=4 $\longrightarrow$ F'=3,4,5 hyperfine transitions of the D2 line as well as the F=4 $\longrightarrow$ F'=3,4; F=4 $\longrightarrow$ F'=4,5; and F=4 $\longrightarrow$ F'=3,5 crossover resonances. F=4 $\longrightarrow$ F'=5 (the right-hand most peak) is the cooling transition marked on figure 4.1 in red. The spacings of these transitions are also illustrated in the energy level diagram of figure 4.1. (Bottom) The corresponding polarisation spectroscopy signal to the above SAS spectra. Due to the features of the polspec signal being dependent on positions and relative absorption coefficients of the hyperfine transitions, there is a locking feature already coincident with the F=4$\longrightarrow$F'=5 transition.

laser is scanning across at-a-glance. It is therefore used as a reference for the true error signal generation method for the cooling laser. The optics to generate the SAS signal are shown in figure 4.4.

4.2.3.3 Polarisation Spectroscopy

Polarisation spectroscopy (polspec), like saturated absorption spectroscopy, involves both a probe and pump beam but offers a better signal to noise ratio [179]. In this technique the pump beam is circularly polarised and induces birefringence in the vapour that can be analysed by a linearly polarised probe beam [180]. This is because the linearly polarised beam can be decomposed into equal magnitudes of left and right-hand circularly polarised components. With the pump beam, these

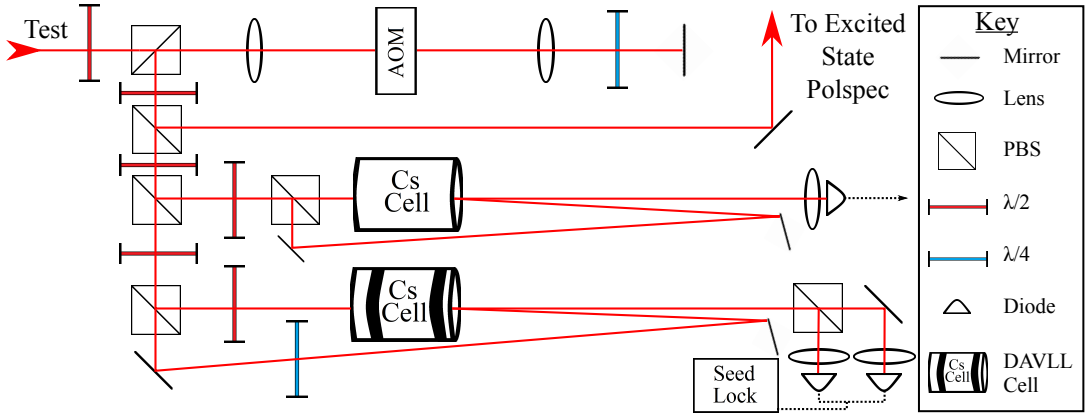

Figure 4.4: Optics used to generate SAS and polspec error signals for locking the tapered amplifier seed laser to the Cs cooling transition. The light noted in red is the test beam from the TA seed that begins from the top left of the diagram marked by the label 'Test' and originates from the seed laser noted in figure 4.5. The beam is initially blue shifted 400 MHz by an AOM in double pass configuration as the first stage of creating an arbitrary red-shift of the TA output. The blue-shifted beam is first split to give some laser power to the excited state polspec setup with the remaining light subsequently split to provide both an SAS reference and polspec error signal.

polarisations experience different refractive indices and absorption coefficients. This rotates the initially linearly polarised probe beam into an elliptical state where the ellipticity and rotation angle are proportional to the induced difference between the left and right-hand circularly polarised coefficients of absorption. The rotation can be detected by a polarising beam splitter, which decomposes the signal into its horizontally and vertically polarised components. By taking the difference of these two signals, a dispersive reference can be generated as can be seen in the lower plot of figure 4.3. Because of the clearly defined features of the spectra, a saturated absorption reference is not required but given here for context as was the case during experimental procedures. As this technique generates a lock point of approximately 15 MHz around the cooling transition of F= 4 $\longrightarrow$F$'$ = 5, does not depend on any external electronics and is insensitive to temperature variations, it is a reference that is easy to calibrate for a non-specialist user and has long-term stability after initial setup. In order to lock the laser, this signal is fed to a Toptica PID 110 which, once initially calibrated, gives reliable and robust laser locking. The optics used to generate the polspec signal are shown in figure 4.4 and include a dual input photodetector that automatically takes the difference of the two inputs to create the

error signal.

4.2.4 TA 100 Modifications

Thus far I have explained why a small red shift of 10-15 MHz to the TA output light is necessary for the cooling process and the first step towards achieving this by locking to offset atomic spectra. Initially, the final step of this process utilised a second AOM and the TA output itself in a double pass configuration before the light was subsequently coupled to a fibre. This could also act as a fast light switch by varying its frequency over 50 MHz via a TTL input which, despite maintaining coupling, would halt any cooling. The issue found with this configuration was an extreme inefficiency in the use of laser power due to the beam characteristics of the TA output. Approximately 65% of the laser light was being lost by the AOM before then being coupled to a fibre with an 60% coupling efficiency, leaving a final cooling power of approximately 150 mW in the experiment chamber to then be expanded for a final beam intensity of 9 mW/cm^2. While there have been successes at making GMOTs at such intensities, these MOTs have fewer atoms and thus are harder to detect meaning a higher beam power would be more desirable as explained in chapter 2.

As the generation of a small red-shift is a critical experimental parameter, the decision was made to instead use an AOM to blue-shift the main seed beam - with a smaller shift than given to the test beam - before it seeded the TA. As the TA output follows the frequency characteristics of its seed, this results in an output that already has the necessary red-shift and so can be immediately coupled to a fibre for maximised efficiency. An important factor to consider here is that the TA is never left unseeded when the fast switch is activated. This is achieved by having the AOM in a double-passed configuration, as when the frequency of the AOM is changed in this configuration there is minimal deflection of the beam. Thus, instead of reducing the light intensity, the output frequency of the TA is instead shifted enough that Doppler cooling becomes impossible. The reasoning for this choice is the more advantageous beam characteristics of the seed versus the TA output that results in much greater double pass efficiency at approximately 75%. Assuming the

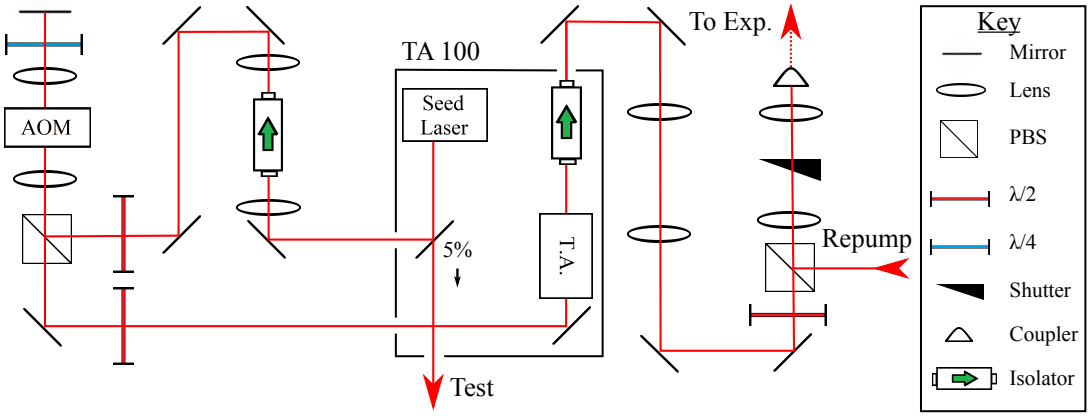

Figure 4.5: Schematic showing the approximate position of holes drilled to allow beams out and back into the TA 100 enclosure so as to be blue-shifted prior to seeding the TA. The 'Test' label indicates the origin of the test beam light in figure 4.4 as through a partially transmitting mirror. The left-hand-side of the diagram shows the double passed AOM configuration to blue-shift the beam by less than 400 MHz, and half-wave plate that allows more efficient seeding and TA power output than in the original design. Meanwhile, the right-hand side of the diagram details the optics used to fibre couple the TA output. The cooling light is joined by cross polarised repumping light at the final polarising beam splitter cube such that the two beams are coupled together.

same maximum output from the TA of 500 mW and a similar 60% fibre coupling efficiency, this results in a final beam intensity of over 25 mW/cm^2.

This method required small holes to be made in the casing of the TA 100 so as to allow the seed beam to be redirected out of the case and then directed back to the coupler of the amplifier after being red-shifted. The internal partially transmitting mirror was also remounted closer to the seed laser than in the original design. To achieve this, a block of stainless steel was machined to include taps with the specifications of the mirror mount dimensions and then fastened to the casing using existing screw holes in the base of the TA 100 enclosure. Using the same mirror in this way preserved the existing optical setup for locking the seed laser via its test beam as this was not at all diverted.

This configuration performed more than adequately as it increased the maximum output power of the TA to around 550 mW at its maximum injection current - this is possibly due to the inclusion of a half-wave plate just prior to seeding that aligns the laser polarisation closer to the axis of the TA coupling fibre, which was not present in the original design.

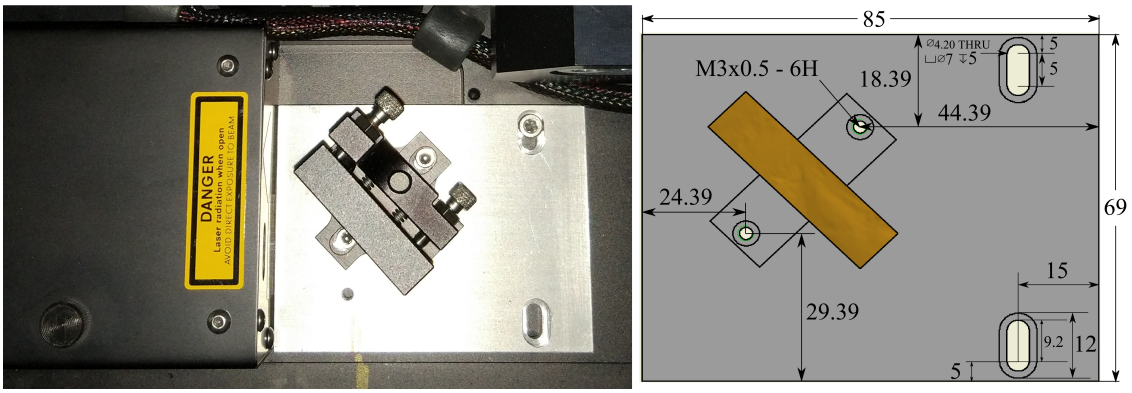

Figure 4.6: The custom TA 100 internal mirror mount (left) was designed to redirect the seed beam directly outward whilst maintaining the test beam with which to lock its frequency. The schematics are also reproduced (right). This modification allowed the more naturally circular seed beam to be shifted by an AOM before coupling to the tapered amplifier thus increasing power efficiency.

Figure 4.5 shows the optical layout used to achieve the red-shift with its view centred on the TA 100: the AOM setup on the left and fibre coupling optics on the right. The left image in figure 4.6 shows the customised mount and mirror directly adjacent to the seed laser casing, while the right image in the same figure shows the schematic used to produce the custom mount. There was an error in the original design that meant only one screw could secure the new mount to the base of the TA 100 enclosure - this has been corrected in the schematic but the true implementation still bears this error. As the mount also neatly aligns to the casing of the seed laser though, this mistake has no consequences in terms of the TA 100 operation or stability. Overall, these modifications were a complete success in terms of the project objectives as they took little effort to realise a greater laser power and were essentially costless with no impact to the system usability.

By comparison, this issue could have been solved by replacing the amplifier chip of the TA 100 with another of higher maximum output, incurring greater initial and running costs, as well as wasting a significantly larger amount of laser power.

4.3 Repumping Transition

4.3.1 Requirements

As mentioned previously, the chosen repumping laser must be able to re-excite the atoms lost to the dark state back into the cooling loop. Thankfully, the ratio of atoms that continue in the cooling cycle to those lost to the dark state is approximately 1000:1 and thus the power output of this laser is a less critical factor than for the cooling laser. This process is also not reliant on the Doppler shift and so does not require any double-passed AOMs nor a locking method as precise as polarisation spectroscopy. While an AOM is not needed for red-shifting the light, it is useful to include one in a single pass configuration as a fast light switch with which to analyse the formation of the trap. In this configuration, the deflection caused by the AOM is not counteracted and so once aligned, if the frequency setting of the AOM varies, the alignment (in this case, to a fibre coupler) is lost.

4.3.2 Laser

Due to these different criteria to meet, the size of the laser itself was prioritised and thus a Toptica DFB 150 mW laser diode (LD-0852-0150-DFB-1) was chosen to act as the repumping laser. While this is still a semiconductor diode, the underlying principles of its operation mean that it can produce MHz linewidths without an external cavity, therefore minimising its form factor to only require a short focal length cylindrical lens to counteract the output astigmatism. Lasers of this nature are limited to the range for which they are initially designed, but within this range they offer mode-hop free continuous tuning of up to 1400 GHz through the variation of input current and temperature control. Even after several months of inactivity, lasers of this type will return to the correct working wavelength with very little or no input from a user, meaning that this laser meets the core objective of being compact while also meeting the secondary criterion of requiring little specialised maintenance.

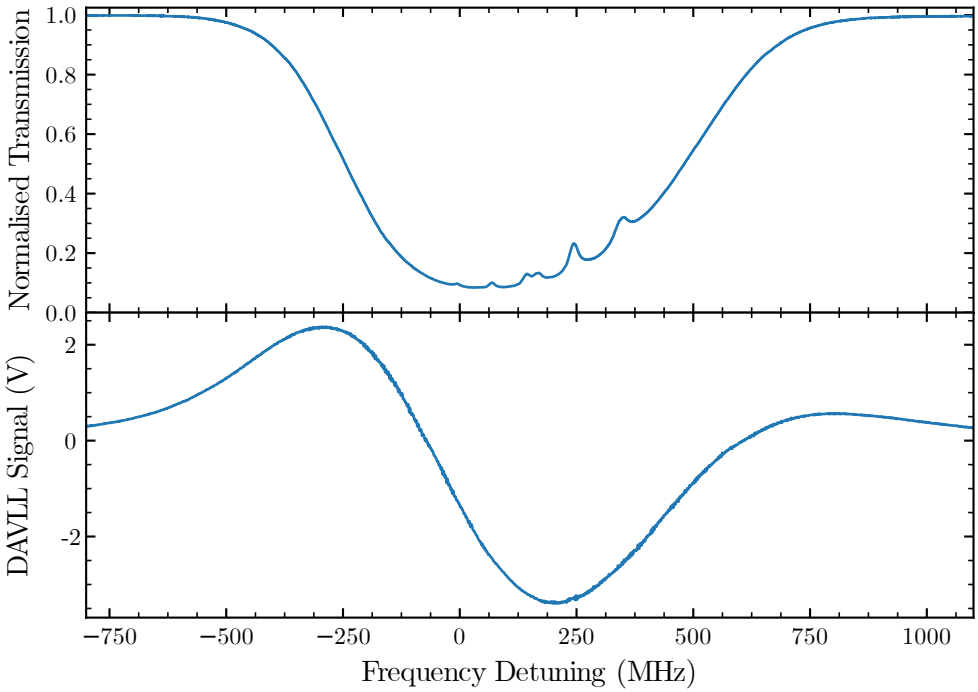

Figure 4.7: (Top) Normalised saturated absorption spectroscopy signal of the $6^2S_{1/2} \longrightarrow 6^2P_{3/2}$ line focusing on the F=3 $\longrightarrow$ F'=2,3,4 hyperfine transitions including the three crossover resonances. F=3 $\longrightarrow$ F'=4 (the right-hand most peak) is the repumping transition marked on figure 4.1 in blue. The spacings of these transitions are also illustrated in the energy level diagram of figure 4.1. (bottom) The corresponding DAVLL signal to the SAS reference. This signal can be given an arbitrary voltage offset in order to have a zero crossing coincident with the F=3$\longrightarrow$F'=4 transition but requires a reference in order to know which feature the laser is being locked to.

4.3.3 Stabilisation

Due to the lessened stabilisation requirements for the repumping laser a more simplistic and broad method for generating the error signal can be used. The 'dichroic atomic vapour laser lock' (DAVLL) technique offers a range of many hundreds of MHz of locking region but no clearly defined hyperfine structures due to its lack of a secondary pump beam (which is present in SAS and polspec arrangements). It was first demonstrated in 1994 [181] and with alkali atoms in 1998 [163] since which time it has been found to be most advantageous for situations in which modulation of the laser is to be avoided or a wide capture range is necessary (or simply not disadvantageous as is the case for this project).

The technique involves applying a weak magnetic field to a vapour cell in order

to separate the Doppler broadened absorption features into constituent Zeeman components. A linearly polarised beam is then shone through the cell, parallel to the magnetic field direction. Upon exit, the light is sent through a quarter wave plate and then incident on a polarising beam splitter that separates the two Zeeman components. The difference of these can be taken to produce a dispersive lineshape. The beam is split in this way because, as has been previously mentioned, linearly polarised light can be considered as equal magnitudes of left and right-hand circularly polarised light. Consider the simplest case of a J=0$\longrightarrow J$=1 transition; in the absence of a magnetic field, the $m_J = \pm 1$ states are degenerate, meaning that both circular polarisations are equally absorbed. This degeneracy is lifted with the application of a weak magnetic field that causes the vapour to become dichroic with each handedness of polarisation shifted away from the line centre, and from each other. A weak magnetic field is specified to only shift the Zeeman components by a frequency akin to their Doppler widths. With only this small shift, the difference of the two signals produces a dispersive lineshape with many locking points and thus, a large capture range [182].

As has been previously stated, the DAVLL technique does not require a secondary pump beam that, while making the initial setup more simple, does preclude using the technique alone as a locking method due to the resulting signal's lack of hyperfine features. To remedy this, a saturated absorption reference must also be included with which to identify the position of the desired lock point. Figure 4.7 shows the SAS reference (top) used to calibrate the DAVLL spectra (bottom) to the F=3 $\longrightarrow$ F'=4 repumping transition. The slope on the right-hand side of the spectra is used to stabilise the laser by introducing a voltage bias to the signal such that the 'zero-point' of the slope is coincident with the correct hyperfine peak on a monitoring oscilloscope.

Due to the inclusion of an AOM to act as a fast switch for the repumping light, the DAVLL stabilisation optics have been placed before this stage so that it is possible for the repumping laser to remain locked in the event of the switch being activated. This mimics the functionality of the TA seed AOM that uses a small shift to stop the cooling process while maintaining the amplifier seeding and the seed lock, which is

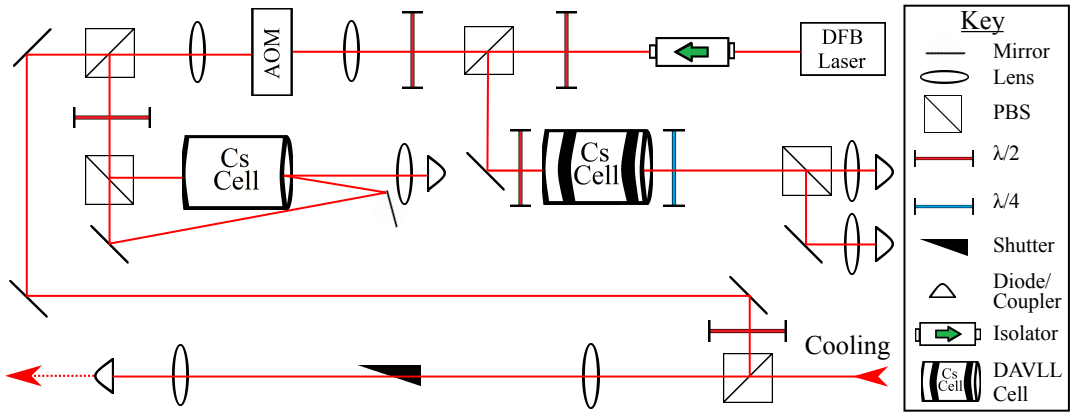

Figure 4.8: Optical arrangement surrounding the DFB repumping laser used to generate a saturated absorption reference and DAVLL locking signal. The AOM placement after the DAVLL locking setup means that the laser can remain locked to the repump transition while the output light is switched off. The final fibre coupling is cross polarised to the cooling light due to combining the beams in a polarising beam splitter, but as the repumping effect is not polarisation dependent that is an adequate arrangement.

independently defined by the test beam AOM. Thus, when activated simultaneously, these AOMs ensure that the trapping effect can be disabled with a response time on the order of nano-seconds. In the event of a switch, it does mean that the SAS reference spectrum view is disabled as its optics are placed after the AOM, but this should not be an issue after initial calibration. One other effect to note about this arrangement is that the SAS reference is shifted by 80 MHz with respect to the DAVLL signal, but this is not an issue due to the wide locking range of the DAVLL method. The final coupling to a fibre is via a polarising beam splitter in order to combine both the repumping and cooling beams within the same cable. The optical arrangement for the repumping section in its entirety can be seen in figure 4.8.

In terms of usability for a non-expert in atomic spectroscopy, DAVLL in combination with SAS has the most simple presentation to understand and troubleshoot, as after initial setup all that one may possibly need to do to alter it after a small drift is apply a small voltage bias such that the reference and DAVLL crossing are again in sync.

4.3.4 1st Excitation Step Summary

At this stage, both the cooling and repumping laser choices have been accounted for in terms of project objectives as well as how they are both stabilised to their respective transitions and coupled to the trapping chamber, thus realising the first step of creating a cold Cs ion source. What remains then, are the higher, 2nd and 3rd excitation steps that I will now address in much the same regard.

4.4 2nd Excitation

4.4.1 Requirements

The reasoning behind choosing to exploit the $6^2P_{3/2} \longrightarrow 7^2S_{1/2}$ transition at 1470 nm, shown in figure 4.2, to the second excited state of Cs has been previously explained in terms of the project objectives. To summarise: a cheaper semiconductor diode laser can be used, the transition will require less laser power to use as it has coupling strength comparable to the cooling transition, the laser can be tightly focused to form as small an ionisation region as possible, it forgoes more dangerous alternatives, and it enables a choice of ionisation methods for the 3rd excitation step. What is required then, is simply a semiconductor diode of moderate power output ($\sim$ 40 mW) with no additional special concerns.

4.4.2 Laser

Such a laser is an independent Toptica DL 100 external cavity laser head system using a diode (LD-1450-0060-AR-1) with an output of 60 mW. While this laser is neither as compact nor as stable as the DFB laser, nor as powerful as the TA 100, as has been previously stated, these are not concerns for the use of this laser and thus a cheaper, non-specialised laser such as this can be used. As this is essentially the same laser system as is present in the TA 100 being used as a seed, they share all characteristics of linewidths and stability but differ in their central wavelength outputs of 1470 nm and 852 nm, respectively.

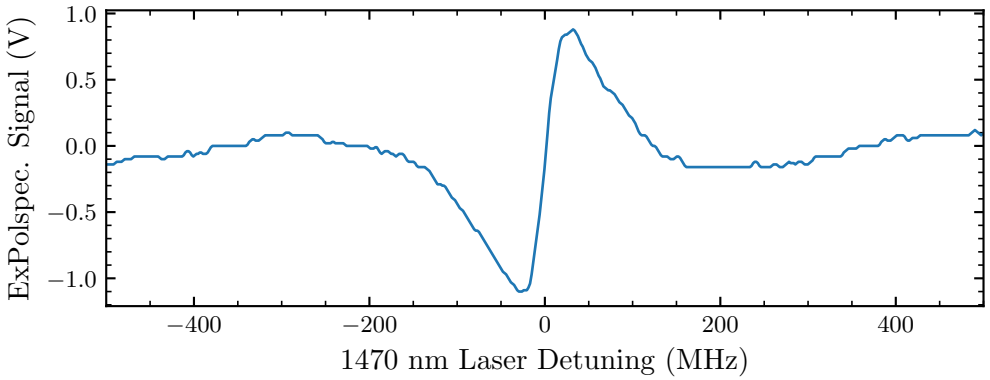

Figure 4.9: Excited state polarisation spectroscopy of the $6P_{3/2} \longrightarrow 7S_{1/2}$ transition in Cs. The vapour is pumped with circularly polarised 852 nm light and the rotation of a linearly polarised 1470 nm probe beam is measured to form a dispersive signal reference. The laser detuning was determined using a Fabry-Pérot etalon. As there is no 1470 nm pump beam, the signal is in the form of a single, broad distribution without any hyperfine transition features present.

4.4.3 Stabilisation

Again, in a similar fashion to the seed laser of the tapered amplifier, the independent DL 100 can be stabilised by using polarisation spectroscopy but of the excited state (expolspec). While the theory of expolspec is consistent with the explanation given in section 4.2.3.3, the experimental method to generate an error signal with the technique is slightly more complex than with the ground state, as it requires a circularly polarised pump of resonant 852 nm light co-linear with a 1470 nm probe. The way this was isolated can be seen in figure 4.4 in which, immediately after the test beam has been blue-shifted, some laser power is siphoned away to the expolspec setup and dichroic mirrors are used to either direct or allow the relevant light. In order to analyse the resonance of the pump, a dichroic mirror redirects the 852 nm pump to a referencing diode. The resulting spectra from recording the 1470 nm beam rotation can be seen in figure 4.9. Once locked, the laser is coupled to a fibre so as to reach the experiment chamber. The full optical arrangement for this section can be seen in figure 4.10.

This technique is similar to DAVLL in that it produces a broad locking feature and so in this regard is convenient to an end user in that, if the feature is there, they can lock to it, but with the additional advantage of not needing to align the signal to a particular resonance feature in an SAS reference, thus increasing its ease

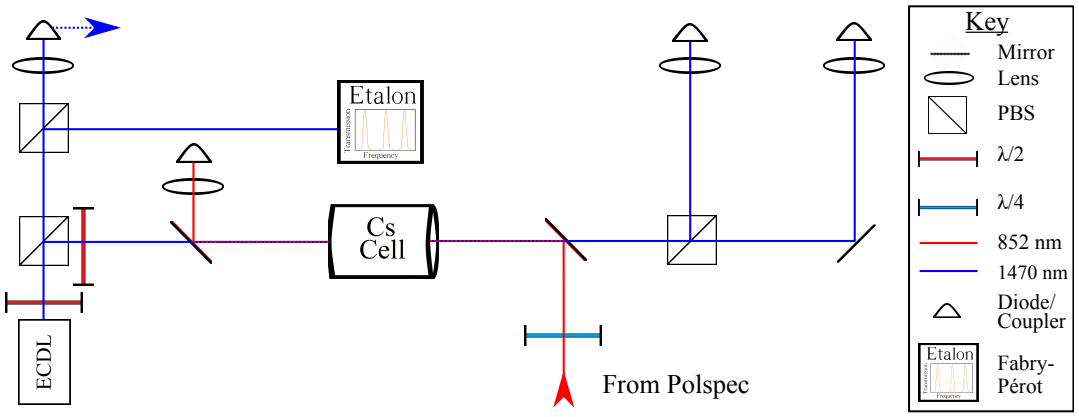

Figure 4.10: Optics used to generate an excited state polarisation spectroscopy error signal in order to stabilise the DL 100 to the $6^2P_{3/2} \longrightarrow 7^2S_{1/2}$ transition at 1470 nm. The light noted in red is the test beam from the TA seed at 852 nm that has been blue-shifted by an AOM shown in figure 4.4 before being isolated and circularly polarised to act as a pump beam. The light noted in blue is at 1470 nm and is generated by an independent DL 100, marked on the diagram as 'ECDL'. The excited state polspec signal generated by this setup through measuring the 1470 nm probe shows no hyperfine features as there is no 1470 nm pump beam. Due to this setup generating only one broad feature in its spectra, a Fabry-Pérot etalon is necessary to give a frequency calibration for the reading.

of use.

In past atomic physics experiments studying highly excited Cs, this has been the first step in a ladder that becomes increasingly reliant on itself for support in that the stabilisation of this transition requires the stabilisation of the previous transition. Given even just three excitation steps, the optics required to stabilise three lasers that are all dependent on each other can be become unwieldy. This is one reason that this method of stabilisation will be the last to use a transition reliant on another; more detail of the reasoning behind this will be given in the following section as the $7^2S_{1/2}$ state allows less conventional methods up the ladder towards ionisation.

4.4.4 2nd Excitation Step Summary

The first two steps towards ionisation of Cs have been defined in terms of the project objectives with the 2nd excitation being coupled using a cheap semiconductor diode laser; a doubly cost effective step due to the strong transition coupling between $6^2P_{3/2} \longrightarrow 7^2S_{1/2}$ requiring a weaker laser and therefore lower running costs. Due

to its cavity design, it also produces kHz linewidths within a relatively compact package. The system needs a limited knowledge of atomic physics to successfully lock and maintain after initial setup because of the simplicity of its expolspec error signal and is stable in the long term as it is based on light from a semiconductor diode laser. All that remains now is to address the final excitation step towards ionisation and how the use of the intermediary 1470 nm transition allows an innovative method of far-off resonant locking to excite the $7^2S_{1/2} \longrightarrow 23^2P_{1/2}$ in Cs, using a ground state transition in another alkali metal atom.

4.5 3rd Excitation

4.5.1 Requirements

While the first two steps were easily accounted for in terms of the transitions being available to cheaply exploit and efficiently lock to (due to the availability of semiconductor diode lasers at those wavelengths and previous research into them [160, 181, 183]), the final step presents more logistical challenges. These stem from the power requirements of the process and the difficulty of making efficient use of that power, as there is no locking reference. This means that, without additional options, the final step would involve using a wavemeter and manually tuning to resonance, with subsequent manual adjustments to remain at resonance, while also being careful to not impart too much energy to the resulting ions - a near impossible feat for an untrained user. This is clearly less than ideal as automation is always welcome but wavemeters that allow PID functions can be prohibitively expensive.

The proposed alternative is to instead utilise two things that the Durham Department of Physics has in great abundance: spare rubidium vapour cells and experience of working with Rydberg atoms. These are atoms that have been excited to a high principle quantum number n and so require relatively weak electric fields to ionise them [147]. The coupling to Rydberg states also means that it requires less laser intensity to achieve than straight light-field ionisation and, crucially, a new method can be devised for locking to an ideal transition using a near-coincident resonance in another element that will provide power efficient and highly stable long term opera-

tion, the process of development, and discussion of which, forms the remaining body of this chapter. Work in this section was achieved with the help of Daniel Whiting, Nikola Šibalić, and Jorge Massayuki Kondo; and is the subject of [64], with early work described in [184].

4.5.2 ZSAR

4.5.2.1 Introduction

As has been discussed previously, sometimes it can be desirable to stabilise a laser's frequency away from resonance, which can be more challenging to achieve. A common approach is to use a second laser which is referenced, or slaved in some way to a laser that is stabilised to an atomic transition. Often this is achieved via a stabilised cavity [185–187]. Alternatively, one can perform a beat measurement between the slave and reference lasers and stabilise the frequency difference between them [188, 189] or apply a sideband to the light using an electro-optic modulator (EOM) and seed the slave with the sideband [190, 191]. Often, it is desirable to stabilise a laser to a transition between two excited atomic states [183], in which case it is necessary to have additional lasers to first couple the ground state population to the lower of the excited states. An example of this is in the study of Rydberg systems where it is typical to use two [170] or more [171, 172] lasers. As transitions to Rydberg states typically have small electric dipole moments [154], large laser intensities can be required. An alternative approach is to use a transition in one atomic or molecular species to serve as a frequency reference to another species with a near-coincident transition energy. For example, iodine cells have long been used as a frequency reference in the infra-red due to the large number of well-characterized spectral lines in that range [192, 193]. There are also examples of one atomic species being used as a frequency reference for another in precision measurement experiments, for example in [194].

Here is presented a simple method to provide a tunable frequency reference, based upon saturated absorption and frequency modulation spectroscopy [167–169] of rubidium vapour in the presence of a large magnetic field. It is demonstrated

that the technique can provide a wide and continuously-tunable locking range in the vicinity of the D1 transition (795 nm) and can be used to provide a frequency reference for the $7^2S_{1/2} \longrightarrow 23^2P_{1/2}$ transition in caesium which is approximately 19 GHz detuned from the unperturbed D1 transition in Rb [195]. The method is essentially drift-free as it relies on large permanent magnets, and unlike methods using Faraday rotation [196], is insensitive to temperature fluctuations. Previously, in other work, demonstrations of using the Zeeman effect to provide a frequency offset have been made. E.g. Ref. [197] uses a 40 μm vapour cell [198] placed between permanent magnets to stabilize a laser to an atomic resonance shifted by > 5 GHz or Ref. [199] wherein a stated application of their scheme is a stable reference setup. Because the Zeeman shifts are greater than the typical Doppler broadening, the method is also useful for simplifying atomic spectra into more cleanly defined systems and thus has applications in enabling precision measurements and quantum optics in thermal vapours [200–203].

4.5.2.2 Theory and Modelling

Hyper Fine Paschen-Back Spectroscopy The principle behind the locking technique is the Zeeman effect and so it has been given the name 'Zeeman Shifted Atomic Reference' (ZSAR). Figure 4.11(b) shows the evolution of the spectral feature locations of the ^{85}Rb D1 line as a function of applied magnetic field strength where detuning is measured relative to the center of gravity of the hyperfine split ground and excited states. Also in Fig. 4.11(b), the opacity of each line indicates its respective transition strength, normalized to the strongest transition of this set. At high field, the atomic medium enters the hyperfine Paschen-Back regime, where the Zeeman interaction is greater than the hyperfine splitting. In this regime the total angular momentum is no longer a good quantum number [204]. Instead, the states are most easily described by the electron spin-orbit (J) and nuclear spin (I) angular momenta and their respective projections onto the magnetic field axis, m_J and m_I. Using the ElecSus software [205], which calculates the electric susceptibility of the medium, one is able to accurately predict the weak probe spectrum at arbitrary magnetic fields [206] and therefore infer the magnetic field strength at the position of

the atoms from transmission measurements. This means that the technique also has the potential to act as a magnetometer with a similar accuracy to a standard Hall probe. Figure 4.11(a) shows the Rb D1 spectrum calculated by ElecSus for a linearly polarised probe passing through a 2 mm vapour cell at 95 °C in a magnetic field of 0.954 T. For comparison, the spectrum at zero field and 20 °C is added in grey. The region inside the dashed box is compared to experimental data in section 4.5.2.3. The vertical lines denote the frequency of $\Delta m_J = \pm 1$ transitions at high field shown in Fig. 4.11(a), where blue are σ^- and red are σ^+ transitions, respectively. The very small features located at detunings of approximately ±9.5 GHz are additional weak transitions that are allowed due to residual hyperfine mixing. This effect is taken into account in the full diagonalization, performed by the ElecSus software, of the atomic Hamiltonian in the presence of the magnetic field. More details of this process and the ElecSus software can be found in [207]. There are no π transitions as, in the model, the k vector of the probe beam and B field vector are parallel.

Rydberg Atoms and Field Ionisation The term 'Rydberg atom' denotes an atom with one or more electrons that have been excited to a high principle quantum number, n. They were first empirically described by Johann Balmer in 1885 and then, more generally, by Johannes Rydberg in his formula for the binding energy of an electron in the nth principle quantum level of hydrogen [208]:

$$E_n = \frac{-R_\mathrm{H}}{n^2}, \tag{4.5.1}$$

where R_H is the Rydberg constant, 13.6 eV. Equation 4.5.1 can also describe any 'hydrogen-like' system where there are separate regions of positive and negative charge - and therefore, is applicable to highly excited ^{133}Cs.

Because the atomic radius scales with n^2, Rydberg atoms can be extremely large. This size means that they are very sensitive to external electric fields and can be easily ionised with an electric field strength that scales with n^{-4} [147]:

$$E = 3.21 \times (\frac{100}{n})^4 \text{ V/cm}. \tag{4.5.2}$$

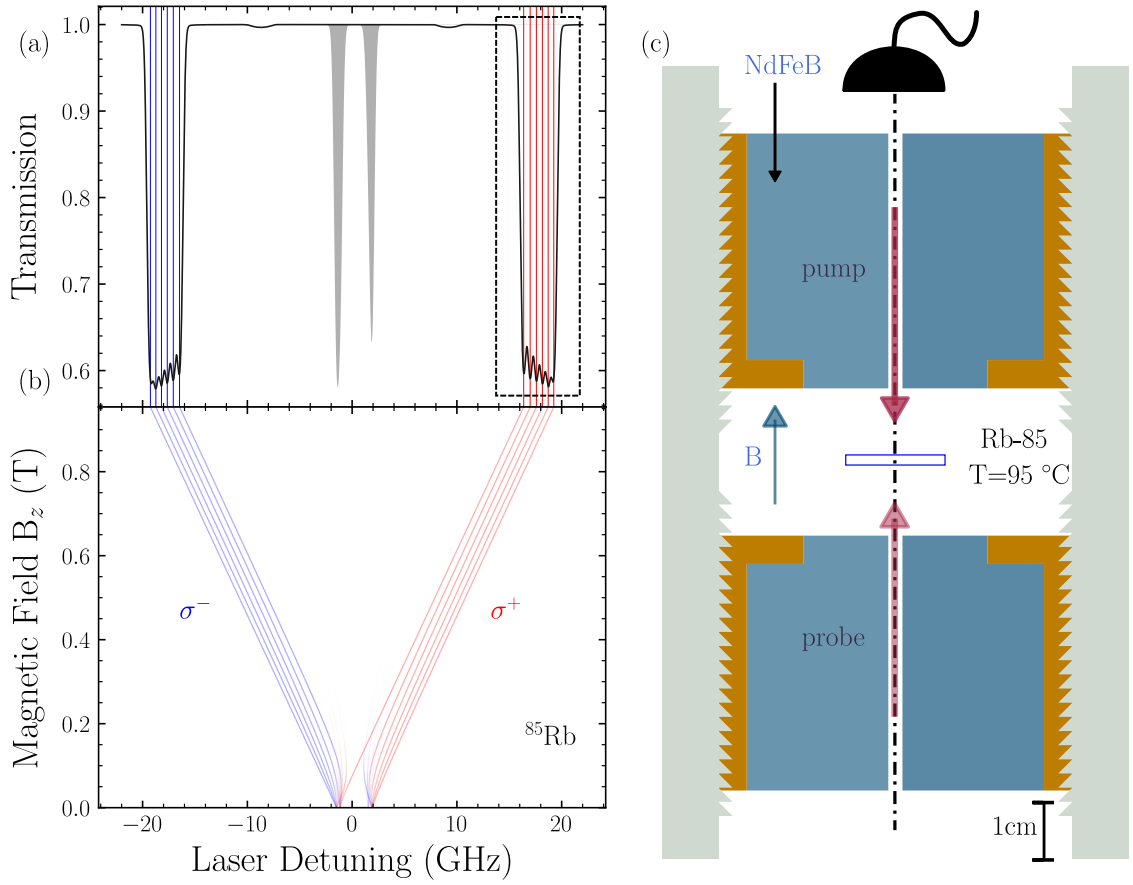

Figure 4.11: (a) A theoretical plot generated by ElecSus showing the transmission spectra of the D1 line of ^{85}Rb at 0.954 T and 95 °C, as well as the same spectral line at zero field and 20 °C displayed in grey for comparison. The region within the dashed box is used to provide the frequency reference in the experimental section. (b) A Breit-Rabi diagram showing the evolution of the spectral feature locations with increasing magnetic field, where σ^+ and σ^- transitions are coloured red and blue respectively. The small dips in transmission at approximately ±9.5 GHz are weak transitions that are allowed due to residual hyperfine mixing. The opacity of the points denote their transition strength normalised to the strongest transition in this set. (c) To scale diagram of the apparatus showing the B-field orientation relative to the probe and pump beam propagation directions. The experiment cell is a heated ^{85}Rb cell with a 2 mm optical path length, flanked by NdFeB magnets.

For the $23P_{1/2}$ state in Cs this gives a field ionisation voltage between plates separated by 9.45 mm (see chapter 6), as 1100 V. This a relatively low requirement compared to the capabilities of modern high voltage power supplies and would therefore be simple to pulse and thus control ion flow. Ionisation by this method has the possibility of lowering spot sizes below the diffraction limit of ionisation lasers despite using minimal electric fields [48].

4.5.2.3 Experiment

A heated vapour cell with an optical path length of 2 mm containing ^{85}Rb is placed between two magnets. To produce the desired magnetic field, a pair of custom designed NdFeB permanent magnets from first4magnets, were mounted in a Helmholtz configuration with a separation of 9.7±0.1 mm. This distance was chosen as it was predicted to give a field strength of 9540 Gauss over the cell (the required field strength); which was later verified using a Hirst GM07 gaussmeter and by fitting weak probe transmission data using the ElecSus software. A diagram of the magnet apparatus is shown in Fig. 4.11(c). The cylindrically symmetric magnets each have an outer diameter of 49 mm and an inner diameter of 3 mm and individually produce an axial field of 0.5 T at the entrance to the bore. The inner bore holes allow clear passage of laser beams. The magnets also feature a small notch on their inward faces to facilitate secure mounting in a custom brace, which is threaded to allow precision adjustment of the magnet positions. In this way the magnetic field strength can be fine-tuned in the region of the vapour cell.

An external cavity diode laser operating at 795 nm is used to produce a weak probe beam and a strong pump beam. These beams, with $1/e^2$ radii of 90±10 μm, counter-propagate and overlap within the vapour cell. In this geometry the beams are aligned with the magnetic field axis. The laser frequency scan is calibrated and linearised using a Fabry-Pérot etalon. As the frequency of the laser is swept over the D1 transition, the probe beam transmission is recorded using a photodiode. At high magnetic field, the optical transitions separate and the optical density on resonance decreases. The temperature of the cell is stabilised at 95 °C to maintain a sufficient optical density. This experimental layout is illustrated in figure 4.12.

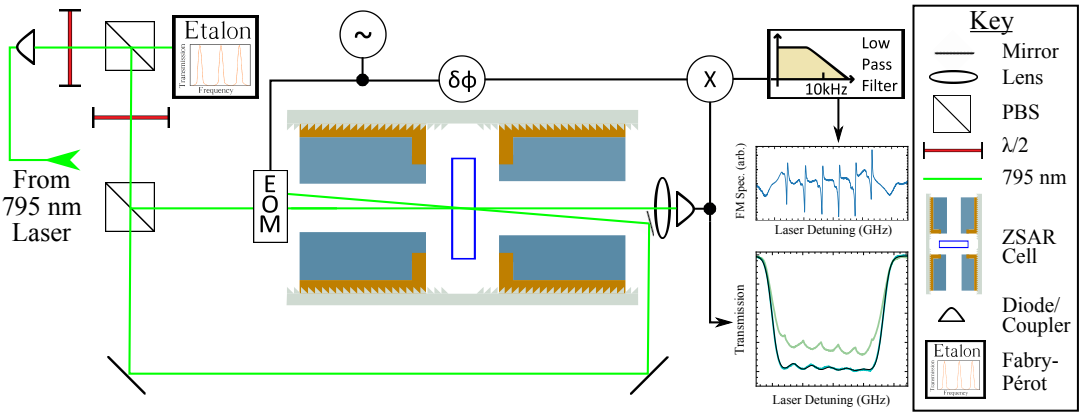

Figure 4.12: The arrangement of optics and electronics used to generate the dispersive ZSAR signal reference. For this setup, the 795 nm input light was provided by a laser in an adjacent lab via an optical fibre. The Fabry-Pérot etalon was used to determine the frequency scaling. The EOM before the 2 mm ^{85}Rb cell (thin lined blue rectangle) was driven at 20 MHz by an arbitrary function generator in order to modulate the probe beam. This driving signal is also given an additional phase correction before being mixed (via a Minicircuits ZX05-1L-S+) with an amplified (via a Minicircuits ZFL-500LN+) Hamamatsu C5460 diode signal and being filtered to reveal the final FM spectroscopy signal. The NdFeB magnets flanking the Rb cell give a ∼1 T magnetic field parallel to the probe beam direction. The figure shows examples of both raw and final FM spectroscopy spectra.

Figure 4.13 shows the experimental transmission of the horizontally polarised probe beam through the cell, with (green) and without (cyan) the counter-propagating pump beam. In order to calibrate the magnetic field strength and cell temperature, it is important to initially use a weak probe, $I/I_{\text{sat}} \approx 8{\times}10^{-3}$ [209], to ensure good agreement with the theory curve (grey) generated by ElecSus. This range of frequencies corresponds to the region in the dashed box in Fig. 4.11(a). The agreement between theory and experiment is excellent when fitting to the experimental parameters of T = 96 °C with an RMS error of 0.2 %. The green plot shows the same probe transmission as before but now with a saturating pump beam ($I/I_{\text{sat}} \approx 4$), counter-propagating the probe, as shown in Fig. 4.11(c). It is from this Doppler-free signal that the reference signal is derived as it resolves all of the individual transitions. There are no cross-over resonances in the spectrum as the features are further apart than the Doppler width. This level of agreement means that measurement with a Hall probe is not strictly necessary as ElecSus is able to determine the magnetic field with a similar degree of accuracy.

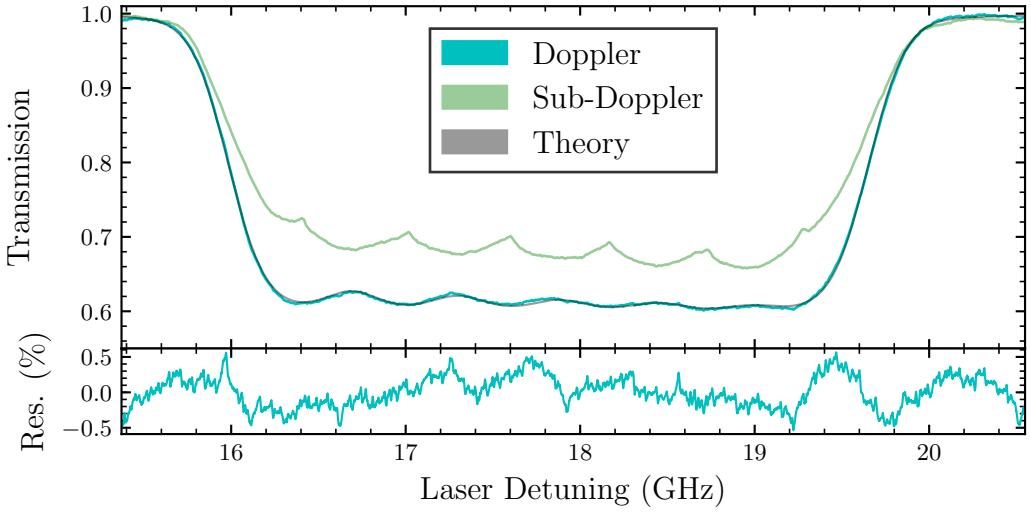

Figure 4.13: ^{85}Rb Doppler broadened spectra which focuses on the positively detuned, σ^+ transition at B = 0.954 T with cell temperature of $\approx$ 95 °C as denoted on Fig. 4.11(b) by the dashed box. The grey line corresponds to an ElecSus theory plot using these experimental parameters, whilst the cyan line is the experimental Doppler spectra data. The residuals between theory and experiment are shown in the lower pane. The green line shows the sub-Doppler spectra of the Rb once a counter-propagating pump beam has been applied. It is from these resolved features that the FM signal is derived.

To generate a suitable dispersive-shaped reference for laser stabilisation, frequency modulation (FM) spectroscopy is employed. To implement this, the probe beam is modulated using a 20 MHz EOM driven by an arbitrary function generator. The probe transmission, measured using a Hamamatsu C5460 20 MHz avalanche photodiode module, is amplified using a Minicircuits ZFL-500LN+ amplifier and mixed with the local-oscillator via a Minicircuits ZX05-1L-S+ mixer. The mixer output is then passed through a low-pass filter to remove the residual high-frequency components, leaving only the dispersive FM signal. Finally, the phase of the local oscillator is adjusted to maximize the FM signal amplitude.

The measured FM spectrum is shown in Fig. 4.14(a) wherein the six dispersive features correspond to the sub-Doppler resonances of the spectra in Fig. 4.13. For the locking signal characterisation, only the 6th, maximally detuned feature, was initially considered (enclosed by the box) as this feature was the most simple to align with our desired frequency. In operation, however, the 5th feature was also used due to the subsequent inclusion of a double-passed AOM before the experiment.

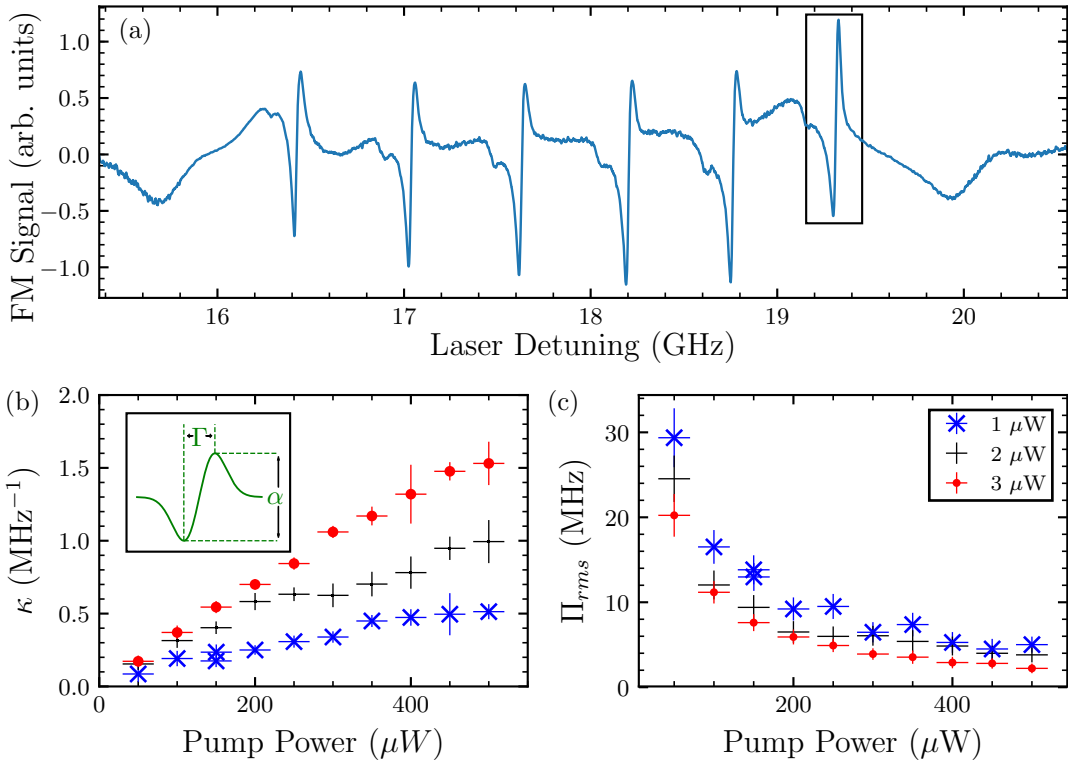

Figure 4.14: (a) Experimentally measured FM spectra showing the six dispersive features associated with the six sub-Doppler resonances appearing on the positively detuned part of the probe transmission spectrum. The feature highlighted by the black box was used to characterize the signal. (b) A study of the gradient, κ of the FM feature contained within the black box as defined by α, its peak to peak height, and Γ; its width. The data exhibits a linear relationship between κ and the pump beam power. (c) An analysis of the uncertainty of the position of the locking feature Π_{rms}, in relation to both probe and pump powers. The minimum uncertainty was found to be 2.2±0.6 MHz.

Characteristics of these features though, appear to be consistent. The analysis begins by investigating the gradient κ of the zero-crossing as the pump and probe beam powers are varied. κ is defined as the ratio of α, the feature peak-to-peak value, and Γ, its width. It is this quantity, along with the noise on the photodiode signal, which will primarily govern the characteristics of the laser frequency stabilization. Figure 4.14(b), shows the evolution of κ as a function of pump power for three different probe powers. There is a clear increase in the gradient with both pump and probe power over the range of parameters used. However, the power of the probe beam is necessarily kept below 5 μW to stay within the linear response range of the photodetector. It is expected that this trend would eventually saturate due

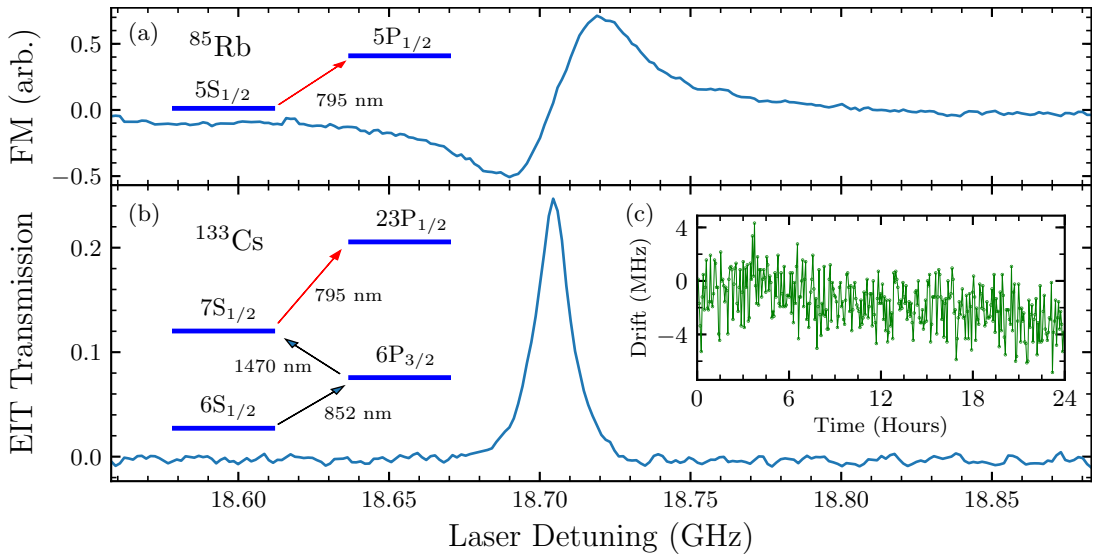

Figure 4.15: (a) Frequency modulation (FM) signal generated using the $5S_{1/2} \longrightarrow 5P_{1/2}$ transition in ^{85}Rb at B = 0.954 T and (b) the simultaneous Rydberg EIT signal generated using Cs atoms on the $7S_{1/2} \longrightarrow 23P_{1/2}$ transition. Both plots are an average of 3 data sets. The FM signal probe and pump powers were 2 μW, and 300 μW respectively. Because of the addition of a double passed AOM to the EIT setup, the EIT signal is shifted by ∼ 400 MHz and therefore coincides with the 5th dispersive feature of the FM spectra. Characteristics of this alternate feature are consistent with the original analysis. (c) The measured long term drift in the relative positions of the EIT and FM spectral features, over a period of 24 hours. The maximum drift values were +4.3 MHz and -6.8 MHz with an RMS deviation of 2.5 MHz.

to power broadening and optical pumping.

Next, using the same data, the RMS frequency uncertainty Π_{rms} of the zero-crossings can be inferred by comparing the gradient at line center with the RMS noise, Σ_{rms} for each signal, i.e. $\Pi_{\text{rms}} = \Sigma_{\text{rms}}/\kappa$. Σ_{rms} was determined by taking the wings of each signal (which should be smooth in the absence of noise) and measuring their RMS deviations. The resulting frequency uncertainty can be seen in Fig. 4.14(c); the minimum uncertainty was found to be 2.2±0.6 MHz in the case of 3 μW probe and 500 μW pump beams, respectively. Note that these were the highest pump and probe powers used and the data sampling rate for these measurements was 50 kHz.

Finally, an upper bound on the drift of the method can be assessed by measuring the resonant frequency of the dispersive feature with respect to the line centre of another atomic resonance, generated independently. For this, a three-photon Ryd-

berg EIT setup [171] in caesium was used, where the $7S_{1/2} \longrightarrow 23P_{1/2}$ transition is in close coincidence to the Rb D1 line. The level diagram is shown as an inset to Fig. 4.15(b), where the $6^2S_{1/2} \longrightarrow 6^2P_{3/2}$ transition is stabilised using polarisation spectroscopy and the $6^2P_{3/2} \longrightarrow 7^2S_{1/2}$ is stabilised via excited state polarisation spectroscopy [160, 183]. Figures 4.15(a) and 4.15(b) show the FM spectroscopy feature in Rb and the Rydberg EIT feature in Cs respectively. The spectra were recorded at the same time and compared over a 24–hour period. Figure 4.15(c) shows the relative drift between the two signals; the maximum recorded deviations were +4.3 MHz and -6.8 MHz with an RMS deviation of 2.5 MHz.

4.5.2.4 Discussion

The long term drift to negative frequency shown in Fig. 4.15(c) is dominated by the instability of the Rydberg EIT reference. This is caused by a drift in the reference voltage which provides an offset to the servo circuit used to stabilize the laser to the $6^2P_{3/2} \longrightarrow 7^2S_{1/2}$ Cs transition. It is therefore expected that the drift in the ZSAR signal is considerably less than the RMS drift measured here.

The short term RMS fluctuation in the reference frequency shown in Fig. 4.15(c) is consistent with fluctuations due to the RMS noise on the photodiode signal Fig. 4.14(c). Thus, it can be inferred that ZSAR is highly robust to local perturbations as, in order to induce a shift of this magnitude, either the laboratory ambient field would have to fluctuate by ± 1.8 Gauss or the magnets themselves move by ~ 200 μm. Both scenarios are highly unlikely. Therefore it can be concluded that the limiting factor to the lock stability is the photodiode. If it were to be replaced with a lower noise detector, a greater signal-to-noise ratio and a reduced frequency uncertainty would be achieved.

It should be stated though that the ZSAR method does not provide absolute frequency calibration but rather allows an arbitrary and stable offset to be applied to a well-defined atomic frequency reference. In addition, the use of weak probe transmission measurements, such as those shown in Fig. 4.13, allows the magnetic field in the vicinity of the cell to be calibrated to approximately 0.5% [205], similar to the precision of standard Hall probes.

4.5.3 3rd Excitation Step Summary

To summarise, what has been demonstrated in this section are the steps involved in the building, and implementation of, a low-drift atomic frequency reference based upon the Zeeman effect with a large continuous, stable tuning range around the D1 line in rubidium, which can be used to replace inefficient alternative locking methods. With the available field of ≈1 T it can achieve detunings of ±20 GHz from line centre of gravity with much greater detunings being possible, only limited by the applied magnetic field strength. It is also important to note that when comparing weak probe spectra to the ElecSus software it is not necessary for the laser to have a scan range that covers the entire spectrum.

In direct comparison with the 3-photon EIT scheme for laser frequency stabilisation [171] which would otherwise have to be used as a locking reference, the scheme presented here has clear advantages. ZSAR has a significantly simpler experimental setup, requiring only a single laser with around 1 mW of optical power. It is therefore cheaper and less sensitive to fluctuations in alignment and power than the EIT method. Additionally, the excellent passive stability and the large continuous tuning range provided by the permanent magnets allows for simple and robust on-resonant and off-resonant locking.

Finally, it is a trivial matter to extend the tuning range of the ZSAR scheme by using stronger magnets and/or choosing another atomic transition. Eg. for the same magnetic field used here, by using the D2 line in ^{87}Rb the detuning can be increased from 19.2 GHz to ∼26 GHz. This stable and versatile off-resonant frequency reference offers flexibility and simplicity for applications in cold atom and quantum optics experiments but crucially fulfils my need for a simple and efficient Rydberg excitation scheme that minimises running costs and initial investment, as well as the system size, while producing a clear, stable locking reference suitable for a user untrained in atomic spectroscopy.

Component	Price ex-VAT (£)	#	Supplier
Lasers	20000	-	Toptica
Optics	5000	-	Thorlabs
AOMs/EOM	1500	4	Photon Lines
Vapour Cells	300	6	Photonics Technologies Ltd.
Locking Circuitry	200	1	MiniCircuits
Power Supplies	157	2	Farnell Element 14
Magnets	150	2	First4Magnets
Total (£):	**33614**		

Table 4.2: Summary table of the laser systems and optical components ordered by individual price. The 'Lasers' elements of the table covers all laser systems and the electronics used to drive them. While optics were acquired from many suppliers, Thorlabs provided the majority.

4.6 Laser Setup Costings

Until this point I have left the purchase prices of the laser systems and their means of locking purposefully vague for two reasons. The first of which was to emphasise what is required to ionise Cs using my specific scheme. This draws from a primary strength of a cold atom source: the variety of species on which it can be based. Broadly speaking, each atom will require similar steps to ionise but each step could present very different challenges to overcome. With this in mind, while the values given in table 4.2 reflect the costs for my Cs scheme, they can be seen as a broadly applicable guideline for prototyping other atomic species.

The second reason is that while the laser systems themselves are appropriate for demonstrating a prototype ion source (as has been justified above), they are inherited systems used largely for convenience - a situation that could be improved with more purposeful designs, some of which will be explained in chapter 6. One simple change that would reduce costs is eliminating extraneous spectra; this would lower both the overall cost of optics as well as the number of vapour cells. Thus, the values given should not be taken as a true indication of final costs as they would likely be far lower.

4.7 Chapter Summary

In this chapter, all excitation steps to the ionisation of Cs have been defined and explained in terms of their methods and rationale as pertains to the project's objectives: namely to produce a cold Cs ion source that is compact and reasonably priced while also being stable in the long term, without any need for special training or maintenance. This has principally been achieved through the use of multiple excitations to allow the use of semiconductor diode lasers and well-known locking techniques for the initial transitions, and the use of ZSAR and Rydberg atoms for the final excitation. The entire optical diagram for this work, subdivided into excitation sections, can be seen in figure 4.16.

With this definition completed, I can now move on to how the light from these lasers is used in the test vacuum chamber to generate a magneto-optical trap and the proposed form of the miniature cold Cs ion source based on a grating chip.

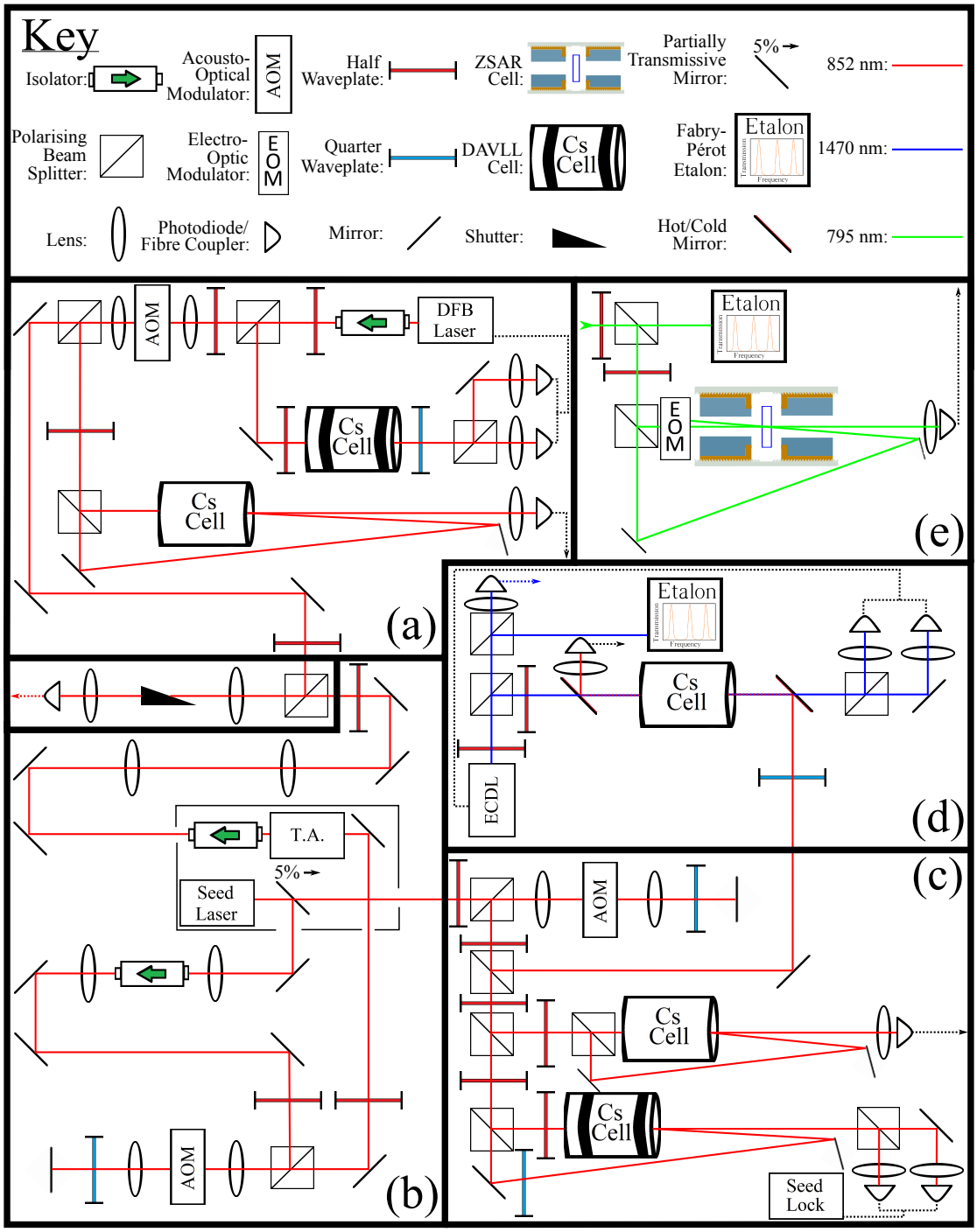

Figure 4.16: Optics diagram subdivided into (a) the repumping section, stabilised using a DAVLL cell and saturated absorption reference with an AOM for fast switching. (b) The tapered amplifier system with AOM shifted input seed. (c) The seed laser locking section using polarisation spectroscopy. Sections (a) and (b) share a common fibre coupler whilst (a-c) share the 852 nm wavelength. (d) The 1470 nm section using excited state polarisation spectroscopy for stabilisation via a circularly polarised beam from section (c). (e) The Zeeman Shifted Atomic Reference optical setup using 795 nm light.

Chapter 5

Experimental Progress

5.1 Introduction

Thus far, I have covered the spectral requirements for the project including the trapping and ionisation of Cs, and how this can be accomplished in terms of lasers and spectroscopy. Therefore, in this chapter, I will detail the current work towards a cold Cs ion source. This will cover the design and operation of a testing vacuum chamber and trapping coils, as well as how the laser systems described in chapter 4 have been implemented. All the current trapping hardware can be controlled using a unified software interface for efficient programming of timed sequences via a National Instruments field programmable gate array card (FPGA) and LabView. The specifics of the interfaces for each hardware component will be given at the appropriate stage. To close the chapter I will give the latest experimental results of this work towards creating a cold Cs ion source based on a diffraction grating chip.

5.2 Test Vacuum Chamber

5.2.1 Introduction

The test chamber was designed for the demonstration of a Cs GMOT using a diffraction chip held in vacuum, and therefore uses components that may considered overly large as compared to those used in other cold atom experiments, but these were

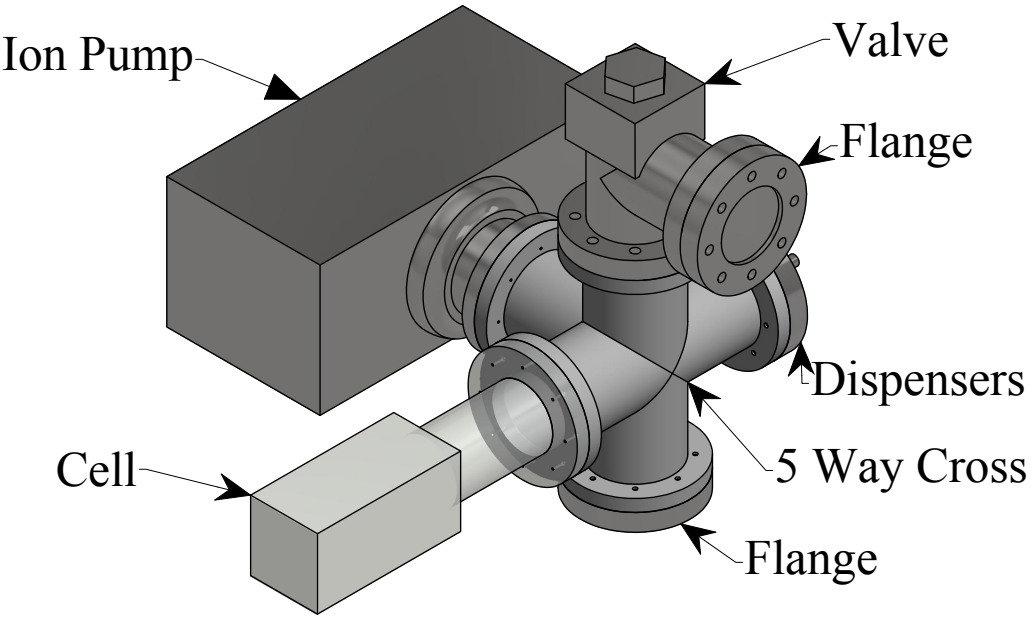

Figure 5.1: CAD rendering of the test vacuum chamber excluding the trapping and shim coils which would be placed around the glass cell. The chamber rests on a table with legs of adjustable height so as to control the tilt of the cell surface.

deemed necessary for flexible demonstration conditions. It is important to note that this is not the chamber to be used for the final ion source as there are many other considerations not accounted for in this design - but rather in a later chamber described in chapter 6.

5.2.2 Chamber Components

The test vacuum chamber itself is comprised of a cuboidal glass cell, approximately 150 mm in length and 80 mm in both height and depth, with a wall thickness of 6 mm. The cell is joined to the chamber by a five-way cross pipe that also connects a valve (used to initially decompress the chamber), a blank ended flange with feedthroughs that allow power to Cs SAES getter dispensers within the chamber, and an Agilent VACION Plus 55 StarCell ion pump. The cell is relatively large compared to those used in other cold atom physics experiments, but this is advan-

tageous because the chip used in this work is held within the vacuum cell itself so as to be closest to the intended usage case. The final connection on the five-way cross has a zero length blank flange attached to it, which is used to balance the chamber.

Exterior to the chamber is a pair of independently constructed magnetic coils held at a separation of 185 mm around the glass cell by plastic coil formers with a diameter of 195 mm. These coils are run in an anti-Helmholtz configuration in order to produce a quadrupole field for trapping. Rectangular shim coils are also placed around the cell and enable control of the field zero location in the x and y axes.

In order to prepare the chamber for use, it needed to be baked. This was accomplished by first evacuating the chamber over a weekend down to 3.4×10^{-7} mbar. The magnets of the ion pump were then removed, the dispensers wired to a power supply, the glass cell covered with aluminium foil, and the entire chamber wrapped in heater tape to then be sealed within a baking oven set to increase the temperature at a rate of 1°C/min. For 3 days the chamber was baked at 150°C upon which time the Cs dispensers were set to alternatively run at 5 A for 5 minutes so as to degass them. This produced a spike in chamber pressure from 1.0×10^{-7} mbar to 5.4×10^{-5} mbar at maximum. Following this, the temperature of the oven was increased to 200°C and the chamber baked for a further week. Before cooling and removing the chamber, the ion gauge indicated an internal pressure of 4.4×10^{-9} mbar but this rose to 8.6×10^{-9} mbar once the chamber was cooled back to room temperature. Given that the dispensers were typically run at 5 A to supply Cs, the pressure increase in the chamber under general use should also be consistent.

A rendering of the test chamber can be seen in figure 5.1, while schematics used in the construction of the main trapping coils can be seen in Appendix A.

Though not related to the trapping chamber itself, another vital component that allows computer control of the experiment is the National Instruments PXI-7852R FPGA card. Field programmable gate arrays are integrated circuits that contain an array of user programmable logic blocks. They are capable of fast parallel computing because each logic block can act independently and are therefore not slowed by their neighbouring blocks. The card used in this work has 96 digital lines that can be configured as either inputs or 3.3 V LVTTL outputs. However, only eight of these

possible lines were used via an included breakout board, leaving a great deal of opportunity for expansion.

5.2.3 Trapping Coils

The main trapping coils were designed to fit around the experiment cell and can generate a magnetic field with a gradient of 15 G/cm at its centre so as to be consistent with prior GMOT calculations with Mathematica.

The modelling for the coils was performed using Python by considering each coil independently while also treating each coil as a sum of individual wires to produce the final field. This method has the advantage of being able to count layers and turns of wire separately for greater accuracy in field calibration. As with any magnetic coils made for cold atom experiments, there was the choice to be made between heat dissipation via coil current and the self-inductance caused by having multiple coils of wire. Due to the coils being a temporary measure, and therefore not wanting to build the additional infrastructure for water cooling, the decision was made to assure the correct field gradient (15 G/cm) by a higher loop number. For an inner loop separation of 185 mm, and current of 4.5 A, this was calculated to be 22 layers with 22 turns per layer of wire. In total, this gives an outer coil radius of 75 mm with an inner radius of 35 mm. Admittedly, this is far from a true anti-Helmholtz configuration using circular coils in which coil separation is equal to $\sqrt{3}\times$ the radius of each coil [210], but the dimensions of the vacuum cell made these measurements necessary.

The coils themselves were wound around a plastic mount that gave the coil its assigned inner radius. These were also designed to only allow the intended number of wire turns by accounting for the wire diameter. Each coil was wound separately from reels of enamelled 15 AWG wire, with necessary joinings being performed using solder and additional insulting coating. Once wound, the coil formers were then connected by three plastic struts which assured the intended separation. This mount, the schematics of which can be seen in Appendix A, was modelled and constructed with the assistance of Mingjiamei Zhang.

Upon completion, the coils were calibrated using the Python program which

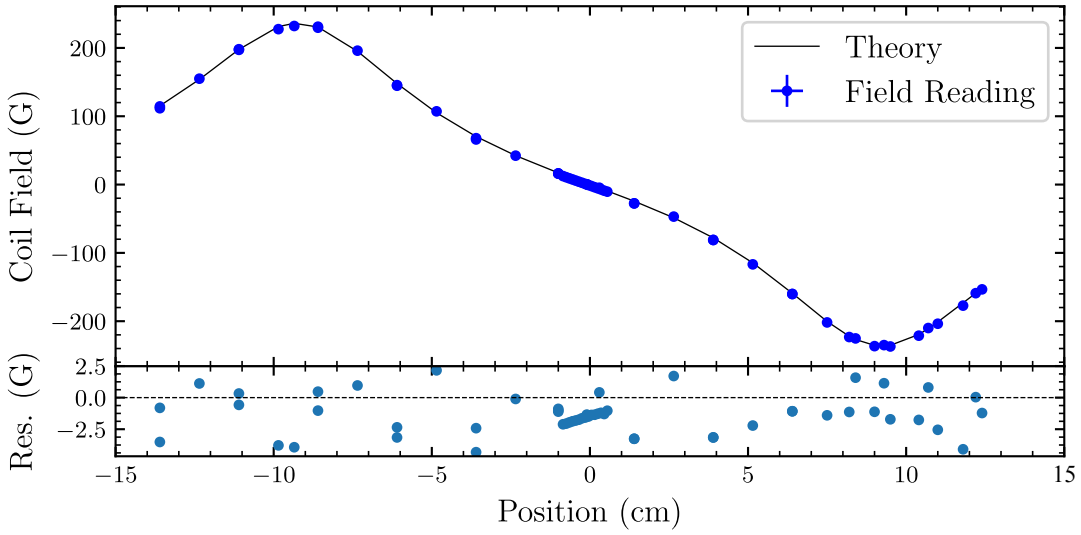

Figure 5.2: A calibration curve of the test coils. This was performed using a current of 4.5 A, an inner separation of 18.5 cm, and inner radius of 3.5 cm. The initial intention was for the coils to both have 22 layers of wire with 22 turns, but this calibration has shown that the second coil (producing a negative field) in fact has 23 layers of wire. Errors in measurements are plotted but too small to see on this scale. The fit is excellent with an RMS deviation of 2.00 G.

predicted that one coil had been miscounted and had an extra layer of wire - a reality validated by measuring the used wire reels, though this is unimportant in terms of the coil operation. The result of this calibration at 4.5 A is shown in figure 5.2. Due to the shape of the vacuum cell it was necessary to also wire the coils independently such that the field zero could be shifted in the z axis.

To better control the magnetic field zero position, shim coils were also placed around the cell in the x and y axes. The shims were originally made for use in this work [211] and are operated in a Helmholtz configuration so as to translate the magnetic field zero along one axis. However, due to lack of original intention to use these coils, their inclusion is rather impromptu in nature, with them simply being hung on lab clamps as closely and evenly to the cell as possible. Both pairs are wired together by a single 10 A bench power supply, and can shift the field zero by several centimetres.

In order to remotely control the switching of the main coils and build experimental sequences, the current was fed through a MOSFET which could be triggered by an up-converted signal from the FPGA card. The current was provided by two 10 A bench DC power supplies while the up-converting circuit, consisting primarily

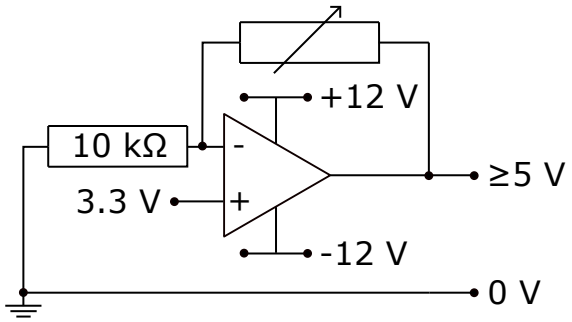

Figure 5.3: OPAMP voltage offset circuit diagram. The AD-744JN-0317 OPAMP is operated in non-inverting mode with the LVTLL 3.3 V signal fed into the non-inverting pin. The inverting pin meanwhile, is pulled to ground via a 10 kΩ resistor and connected to the output pin by a 100 kΩ variable resistor. This circuit is used to operate the experiment shutter controller and activate the test coils MOSFET as they require a 5 V activation signal.

of an opamp and variable resistor, can be seen in figure 5.3. The shim coils were not wired to this system as they could not produce a trapping effect on their own.

5.2.4 Optics

5.2.4.1 1st Revision

In line with the project objectives, the first attempt at building a trap was a simple implementation of a GMOT. At this stage, the cooling and repumping lasers had been accounted for, and their light made available to the experiment via a fibre cable coupled to a free space output. Due to a GMOT requiring a single input beam the optics for this first trap were also very simple. They included the free space coupler (with an added short focal length lens so as to collimate the output beam), a half wave plate, a quarter wave plate, and two mirrors. These optics were secured to a 150 mm^2 section of optical breadboard which was mounted perpendicular to the tabletop, on a Thorlabs ø1″ 50 cm pillar post. This setup allowed a collimated beam to be directed skywards from the coupler, in order to keep the fibre cable under less strain, and then reflected downwards through the wave plates for the correct polarisation. Superfluous mounting spaces also allowed polarising beam splitters to be used to analyse the beam polarisation before leaving the breadboard. Once mounted at a height of 50 cm on the pillar post, the output beam could be directed

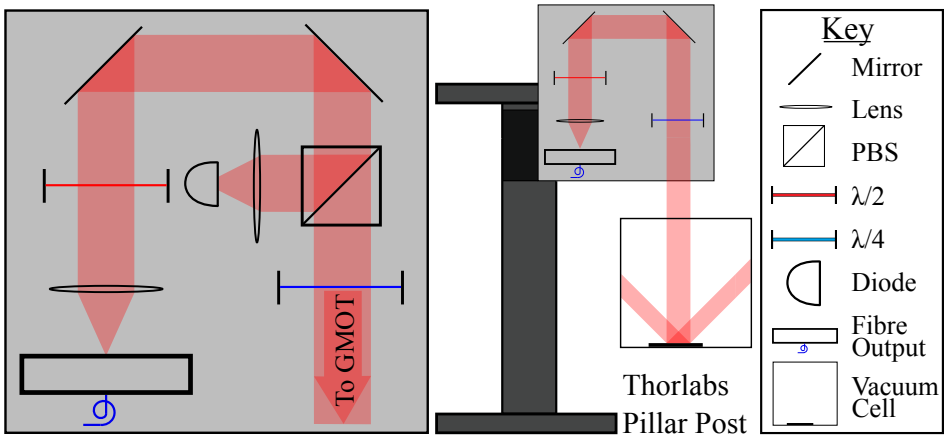

Figure 5.4: The first arrangement of optics used in the attempt to make a Cs GMOT. Due to the vertical mounting of the breadboard on a pillar, no mirrors were required to change the beam level. When in operation, the PBS was removed else it would separate the cross polarised cooling and repumping light. Omitted in the figure are two magnetic coils above and below the cell.

downwards onto the grating chip. A demonstration of this setup is shown in figure 5.4.

This arrangement had many virtues in terms of the project objectives, as it would have represented a single step away from the proposed integrated ion source in terms of being compact while also using standard Thorlabs optical elements. The modular nature of this setup meant that it was easy to level the output beam parallel to the optical table by first laying the pillar post flat on its feet and aligning the beam through a set of irises, before standing it upright. This ensured a perpendicular beam to the grating, and thus minimised the back-reflection from the grating (as measured by the polarising beam splitting cube). It was in this configuration though that the trapping beam had a collimated $1/e^2$ radius of 1.2 cm which may have been why a GMOT was not seen at this stage (see chapter 2). The design was nonetheless iterated upon for greater diagnostic capabilities when no GMOT was seen.

5.2.4.2 2nd Revision

In order to eliminate all possible issues relating to laser locks, detuning, beam width, polarisation, and magnetic field zero location, the MOT optics were redeployed such that it was possible to seamlessly switch between six and single beam operation, or even operate in a 'hybrid' fashion with the grating chip acting as a mirror for the

axial trapping beam.

This was accomplished by first adding an elongated section to the initial breadboard so as to facilitate expanding the input beam to a $1/e^2$ radius of 2.2 cm. This addition was motivated by concerns relating to beam uniformity, noted in chapter 2, and also included an iris immediately following the new $2''$ diameter lens so as to truncate the newly expanded beam to a more manageable radius. The subsequent polarising beam splitting cube was mounted on a magnetic flipper mount, such that in its absence the input beam continued on its path uninterrupted to then be redirected downwards (a reorientation from the x-y to the z-x plane) and onto the grating chip. Due to the increased complexity of optical arrangement, it was necessary to operate this setup on two levels: one upper plane containing the output fibre mount, collimation optics, and a 45° mirror to provide the axial trapping beam - while a lower plane provided the transverse beams. To operate in 6 beam mode, the flipper PBS cube must be in place and grating chip moved to one edge of the cell so as to not block the axial beam retro reflection, while the opposite is true for single beam operation. An illustration of the setup working in six beam configuration is shown in figure 5.5.

5.2.4.3 Imaging

Another welcome addition to the second optics revision was the ability to digitally image and record the plane of the trap with a 2 mm depth of field using a pco.pixelfly usb camera. Prior to this, any sightings of a MOT had to be accomplished using either an analogue NIR camera or hand-held viewing scope with no recording options. The two cameras can act in tandem at right angles to infer trap dimensions, while the pixelfly camera can be triggered and controlled using the FPGA card LVTLL output. In order to analyse any images from this camera and therefore determine trap size, a scale had to be established. This involved first finding the desired working distance by measuring between the tip of a gaussmeter probe (placed at the zero test coils field) and the camera position. This working distance was then replicated between the camera and a steel ruler, with lenses selected to bring the ruler to focus. An image was then taken of the ruler wherein the pixels between the centres of each

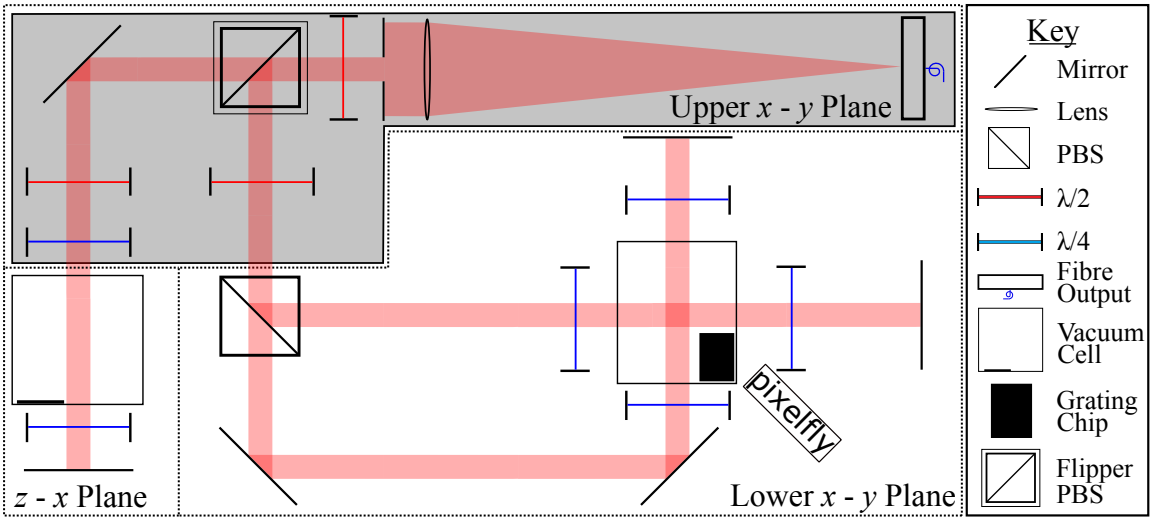

Figure 5.5: The second apparatus used in the attempt to generate a Cs GMOT. For this version, the fibre output and lens were decoupled to allow beam expansion with an iris placed after this lens to truncate the beam. A PBS cube mounted magnetically allows the seamless switching between six and single beam operation. The optics noted on the grey section (an optical breadboard) are mounted ∼50 cm above the optical table, whereas the optics on the lower plane are mounted ∼20 cm above the table. A beam crossing a dashed line indicates a change of level via a mirror or periscope omitted for clarity. A pco.pixelfly usb camera was also added to record any MOT.

millimetre marking were counted to give a pixels/mm calibration.

5.2.4.4 Optical Switches

There are two main optical controls for the chamber are a Uniblitz LS2 2 mm laser shutter, and the AOMs when cycled between their assigned frequencies. The shutter is placed at the focal point of the 1:1 telescope immediately prior to the launch fibre of the cooling and repumping light. This allows the fastest possible mechanical blocking of both beams, but it is mainly used as a safety feature while manipulating the other end of the fibre cable. While it can be operated with nanosecond timing precision due to the digital line control, the mechanism is limited to a closing time of 1 ms making it unsuitable for fast laser switching. The shutter controller is the D880C open frame shutter driver and requires a TTL 5 V signal in order to trigger which was provided by the offset circuit.

The AOMs however, using a Durham-built driver outputting either 80 MHz (for the repump) or 200 MHz (for the cooling light), are able to directly interface with

the FPGA LVTLL output to switch their frequencies between one of two presets. On an LVTLL signal, the AOM drivers are programmed to switch their output from one close to the desired detuning (e.g 204 MHz) to another, far from this value (250 MHz). This has the effect of both slightly misaligning the laser beam path and making it a non-resonant frequency, thus essentially switching the laser 'off' and 'on' with nanosecond level precision timing - an ability useful in various cold atom analysis techniques and far faster than can be achieved using a mechanical shutter.

5.2.5 Experimental Optimisations

In any long running experiment there are many day-to-day optimisations to be made, especially critical alignments such as fibre and AOM couplings, or small misalignments such as heavier mirrors sagging over time. For this reason it is important to establish and note baselines of performance once in an adequate operating mode, and to try to maintain the experiment at this level.

5.2.5.1 TA 100 Seeding

One critically important alignment to maintain is the seeding for the tapered amplifier. This is for two reasons, firstly that the power output of the TA is highly dependent upon this alignment, with a small deviation resulting in many hundreds of mW's less laser power. Secondly is the possibility of damaging the TA if it were to be operated with a high injection current without the appropriate level of seeding. Due to custom setup for seeding the TA explained in chapter 4, the baseline for performance of the amplifier is 550 mW. Admittedly there are two additional contributing factors to this level of power aside from alignment, including the amplifier injection current, and seed laser diode output, but these can also be accounted for. The former is set to the maximum advised current, 2250 mA, while the latter will be explained in the following subsection.

Figure 5.6 shows the physical arrangement of the optics used to first offset the seed laser output with an AOM and then seed the TA. The mirrors and lenses used to collimate the beam before the AOM, as well as in the double-passed setup itself, are all mounted vertically and so only require very small adjustments to maintain the

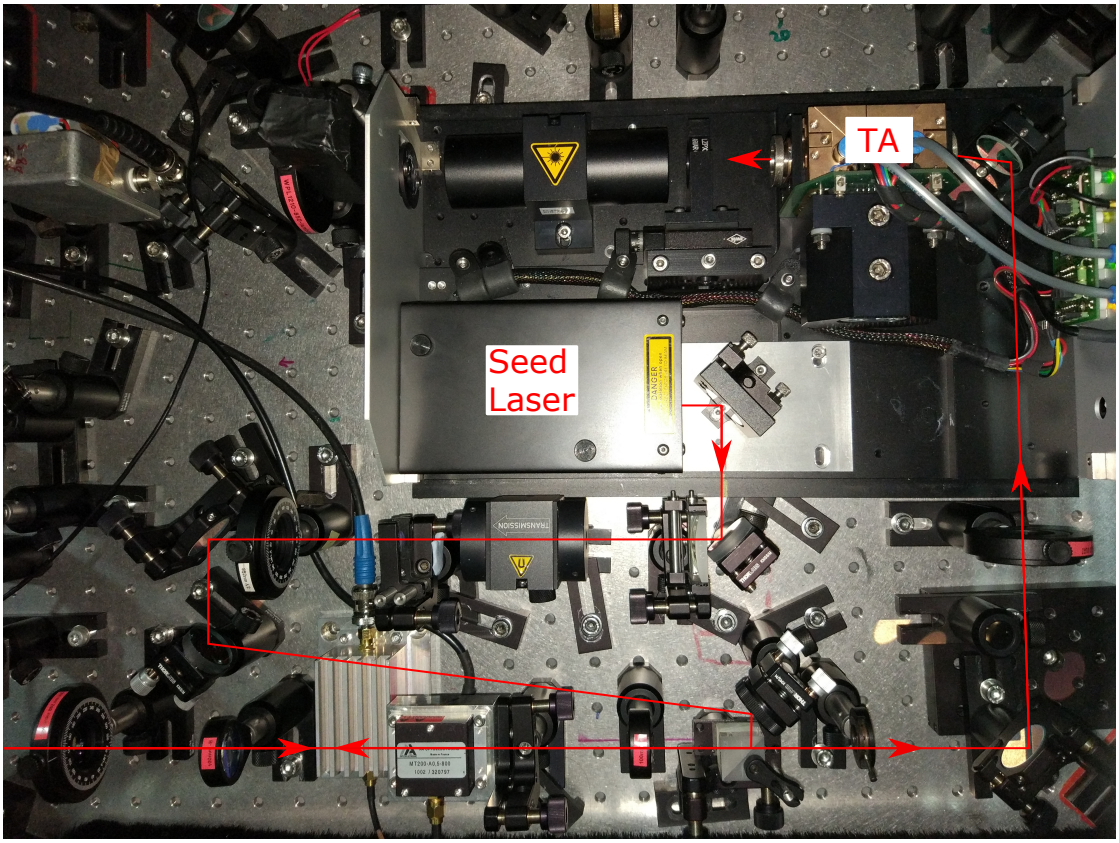

Figure 5.6: Approximate seed laser alignment while using an AOM to offset the frequency. The image shows the TA 100 amplifier system without its casing. Not indicated is the leakage light from the initial mirror that is used to lock the seed laser.

efficiency of the section at ∼70%. This means that optimally, the power measured after the double-pass from the 90 mW diode (including a loss of approximately 10 mW from the optical isolator) should be ∼56 mW. If the diode does measure 90 mW, then less than this figure requires slight adjustments of the optical mounts.

The subsequent section is more critically aligned as it determines the overall TA output and whether the amplifier is damaged during operation. It consists of two mirrors that control the seeding of the TA, one Thorlabs 3-axis precision mirror mount, and one standard internal TA 100 mirror. In the event of power output below 550 mW these mirrors must be carefully adjusted with reference to maintenance back-propagating beam from the amplifier itself.

5.2.5.2 Laser Diode Outputs

The power outputs of the individual laser diodes can also vary and require some maintenance. The most stable in terms of output power is the repumping laser. This is a distributed feedback style laser and so its output is defined primarily by the input current. As diodes of this nature age their power output naturally lowers, but this is an unimportant effect on the timescale of this project. With an input current of 185 mA the laser achieves an output power of 90 mW, a figure greatly in excess of the ∼10 mW required for repumping. A drop in power significant enough to fall below this threshold would mean simply replacing the laser as it would clearly be faulty.

All the other lasers used in this work are of the external cavity semiconductor diode design, and so their power outputs depend on the feedback alignment of their grating as well as the input current. Due to the complex relationship between both these factors and lasing output mode, it can be necessary to adjust either facet to maintain power and the correct wavelength. This is most important for the seeding laser, that must be maintained at its maximum possible output of 90 mW so as to ensure adequate power from the tapered amplifier.

5.2.5.3 Fibre Coupling

The final critical alignment to maintain is the fibre coupling to the experiment chamber. This carries both the cooling and repumping light to the MOT setup and includes 1:1 telescope system with a shutter at the focus as a safety feature. The two beams are combined at a polarising beam splitter, with the alignment of the cooling beam prioritised due to its greater importance. This priority is assured by using an 60FC-4-A7.5-01 coupler with a variable focal distance to maximise the coupling of the cooling light.

The maximum efficiency achieved through this fibre for the cooling light was ∼70% which is also implied to be a good level of power for a GMOT, as explained in chapter 2. The maintenance of this figure is performed by adjusting two mirrors placed before the polarising beam splitter, and then finely adjusted using the lenses of the 1:1 telescope which include micrometer translation mounts. The repumping

light meanwhile, is a secondary priority and, largely due to a substantially different beam shape, only reaches ∼40% efficiency through the fibre. This figure can only be influenced by two mirrors prior to the beam splitter as the finer controls prioritise the cooling light.

5.2.5.4 MOT Mirrors

Moving to be able to easily create both standard and grating MOTs with the same setup naturally increased the complexity of optical arrangements. The most pressing of alignments relate to the three mirrors involved in changing the beam level - one for the z axis and two more for the $x - y$ plane. These mirrors are held at 45° to the plane and thus are more susceptible to sag than their level counterparts. The optimal alignment for these mirrors is determined by the inferred size of the trap as imaged by the pixelfly camera.

5.3 Controlling the Experiment

As has already been mentioned, a number of components within the experiment can be controlled remotely using a software interface that also allows for complex sequences of events to be programmed with timings to nano-second level precision. In this section I will give details of the software interface used to control the PXI-7852R and instructions for its use.

5.3.1 Labview VIs

The FPGA card is programmed and controlled by the National Instruments LabVIEW 2014 software. The main advantages of LabVIEW is that it is a highly visual programming language and automatically generates a graphical user interface (GUI) with which to control the program. Each individual GUI is known as a virtual interface (VI) which together form the program. For this work, three main VIs were made; the first can be used to statically control the wired digital lines to be either 'on' or 'off'. The second VI enables variable timed control of all wired digital lines with definable on and off periods. The third VI gives the ability to perform timed

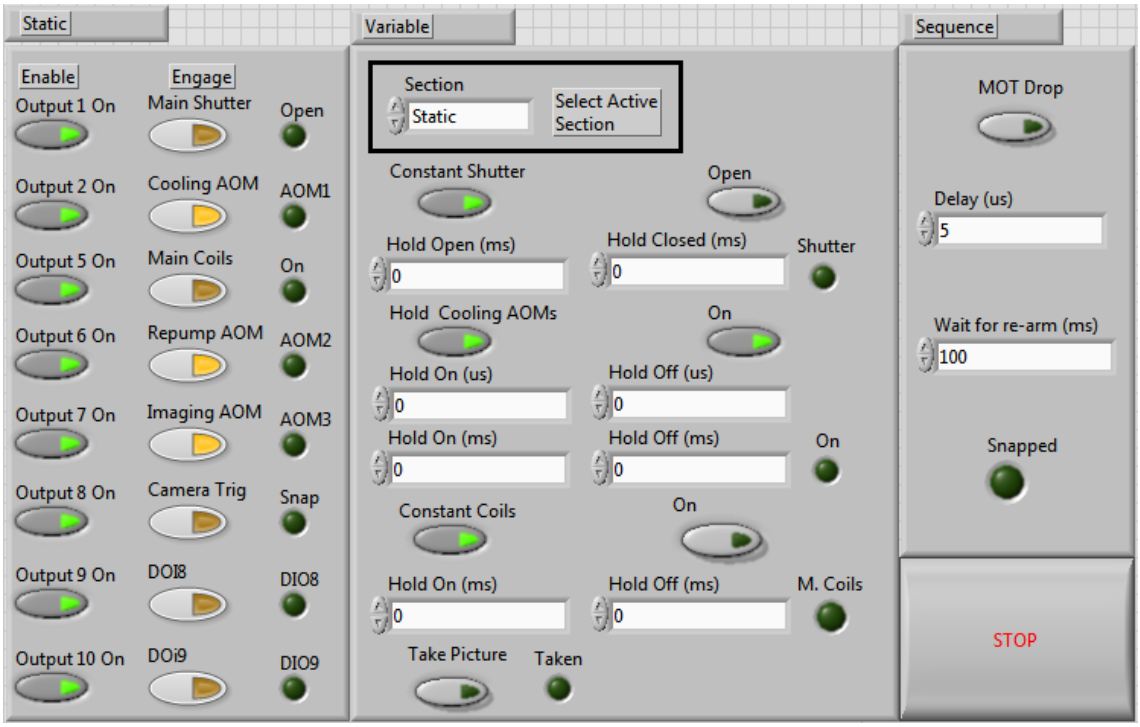

Figure 5.7: The main LabVIEW GUI for controlling the experiment. When switching between sections, similar wired outputs will have their executing commands overridden. The default initialising section is static as this contains the digital line enabling controls.

sequences which, while having not yet been used in this work, allows complex cold atom trap analysis on very short time scales. Currently the sequence section VI is coded to perform a 'MOT drop', wherein once a hypothetical trap is created pressing the button will trigger the pixelfly camera to take an image of the trap. After this is taken, both the AOMs and test coils will switch off before another image is captured after a timed delay while both AOMs are flashed to their on states. The system will then reset and wait for a defined 're-arm' interval before beginning the sequence again. This loop was designed to be able to measure the temperature of the trap by imaging its rate of expansion. The three sections of the GUI can be seen in figure 5.7.

On the far left of the figure are the static controls which must be initialised first to ensure that all the digital lines are enabled in software. Under normal operation, when an output is engaged, the corresponding green 'LED' will alight - if this is not the case, it indicates an issue with the hardware circuit not reaching the proper 3.3 V signal. The middle variable can be switched to after the program has initialised

and offers timing variations that override previously laid commands from the static section. This also means that unless altered from section-to-section, all commands will persist and outputs not wired in the variable section cannot be affected by this nature of switch. The sequencing section behaves differently though and will cancel any on going loops from the variable section, and mimic the initial settings held on the static section before initiating any sequence to override them.

In order that these functions do not interfere with each other, the main GUI gives an option of which VI to use at any given time. The initial architecture of the program was limited in that once a run had begun, no settings could be amended until a sequence was complete - a flaw that was fixed through the diligent work of the summer student, Sansith Hewapathirana. Due to the modular nature of the program it is easily expandable, with additional functionality being able to be added to the internal case structure.

A separate VI gives the ability to analyse and process trap images captured by the pixelfly camera. It does this by reading from the camera buffer and displaying the image. It is then for the user to define the region of interest within the image as well as a background subtraction image. Once this is done, the VI will measure the FWHM of the trap based on a prior calibration of pixels/mm. This VI was also improvised from the included pixelfly software for this project by the aforementioned summer student.

5.4 Results and Evaluation

5.4.1 Trapped Atoms

The second optical revision, detailed previously, was a success as a condensed atomic cloud was sighted within the chamber. This means that all issues related to standard magneto-optical trapping have been eliminated, including any uncertainty about the zero field location as the trap formed at the predicted position. The trap is shown in figure 5.8(a) (central bright oval). This discovery led to experimentation into creating a GMOT by asymptotically changing from a multiple to a singular beam regime. This essentially consisted of tuning from an even three way split of laser

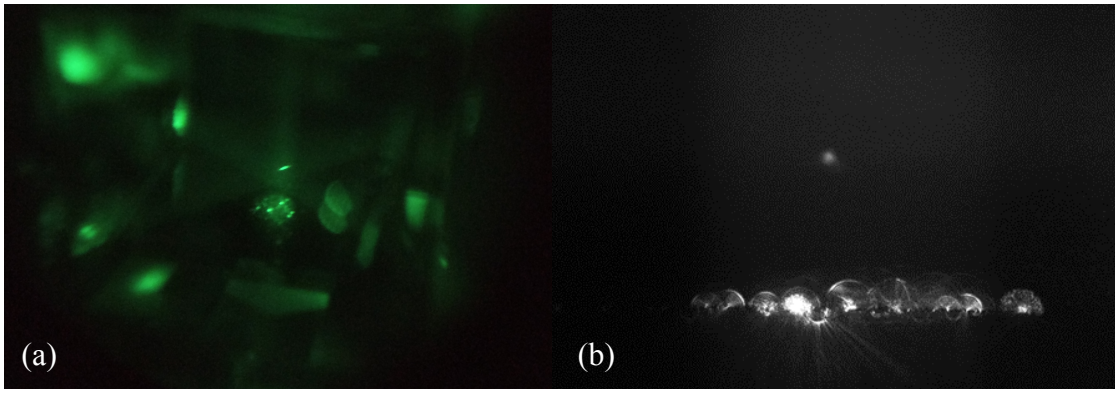

Figure 5.8: (a) The first standard six beam MOT recorded using the second GMOT setup operating in six beam mode (bright central oval). The image was captured using an infrared scope and a camera phone. (b) The 'hybrid' MOT suspended above a single diffraction grating section as captured by the pixelfly camera (central bright spot) is very small and measures only 0.08 ± 0.01 mm^2 from this perspective. For comparison, the largest recorded six-beam MOT was more oblong in shape, measuring 2.4 ± 0.1 mm in length and 1.1 ± 0.1 mm in height.

power from each PBS cube direction, to a majority of power in the axial beam. There were some successes in doing this, with the most interesting result being the generation of a 'hybrid' MOT above the grating chip itself (with no axial retro reflection) but not centrally, instead hovering over the centre of a single grating section (figure 5.8(b)). The hybrid was unfortunately not stable in the face of field zero manipulation and was highly sensitive to changes in beam power ratio, and so was likely merely caused by a fluke in the extremely complex case of overlapping GMOT and standard 6 beam MOT laser field geometries.

The sighting of the errant MOT motivated one final addition to the chamber in order to remedy a shortcoming introduced by the hybrid MOT setup - a tilting table. The importance of having input beams perpendicular to the grating chip was mentioned previously in chapter 2 and discussed in [91], but in removing the pillar post mounting arrangement a level beam relative to the chip was made more difficult to assure. In previous experiments using grating chips of this nature, they were always used outside of the vacuum chamber and thus could be arbitrarily tilted. In this work, the chip axis is determined by the cell plane and therefore the tilt of the vacuum chamber itself. In the first arrangement the beam could be first levelled independently and then finely adjusted using the PBS cube. In the

hybrid system however, the axial beam cannot be aligned independently, only finely adjusted using diminishing beam feedback. To correct this, a stainless steel platform was constructed with four legs that could be individually raised and lowered for the desired correcting angle, as determined by a spirit level placed on the cell ceiling (this method reasonably assumes that cell planes are parallel). Unfortunately, while this did correct an angular discrepancy of approximately 3°, no differences were noted in trap formation.

This effectively only leaves problems specifically related to the creation of GMOTs which include a greater dependency on polarisation purity (the wave-plate orientations were optimised by noting the change in MOT fluorescence on the pco.pixelfly camera) than standard MOTs or issues with the grating itself. If this is also assured but returns a weak or non-existent trap then further investigations into the grating chip itself must be made.

5.4.1.1 3rd Revision

The third optics revision shown in figure 5.9 was in response to questions of polarisation purity from the hybrid GMOT arrangement. In order to ensure this purity, a PBS must be mounted immediately before a quarter wave-plate so that the definitely linearly polarised light is subsequently circularly polarised with no interference. The previous incarnation of optics had the linearly polarised light first rebounding from two mirrors which may have altered the polarisation state.

To begin, the repumping light was coupled into a secondary fibre in order for the possible trap to be side-loaded. This was necessary as, in the previous iteration, the cooling and repumping beams were cross-polarised meaning that mounting a beam splitter before the grating would reject the vast majority of the already weak repumping light. This was not an issue for the hybrid setup as when the power was split, each beam received an inverse proportion of cooling and repumping power but the total overall remained consistent. When operating in single beam mode though, the hybrid setup did not ensure polarisation purity as the PBS had to be removed for it to function and not reject the repumping light. Due to needing space for this extra fibre output, the pco.pixelfly camera had to be removed. Aside from the

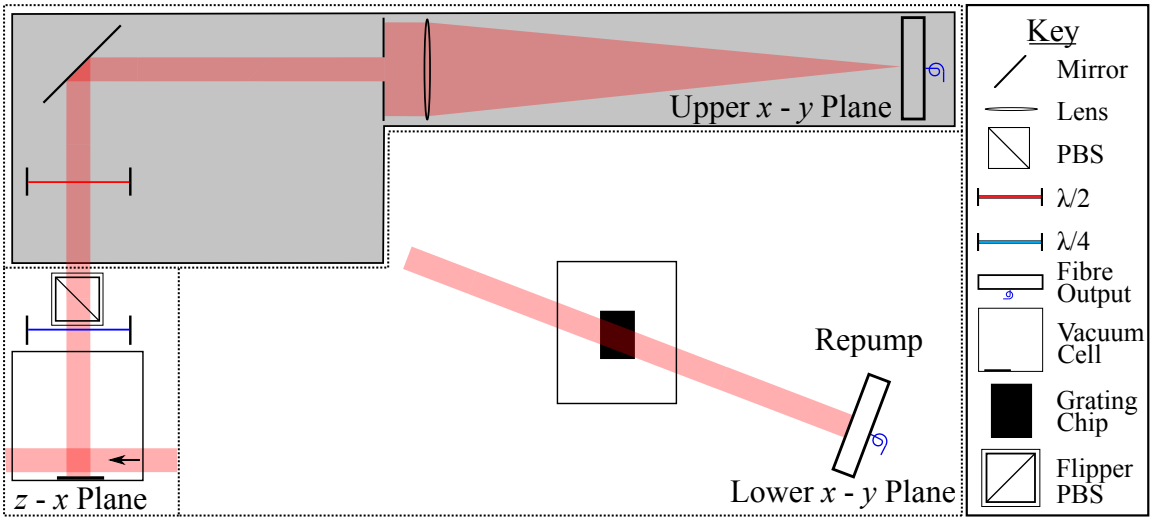

Figure 5.9: The third apparatus used in the attempt to generate a Cs GMOT. For this version, the cooling and repumping beams were decoupled such that the trap would be side-loaded by the repump but still illuminated from above by the cooling beam. The half-wave plate was moved to being immediately prior to the axis changing mirror and PBS mounted between the this mirror and the quarter wave-plate. This arrangement ensures circular polarisation purity. The optics noted on the grey section (an optical breadboard) are mounted ∼50 cm above the optical table, whereas the optics on the lower plane are mounted ∼20 cm above the table. A beam crossing a dashed line indicates a change of level via a mirror or periscope omitted for clarity. The pco.pixelfly usb camera was also removed in order to make room for side-loading.

additional fibre coupling, the cooling light power was also halved due to changes in the optics necessary for other work, bringing the total intensity at the grating to ∼15 mW/cm^2. It was in this configuration though that an extremely small and weak trap was seen but, with great regret, was unable to be imaged due to removing the pco.pixelfly camera, and the CRT monitor used to display the secondary camera output being too unclear to be photographed and upon reinstalling the primary camera, the trap no longer appeared.

There are a number of factors that could have enabled this weak-yet-present trap, as many variables within the experiment overall had changed. Unfortunately, due to the lack of imaging apparatus, I cannot give quantified analysis of the trap as I tried to optimise it, only reports of changes to the trap intensity and size by eye as variables were changed. The most obvious is the polarisation state of the cooling beam which was the aim of this revision. Interestingly, removing the PBS from the

beam line only seemed to have a small detrimental effect to the trap fluorescence and so this may not have been the limiting factor for trap formation in this case but a point of optimisation. An important note to mention is that throughout my attempts to form a Cs GMOT, my available cooling light power had been a concern, as my analysis implied that I may require more laser intensity for a similar result to a Rb GMOT - and while I cannot numerically compare the traps: for a beam waist size of 2.2 cm and intensity as low as $\sim$3 mW/cm^2, I could still see a (albeit an extremely weak) trap that responded to changes in the magnetic field zero position. As the cooling and repumping beams were decoupled in this arrangement there was also far more repumping intensity in this side-loading configuration, but as so little is actually necessary in the cooling process, I cannot see this being a crucial factor.

Until this point I had omitted the fact that another grating chip was donated by the Strathclyde Photonics group. This was gifted in response to queries as to the performance of damaged gratings in light of the damage inflicted upon the initial grating and assurances that this chip, despite also being damaged had been used to make Rb GMOTs. Functionally, the chip is identical to the first with the same pitch, etch depth, and duty cycle, but without a central hole as it was not designed to be used in an ion source, and a different pattern of surface scarring. The omission of this detail was made because until the third optics revision, the second grating had also not shown any signs of trapping, but it was this chip that produced the trap. The other most interesting change that seemed necessary to generate a trap was a much higher field gradient at approximately 20 G/cm. This is far in excess of what was suggested as necessary by modelling, and much higher than what was used in prior experimental attempts which stayed close to a gradient of 15 G/cm and caused this weak trap to lose visible cohesion. When at this higher field gradient, and trying to optimise the intensity using horizontal bias fields, there were visible gains in brightness even towards the maximum possible bias currents of 10 A but these fields are much weaker than the main coil field due to the smaller number of turns. Overall, this implies an issue, not with the input beam power, but of intensity imbalance, as bias fields can be used to counteract that effect.

Section 2.2.1 describes how power balance is achieved by the grating in an ideal

fashion through a number of assumptions. First is that the grating itself has been constructed as intended, and second, that the input is perpendicular to the grating surface. Given the evidence of power imbalance in the first chip through figure 2.16 and necessity of much stronger fields to form a trap on the second chip this may play a role in the weak or non-existent trapping. As to the second point, from seeing a trap, to no longer being able to generate one at all, the only thing that changed was moving the chamber out of the beam path in order to re-align the pco.pixelfly camera back to the magnetic field zero and then shifting the chamber back. All that could have happened from this is a small change in tilt of the chamber, and thus the grating in the vacuum cell, relative to the beam direction. This would be due to the platform upon which the chamber rests having a small unintended tilt induced upon it because of its threaded legs that allow the platform to be raised or lowered. This was originally introduced to correct a small error in the cell orientation but does not allow for small or precise changes, only ones that can be detected using a spirit level. There is also an additional flaw to this method in that the levelling of the cell cannot be performed when the chamber is in place as there is no way to fit the spirit level on top of the chamber due to the main coils being so close to the glass - meaning that any change in tilt as the chamber is moved back into position cannot be verified. While this may normally be a small effect with little consequence to an undamaged grating, in this case, the effect may be compounded by the damage. Overall though, this is a good indication that there is nothing fundamentally hindering the creation of a viable Cs GMOT.

5.4.2 Hardware Evaluation

While both the chamber and trapping coils have been shown to be able to produce a standard MOT, facets of their design limited the possible experimentation and thus the breadth of results in this chapter.

The main limiting factor of the test chamber is the vacuum cell. It is much larger than necessary - especially in height, as well as having thick walls that lack any anti-reflection (AR) coating. At 6 mm, the thickness of the cell walls make it impossible to consider removing the grating chip from the cell to instead mount it

beneath the cell, as has been the case in other experiments, because it would be unlikely that the MOT would have enough space to form. A lack of AR coating also means that in either case, chip in or outside vacuum, there are a multitude of reflected beams within the chamber. With the chip outside of vacuum, in addition to the errant beams, the trap would become less intensity balanced axially due to the loss of power on the second and third wall transits. The height of the cell meanwhile, has knock-on effects for the trapping coils and their construction.

Due to the height of the cell, a greater separation for the trapping coils was necessary. This left two options to achieve the required field gradient: increase the number of coil loops, or provide a greater current to each coil. The decision to prioritise more coil loops was due to considering these coils a temporary measure, designed only to demonstrate the principle of a GMOT, and also to not build the infrastructure for water cooling. The result of this is a self-inductance value of approximately 60 mH per coil, which can be inferred from a switching time of 60 ms as measured by a Honeywell sensor, and therefore the impossibility of performing any thermal characterisation of the MOT that was achieved. Learning from this fault, the trapping coils for the fully integrated ion source described in chapter 6 were designed so as not to be limited in the same way by minimising both their coil count and design current.

Something can also be said of the optical systems and their need for maintenance being far above what one might expect of a non-expert to perform. The more extensive use of mirrors to create a hybrid trap would not be present in a final design, but issues of fibre coupling and amplifier seeding would always be present. For problems such as these, more sturdy mounting of optics would have to be used, or even an autonomous optimisation routine using motorised mounts and leakage light.

5.5 Chapter Summary

In this chapter I have described the hardware and software associated with the first attempts at creating a Cs GMOT, and how the optical arrangements have led to

an ever decreasing set of possible issues that are stopping the formation of a viable grating based trap. Despite the disappointing result, the final experimental outlook is hopeful given that all work thus far indicates that there is nothing fundamentally lacking for the creation of a viable Cs GMOT.

Chapter 6

An Integrated Cold Ion Source

6.1 Introduction

In this chapter I will begin to discuss in earnest the proposed compact cold Cs ion source based on grating MOT technology. First, I will address the alternative vacuum chamber that has been designed to entirely encompass the proposed miniature GMOT and characterisation hardware, while maintaining a minimised footprint. Second, I will provide all detail associated with the integrated source assembly including its design, construction, and likely operation. Third, I will attempt to predict the performance of the source using its nature as a transversely ionised MOT between extraction plates of controllable electric potential. With discussion of the first concept complete, I will then move on to improvements that could be made to the second implementation.

For all components of the system I will provide a summary cost analysis in terms of materials and manufacturing with reference to how these compare to industry standards when appropriate, as well as certain decisions made with an emphasis on the project objectives of creating a compact and relatively inexpensive Cs ion source.

Reference CAD renderings of the proposed vacuum chamber and fully integrated cold ion source assembly to be held in vacuum can be seen in figures 6.1 and 6.2. More detailed construction schematics can be found in the appendices.

6.2 Chamber Components

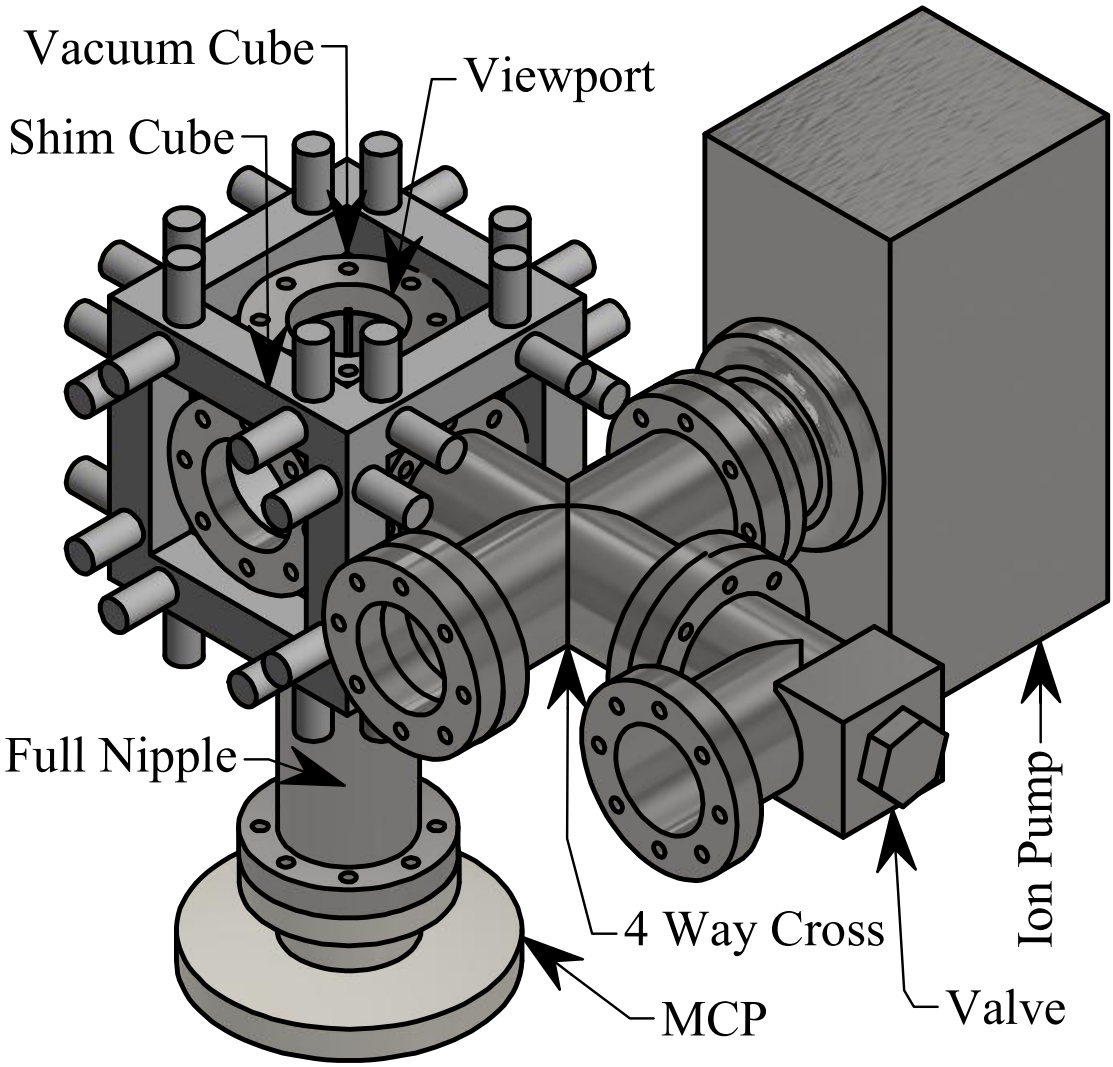

Figure 6.1: A rendering of the proposed vacuum chamber. The ion assembly is obscured from view but is held within the vacuum cube attached to the uppermost viewport. A valve is shown connected to one of the spare ports but it could be placed in either orientation. Due to the baking procedure, the shim cube would have to be constructed and wired around the completed chamber.

The proposed vacuum chamber would retain both the Agilent VACION Plus 55 StarCell ion pump and Cs SAES getter dispensers: the former because it has a suitably compact form factor with desirable characteristics, whilst the latter are essential and thus are more closely integrated into the source assembly design through spot welding. It does however do away with the large glass vapour cell in favour of a single stainless steel cube as the central component. It measures 113.8 mm in

all dimensions and has an internal cavity formed of 3 through-holes, each 63 mm in diameter for greatest accessibility. In addition to this, each face is compliant as a fixed CF63 vacuum flange so as to allow connections in all directions.

On the 'back' face of the cube a 4-way cross connects a vertically mounted ion pump to the chamber (so as not to block a cube aperture), leaving two spare flange spots. One must be used for the valve when pumping down the chamber but this can be decided by the logistics at the time. In the event that no use can be found for the final expansion port it can simply be sealed with a zero-length flange.

Turning once again to connections on the vacuum cube: the 'front', 'left', and 'right' faces will be covered by borosilicate viewports. These are standard glass windows lacking an anti-reflection coating, due to the costs this would incur for the employed wavelengths. The final window for the 'top' side meanwhile, includes 8 SHV-5 electrical feedthroughs as well as 4 M4 blind tapped holes on the inner face and 4 layer BBAR coating optimised for 852 nm. These special features allow the necessary electrical and optical power to the ion assembly as well as provide anchoring points such that it is suspended at the correct level within the cube. More details on this will be given in the subsequent section. Finally, the 'bottom' cube face interfaces with a micro channel plate (MCP) via a 209.6 mm full nipple. The MCP consists of a highly resistive plate of material with one side that is exposed to the ion current. Within this section is a dense array of small slots (microchannels) which are approximately 6 μm in diameter and cut into the plate at small angle. The effects of single particles are difficult to detect individually and so the MCP acts as a signal amplifier by converting the impact of a single particle into a cascade of electrons as it impacts onto the angled walls of the microchannels. My MCP allows this signal to be spatially resolved and thus it can be used to characterise the ion source. Externally, shim coils are mounted around the edges of the vacuum cube that allow fine control of the B field zero position. These will also be addressed in greater detail in a subsequent section. The final chamber accessories are external in the form of two high voltage power supplies whose purpose is to drive the in-vacuum assembly ionisation/extraction electrodes.

Figure 6.1 shows a rendering of the chamber, while figure 6.2 shows the expected

positioning of the ion source within the vacuum cube. Engineering and CAD diagrams of the chamber and its components are available to view in the Appendix B.

6.2.1 Chamber Costings

As has been the case with all prior decisions in this work, the project motivations of creating an ion source that is both compact and relatively inexpensive have held overarching influence. It is only at this stage however, that true creative freedom in terms of design ethos and purchasing decisions was present. This means that the new chamber and its accessories are the first fully original work without historical encumbrance.

Table 6.1 lists the final components of the new chamber with their prices (at the time of purchase) and supplier. The most expensive component is clearly the micro channel plate, a device that can characterise the produced ion beam, but this is only necessary for this first design and would not be included in the final product.

The next most costly components of the chamber when considered together are the Agilent ion pump (Star Cell VacIon Plus 55) and its controller (MiniVac). This duo is absolutely necessary as they provide enough pumping power (50 L/s) to maintain the chamber of the proposed volume at ultra-high vacuum pressures. Only for a second iteration with a further streamlined design could costs be reasonably saved with a smaller and less powerful ion pump.

Continuing to approach the analysis in pairs leads to the combination of the stainless steel vacuum cube and feed-through viewports. Together these parts define the operational capacity of the chamber, as the cavity of the cube sets the length scale of the ion source assembly, while the specialised viewport gives it anchoring points (as well as electrical power) - thus their expenses are justified.

The remaining listed components are simply necessities of a vacuum chamber and ion system that also allow for some possible expansion. The valve is required to bring the chamber down in pressure and then seal it, while the 4-way cross and full nipple connect the components together. The standard, uncoated viewports, meanwhile, act to both seal the chamber and provide cheap optical access to the

Component	Price ex-VAT (£)	#	Supplier
MCP	8315	1	Hamamatsu
Ion Pump	1684	1	Agilent
Feed-through Viewports	1171	1	Torr Scientific
Vacuum Valve	1091	1	Kurt J. Lesker
Vacuum Cube	1000	1	Lewvac
Pump Controller	615	1	Agilent
4-Way Cross	305	1	Kurt J. Lesker
HV Power Supplies	300	2	Information Unlimited
Power Supplies	157	6	Farnell Element 14
Full Nipple	145	1	Kurt J. Lesker
Borosilicate Viewports	85	4	Lewvac
Total (£):	**16008**		

Table 6.1: Summary table of the vacuum chamber components order by individual price. Prices noted reflect those at time of purchase, the most recent of which being the BS viewports on 10/06/2016 and the earliest, the micro channel plate, on 31/10/2012. While the MCP is required for source characterisation it would not be included in the final product and would be replaced by a sample chamber. This would leave the total cost closer to £10,000.

vacuum cube, while the power supplies drive all electrical connections. Finally, the high voltage power supplies rated between 0.5-35 kV are required to drive the ionisation and extraction electrodes.

In reality, the final version of any ion source based on this method would not require the MCP or full nipple to attach it. Neglecting these parts reduces the total cost to around £7548 and immediately makes room for what would be an ion column and sample manipulation chamber.

6.3 Integrated Source Assembly

6.3.1 Introduction

The ion source assembly proposed in this work is the culmination of careful design and modelling to balance the objectives of the project with the physical realities of working with cold atoms. The apparatus miniaturises all that is required to create an in vacuo cold ion source: field coils, electrodes etc., into an easily constructable package measuring 75.94 mm × 61.9 mm × 61.9 mm which has been successfully

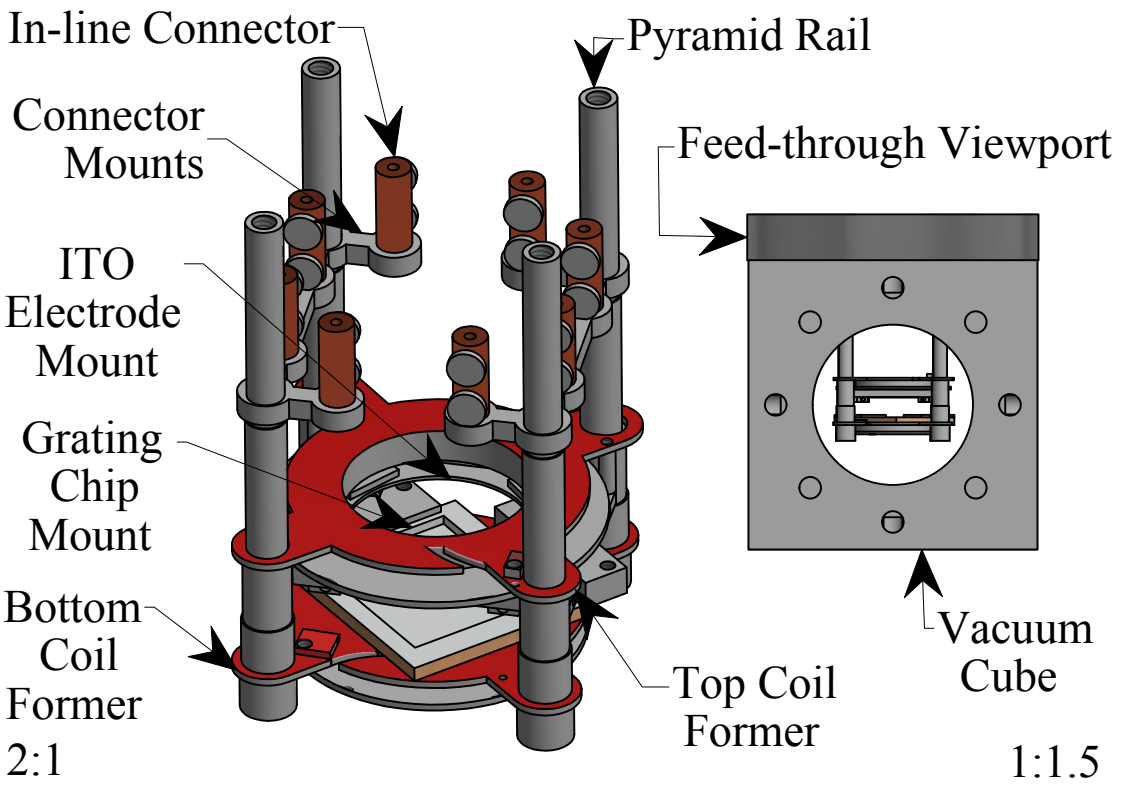

Figure 6.2: The cold ion source assembly with all components noted and shown within the vacuum cube. The structure of the source is determined by the four pyramid rails onto which all other components rest. Each rail has been tapped such that they can be secured to the inside of a flange and thus be held within vacuum. The in-line connectors and mounts provide insulated electrical routing to all necessary components of the source including the MOT coils, electrodes, and dispensers (not shown).

manufactured in a university mechanical workshop. The full assembly can be seen in figure 6.2 with scale diagrams of the components given through subsequent sub-sections. Full construction engineering diagrams used to build the assembly can be found in Appendix C, as well an image of it attached to the electrical feed-through viewport.

6.3.2 Rail Design and Electrical Connections

All components of the assembly are designed to be held in their correct positions, relative to the vacuum cube, by four 'pyramid rails', which are themselves secured to the upper vacuum viewport by vented M4 grub screws. Using a method such as this means reduced complexity for both production and construction, as well as a lower

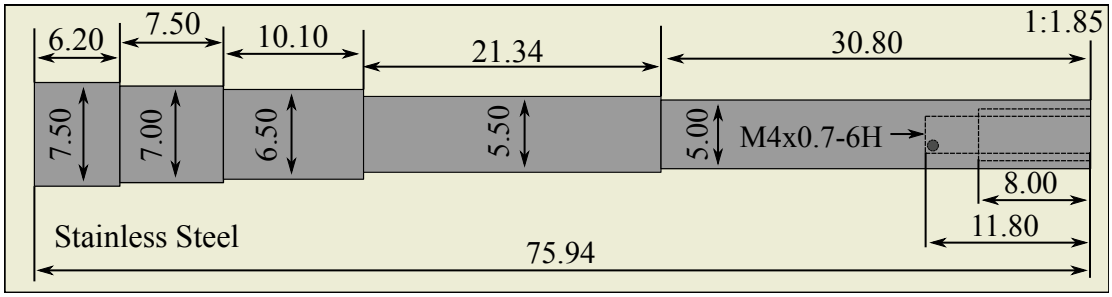

Figure 6.3: Scale diagram of the pyramid rail used to secure the integrated GMOT assembly within the vacuum chamber. This design allows the source to be screw-less internally, aside from the grub screw to attached the rail to the viewing port, and thus easier to assemble. Each step of increasing width denotes the resting place of a component as has been determined by the widths of their mounting holes which ensures correct placement. The 6.50 mm to 7.00 mm step does not have a component associated with it but it instead denotes the expected level of the B field zero.

cost because fewer screws or adhesives are required. During assembly, components are simply slotted onto each rail and fall to their correct positions. With grub screws in place the rails are still free to rotate, and thus screw into the viewport mounting points. By virtue of these positions, the rails do not obstruct optical access to the chamber in either the x or y axes.

Figure 6.3 shows a 185% scaled schematic of a single rail, detailing all of the steps of increasing cylindrical diameter from which the rail derives its name. At the right-hand-most side of the figure, one can see the drilled thread used to secure the M4 grub screw. The hole is also vented to prevent virtual leakage points. This section, 5.00 mm in diameter, is the longest of all the steps as it has to accommodate the in-line connector interface into which the in-line connectors themselves slot.

The in-line connectors allow electrical power to be taken from any of the 8 viewport feedthroughs into the appropriate places in vacuum. Figure 6.4 shows a 150% scale schematic of the in-line connector interface. Two of these stainless steel interfaces slot onto two separate pyramid rails until the first step, as defined by the 5.00 mm mounting holes at either end of the component. This provides a total of eight resting places for in-line connectors, accounting for all feedthroughs provided by the custom viewport. The in-line connectors are standard vacuum components purchased from LewVac. They are hollow BeCu cylinders with two stainless steel screws that can be used to connect wires in vacuum without needing any adhesives

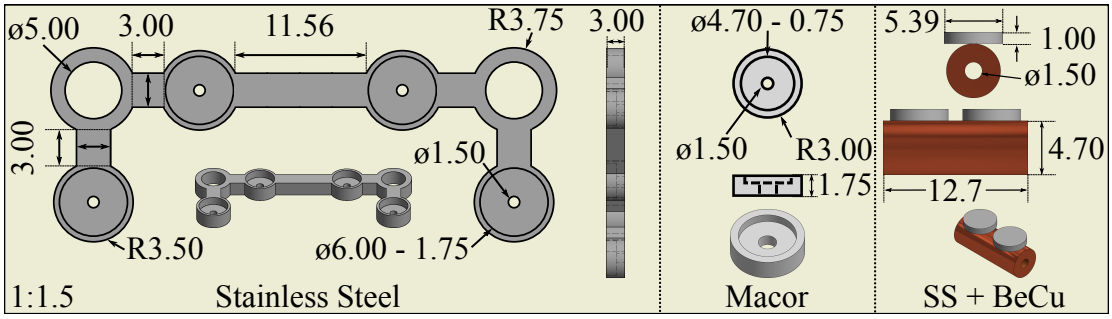

Figure 6.4: (Left) In-line connector mount that rests on the 5.00 mm to 5.50 mm interface of the pyramid rail. Each mount allows for 4 electrical connections, for a total of 8 when mounted in parallel configuration. A MACOR insert (centre) can be placed in each 6 mm diameter pads in order to insulate the stainless steel mount from the beryllium copper in-line connectors (right). Together these components provide insulated electrical connections to anywhere in the assembly without needing to solder or use adhesives.

or welding. However, the combination of these components does introduce the issue of stray current loops due their construction materials. This issue is solved by introducing a buffer between the interface and connector - a non-conducting insert made of MACOR, an ultra-high vacuum compatible glass ceramic. Altogether, this step on the pyramid rail provides an insulated launching point for all electrical connections which in totality are the MOT coils (up to 2 per coil), 2 SAES getter Cs dispensers running in series, and two electrodes.

The type of wire used in the assembly was chosen for its size and durability, as it not only had to provide basic electrical connections, but also survive being coiled to form the MOT. The final assembly design assumes the use of Kapton insulated single core wire with a jacket diameter of 0.64 mm and current rating of 3 A. The width of the wire is crucial as this defines the outer radial width of the MOT coils through field modelling of the required number of wire layers - a value that should be limited to ensure a lower self-inductance of the coils and thus avoid the issue that plagued the test coils.

The next pyramid steps from 5.50 mm to 7.00 mm in width define where the MOT coils rest on the assembly and thus where the MOT is produced. The cumulative lengths of the steps until the 7.50 mm interface have been engineered such that, with a coil size as calculated with the noted Kapton wire, the MOT should be produced at a level marked by the 6.50 mm interface. To give the best possible optical access

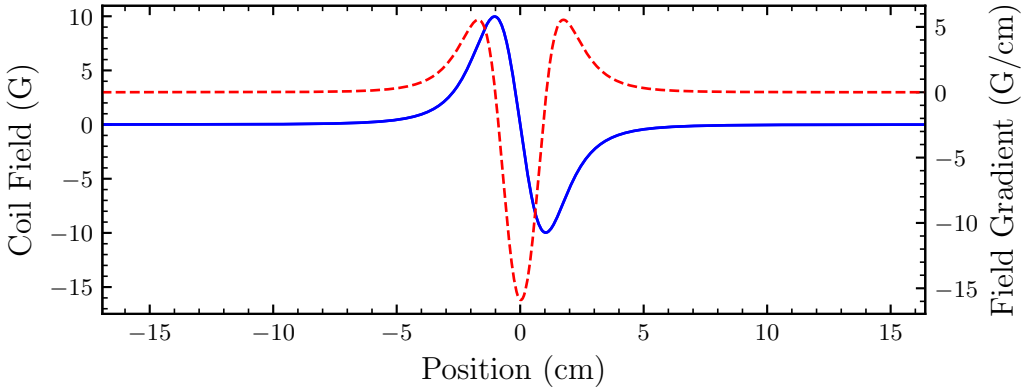

Figure 6.5: B field predicted to be generated by assembly MOT coils. The blue line indicates the field strength in Gauss, while the dashed red line indicates the field gradient at that point. This figure assumes a current of 1 A through both coils, a coil separation and inner radius of 1.5 cm, and 7 layers of wire with 6 turns per layer. The minimum current for this model to achieve a 15 G/cm gradient is 945 mA.

this position also coincides with the central axes of the vacuum viewports. These steps, along with the depths of the coil formers, also help to define the field strength generated by the electrodes as they ensure a gap of 9.45 mm.

6.3.3 MOT Coils

The main considerations when designing the MOT coils, aside from the obvious challenge of minimising an anti-Helmholtz coil arrangement that can produce a field gradient of 15 G/cm, were to keep both the current and number of wire turns as low as possible. A low current ensures that the assembly can be run continuously with minimal heat dissipation as the design does not account for any kind of cooling systems other than the metal formers acting as heat sinks. Having fewer wire turns also reduces the radius of the coil and thus lowers self-inductance, which would negate any possibility of fast field switching and thus trap temperature measurements or optical molasses.

The coil formers themselves rest near the bottom of the pyramid rails on the 6.00 mm and 7.50 mm steps and define the outer extents of the assembly (61.9 mm). These platforms are designed such that the separation of the coils is closer to the coil radius than was the case for the test coils, but also placed such that they produce a tighter B field to account for the small field overlap region. Once this length scale

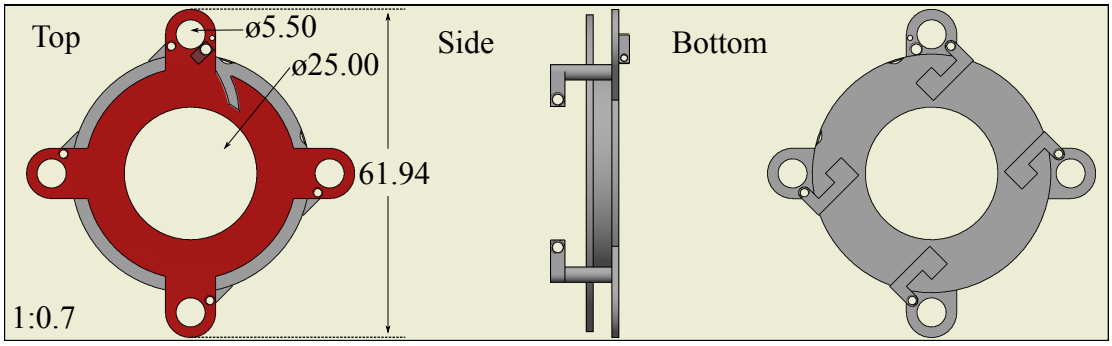

Figure 6.6: (Left) Top-down view of the upper coil former. This component rests on the 5.50 mm to 6.50 mm interface of the pyramid rail as defined by its outer mounting holes. The top face of the former has a chamfered notch cut into it to allow easier wiring of the coil and small attachments with which to route the cable, seen prominently by the 'north' facing mounting strut. In addition, this face also has four screw holes on each mounting strut with which to connect the electrode tray holding arms seen in the middle and right sections of the figure. Schematics of the former noting more details of the mounting method can be found in Appendix C.

was defined, modelling of the coils began to determine an adequate number wire of loops and current to produce the correct field gradient.

The coil field was calculated using the same method as had been previously done with the test coils, due its excellent agreement with experimental data. Figure 6.5 shows both the predicted field strength (blue) and field gradient at that point (red dashed). The figure gives an estimate of the maximum field gradient for 7 layers of 6 turns of Kapton insulated single core wire per coil with a starting inner radius of 15 mm as ∼15.9 G/A/cm and thus 945 mA should be sufficient to reach 15 G/cm. The total amount of wire required for a set of coils with this configuration is 12.1 m, which when run in series could dissipate approximately 0.72 W of heat per coil - a value easily accounted for by simple passive dissipation through the stainless steel assembly, thus both matters of self inductance and heat have been accounted for. Also, as the coils are designed to more closely follow the Helmholtz condition, their predicted field gradient is much greater than the field generated by the test coils (figure 5.2).

Both the upper and lower coil formers shown in figures 6.6 and 6.7 have been designed with ease of wiring in mind. An additional output of the field calculation was the final width of the coils, estimated to be under 2 cm. This was taken into

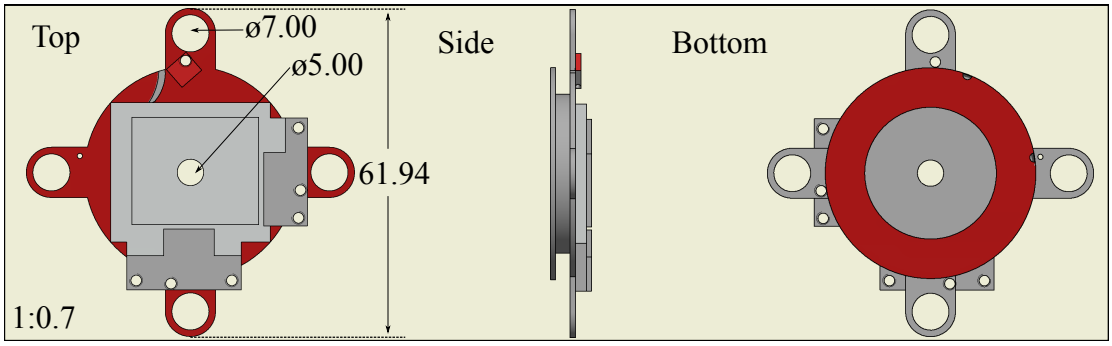

Figure 6.7: (Left) Top-down view of the lower coil former. This component rests on the 7.00 mm to 7.50 mm interface of the pyramid rail as defined by its outer mounting holes. Like its partner coil former (figure 6.6), the upper face of the former has both a chamfered notch and wire routing solutions but they are mirrored to account for the necessary opposing current direction. Also included on the upper face is a MACOR grating chip mount and clamping system to allow the chip to be used as an electrode. More schematics of the former noting more details of the clamping mechanism can be found in Appendix C.

account in the design to avoid over-wiring a coil and thus the prominent edge of the coils were defined to have a 2 cm radius. In order to best preserve the wire enamel during the wiring process chamfered cuts were also made into the entrance sides of the coils, as well as small wire channels designed to serve as anchoring points and avoid loose wiring.

Due to the length scales involved the spacing of the coils is crucial, and thus many aspects of the formers have been designed with this mind. As has been mentioned previously, the pyramid rail notes the modelled position of the B field zero which is determined using knowledge of the resting positions of the coils on the rails as well as their extension in free space. With all pieces of the assembly in place, this leaves an 8.5 mm gap in which the MOT can form. Using equation 2.3.1 we can see that the trap extents for the given wavelength and grating spacing is 0.3 mm to 17 mm above the chip. Given this, at first glance, it may seem counter-intuitive to aim to form the trap 7.5 mm above the chip and only leave an 8.5 mm gap, but due to the complex geometry of the GMOT only 27% of the trapping volume is situated above the mid-point of the light field crossover.

6.3.4 Shim Coils

While the main in-vacuum MOT coils can be wired independently and thus control the z axis position of the field zero, adjustments may be necessary in x and y axes to generate a MOT. The shim coils designed to achieve this take the form of a cube shaped frame that fits around the vacuum cube. By combining the calculated field of the main coils with the Helmholtz shim field, an estimate can be made of how far the B field zero will be moved. For a shim box of side length 11.5 cm and 10 turns per side this amounts to a B field zero shift of 0.53 mm/A, which is appropriate for the working length scale established by the dimensions of the integrated assembly.

The box is constructed using 12 struts of extrusion, measuring 115 mm in length and 30 mm in cross section. These are connected into a cubic frame using 3-way corner brackets. On each face of the cube 8 45 mm M6 screws are secured within the grooves of the extrusion, around which wire can be coiled. Due to the chamber requiring baking before depressurising, the shim box must be constructed and wound one face at a time around the vacuum cube.

6.3.5 Grating Chip Mounting

As modelling progressed it became apparent that the MOT formers could serve multiple purposes by integrating other components into them, thus compacting the assembly. The first component to be treated in this way was the mounting platform for the grating chip, which instead of being separately placed along the pyramid rail was integrated onto the top side of the bottom coil former. This was achieved by a clamping mechanism formed of two thin stainless steel plates and the pairing of M2 sized screws and nuts. With these plates in place, the alignment of chip mount is assured by simply pressing against the inner edge of the plates and then clamping down. This part of the assembly can be seen in the left-hand section of figure 6.7 in which the grating chip would rest in the central rectangular hole. More in depth engineering diagrams that were used for production can be found in the appendix. Admittedly this method does add some complexity to the assembly with small threaded holes, but it allows the mount to be made of the insulating ceramic

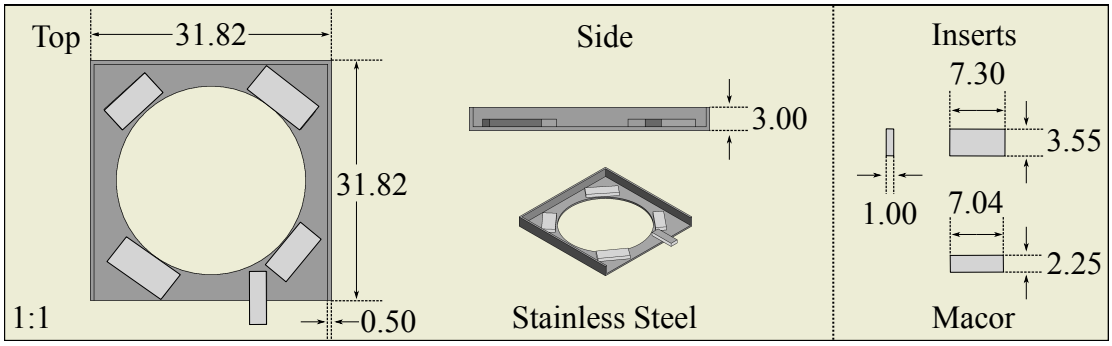

Figure 6.8: 1:1 scale CAD renderings of the ITO slide mount. The electrode is isolated from the body of the assembly by non-conductive MACOR pads which also add some friction such that glass does not slide as readily. The only dimension of these pads that is strictly necessary are their depths, which are used to help define the electrode separation of 9.45 mm.

MACOR, and thus the utilisation of the grating chip itself as an electrode measuring 23.5 mm × 20 mm.

6.3.6 Transparent Electrode and Mounting

In a similar manner to the grating chip mount a second electrode was originally planned to have its own harness along the pyramid rail, but was instead integrated into the bottom of the upper coil former to save space. Due to its position above the chip this electrode needs to be transparent, and therefore uses an Indium Tin Oxide (ITO) coated glass slide provided by VisionTek Systems Ltd.

The right-hand-side of figure 6.6 shows the four mounting arms used to secure the stainless steel tray (figure 6.8) into which the electrode slots. Due to the alignment of the tray being less critical than the grating mount there are no notches with which to position it. Like the grating mount, the tray is secured by way of clamping with the four stainless steel arms providing pressure that can be determined by M2 screws and bolts.

In order to isolate the electrode from the mount, several MACOR inserts are strategically placed to create a buffer between the mount and the 30 mm × 30 mm ITO coated surface. Together with the grating chip, these electrodes generate the extraction field to either ionise Rydberg atoms and/or guide ions generated by the overlapping ionisation beams. When mounted, the separation of the electrodes is

9.45 mm. This short distance means that a lower voltage is required to generate the necessary electric field strength, and therefore less expensive power supplies can be used. Using this distance and equation 4.5.2 the potential difference required to field ionise from the $23P_{1/2}$ Rydberg state is calculated to require 1100 V. By using the ITO coated slide as an anode and grating chip as a cathode, held at ±550 V respectively, this necessary difference can be achieved well within the voltage rating of the kapton wire (600 V).

6.3.7 Assembly Costings

Continuing with the project objectives, component costs have been minimised where possible, but some large expenditures have been necessary. The most vital component of the assembly, the grating chip, is also potentially the most costly per unit with an estimate per chip being £1000. In order to further justify this cost the chip serves a dual purpose by eliminating the need for a secondary, separate electrode.

Unfortunately, unlike the vacuum chamber that does not require special training to assemble, the components of the integrated assembly need trained technicians to operate fabrication equipment. This work was performed solely by Malcolm Robertshaw in the Durham University mechanical workshop with an estimate taken of his hourly rate being £20/hr. While this is a large expense, it could be improved upon as this cost represents the first attempt at creating what is a very small and intricate device with delicate pieces to machine (especially with regards to the MACOR components). With practice and improved processes this cost per unit could be greatly reduced.

While the assembly consists mostly of stainless steel by weight, the cost of materials for the assembly is dominated by the cost a cylinder of the ceramic. However, due to the relatively low volume required for a single assembly, this can be seen as an initial investment cost, as many copies can be made with a small amount of MACOR.

The remaining components of the assembly are directly purchasable from a number of suppliers, and so with market analysis these costs could be reduced. It is important to note though that all of these components provide more than is necessary

Component	Price ex-VAT (£)	#	Supplier
Grating Chip	1000	1	Strathclyde University
Fabrication Costs	20/hr	74.5	Malcolm Robertshaw
Materials	52.20	1	Durham University
10 In-Line Connectors	36	1	LewVac
10 m Kapton Wire	25	2	Lewvac
Cs Getter Dispensers	15.10	10	SAES Getters
Vacuum Screws Set	14	2	LewVac
10 ITO Coated Slides	10	10	VisionTek Systems Ltd.
Total (£):	**2893.2**		

Table 6.2: Summary table of the integrated assembly components order by individual price. Prices noted reflect those at time of purchase or estimates where no invoices or quotations are available. The materials supplier noted as 'Durham University' refers to metals and ceramics acquired by the mechanical workshop through their suppliers.

for one assembly, and so their effective costs are reduced.

6.3.8 Cold Cs Ion Cost Analysis

When considering the total cost of the system and how it compares to more traditionally based FIB sources such as a Ga needle, one must remember that the values given for both the chamber and assembly are subject to change. For the chamber this is primarily due to it representing the first iteration of a design, and thus including characterisation components such as an MCP rather than a sample stage. The cost of the assembly would likely reduce due to the lowering prices of diffraction grating manufacturing and the streamlining of component production. It is also important to note that the costings for both the vacuum chamber and ion assembly do not include any ion optical elements such as Einzel lenses, as this project only addresses the source itself and not any kind of generically available beam column.

Also, while justifications have been given for the laser systems that have been employed in this project in terms of their costs and abilities, there are many improvements that could be made to further minimise both expenditure and experimental footprint - some examples of which will be expanded upon in a subsequent section.

From the tables above it can be seen that the total proposed spending on a prototype cold Cs ion source is ∼£52,500. The majority of this cost (£33,614)

derives from the ionisation scheme and extraneous features of the optical setup that, while allowing a great amount of troubleshooting, incur costs that would not be present in a final design.

The costs of the proposed trapping hardware meanwhile are much lower by comparison, only reaching $\sim$ £18,900, with this estimate being dominated by a single component that would not be present in the final chamber iteration. Aside from this, there are the other ways that this cost could be reduced, some of which have already been outlined above.

Now that the costs involved with this first generation of cold ion source have been identified, an effort can be made to compare it to more established and commercial implementations of FIB systems. In order to give a more fair comparison though, the additional costs of ion optics must be included which, for the purposes of this comparison, amount to an Einzel lens, acceleration tube, and beam deflectors, for an estimated cost of $\sim$ £30,000. Including this beam line brings the cold Cs FIB to an approximate total of £80,000. Using this figure the Cs source can be compared to two prominent FIB systems manufactured by Zeiss International: the Crossbeam and ORION NanoFab integrated ion beam systems.

Both of these are some of the best available instruments for their purposes, the first combines an SEM with a FIB to provide high resolution scanning as well as milling applications using a gallium based LMIS. While the second combines a GFIS, for sub-10 nm resolutions, utilising either helium or neon, with a more standard gallium LMIS for larger scale mass removal. In addition to these features, due to being fully engineered commercial solutions, both systems offer capabilities such as automatic sample ROI search. The purchase price of these instruments is normally in excess of $1 million with an economy of scale already applied. This is in contrast to the ion source described in this chapter, that has the potential to offer similar characteristics in terms of resolution and milling abilities to these full systems if given the appropriate optics and computer control.

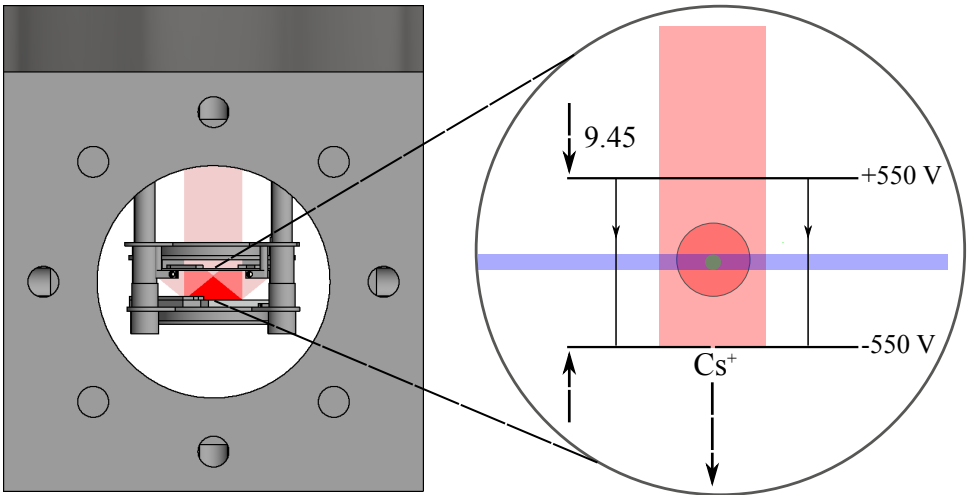

Figure 6.9: (Left) An illustration of the assembly operating within the vacuum cube including an input beam. While (right) shows a simplified digram of the operating parameters of the electrodes on the overlap region of the MOT and additional ionisation beams. In this illustration, the source is assumed to be operating near the threshold voltages required to ionise the $23P_{1/2}$ Rydberg state.

6.4 Ionisation Schemes

6.4.1 Geometry

The assembly has been designed such that when it is placed inside the vacuum cube there is a clear line of sight to the MOT along both the x and y axes, as can be seen in figure 6.9. It is along these sight lines that the two additional lasers, represented in the figure as blue and green areas, can impinge upon the trap and form the three photon ionisation region.

This takes place between two electrodes, the upper ITO coated glass measuring 30 mm × 30 mm and the grating chip, measuring 23.5 mm × 20 mm. The ITO coated glass acts as an anode and is positively charge to repel the ions while the grating chip works in tandem by providing an attractive force from its negative potential as a cathode. The distance between the electrodes has been designed to be able to generate the necessary potential gradient given the limitations of the kapton wire rated at 600 V.

6.4.2 Light Field and Rydberg Ionisation

A strength of this ion source design is its ability to run in two distinct modes of ionisation, either of which can provide differing characteristics depending on the intended outcome. The first is straight laser field transverse ionisation via the three photon process at the intersection of all light fields. This could be considered to be the more conventional approach, and offers benefits such as being able to use entirely arbitrary acceleration fields for extremely low energy ion beams - an impossibility for conventional sources. While this approach may enable techniques such as these to be used, this ionisation scheme is very wasteful in terms of power usage and would require increasing the overall cost of the source for reasons explained in chapter 4.

The second operating mode involves Rydberg excitation at the intersection of the two ionisation beams, and then ionising these atoms using an electric field. Using equation 4.5.2 one can calculate that the field strength required to singly ionise the $23P_{1/2}$ state is 1147 V/cm while a voltage of 1100 V between electrodes of 9.45 mm separation gives a field strength of 1164 V/cm. If this rating does prove to be insufficient then the voltage can also be increased to the maximum allowed by the kapton wires for a final field strength of 1270 V/cm. This mode omits low field operation as it requires at least the threshold ionisation field, but would be feasible for all strengths above this. It would also be less wasteful in terms of power usage as it would employ the locking method described in chapter 4, making it the primary mode of operation for this system.

Performance of this system can be estimated to be comparable to other ion sources based on 3D MOTs when including similar beam lines and extraction potentials. These include systems found in references: [43, 44, 53, 54, 133–138] with additional modelling that can be found in [45, 48, 50, 51, 141]. Due to limitations in voltages that can be carried in this system by the kapton wire it is not possible to reach some of the beam energies described in those systems, and thus, absolute performance. It should also be noted that even with equivalent potentials, the performance will be far lower than LoTIS but still smaller and easier to make.

6.5 Chapter Summary

In this chapter I have introduced the proposed integrated ion source assembly, including its vacuum chamber and how the pieces necessary to produce ions were compacted. Using market prices I then analysed the components of the chamber and assembly to justify their expense, as well as compared the total costings to industry standard devices. The result of this was a favourable conclusion given the low cost of this first iteration of a cold Cs ion source and the space remaining to improve upon aspects of this design. Figure 6.10 shows the fully constructed assembly.

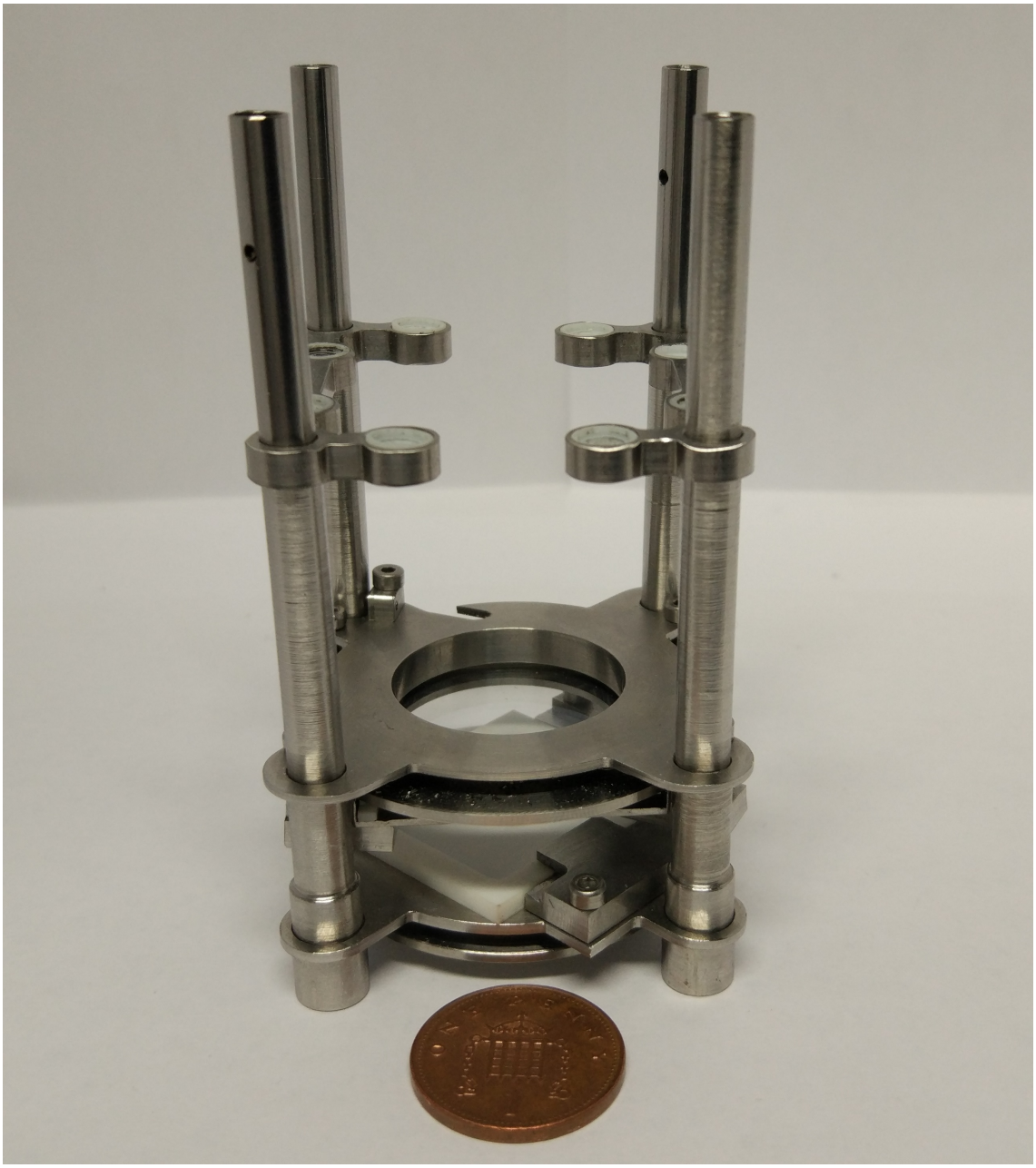

Figure 6.10: Fully assembled integrated ion source with a penny given for scale.

Chapter 7

Discussion and Conclusions

7.1 Discussion

As a first iteration of an ion source design, there are a number of key points that could be addressed given the benefit of hindsight, both in terms of experimental characterisation and decisions on hardware as well as methodology.

7.1.1 Laser Systems

While a trap was briefly spotted in the later stages of the experiment and demonstrated that high intensities were not required to form a trap, until this point, there was a great deal of anxiety about the difficulty of providing enough power to produce a trap with known experimental uncertainties. Given this, there are a number of questions that can be asked of the design and methodology employed when planning the laser systems.

7.1.1.1 A Less Ambitious Starting Point

As has been touched upon in the section heading, an overly ambitious goal may have contributed to the transient result of this work. As was discussed in chapter 4, the maximum output of the TA 100 was initially 500 mW but this was bolstered to 550 mW using unconventional means. For a standard Cs MOT using retro-reflection to enable 6-beam trapping, this was shown to be more than sufficient to produce

the necessary beam intensity, as was seen in figure 5.5. This should also have been enough to produce a stable GMOT but some optics were later repurposed for other experiments leaving only half the possible laser power for cooling which may have contributed to the weak trapping effect. My fear is that in determination to use less powerful laser systems I denied myself the capacity to eliminate this factor of anxiety and press ahead with other issues which may have been more important in hindsight such as those specifically pertaining to the grating chip.

Thus the question remains as to whether a less zealous approach in aligning to the project objectives would have been more appropriate for this first demonstration. A fast remedy to the problem of power may be the introduction of a new tapered amplifier chip to the TA 100, effectively keeping the same system whilst increasing its power output dramatically. A recent valuation of a compatible 2 W chip would add an additional £2098 to the cost of the project and would provide intensities far in excess of the predicted necessity.

7.1.1.2 Alternative Laser Options

As the discussion of laser systems has already touched on ideas of changing aspects of the setup, it must be said that it is not outside the realms of possibility to replace the entire setup for alternative arrangements. While justifications have been given for the laser systems as they are implemented, there are changes that can be made which would enhance the ease of use of the system as well as reduce the device footprint. The most simple way to achieve this would be to replace the external cavity diode lasers with DFB equivalents. A main advantage of ECDLs are their vast tunability but this is unnecessary for the ion source - the lasers must simply remain at their designated frequencies whilst being free from mode hops, a key feature of DFB diodes. When paired with a suitable tapered amplifier, these DFB alternatives would provide all the necessary trapping, repumping, and ionising light whilst maintaining a reduced form factor. Since beginning this work there has also been successful development of compact methods to generate Cs cooling light in the 1 W power range using telecoms wavelength lasers [212]. It must also be mentioned that despite aiming for a system that would be stable in the long term, the amount

of user adjustment required to maintain laser system performance is far from ideal. Thus, for any changes, more stability must be prioritised through means such as (but not limited to) more sturdy mounting in the case of amplifier seeding and fibre coupling, or better isolation from temperature gradients and magnetic fields for the laser locks.

7.1.1.3 Ionisation Lasers in a Drawer

While one of the main project goals was to produce a 'compact' ion source, this was largely overlooked when designing and implementing the lasers and their optics. Currently the optics for the source fill approximately 2 m^2 on an optical table and therefore represent the greatest use of space when comparing all sections of the project. This is primarily for ease of construction and testing purposes as creating a compact laser system, including the required optical elements for stabilisation and efficient outputs, can be an extremely involved endeavour. However, there is a precedent for such compact systems, with early work on this project being based around, as the subsection heading suggests, placing all optics and lasers required for the initial trapping into a single rack mounted drawer less than 0.2 m^2 in area. The plans involved having a single DFB laser providing both the cooling and repumping light by modulation with an EOM. Unfortunately this was unsuccessful due to an earlier grating chip of a different design having too high a level of back-reflectance. Given the benefit of hindsight though, there would be cause to return to such an arrangement and when doing so, also include the two additional ionisation lasers in close proximity to greatly reduce the system footprint.

7.1.1.4 ZSAR

I would be remiss if I failed to mention the greatest success story of this work in the laser systems discussion section. The motivation to create the Zeeman Shifted Atomic Reference was born from the need to find more efficient methods with which to ionise caesium, a function that it performed admirably. Initially, ionisation was planned to take place from the $7^2S_{1/2}$ state using a 777 nm laser, but optical complexity and power inefficiency made this an undesirable prospect. The remedy to

this came by a literal coincidence - or rather, a near-coincidence, as a ground state transition in Rb^{85} was found to be within 20 GHz of detuning away from the Cs Rydberg transition: $7^2S_{1/2} \longrightarrow 23P_{1/2}$. The magnetic field necessary to generate this detuning was a simple matter to calculate using the ElecSus software and therefore purchasing the appropriate permanent magnets was also an easy task. Once installed, ElecSus could then be used to fit the spectrum and confirm the detuning. The most difficult aspect of this work arose from providing an additional reference with which to measure frequency drift, ironically by the very system that the ZSAR sought to replace: a 3-photon EIT setup - a process that highly emphasised the simplicity of ZSAR.

Aside from pure optical simplicity, this novel stabilisation technique also requires very little laser power as compared to its alternative (<1 mW vs ∼200 mW) and is more stable due to not relying on multiple transition locks. Further, through the use of ElecSus, it has the potential to act as a magnetometer for any of the alkali atoms currently available for calculation; given that the weak probe fits using the software have shown such excellent agreement with both theory and measurements using a Hall probe. In line with this reasoning, it is also pertinent to mention that as this technique is open for use with any of these alkali atoms, it has many available central frequencies from which to detune, and thus many possibilities that one may explore as related to their own work and coincidental frequencies. One example of this would be to change the use of Rb^{85} in this work to Rb^{87} for an additional 6 GHz of detuning with the same magnetic field strength. The reason that this was not attempted with ZSAR in this project was due to an appropriate cell not being available at the time and calculations showing that Rb^{85} would be perfectly viable. A further use for ZSAR, other than acting as a locking frequency reference, is to enable studies of thermal vapours in the hyper-fine Paschen-Back regime - a regime in which atomic spectra are highly simplified and cleanly defined, making ZSAR useful for enabling precision measurements and quantum optics experiments.

7.1.2 Chamber

Despite the vacuum chamber never having been built, it can still be considered the first version of the ion source chamber and thus is open for discussion of improvements and extensions to the design for the next iteration.

7.1.2.1 Absorption and Fluorescence Imaging

While there are many additional troubleshooting and analysis techniques that could be added to the setup, the main technique currently lacking is the ability to perform either absorption or fluorescence imaging of any MOT. These are techniques that can be used to determine the number of atoms in a MOT and therefore its density, an important characteristic for an ion source where its current depends on the trap density.

Fluorescence imaging is the more simple of the two techniques and involves trying to focus the radiant light from a MOT onto a photodetector to measure its optical power. Such a technique can also be performed with a CCD such as the pixelfly camera - a device currently only intended to image the trap, but this can produce erroneous readings due to saturation of the CCD. The optical power released from a MOT is related to the linewidth of the emitting transition, the energy of these photons, and the number of atoms in the trap. When collecting this fluorescence with a photodetector, the power recorded is registered as a voltage that is affected by the gain and impedance of the circuit in question, as well as the sensitivity of the given photodiode. Due to the radiance of the trap being isotropic, the received power can also be considered as inversely proportional to solid angle occupied by the lens used to collect the fluorescence. Using these relations, an estimate for the number of atoms in the trap can be obtained [213]. This analysis technique would be the easiest to implement after setting up the vacuum chamber, due to it not relying on many extra optical elements.

In comparison, absorption imaging is more complex and would require modifications to the initial laser setup and many more optics around the vacuum chamber [214]. The principle of the technique is to shine a collimated, resonant beam of light with a known non-saturating power at the trap and then record the resul-

tant power on the other side. The loss of power is related to the scattering rate of the transition and the density of the MOT and thus, using known factors such as the optical cross section and saturation intensity, the number of atoms in the cloud can be calculated. To implement this technique, an additional fibre coupling of resonant light would have to be added to the optical setup, in addition to all the optics required to ensure the output of that fibre is collimated through the MOT chamber, to then be collected by a photodetector. Given the small dimensions of the assembly, it may be wise to opt for fluorescence imaging over absorption for future characterisation.

7.1.2.2 Ion Beam Line and Imaging Chamber

At no stage of the development of the initial project design was the addition of a beam line of ion optics, nor an imaging chamber, ever considered. In contrast to the design of the laser systems, where it has been highlighted that the initial plan may have been over-ambitious, this aspect of the project could be seen to have lacked ambition.

Mostly this was due to the project aim of creating an ion source, not a fully functioning focused ion beam system, as far more development time would have been necessary to approach competing with cutting edge of commercial systems. The project end point was always envisaged as producing an ion source that could be attached to a standard beam column; a mindset that may have required adjusting if the creation of Cs GMOT were successful at an earlier predicted stage. A compromise between the current design and full implementation of beam line and imaging chamber would be to forgo the second component in favour of retaining the MCP, thus allowing the produced ions to be characterised with more suitable energies and focussing.

7.1.3 Assembly

The design of the integrated assembly was influenced by the project aims to become a delicate balancing act of constraints, each coupled to one another in a number of ways. While I am confident in the functioning capacity of the current iteration, I

am conscious of its limitations, which could be remedied.

7.1.3.1 Maximising Margins of Error

An issue that arose in relation to the manufactured assembly were the small margins of error that it had to be produced within. This is most apparent in how the components rest on the pyramid rail and how through compounded errors they can make twisting the rail of the fully constructed assembly an arduous task. Considering the need for the rail to remain mobile in order to attach to its anchoring points on the viewport, this could have disastrous consequences. In order to maximise these margins it would be necessary to increase certain dimensions of the assembly, chiefly the pyramid rail step interfaces and mounting rings. If they were to increase by 2 or more millimetres the burden of production accuracy would be reduced while maintaining a similar form factor and capabilities.

7.1.3.2 Expansion Within the Chamber

Fundamentally though, there are only three aspects of the assembly that must remain consistent through any design that is held within the vacuum cube. The central point of the cube, as defined by the intersection of the x, y and z axes, must be the point at which the magnetic coils are to generate a B field zero, with electrodes designed to create an electric field through this volume, all while ensuring open sight lines to this point so that the atomic cloud can be interacted with. There are many designs that would accomplish this, optimally or not, but the overall performance and limitations of the source are determined by how it is implemented. The final design of this project can be noted to be extremely compact, measuring less than 8 cm with an active length of approximately 2.5 cm, but it has some stark limitations that are the result of working at this length scale.

The main possible issues introduced by this are the volume in which an ionisable trap can form and the limiting of maximum field strengths. Despite the predictions of equation 2.3.1 stating that 73% of the volume of the trap will be present below its mid-level, it may still have been wise to not constrict the MOT forming region as tightly. The decision to do this was a compromise with the electrode placements

in order to maximise the electric field that could be generated given the restrictions of the kapton wires (which are necessary to work at this length scale), as well as to minimise the current and wire needed to generate the B field, and thus the dissipated heat.

An alternative solution to this would require maximising the usage of space within the cavity of the vacuum cube. The current design centres its active area around the centre point of the cube, with an inner separation of the closest active components being the electrodes at 9.45 mm, as defined by the coil formers. This could be increased by doubling the separation of the coil formers and then similarly increasing the distance between the electrodes while restoring them each to a respective independent mount.

At this new separation, the current required to produce a field gradient of 15 G/cm would increase to 1.58 A with 36 turns per coil. Reducing the number of turns decreases the dissipated heat, but this configuration would still produce approximately 3× the wasted heat of the previous design. To accommodate for this, the thickness of the coil formers and rails would have to be increased so as to better conduct the thermal load.

Finally, due to the increased spacing of the electrodes to ∼2 cm, new wires would have to be used as the kapton wire would no longer be able to carry a sufficient voltage. This is fine though as the increased distance also means more space for larger wiring. The knock-on effect of this would be the redesigning of some of the in line connector mounts so as to accommodate a new, thicker variation of wire. If all of these changes were to be made, it would enable a larger MOT to form as well as enable the source to produce ion beams at comparable energies to commercial systems without including such a capability in an additional beam line.

7.2 Concluding Remarks

In summary, during the course of this project, the optics necessary for the cooling and ionisation of Cs have been implemented, with an entirely new locking technique devised for accessing the $23P_{1/2}$ Rydberg state of Cs. A vacuum chamber was

also designed to contain the ion source assembly, which compacted the necessary hardware onto a rail measuring less than 8 cm in length whilst providing optical access for ionisation lasers. Despite the many improvements that could be made to the designs of the project, I am confident that even the current iteration would function as intended, given the formation of a trap. Thus, despite the short-lived formation of a Cs GMOT, the predictions of chapter 2 and results of chapter 5 give hope that such a trap is entirely possible and can be integrated into the proposed compact cold ion source as a basis for further development.

Appendices

Appendix A

Test Coil Schematics

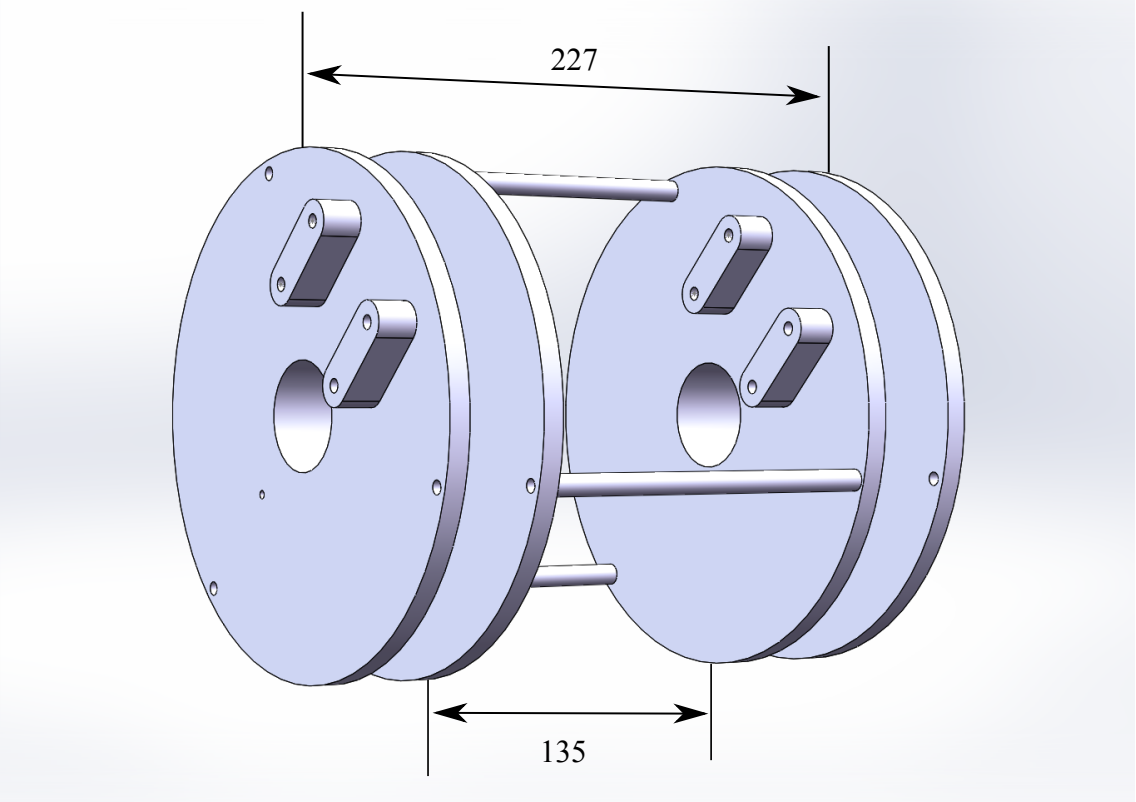

Figure A.1: 3D rendered model of test coil formers generated by Mingjiamei Zhang.

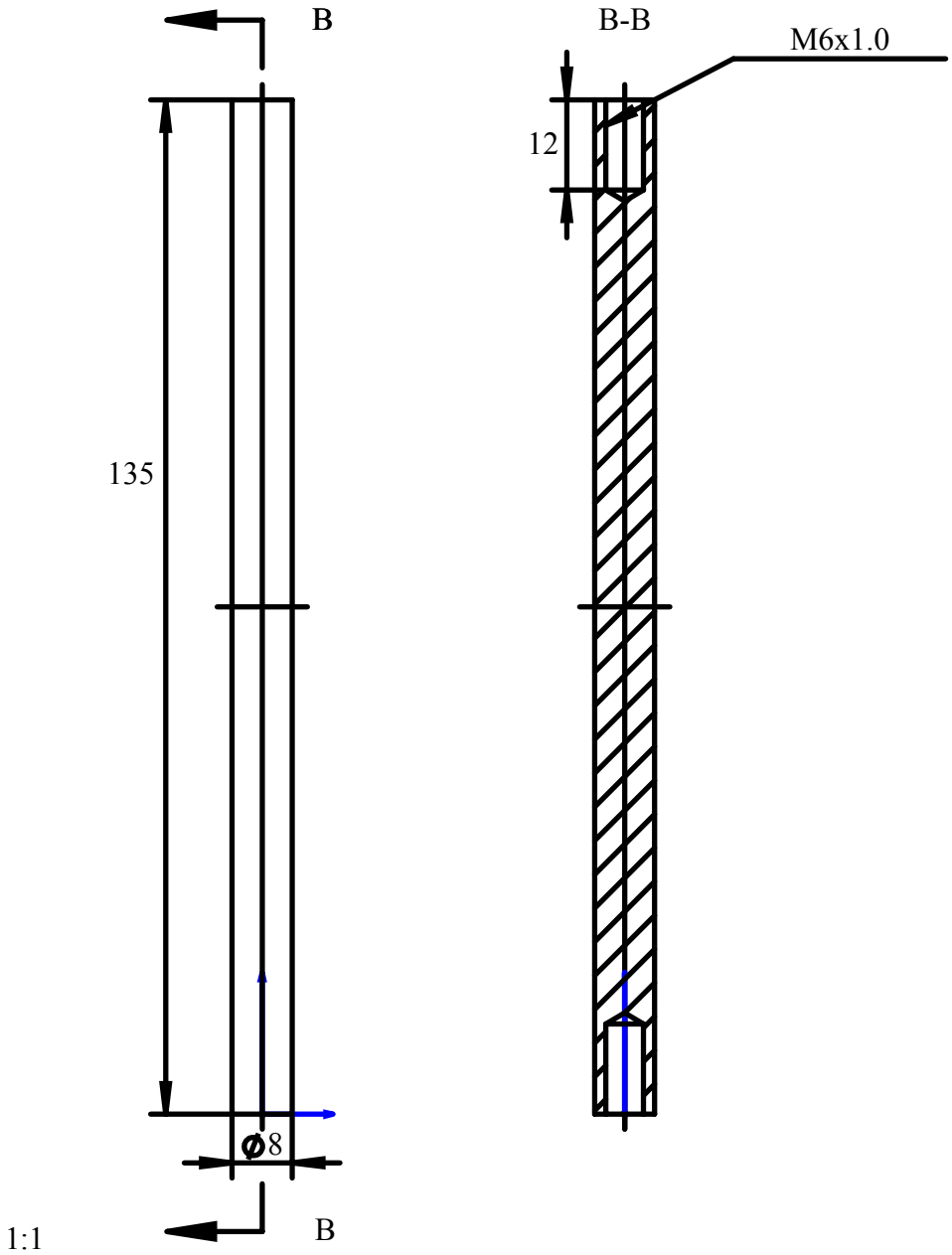

Figure A.2: Test coil former connecting strut production measurements drawn by Mingjiamei Zhang.

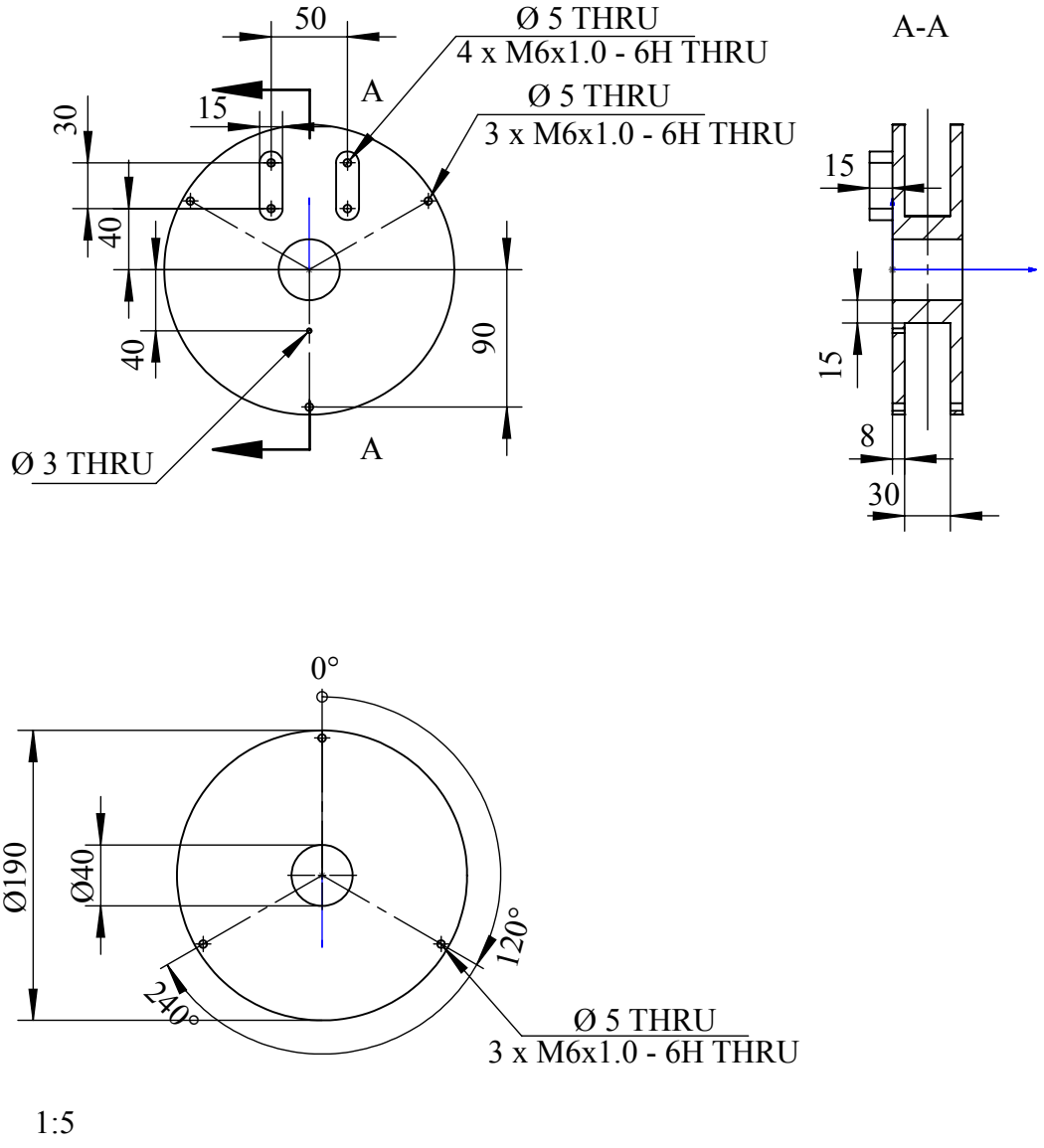

Figure A.3: Test coil former production measurements drawn by Mingjiamei Zhang.

Appendix B

Vacuum Chamber Schematics

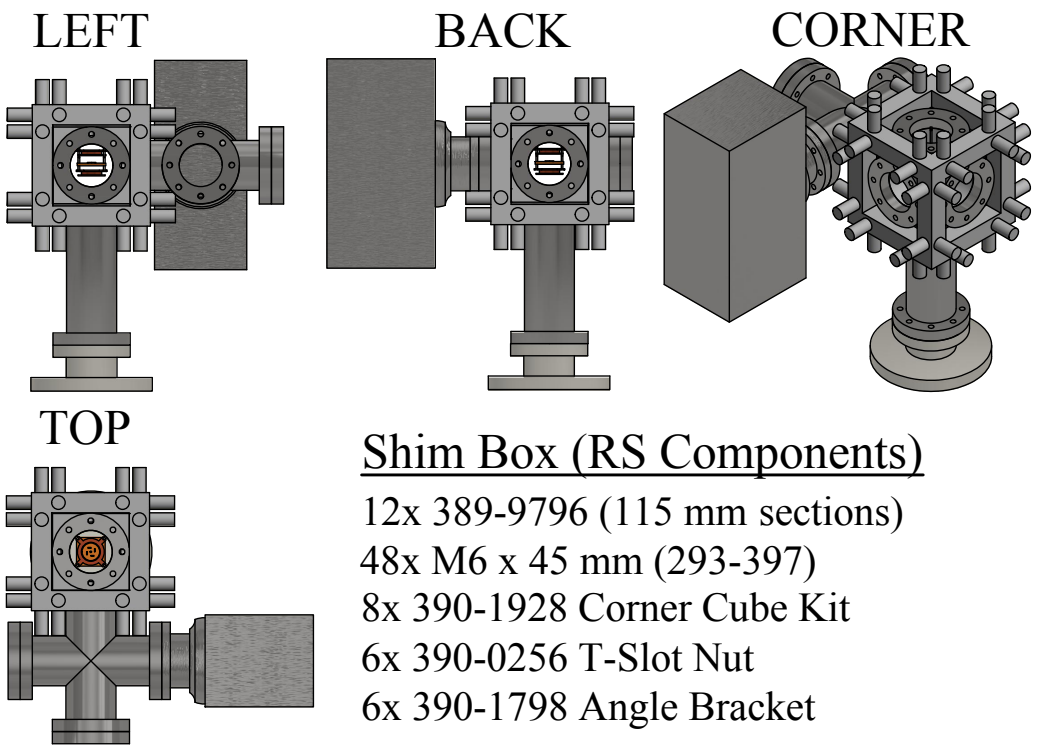

Figure B.1: Angled CAD drawings of the assembled vacuum chamber.

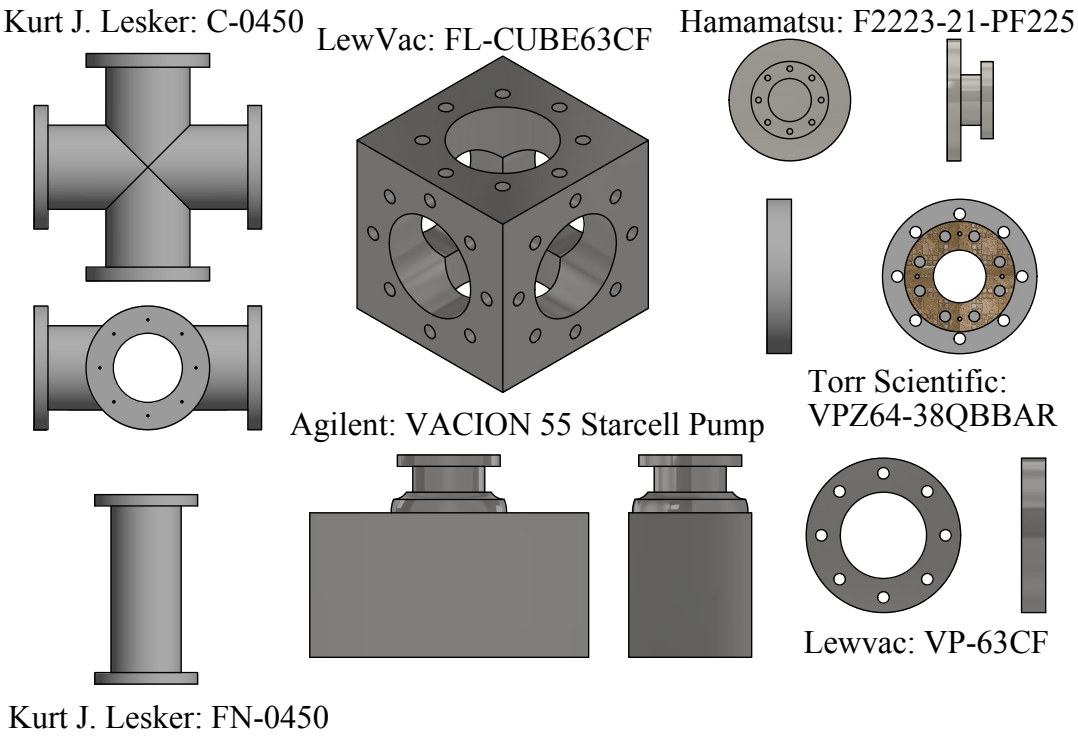

Figure B.2: Rendered components of the vacuum chamber at multiple scales.

Appendix C

Ion Source Assembly Construction Schematics

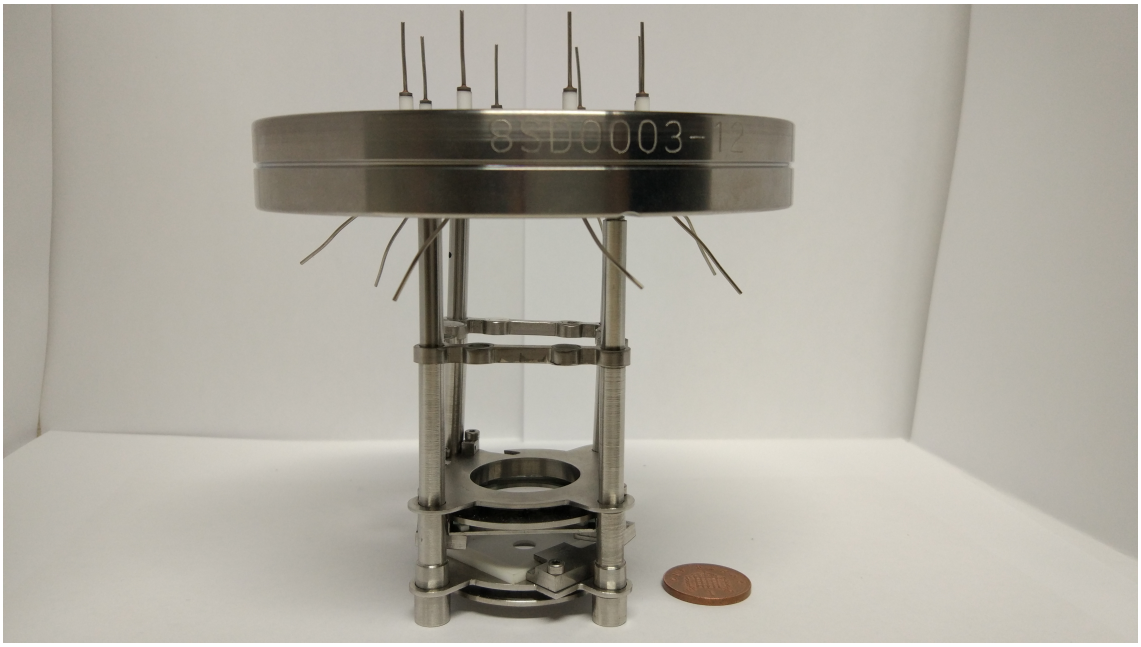

Figure C.1: Fully constructed integrated ion assembly attached to the viewport with electrical feedthroughs.

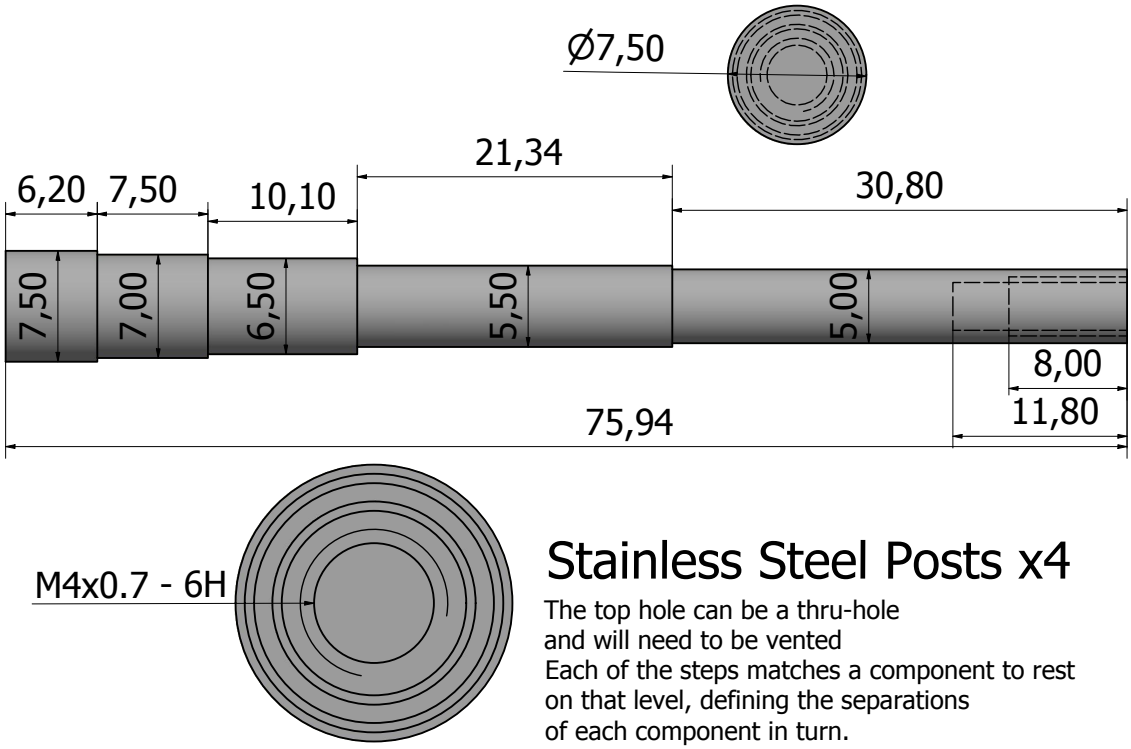

Figure C.2: Full pyramid rail construction schematics used to build the prototype.

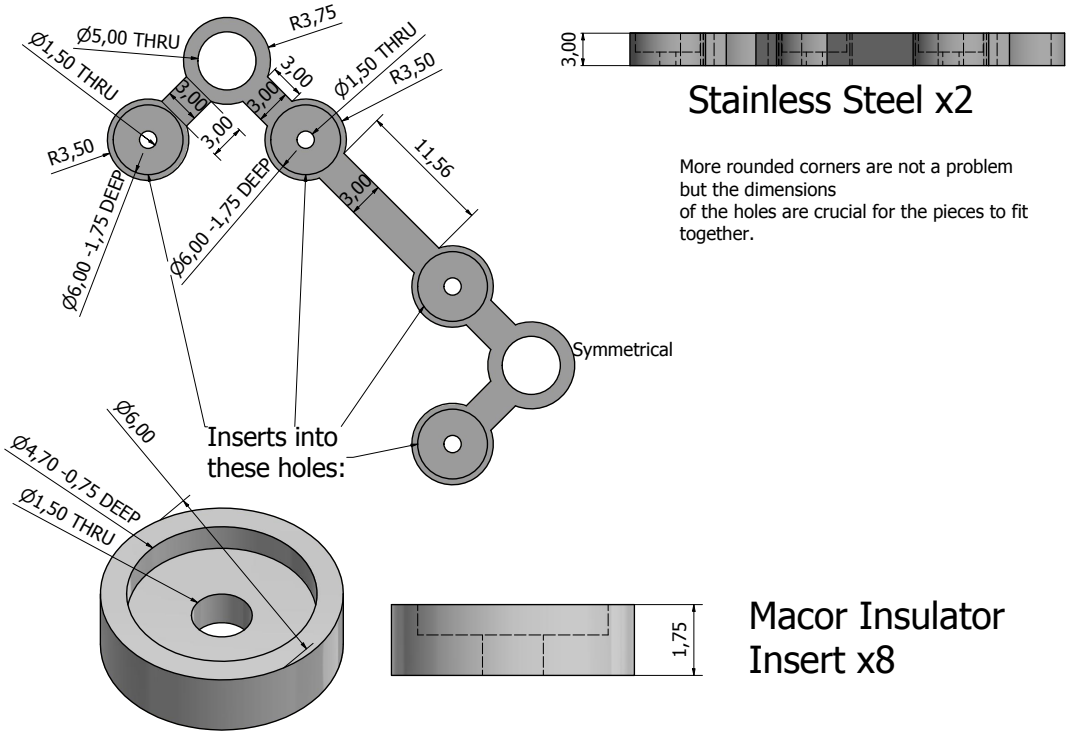

Figure C.3: Full construction schematics for the electrical isolation components.

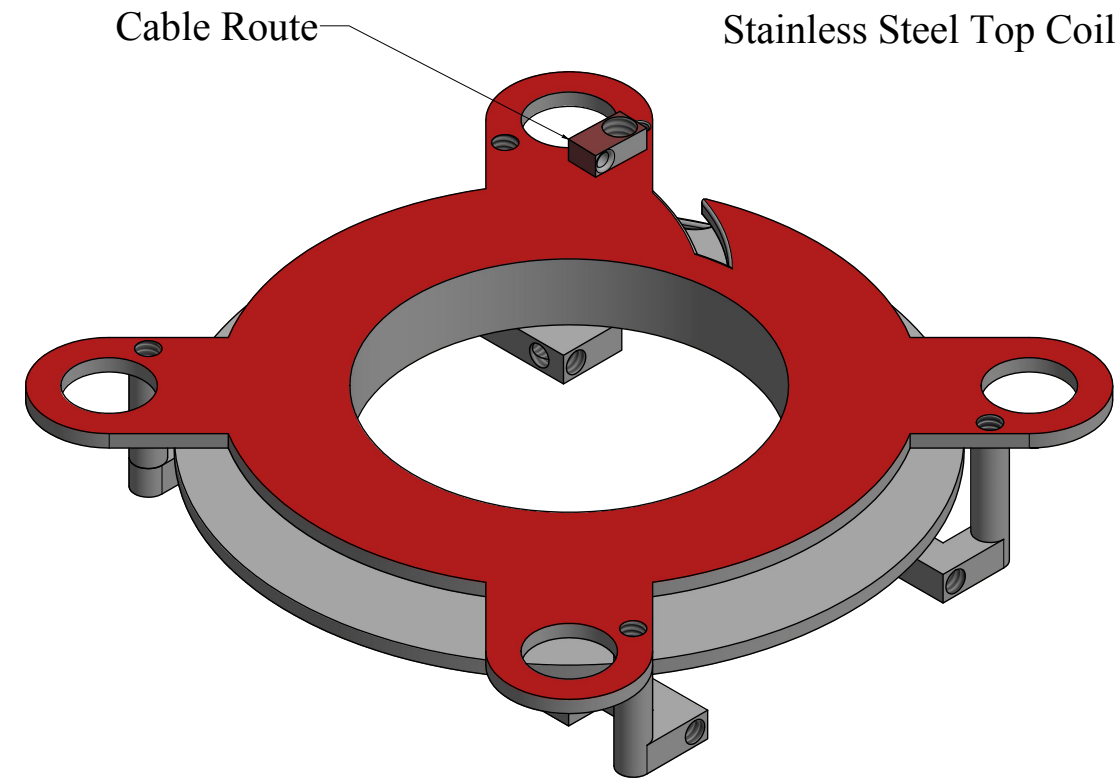

Figure C.4: Example CAD rendering of the top coil former.

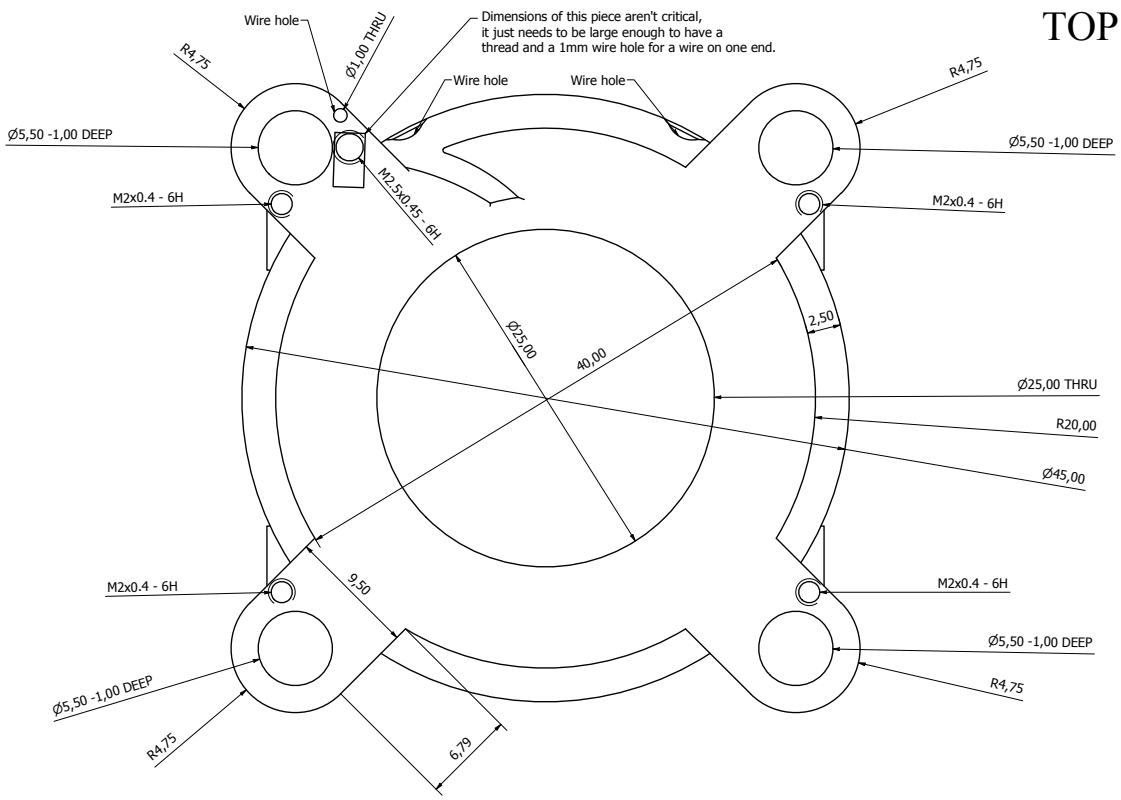

Figure C.5: Design schematic of the top face of the upper coil former.

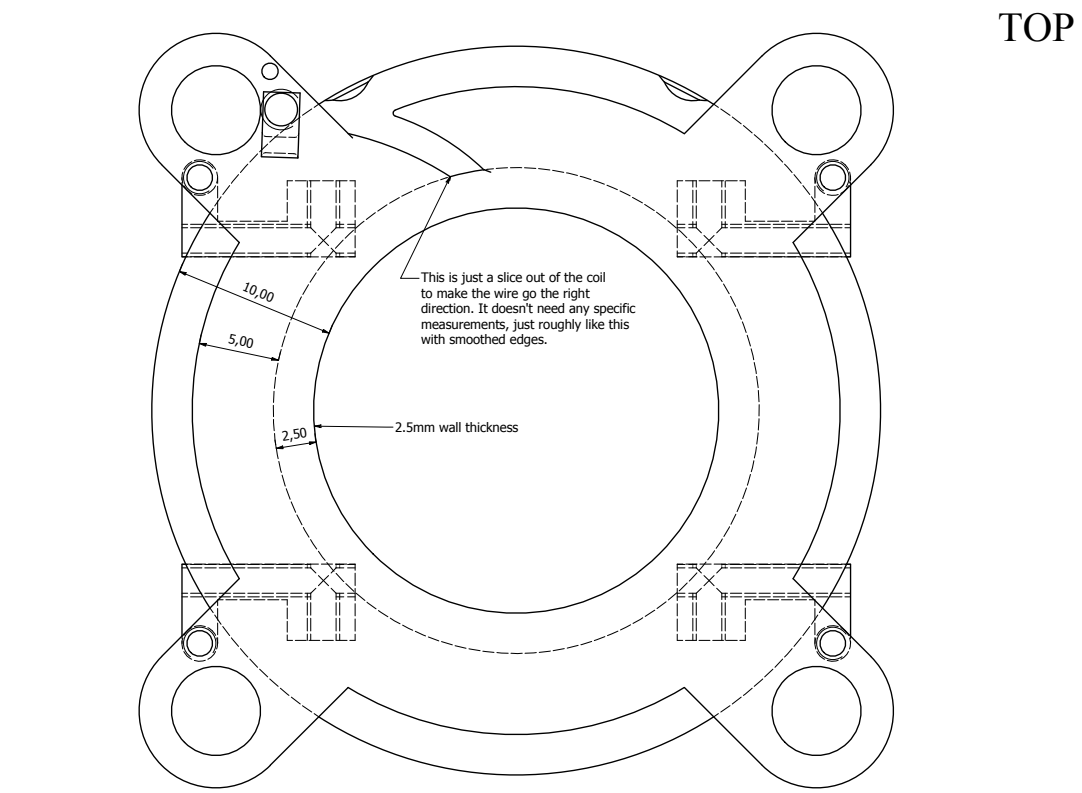

Figure C.6: Similar schematic of the upper coil former revealing inner measurements.

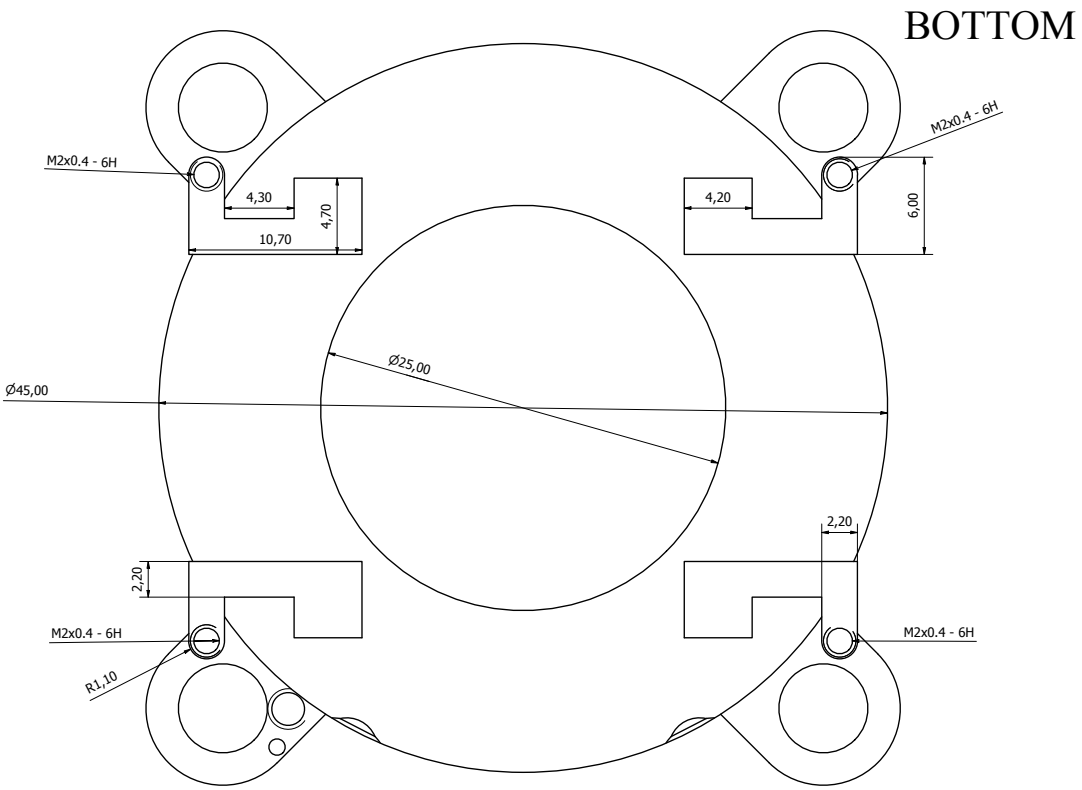

Figure C.7: Design schematic of the bottom face of the upper coil former.

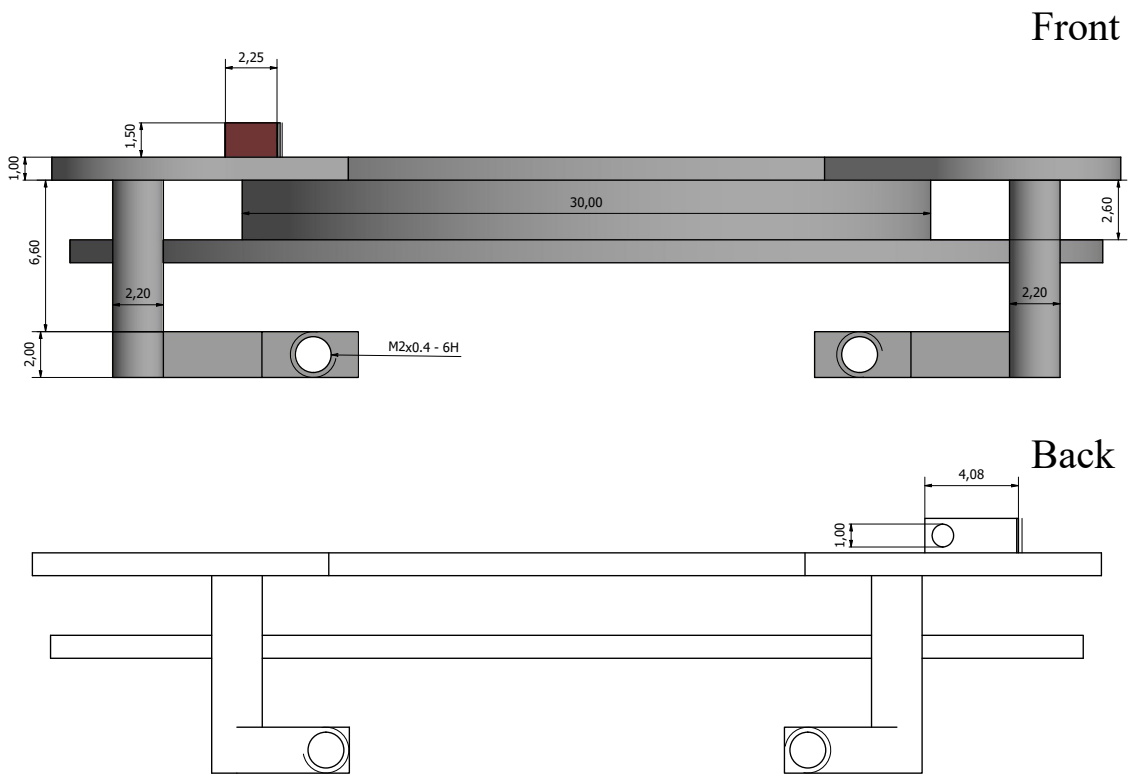

Figure C.8: Design schematic of the side faces of the upper coil former.

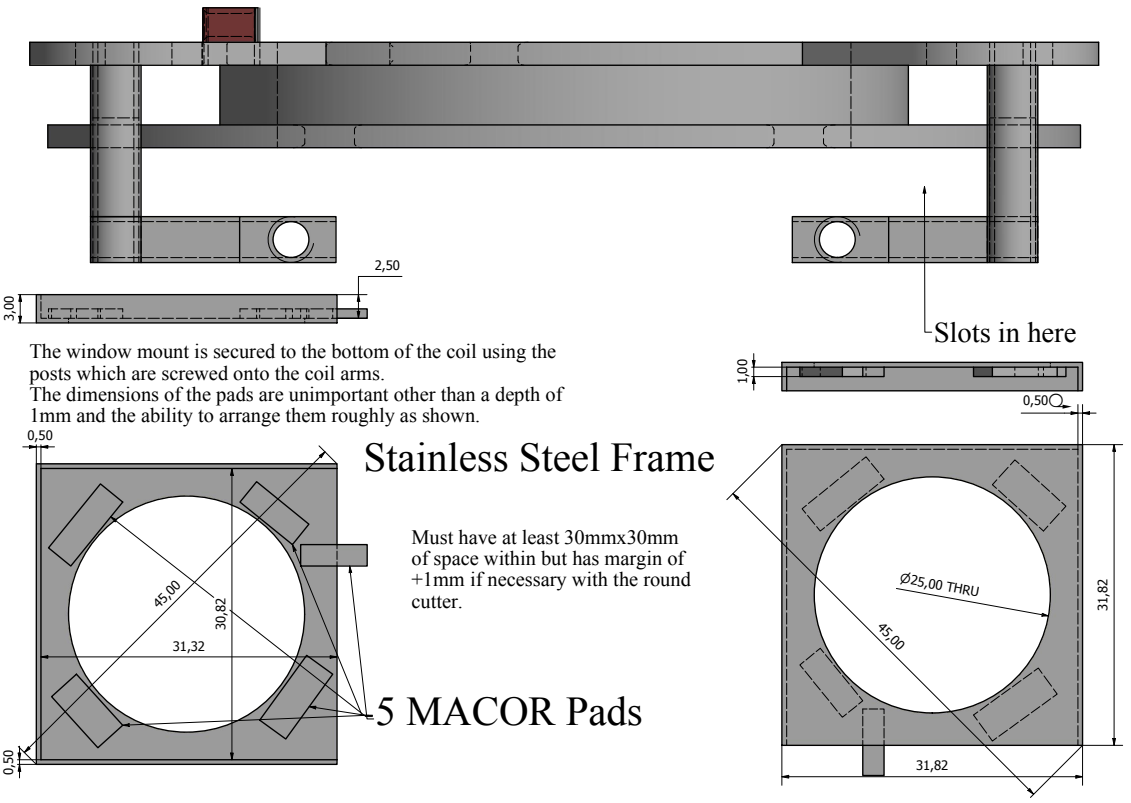

Figure C.9: Design schematic of the electrode mounting mechanism.

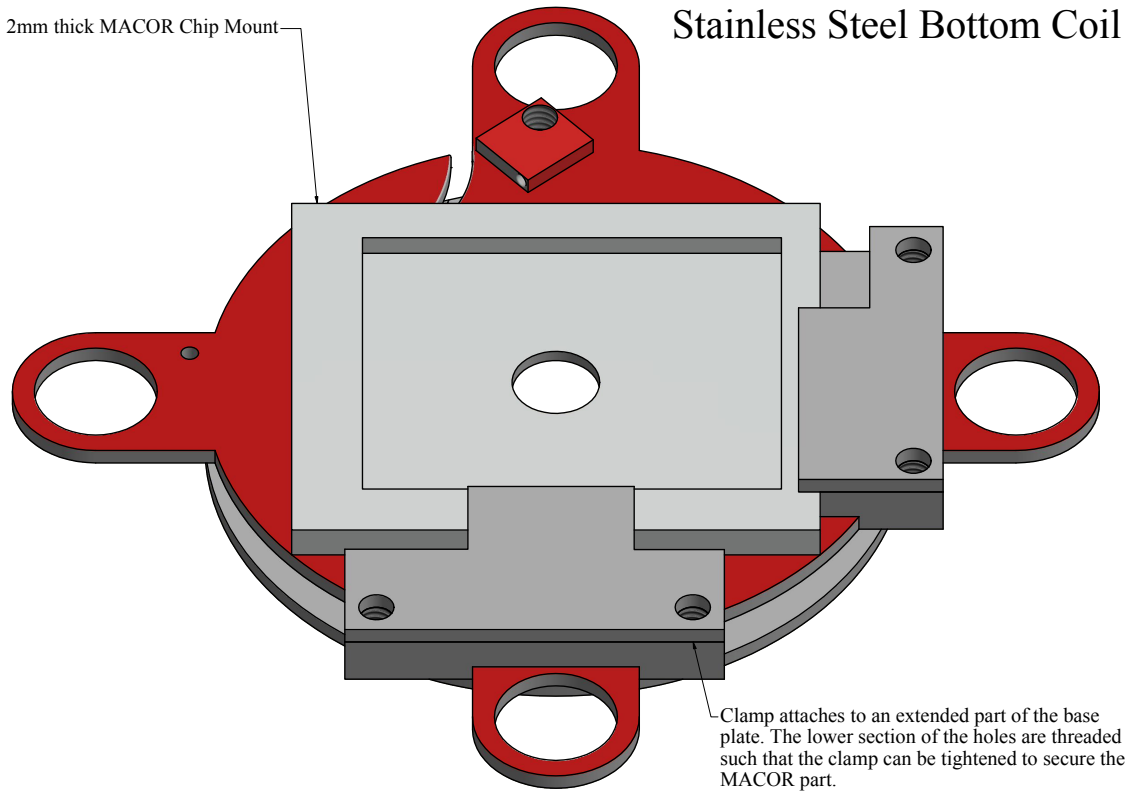

Figure C.10: CAD rendering of the lower coil former.

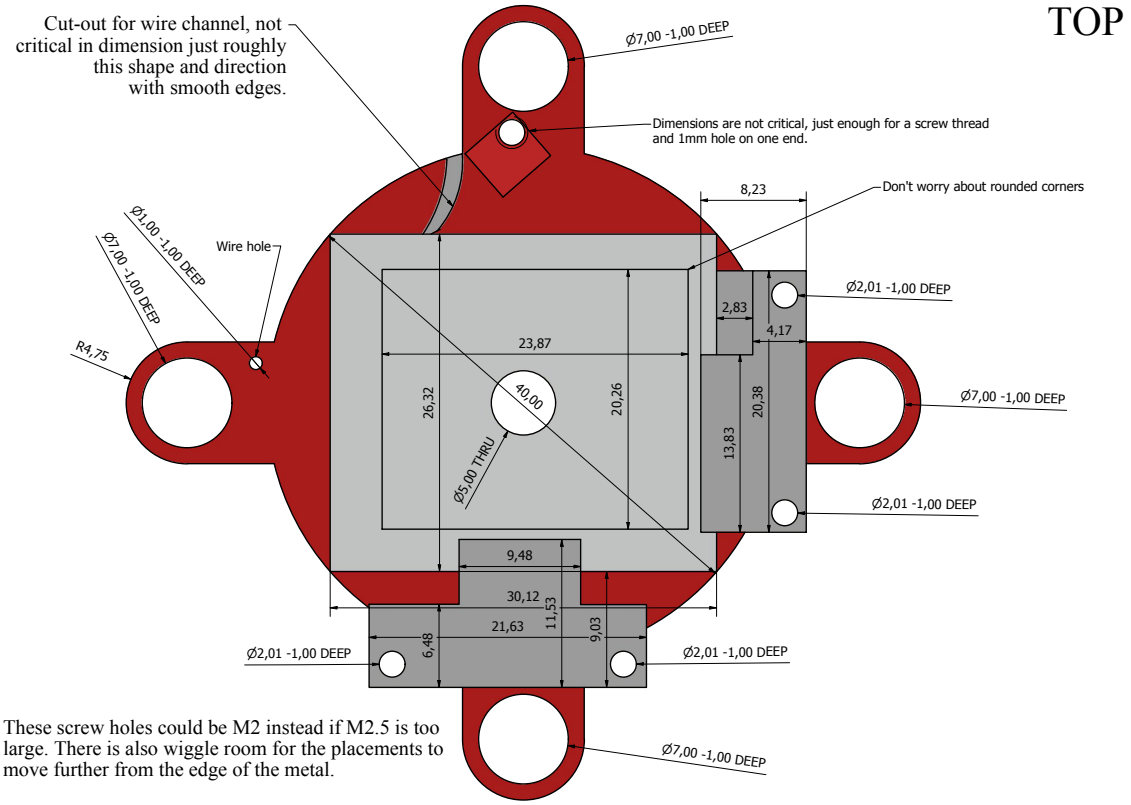

Figure C.11: Design schematic of the lower coil former and mounting mechanism.

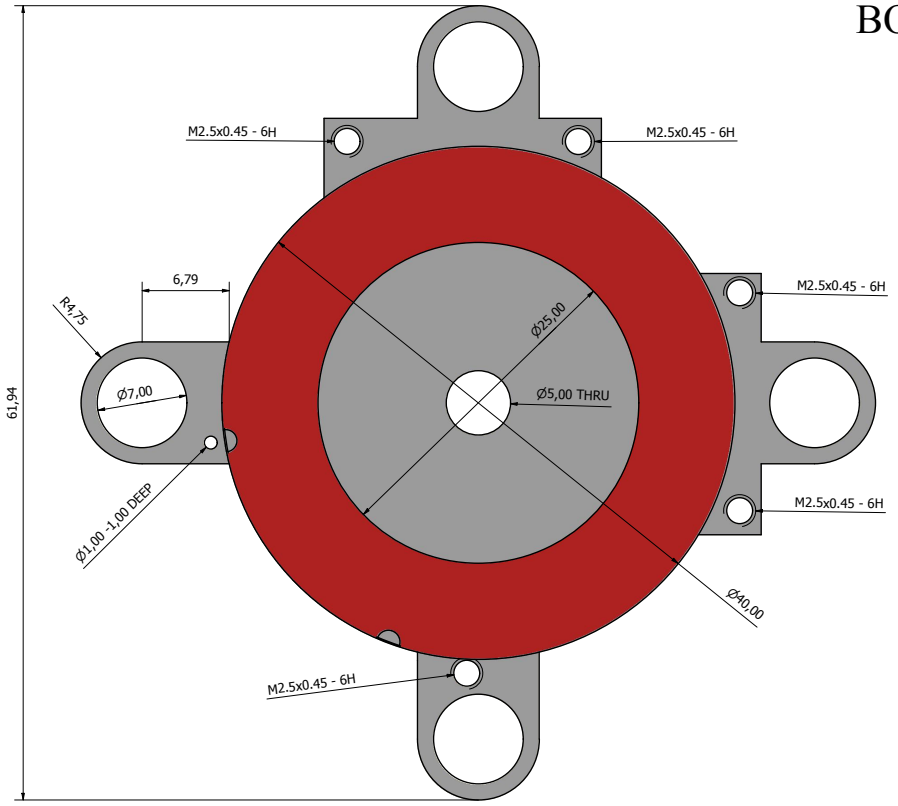

Figure C.12: Design schematic of the lower coil former with planar measurements.

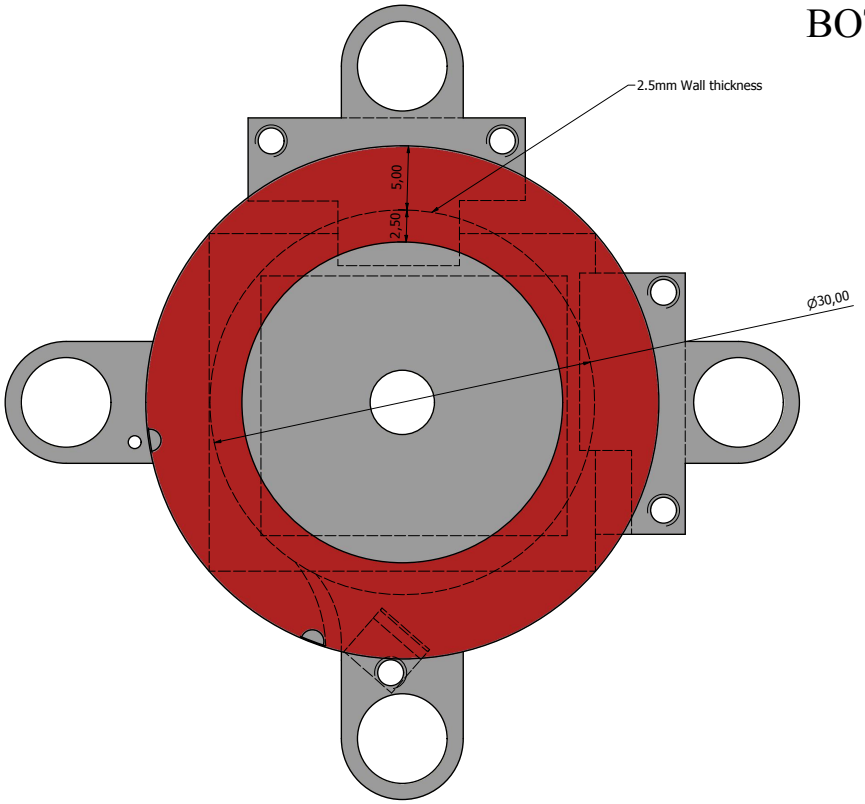

Figure C.13: Design schematic of the lower coil former with hidden measurements.

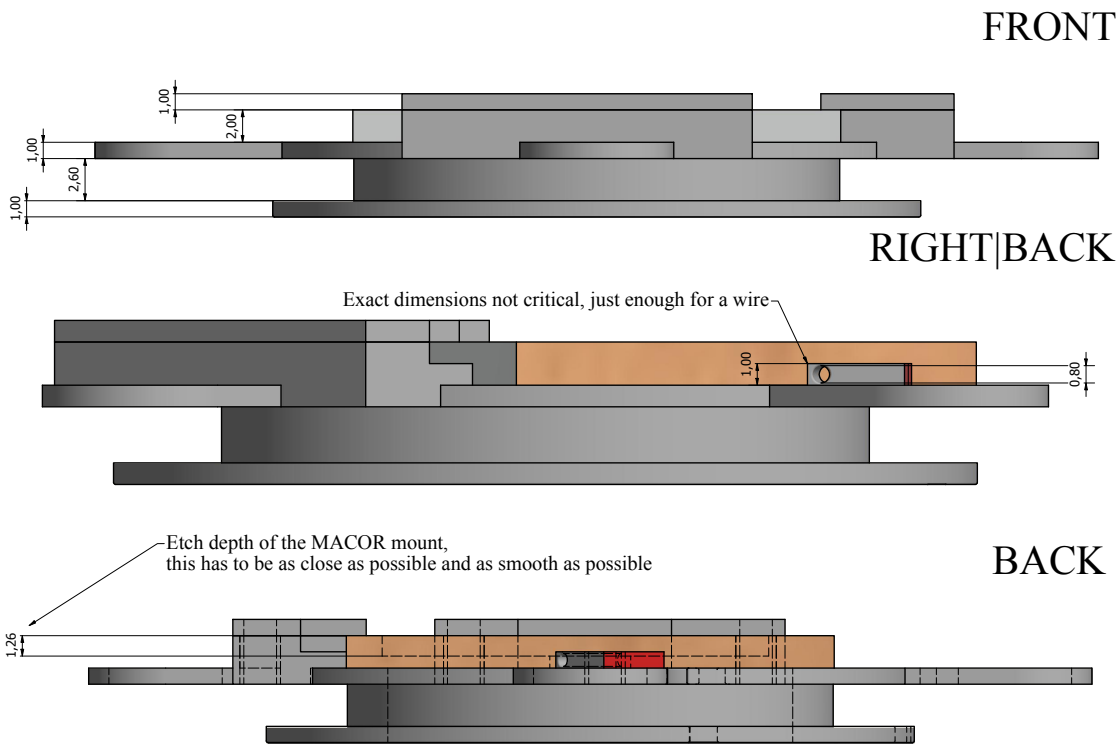

Figure C.14: Design schematic of the lower coil former with profile measurements.

Bibliography

[1] E. W. Muller and T. T. Tsong, "Field ion microscopy: Principles and applications," *Science*, vol. 169(3949), p. 970, 1970.

[2] E. W. Müller, "The field ion microscope," *EWZ Phys.*, vol. 131(1), pp. 136–142, 1951.

[3] E. W. Müller and K. Bahadur, "Field ionization of gases at a metal surface and the resolution of the field ion microscope," *Phys. Rev.*, vol. 102(3), pp. 624–631, 1956.

[4] V. Krohn and G. R. Ringo, "Secondary-ion collection system for an ion microprobe analyzer of high mass resolution," *Rev. Sci. Instr.*, vol. 43(12), pp. 1771–1772, 1972.

[5] V. Krohn and G. R. Ringo, "Ion source of high brightness using liquid metal," *Appl. Phys. Lett.*, vol. 27(9), pp. 479–481, 1975.

[6] R. L. Selinger, J. W. Ward, V. Wang, and R. L. Kubena, "A high-intensity scanning ion probe with submicrometer spot size," *Appl. Phys. Lett.*, vol. 34(5), pp. 310–312, 1979.

[7] A. Benninghoven, F. G. Rudenauer, and H. W. Werner, "Secondary ion mass spectrometry–basic concepts, instrumental aspects, applications and trends," *Surface and Interface Analysis*, vol. 10, no. 8, pp. 435–435, 1987.

[8] L. W. Swanson and G. A. Schwind, "Electron emission from a liquid metal," *J. Appl. Phys.*, vol. 49(11), p. 5655, 1978.

[9] P. D. Prewitt and G. L. R. Mair, *Focused Ion Beams from Liquid Metal Ion Sources*. John Wiley, New York, 1987.

[10] L. W. Swanson, "Liquid metal ion sources: Mechanism and applications," *Nuclear Instruments and Methods in Physics Research*, vol. 218(1-3), pp. 347–353, 1983.

[11] J. Orloff, "High-resolution focused ion beams," *Rev. Sci. Instr.*, vol. 64, p. 1105, 1993.

[12] P. W. H. de Jager and P. Kruit, "Applicability of focused ion beams for nanotechnology," *Microelectronic engineering*, vol. 27(1-4), pp. 327–330, 1995.

[13] N. P. Economou, J. A. Notte, and W. B. Thompson, "The history and development of the helium ion microscope," *Scanning*, vol. 34, p. 83, 2012.

[14] T. Hansch and A. Schawlow, "Cooling of gases by laser radiation," *Opt. Commun.*, vol. 13, pp. 68–71, 1975.

[15] D. Wineland and H. Dehmelt, "$10^{14}\delta\nu/\nu$ laser fluorescence spectroscopy on ti^{+} mono-ion oscillator," *Bull. Am. Phys. Soc.*, vol. 20, p. 637, 1975.

[16] A. Ashkin, "Trapping of atoms by resonance radiation pressure," *Phys. Rev. Lett.*, vol. 40(12), p. 729, 1978.

[17] D. J. Wineland, R. E. Drullinger, and F. L. Walls, "Radiation-pressure cooling of bound resonant absorbers," *Phys. Rev. Lett.*, vol. 40(25), pp. 1639–1642, 1978.

[18] J. E. Bjorkholm, R. R. Freeman, A. Ashkin, and D. B. Pearson, "Observation of focusing of neutral atoms by the dipole forces of resonance-radiation pressure," *Phys. Rev. Lett.*, vol. 41(20), p. 1361, 1978.

[19] S. Chu, L. Hollberg, J. Bjorkholm, A. Cable, and A. Ashkin, "Three-dimensional viscous confinement and cooling of atoms by resonance radiation pressure," *Phys. Rev. Lett.*, vol. 55, p. 48, 1985.

[20] E. Raab, M. Prentiss, A. Cable, S. Chu, and D. Pritchard, "Trapping of neutral-sodium atoms with radiation pressure," *Phys. Rev. Lett.*, vol. 59, p. 2631, 1987.

[21] W. D. Phillips, J. V. Prodan, and H. Metcalf in *Conference on Lasers and Electro-Optics*, p. TUD1, Optical Society of America, 1983.

[22] W. D. Phillips, J. V. Prodan, and H. Metcalf, "Laser cooling and electromagnetic trapping of neutral atoms," *J. Opt. Soc. Am. B*, vol. 2, pp. 1751–1767, 1985.

[23] J. Nellessen, J. Werner, and W. Ertmer, "Magneto-optical compression of a monoenergetic sodium atomic beam," *Opt. Comm.*, vol. 78(3-4), pp. 300–308, 1990.

[24] J. Mlynek, V. Balykin, and P. Meystre, "Optics and interferometry with atoms," *J. Phys. B*, vol. 54(5), pp. 319–320, 1992.

[25] C. C. Tsao, Y. Wang, J. Weiner, and V. S. Bagnato, "Optical collimation and compression of a thermal atomic beam," *J. Appl. Phys.*, vol. 80, no. 1, pp. 8–14, 1996.

[26] W. Rooijakkers, W. Hogervorst, and W. Vassen, "An intense collimated beam of metastable helium atoms by two-dimensional laser cooling," *Opt. Comm.*, vol. 123, pp. 321–330, 1996.

[27] J. G. C. Tempelaars, R. J. W. Stas, P. G. M. Sebel, H. C. W. Beijerinck, and E. J. D. Vredenbregt, "An intense, slow and cold beam of metastable Ne(3s) $3P_2$ atoms," *Eur. Phys. J. D*, vol. 18, pp. 113–121, 2002.

[28] K. Dieckmann, R. J. C. Spreeuw, M. Weidemüller, and J. T. M. Walraven, "Two-dimensional magneto-optical trap as a source of slow atoms," *Phys. Rev. A*, vol. 58, p. 3891, 1998.

[29] J. J. McClelland, R. E. Scholton, E. C. Palm, and R. J. Celotta, "Laser-focused atomic deposition," *Science*, vol. 262, no. 5135, pp. 877–880, 1993.

[30] B. G. Freinkman, A. V. Eletskii, and S. I. Zaitsev, "Laser ion beam formation for nanotechnologies," *J. Exp. Theor. Phys. Lett.*, vol. 78, p. 255, 2003.

[31] B. J. Claessens, S. B. van der Geer, G. Taban, E. J. D. Vredenbregt, and O. J. Luiten, "Ultracold electron source," *Phys. Rev. Lett.*, vol. 95, p. 164801, 2004.

[32] W. J. Engelen, E. P. Smakman, D. J. Bakker, O. J. Luiten, and E. J. D. Vredenbregt, "Effective temperature of an ultracold electron source based on near-threshold photoionization," *Ultramicroscopy*, vol. 136, pp. 73–80, 2014.

[33] G. Xia, M. Harvey, A. J. Murray, L. Bellan, W. Bertsche, R. B. Appleby, O. Mete, and S. Chattopadhyay, "An ultracold low emittance electron source," *J. Intrum.*, vol. 9, no. 06, p. P06011, 2014.

[34] J. L. Hanssen, E. A. Dakin, J. J. McClelland, and M. Jacka, "Using laser-cooled atoms as a focused ion beam source," *J. Vac. Sci. Technol. B: Microelectron. Nanom. Struct*, vol. 24, p. 2907, 2006.

[35] J. L. Hanssen, J. J. McClelland, E. A. Dakin, and M. Jacka, "Laser-cooled atoms as a focused ion-beam source," *Phys. Rev. A*, vol. 74, no. 6, p. 063416, 2006.

[36] B. J. Claessens, M. P. Reijnders, G. Taban, O. J. Luiten, and E. J. D. Vredenbregt, "Cold electron and ion beams generated from trapped atoms," *Phys. of Plasmas*, vol. 14(9), p. 093101, 2007.

[37] J. L. Hanssen, S. B. Hill, J. Orloff, and J. J. McClelland, "Magneto-optical-trap-based, high brightness ion source for use as a nanoscale probe," *Nano Lett.*, vol. 8(9), pp. 2844–2850, 2008.

[38] A. V. Steele, B. Knuffman, J. J. McClelland, and J. Orloff, "Focused chromium ion beam," *J. Vac. Sci. Tech. B*, vol. 28(6), p. C6F1, 2010.

[39] B. Knuffman, A. V. Steele, J. Orloff, and J. J. McClelland, "Nanoscale focused ion beam from laser-cooled lithium atoms," *New Journal of Phys.*, vol. 13, p. 103035, 2011.

[40] K. A. Twedt, L. Chen, and J. J. McClelland, "Scanning ion microscopy with low energy lithium ions," *Ultramicroscopy*, vol. 142, pp. 24–31, 2014.

[41] J. R. Gardner, W. R. McGehee, and J. J. McClelland, "Characterization of a high-brightness, laser-cooled Li+ ion source," *J. Appl. Phys.*, vol. 125(7), p. 074904, 2019.

[42] L. Kime, A. Fioretti, Y. Bruneau, N. Porfido, F. Fuso, M. Viteau, G. Khalili, N. Šantić, A. Gloter, B. Rasser, P. Sudraud, P. Pillet, and D. Comparat, "High-flux monochromatic ion and electron beams based on laser-cooled atoms," *Phys. Rev. A*, vol. 88, p. 033424, 2013.

[43] G. Shayeganrad, A. Fioretti, I. Guerri, F. Tantussi, D. Ciampini, M. Allegrini, M. Viteau, and F. Fuso, "Low-energy ions from laser-cooled atoms," *Phys. Rev. Appl.*, vol. 5, p. 054020, 2016.

[44] D. Murphy, R. W. Speirs, D. V. Sheludko, C. T. Putkunz, A. J. McCulloch, B. M. Sparkes, and R. E. Scholten, "Detailed observation of space–charge dynamics using ultracold ion bunches," *Nat. Comm.*, vol. 5, p. 4489, 2014.

[45] D. Murphy, R. Scholten, and B. Sparkes, "Increasing the brightness of cold ion beams by suppressing disorder-induced heating with rydberg blockade," *Phys. Rev. Lett.*, vol. 115, p. 214802, 2015.

[46] B. M. Sparkes, D. Murphy, R. J. Taylor, R. W. Speirs, A. J. McCulloch, and R. E. Scholten, "Stimulated raman adiabatic passage for improved performance of a cold-atom electron and ion source," *Phys. Rev. A*, vol. 94, p. 023404, 2016.

[47] D. Thompson, D. Murphy, R. Speirs, R. van Bijnen, A. McCulloch, R. Scholten, and B. Sparkes, "Suppression of emittance growth using a shaped cold atom electron and ion source," *Phys. Rev. Lett.*, vol. 117, p. 193202, 2016.

[48] A. J. McCulloch, R. W. Speirs, J. Grimmel, B. M. Sparkes, D. Comparat, and R. E. Scholten, "Field ionization of rydberg atoms for high-brightness electron and ion beams," *Phys. Rev. A*, vol. 95, p. 063845, 2017.

[49] A. J. McCulloch, R. W. Speirs, S. H. Wissenberg, R. P. M. Tielen, B. M. Sparkes, and R. E. Scholten, "Heralded ions via ionization coincidence," *Phys. Rev. A*, vol. 97, p. 043423, 2018.

[50] M. Viteau, P. Huillery, M. G. Bason, N. Malossi, D. Ciampini, O. Morsch, E. Arimondo, D. Comparat, and P. Pillet, "Cooperative excitation and many-body interactions in a cold rydberg gas," *Phys. Rev. Lett.*, vol. 109(5), p. 053002, 2012.

[51] E. Moufarej, M. Vielle-Grosjean, G. Khalili, A. J. McCulloch, F. Robicheaux, Y. J. Picard, and D. Comparat, "Forced field ionization of rydberg states for the production of monochromatic beams," *Phys. Rev. A*, vol. 95, p. 043409, 2017.

[52] M. Delobbe, M. Reveillard, M. Viteau, A. Houel, and D. Comparat, "Coldfib - the new fib source from laser cooled atoms," *Procee. Microsc. Microanal.*, vol. 24(S1), pp. 804–805, 2018.

[53] C. Lopez, A. Trimeche, D. Comparat, and Y. Picard, "Real-time trajectory control of deterministically produced ions," *Phys. Rev. Appl.*, vol. 11(6), p. 064049, 2019.

[54] M. Harvey, J. Agomuo, A. Sakaamini, and A. Murray, "Studying cold potassium rydberg atoms with an ac-mot," *IOP Conf. Series: J. Phys.: Conf. Series*, vol. 875, p. 022046, 2016.

[55] B. Knuffman, A. V. Steele, and J. J. McClelland, "Cold atomic beam ion source for focused ion beam applications," *J. Appl. Phys.*, vol. 114(4), p. 044303, 2013.

[56] N. S. Smith, J. A. Notte, and A. V. Steele, "Advances in source technology for focused ion beam instruments," *MRS Bull.*, vol. 39(4), pp. 329–335, 2014.

[57] A. V. Steele, A. Schwarzkopf, J. J. McClelland, and B. Knuffman, "High-brightness Cs focused ion beam from a cold-atomic-beam ion source," *Nano Futures*, vol. 1(1), p. 015005, 2017.

[58] G. ten Haaf, S. H. W. Wouters, D. F. J. Nijhof, P. H. A. Mutsaers, and E. J. D. Vredenbregt, "Measurements of the energy distribution of a high brightness rubidium ion beam," *Ultramicroscopy*, vol. 190, pp. 12–20, 2018.

[59] J. P. McGilligan, P. F. Griffin, E. Riis, and A. S. Arnold, "Phase-space properties of magneto-optical traps utilising micro-fabricated gratings.," *Opt. Express*, vol. 23, pp. 8948–8959, Apr 2015.

[60] J. Franssen, T. de Raadt, M. van Ninhuijs, and O. Luiten, "Compact ultracold electron source based on a grating magneto-optical trap," *Phys. Rev. Accel. Beams*, vol. 22, p. 023401, 2019.

[61] J. Lee, J. A. Grover, L. A. Orozco, and S. L. Rolston, "Sub-doppler cooling of neutral atoms in a grating magneto-optical trap," *J. Opt. Soc. Am. B*, vol. 30, no. 11, pp. 2869–2874, 2013.

[62] E. Imhof, B. K. Stuhl, B. Kasch, B. Kroese, S. E. Olson, and M. Squires, "Two-dimensional grating magneto-optical trap," *Phys. Rev. A*, vol. 96, p. 033636, 2017.

[63] D. S. Barker, E. B. Norrgard, N. N. Klimov, J. A. Fedchak, J. Scherschligt, and S. Eckel, "Single-beam zeeman slower and magneto-optical trap using a nanofabricated grating," *Phys. Rev. A*, vol. 11(6), 2019.

[64] D. J. Reed, N. Šibalić, D. J. Whiting, J. M. Kondo, C. S. Adams, and K. J. Weatherill, "Low-drift zeeman shifted atomic frequency reference," *OSA Continuum*, vol. 1, pp. 4–12, Sep 2018.

[65] D. Wineland and W. Itano, "Laser cooling of atoms," *Phys. Rev. A*, vol. 20, pp. 1521–1540, 1979.

[66] C. J. Foot, *Atomic Physics*. Oxford Master Series In Atomic, Optical, and Laser Physics, Oxford University Press, 12 ed., 2014.

[67] H. J. Metcalf and P. van der Straten, *Laser Cooling and Trapping*. Graduate Texts in Contemporary Physics, Springer-Verlag New York, Inc., 2 ed., 2002.

[68] P. Meystre and S. S. (Eds.), "The mechanical effects of light," *J. Opt. Soc. Am. B*, vol. 2, pp. 1705–1872, 1985.

[69] S. Chu and C. W. (Eds.), "Laser cooling and trapping of atoms," *J. Opt. Soc. Am. B*, vol. 6, pp. 1961–2288, 1989.

[70] W. Phillips and H. Metcalf, "Laser deceleration of an atomic beam," *Phys. Rev. Lett.*, vol. 48, p. 596, 1982.

[71] J. Prodan, W. Phillips, and H. Metcalf, "Laser production of a very slow monoenergetic atomic beam," *Phys. Rev. Lett.*, vol. 49, p. 1149, 1982.

[72] J. Dalibard and W. Phillips, "Stability and damping of radiation pressure traps," *Bull. Am. Phys. Soc.*, vol. 30, p. 748, 1985.

[73] J. Prodan and W. Phillips, "Chirping the light fantastic - recent nbs atom cooling experiments," *Prog. Quant. Elect.*, vol. 8, p. 231, 1984.

[74] R. Watts and C. Wieman, "Manipulating atomic velocities using diode lasers," *Opt. Lett.*, vol. 11, p. 291, 1986.

[75] A. Pratt, A. Roskoss, H. Mènard, and M. Jacka, "Improved metastable de-excitation spectrometer using laser-cooling techniques," *Rev. Sci. Instrum.*, vol. 76, p. 053102, 2005.

[76] P. Lett, R. Watts, C. Westbrook, W. Phillips, P. Gould, and H. Metcalf, "Observation of atoms cooled below the doppler limit," *Phys. Rev. Lett.*, vol. 61, p. 169, 1988.

[77] H. Metcalf, "Magneto-optical trapping and its application to helium metastables," *J. Opt. Soc. Am. B*, vol. 6, pp. 2206–2210, 1989.

[78] K. Lindquist, M. Stephens, and C. Wieman, "Experimental and theoretical study of the vapor-cell zeeman optical trap," *Phys. Rev. A*, vol. 46(7), p. 4082, 1992.

[79] P. D. Lett, W. D. Phillips, S. L. Rolston, C. E. Tanner, R. N. Watts, and C. I. Westbrook, "Optical molasses," *J. Opt. Soc. Am. B*, vol. 6, pp. 2084–2107, 1989.

[80] J. J. Waterson and J. W. Strutt, "On the physics of media that are composed of free and perfectly elastic molecules in a state of motion," *Phil. Trans. Roy. Soc. A*, vol. 183, pp. 1–79, 1892.

[81] T. Walker, D. Sesko, and C. Wieman, "Collective behavior of optically trapped neutral atoms," *Phys. Rev. Lett.*, vol. 64(4), p. 408, 1990.

[82] K. I. Lee, J. A. Kim, H. R. Noh, and W. Jhe, "Single-beam atom trap in a pyramidal and conical hollow mirror," *Opt. Lett.*, vol. 21(15), pp. 1177–1179, 1996.

[83] J. J. Arlt, O. Maragò, S. Webster, S. Hopkins, and C. J. Foot, "A pyramidal magneto-optical trap as a source of slow atoms," *Opt. Comm.*, vol. 157(1-6), pp. 303–309, 1998.

[84] J. Reichel, W. Hänsel, and T. W. Hänsch, "Atomic micromanipulation with magnetic surface traps," *Phys. Rev. Lett.*, vol. 83, p. 3398, 1999.

[85] R. Folman, P. Krüger, D. Cassettari, B. Hessmo, T. Maier, and J. Schmiedmayer, "Controlling cold atoms using nanofabricated surfaces: Atom chips," *Phys. Rev. Lett.*, vol. 84, p. 4749, 2000.

[86] E. A. Hinds and I. G. Hughes, "Magnetic atom optics: mirrors, guides, traps, and chips for atoms," *J. Phys. D. Appl. Phys.*, vol. 32(18), p. R119, 1999.

[87] M. Vangeleyn, P. F. Griffin, E. Riis, and A. S. Arnold, "Single-laser, one beam, tetrahedral magneto-optical trap," *Opt. Express*, vol. 17, pp. 13601–13608, Aug 2009.

[88] M. Vangeleyn, P. F. Griffin, E. Riis, and A. S. Arnold, "Laser cooling with a single laser beam and a planar diffractor," *Opt. Lett.*, vol. 35, pp. 3453–3455, Oct 2010.

[89] C. C. Nshii, M. Vangeleyn, J. P. Cotter, P. F. Griffin, E. A. Hinds, C. N. Ironside, P. See, A. G. Sinclair, and A. S. Arnold, "A surface-patterned chip as a strong source of ultracold atoms for quantum technologies," *Nature Nanotechnology*, vol. 8, p. 321, April 2013.

[90] J. P. Cotter, J. P. McGilligan, P. F. Griffin, I. M. Rabey, K. Docherty, E. Riis, A. S. Arnold, and E. A. Hinds, "Design and fabrication of diffractive atom chips for laser cooling and trapping," *Applied Physics B*, vol. 122, p. 172, Jun 2016.

[91] J. P. McGilligan, P. F. Griffin, E. Riis, and A. S. Arnold, "Diffraction-grating characterization for cold-atom experiments," *J. Opt. Soc. Am. B*, vol. 33, pp. 1271–1277, Jun 2016.

[92] J. P. McGilligan, P. F. Griffin, R. Elvin, S. J. Ingleby, E. Riis, and A. S. Arnold, "Grating chips for quantum technologies," *Scientific Reports*, vol. 7, March 2017.

[93] J. P. McGilligan, *Micro-fabricated Diffractive Optics for Quantum Sensors and Atomic Clocks*. PhD thesis, University of Strathclyde, August 2017.

[94] C. A. Palmer and E. G. Loewen, "Diffraction grating handbook," *Newport Corporation*, 2005.

[95] D. W. Sesko, T. G. Walker, and C. E. Wieman, "Behavior of neutral atoms in a spontaneous force trap," *J. Opt. Soc. Am. B*, vol. 8, pp. 946–958, 1991.

[96] W. Ketterle, K. B. Davis, M. A. Joffe, A. Martin, and D. E. Pritchard, "High densities of cold atoms in a dark spontaneous force optical trap," *Phys. Rev. Lett.*, vol. 70, pp. 2253–2256, 1993.

[97] A. S. Arnold and P. J. Manson, "Atomic density and temperature distributions in magneto-optical traps," *J. Opt. Soc. Am. B*, vol. 17, pp. 497–506, 2000.

[98] N. Radwell, G.Walker, and S. Franke-Arnold, "Cold-atom densities of more than 10^{12} cm^3 in a holographically shaped dark spontaneous-force optical trap," *Phys. Rev. A*, vol. 88, p. 043409, 2013.

[99] I. S. Grant and W. R. Phillips, *Electromagnetism (2nd Edition)*. John Wiley & Sons, 2013.

[100] P. M. Bersier, J. Howell, and C. Bruntlett, "Tutorial review. advanced electroanalytical techniques versus atomic absorption spectrometry, inductively coupled plasma atomic emission spectrometry and inductively coupled plasma mass spectrometry in environmental analysis," *Analyst*, vol. 119(2), pp. 219–232, 1994.

[101] H.-K. Kim, J. W. Bae, T.-K. Kim, K.-K. Kim, T.-Y. Seong, and I. Adesida, "Inductively coupled plasma reactive ion etching of zno using bcl_3-based plasmas," *J. Vac. Sci. Tech. B*, vol. 21, p. 1273, 2003.

[102] K. J. Kanarik, T. Lill, E. A. Hudson, S. Sriraman, S. Tan, J. Marks, V. Vahedi, and R. A. Gottscho, "Overview of atomic layer etching in the semiconductor industry," *J. Vac. Sci. Technol. A*, vol. 33, p. 020802, 2015.

[103] J. Melngailis, "Focused ion beam technology and applications," *J. Vac. Sci. Technol. B*, vol. 5, p. 469, 1987.

[104] K. Gamo, "Focused ion beam technology," *Vacuum*, vol. 42, p. 89, 1991.

[105] S. Reyntjens and R. Puers, "A review of focused ion beam applications in microsystem technology," *J. Micromechanics Microengineering*, vol. 11, p. 287, 2001.

[106] M. Sugiyama and G. Sigesato, "A review of focused ion beam technology and its applications in transmission electron microscopy," *J. Electron Microsc. (Tokyo)*, vol. 53, p. 527, 2001.

[107] A. A. Tseng, "Recent developments in micromilling using focused ion beam technology," *J. Micromech. Microeng.*, vol. 14(4), pp. R15–R34, 2004.

[108] J. Gierak, "Focused ion beam technology and ultimate applications," *Semicond. Sci. Technol.*, vol. 24, p. 043001, 2009.

[109] J. E. E. Baglin, "Ion beam nanoscale fabrication and lithography—a review," *Appl. Surf. Sci.*, vol. 258, p. 4103, 2012.

[110] C.-S. Kim, S.-H. Ahn, and D.-Y. Jang, "Review: Developments in micro/nanoscale fabrication by focused ion beams," *Vacuum*, vol. 86, p. 1014, 2012.

[111] N. Bassim, K. Scott, and L. Giannuzzi, "Recent advances in focused ion beam technology and applications," *MRS Bull.*, vol. 39, no. 4, pp. 317–325, 2014.

[112] N. Yao, *Focused ion beam systems: basics and applications*. Cambridge University Press, 2007.

[113] L. A. Giannuzzi *et al.*, *Introduction to focused ion beams: instrumentation, theory, techniques and practice*. Springer Science & Business Media, 2004.

[114] A. Karmous, A. Cuenat, A. Ronda, I. Berbezier, S. Atha, and R. Hull, "Fabrication of a gaas quantum-well-wire structure by ga focused-ion-beam implantation and its optical properties," *Appl. Phys. Lett.*, vol. 85(26), p. 6401, 2004.

[115] W. M. C. Jr., R. L. Seliger, M. W. Utlaut, A. E. Bell, L. W. Swanson, G. A. Schwind, and J. B. Jergenson, "Long-lifetime, reliable liquid metal ion sources for boron, arsenic, and phosphorus," *J. Vac. Sci. Technol. B*, vol. 5(1), pp. 197–202, 1987.

[116] Y. Hirayama, S. Tarucha, Y. Suzuki, and H. Okamoto, "Fabrication of a gaas quantum-well-wire structure by ga focused-ion-beam implantation and its optical properties," *Phys. Rev. B*, vol. 37(5), p. 2774, 1987.

[117] P. Heard, J. Cleaver, and H. Ahmed, "Application of a focused ion beam system to defect repair of vlsi masks," *J. Vac. Sci. Technol. B*, vol. 3(1), pp. 87–90, 1985.

[118] H. A. Storms, K. F. Brown, and J. D. Stein, "Evaluation of a cesium positive ion source for secondary ion mass spectrometry," *Anal. Chem.*, vol. 49(13), pp. 2023–2030, 1977.

[119] J. C. Vickerman, A. Brown, and N. M. Reed, *Secondary Ion Mass Spectrometry: Principles and Applications*. (Oxford University Press), 1990.

[120] L. Scipioni, L. A. Stern, J. Notte, S. Sijbrandij, and B. Griffin, "Helium ion microscope," *Adv. Mater. Process.*, vol. 166(6), pp. 27–30, 2008.

[121] H. H. Brongersma, M. Draxler, M. de Ridder, and P. Bauer, "Surface composition analysis by low-energy ion scattering," *Surf. Sci. Rep.*, vol. 62(3), pp. 63–109, 2007.

[122] M. Reiser, *Theory and design of charged particle beams*. John Wiley & Sons, 2008.

[123] H. Goldstein, C. P. P. Jr, and J. L. Safko, *Classical Mechanics*. Addison-Wesley, San Francisco, 2001.

[124] P. W. Hawkes and E. Kasper, *Principles of Electron Optics, Volume 1: Basic Geometrical Optics*. Academic Press, San Diego, 1989.

[125] J. F. Barth and P. Kruit, "Addition of different contributions to the charged particle probe size," *Optik*, vol. 101, pp. 101–109, 1996.

[126] Y. Wang and Z. Shao, "Design principles of an optimized focused ion beam system," *Adv. Electron. Electron Phys. Suppl.*, vol. 81, pp. 177–209, 1991.

[127] A. Wagner, "The hydrodynamics of liquid metal ion sources," *Appl. Phys. Lett.*, vol. 40(5), p. 440, 1982.

[128] J. Orloff and L. W. Swanson, "Study of a field-ionization source for microprobe applications," *J. Vac. Sci. Technol. B*, vol. 12, p. 1209, 1975.

[129] B. W. Ward, J. A. Notte, and N. P. Economou, "Helium ion microscope: A new tool for nanoscale microscopy and metrology," *J. Vac. Sci. Technol. B*, vol. 24(6), p. 2871, 2006.

[130] F. H. M. Rahman, S. McVey, L. Farkas, J. A. Notte, S. Tan, and R. H. Livengood, "The prospects of a subnanometer focused neon ion beam," *Scanning*, vol. 34(2), pp. 129–134, 2012.

[131] J. L. Hanssen, S. B. Hill, J. Orloff, and J. J. McClelland, "Magneto-optical-trap-based, high brightness ion source for use as a nanoscale probe," *Nano Lett.*, vol. 8(9), pp. 2844–2850, 2008.

[132] J. J. McClelland, A. V. Steele, B. Knuffman, K. A. Twedt, A. Schwarzkopf, and T. M. Wilson, "Bright focused ion beam sources based on laser-cooled atoms," *Appl Phys Rev.*, vol. 3(1), p. 011302, 2016.

[133] M. P. Reijnders, P. A. van Kruisbergen, G. Taban, S. B. van der Geer, P. H. A. Mutsaers, E. J. D. Vredenbregt, and O. J. Luiten, "Low-energy-spread ion bunches from a trapped atomic gas," *Phys. Rev. Lett.*, vol. 102, p. 034802, 2009.

[134] M. P. Reijnders, N. Debernardi, S. B. van der Geer, P. H. A. Mutsaers, E. J. D. Vredenbregt, and O. J. Luiten, "Phase-space manipulation of ultracold ion bunches with time-dependent fields," *Phys. Rev. Lett.*, vol. 105, p. 034802, 2010.

[135] M. P. Reijnders, N. Debernardi, S. B. van der Geer, P. H. A. Mutsaers, E. J. D. Vredenbregt, and O. J. Luiten, "Time-dependent manipulation of ultracold ion bunches," *J. Appl. Phys.*, vol. 109, p. 033302, 2011.

[136] N. Debernardi, R. W. L. van Vliembergen, W. J. Engelen, K. H. M. Hermans, M. P. Reijnders, S. B. van der Geer, P. H. A. Mutsaers, O. J. Luiten, and E. J. D. Vredenbregt, "Optimization of the current extracted from an ultracold ion source," *New J. Phys.*, vol. 14, p. 083011, 2012.

[137] S. B. Hill and J. J. McClelland, "Atoms on demand: Fast, deterministic production of single cr atoms," *Appl. Phys. Lett.*, vol. 82(18), p. 3128, 2003.

[138] B. Knuffman, A. V. Steele, J. Orloff, and J. J. McClelland, "Nanoscale focused ion beam from laser-cooled lithium atoms," *New J. Phys.*, vol. 13(10), p. 103035, 2011.

[139] S. H. W. Wouters, G. ten Haaf, R. P. M. J. W. Notermans, N. Debernardi, P. H. A. Mutsaers, O. J. Luiten, and E. J. D. Vredenbregt, "Performance pre-

dictions for a laser-intensified thermal beam for use in high-resolution focused-ion-beam instruments," *Phys. Rev. A*, vol. 90, p. 063817, 2014.

[140] M. Viteau, M. Reveillard, L. Kime, B. Rasser, P. Sudraud, Y. Bruneau, G. Khalili, P. Pillet, D. Comparat, I. Guerri, A. Fioretti, D. Ciampini, M. Allegrini, and F. Fuso, "Ion microscopy based on laser-cooled cesium atoms," *Ultramicroscopy*, vol. 164, pp. 70–77, 2016.

[141] S. B. van der Geer, M. P. Reijnders, M. J. de Loos, E. J. D. Vredenbregt, P. H. A. Mutsaers, and O. J. Luiten, "Simulated performance of an ultracold ion source," *J. Appl. Phys.*, vol. 102(9), p. 094312, 2007.

[142] A. V. Steele, B. Knuffman, and J. J. McClelland, "Inter-ion coulomb interactions in a magnetooptical trap ion source," *Appl. Phys.*, vol. 109, p. 104308, 2011.

[143] J. M. Maxson, I. V. Bazarov, W. Wan, H. A. Padmore, and C. E. Coleman-Smith, "Fundamental photoemission brightness limit from disorder induced heating," *New J. Phys.*, vol. 15(10), p. 103024, 2013.

[144] G. ten Haaf, S. H. W. Wouters, S. B. van der Geer, E. J. D. Vredenbregt, and P. H. A. Mutsaers, "Performance predictions of a focused ion beam from a laser cooled and compressed atomic beam," *J. Appl. Phys.*, vol. 116(24), p. 244301, 2014.

[145] G. ten Haaf, T. C. H. de Raadt, G. P. Offermans, J. F. M. van Rens, P. H. A. Mutsaers, E. J. D. Vredenbregt, and S. H. W. Wouters, "Direct magneto-optical compression of an effusive atomic beam for high-resolution focused ion beam application," *Phys. Rev. Appl.*, vol. 7(5), p. 054013, 2017.

[146] J. F. Walker, J. C. Reiner, and C. Solenthaler, "Focused ion beam sample preparation for tem," *Proc. Microsc. Semicond. Mater. Conf.*, vol. 146, pp. 629–634, 1995.

[147] D. Comparat and P. Pillet, "Dipole blockade in a cold rydberg atomic sample," *J. Opt. Soc. Am. B*, vol. 27(6), pp. A208–A232, 2010.

[148] J. Gierak, A. Septier, and C. Vieu, "Design and realization of a very high-resolution fib nanofabrication instrument," *Nucl. Instr. and Methods in Phys. Res. Sec. A: Accel., Spectro., Detect. and Assoc. Equip.*, vol. 427(1.2), pp. 91–98, 1999.

[149] G. D. Alton and P. M. Read, "Emittance measurements of gallium liquid-metal ion sources," *Nucl. Instr. and Methods in Phys. Res. Sec B: Beam Interactions with Materials and Atoms*, vol. 54.1(3), pp. 7–11, 1991.

[150] D. A. Steck, "Cesium d line data." available online at http://steck.us/alkalidata (revision 2.1.4, 23 December 2010).

[151] V. Gerginov, A. Derevianko, and C. E. Tanner, "Observation of the Nuclear Magnetic Octupole Moment of ^{133}Cs," *Phys. Rev. Lett.*, vol. 91, p. 072501, 2003.

[152] E. Arimondo, M. Inguscio, and P. Violino, "Experimental determinations of the hyperfine structure in the alkali atoms," *Rev. Mod. Phys.*, vol. 49, p. 31, 1989.

[153] M. S. Safronova, W. R. Johnson, and A. Derevianko, "Relativistic many-body calculations of energy levels, hyperfine constants, electric-dipole matrix elements, and static polarizabilities for alkali-metal atoms.," *Phys. Rev. A*, vol. 60, no. 6, p. 4476, 1999.

[154] N. Šibalić, J. D. Pritchard, C. S. Adams, and K. J.Weatherill, "Arc: An open-source library for calculating properties of alkali rydberg atoms," *Comput. Phys. Commun.*, vol. 220, p. 319, 2017.

[155] W. Demtröder, *Laser Spectroscopy.* (Springer-Verlag,1981), 1981.

[156] J. L. Hall, M. S. Taubman, and J. Ye, *Laser stabilisation.* (McGraw-Hill,2001), 2001.

[157] C. E. Wieman and L. Hollberg, "Using diode lasers for atomic physics," *Rev. Sci. Instrum.*, vol. 62(1), pp. 1–20, 1991.

[158] T. W. Hänsch, A. L. Schawlow, and G. W. Series, "The spectrum of atomic hydrogen," *Sci. Am.*, vol. 240(72), pp. 94–111, 1979.

[159] M. D. Levenson, *Introduction to Nonlinear Laser Spectroscopy.* (Academic Press, 1982), 1982.

[160] C. P. Pearman, C. S. Adams, S. G. Cox, P. F. Griffin, D. A. Smith, and I. G. Hughes, "Polarization spectroscopy of a closed atomic transition: applications to laser frequency locking," *J. Phys. B*, vol. 35, p. 5141, 2002.

[161] M. L. Harris, C. S. Adams, S. L. Cornish, I. C. McLeod, E. Tarleton, and I. G. Hughes, "Polarization spectroscopy in rubidium and cesium," *Phys. Rev. A*, vol. 73(6), p. 062509, 2006.

[162] A. Millett-Sikking, I. G. Hughes, P. Tierney, and S. L. Cornish, "DAVLL lineshapes in atomic rubidium," *J. Phys. B*, vol. 40(1), p. 187, 2006.

[163] K. L. Corwin, C. F. H. Z. Lu, R. J. Epstein, and C. E.Wieman, "Frequency-stabilized diode laser with the zeeman shift in an atomic vapor," *Appl. Opt.*, vol. 37, pp. 3295–3298, 1998.

[164] S. Balushev, N. Friedman, L. Khaykovich, D. Carasso, B. Johns, and N. Davidson, "Tunable and frequency-stabilized diode laser with a doppler-free two-photon zeeman lock," *Appl. Opt.*, vol. 39(27), pp. 4970–4974, 2000.

[165] J. H. Shirley, "Modulation transfer processes in optical heterodyne saturation spectroscopy," *Opt. Lett.*, vol. 7, pp. 537–539, 1982.

[166] D. J. McCarron, S. A. King, and S. L. Cornish, "Modulation transfer spectroscopy in atomic rubidium," *Meas. Sci. Technol.*, vol. 19(10), p. 105601, 2008.

[167] G. C. Bjorklund, "Frequency-modulation spectroscopy: a new method for measuring weak absorptions and dispersions," *Opt. Lett.*, vol. 5(1), pp. 15–17, 1980.

[168] J. L. Hall, L. Hollberg, T. Baer, and H. G. Robinson, "Optical heterodyne saturation spectroscopy," *Appl. Phys. Lett.*, vol. 39, p. 680, 1981.

[169] G. C. Bjorklund, M. D. Levenson, W. Lenth, and C. Ortiz, "Frequency modulation (fm) spectroscopy; theory of lineshapes and signal-to-noise analysis," *Appl. Phys. B*, vol. 32(3), pp. 145–152, 1983.

[170] R. P. Abel, A. K. Mohapatra, M. G. Bason, J. D. Pritchard, K. J. Weatherill, U. Raitzsch, and C. S. Adams, "Laser frequency stabilization to excited state transitions using electromagnetically induced transparency in a cascade system," *Appl. Phys. Lett.*, vol. 94(7), p. 071107, 2009.

[171] C. Carr, M. Tanasittikosol, A. Sargsyan, D. Sarkisyan, C. S. Adams, and K. J. Weatherill, "Three-photon electromagnetically induced transparency using rydberg states," *Opt. Lett.*, vol. 37(18), pp. 3858–3860, 2012.

[172] J. M. Kondo, N. Šibalić, A. Guttridge, C. G. Wade, N. R. D. Melo, C. S. Adams, and K. J. Weatherill, "Observation of interference effects via four-photon excitation of highly excited rydberg states in thermal cesium vapor," *Opt. Lett.*, vol. 40, pp. 5570–5573, 2015.

[173] A. L. Schawlow, "Spectroscopy in a new light," *Rev. Mod. Phys.*, vol. 54(3), pp. 697–707, 1982.

[174] N. Bloembergen, "Nonlinear optics and spectroscopy," *Rev. Mod. Phys.*, vol. 54(3), pp. 685–695, 1982.

[175] D. A. Smith and I. G. Hughes, "The role of hyperfine pumping in multilevel systems exhibiting saturated absorption," *Am. J. Phys.*, vol. 72, p. 631, 2004.

[176] D. W. Preston, "Doppler-free saturated absorption: Laser spectroscopy," *Am. J. Phys.*, vol. 64(11), pp. 1432–1436, 1996.

[177] A. Siegman, *Lasers*. University Science Books, 1986.

[178] K. B. MacAdam, A. Steinbach, and C. Wieman, "A narrow-band tunable diode laser system with grating feedback, and a saturated absorption spectrometer for cs and rb," *Am. J. Phys.*, vol. 60, p. 1098, 1992.

[179] C. Wieman and T. Hänsch, "Doppler-free laser polarization spectroscopy," *Phys. Rev. Lett.*, vol. 36, p. 11170, 1976.

[180] R. E. Teets, F. V. Kowalski, W. T. Hill, N. Carlson, and T. W. Hänsch, "Laser polarization spectroscopy," *Proc. SPIE 0113*, vol. Advances in Laser Spectroscopy I, 1977.

[181] B. Cheron, H. Gilles, J. Hamel, and O. Moreau, "Laser frequency stabilization using zeeman effect," *J. Phys. III France*, vol. 4, pp. 401–406, 1994.

[182] V. Yashchuk, D. Budker, and J. Davis, "Laser frequency stabilization using linear magneto-optics: Technical notes," *REPORT LBNL*, vol. 43523, 1999.

[183] C. Carr, C. S. Adams, and K. J. Weatherill, "Polarisation spectroscopy of an excited state transition," *Opt. Lett.*, vol. 37, pp. 118–120, 2012.

[184] N. Šibalić, *Rydberg atom ensembles under dephasing and dissipation: from single- to many-body dynamics*. PhD thesis, University of Durham, 2017.

[185] R. W. Fox, C. W. Oates, and L. W. Hollberg, "1. stabilizing diode lasers to high-finesse cavities," *Exp. Meth. Phys. Sci.*, vol. 40, pp. 1–46, 2003.

[186] T. W. Hänsch and B. Couillard, "Laser frequency stabilization by polarisation spectroscopy of a reflecting reference cavity," *Opt. Commun.*, vol. 35, pp. 441–444, 1980.

[187] P. M. T. Barboza, G. G. Nascimento, M. O. Araújo, C. M. da Silva, H. L. D. de S. Calvalcante, M. Oriá, M. Chevrollier, and T. P. de Silans, "Stabilization of a laser on a large-detuned atomic-reference frequency by resonant interferometry," *J. Phys. B*, vol. 49(8), p. 085401, 2016.

[188] U. Schünemann, H. Engler, R. Grimm, M.Weidemüller, and M. Zielonkowski, "Simple scheme for tunable frequency offset locking of two lasers," *Rev. Sci. Instrum.*, vol. 70(1), pp. 242–243, 1993.

[189] F. Friederich, G. Schuricht, A. Deninger, F. Lison, G. Spickermann, P. H. Bolívar, and H. G. Roskos, "Phase-locking of the beat signal of two distributed-feedback diode lasers to oscillators working in the mhz to thz range," *Opt. Express*, vol. 18(8), pp. 8621–8629, 2010.

[190] W. Li, X. Pan, N. Song, X. Xu, and X. Lu, "A phase-locked laser system based on modulation technique for atom interferometry," *Appl. Phys. B*, vol. 123, 07 2017.

[191] J. L. Gouët, J. Kim, C. Bourassin-Boucheta, M. Loursa, A. Landragina, and F. P. D. Santosa, "Wide bandwidth phase-locked diode laser with an intra-cavity electro-optic modulator," *Opt. Commun.*, vol. 282(5), pp. 977–980, 2009.

[192] Y. Huang, Y. Guan, T. Suen, J. Shy, and L.Wang, "Absolute frequency measurement of the molecular iodine hyperfine transitions at 647 nm," *Appl. Opt.*, vol. 57, pp. 2102–2106, 2018.

[193] P. A. Jungner, S. Swartz, M. Eickhoff, J. Ye, J. L. Hall, and S. Waltman, "Absolute frequency of the molecular iodine transition r (56) 32-0 near 532 nm," *IEEE Trans. Instrum. Meas.*, vol. 44(2), pp. 151–154, 1995.

[194] Y. W. Liu and P. Baird, "Measurement of the caesium $^{6}\mathrm{s}_{1/2}$ $^{8}\mathrm{p}_{1/2}$ transition frequency," *Appl. Phys. B*, vol. 71, p. 567, 2000.

[195] A. Banerjee, D. Das, and V. Natarajan, "Absolute frequency measurements of the d1 lines in 39k, 85rb, and 87rb with $\tilde{0}$.1 ppb uncertainty," *Europhys. Lett.*, vol. 65(2), pp. 172–178, 2008.

[196] A. L. Marchant, S. Händel, T. P. Wiles, S. A. Hopkins, C. S. Adams, and S. L. Cornish, "Off-resonance laser frequency stabilization using the faraday effect," *Opt. Lett.*, vol. 36, pp. 64–66, 2011.

[197] A. Sargsyan, A. Tononyan, R. Mirzoyan, D. Sarkisyan, A. M.Wojciechowski, A. Stabrawa, and W. Gawlik, "Saturated absorption spectroscopy revisited: atomic transitions in strong magnetic fields (>20 mt) with a micrometer-thin cell," *Opt. Lett.*, vol. 39, pp. 2270–2273, 2014.

[198] A. Sargsyan, B. Glushko, and D. Sarkisyan, "Micron-thick spectroscopic cells for studying the paschen-back regime on the hyperfine structure of cesium atoms," *J. Exp. Theor. Phys.*, vol. 120(4), pp. 579–586, 2015.

[199] S. Scotto, D. Ciampini, C. Rizzo, and E. Arimondo, "Four-level n-scheme crossover resonances in rb saturation spectroscopy in magnetic fields," *Phys. Rev. A*, vol. 92, p. 063810, 2015.

[200] D. J. Whiting, E. Bimbard, J. Keaveney, M. A. Zentile, C. S. Adams, and I. G. Hughes, "Electromagnetically induced absorption in a nondegenerate three-level ladder system," *Opt. Lett.*, vol. 40(18), pp. 4289–4292, 2015.

[201] D. J. Whiting, J. Keaveney, C. S. Adams, and I. G. Hughes, "Direct measurement of excited-state dipole matrix elements using electromagnetically induced transparency in the hyperfine paschen-back regime," *Phys. Rev. A*, vol. 93(4), p. 043854, 2016.

[202] D. J. Whiting, R. S. Mathew, J. Keaveney, C. S. Adams, and I. G. Hughes, "Four-wave mixing in a non-degenerate four-level diamond configuration in the hyperfine paschen-back regime," *J. Mod. Opt.*, vol. 65(2), pp. 119–128, 2018.

[203] D. J. Whiting, N. Šibalić, J. Keaveney, C. S. Adams, and I. G. Hughes, "Single-photon interference due to motion in an atomic collective excitation," *Phys. Rev. Lett.*, vol. 118, p. 253601, 2017.

[204] A. Sargsyan, G. Hakhumyan, C. Leroy, Y. Pashayan-Leroy, A. Papoyan, D. Sarkisyan, and M. Auzinsh, "Hyperfine paschen-back regime in alkali metal atoms: consistency of two theoretical considerations and experiment," *J. Opt. Soc. Am. B*, vol. 31(5), pp. 1046–1053, 2014.

[205] M. A. Zentile, J. Keaveney, L. Weller, D. J. Whiting, C. S. Adams, and I. G.Hughes, "Elecsus: a program to calculate the electric susceptibility of an atomic ensemble," *Comput. Phys. Commun.*, vol. 189, pp. 162–174, 2015.

[206] M. A. Zentile, R. Andrews, L. Weller, S. Knappe, C. S. Adams, and I. G. Hughes, "The hyperfine paschen-back faraday effect," *J. Phys. B*, vol. 47(7), p. 075005, 2014.

[207] M. A. Zentile, *Applications of the Faraday effect in hot atomic vapours*. PhD thesis, University of Durham, 2015.

[208] N. Šibalić and C. S. Adams, *Rydberg Physics*. 2399-2891, IOP Publishing, 2018.

[209] B. E. Sherlock and I. G. Hughes, "How weak is a weak probe in laser spectroscopy?," *Am. J. Phys.*, vol. 77(2), pp. 111–115, 2009.

[210] D. M. Petković and M. D. Radić, "Generalization of helmholtz coil problem.," *Serbian Journal of Electrical Engineering*, vol. 12(3), pp. 375–384, 2015.

[211] K. J. Weatherill, *A CO_2 laser lattice experiment for cold atoms*. PhD thesis, Durham University, 2007.

[212] L. Antoni-Micollier, M. Viteau, B. Battelier, B. Cadier, D. Comparat, B. Desruelle, G. Guiraud, E. Pinsard, M. Reveillard, S. Rota-Rodrigo, G. Stern, N. Traynor, and G. Santarelli, "Watt-level narrow-linewidth fibered laser source at 852 nm for fib application," *Opt. Lett.*, vol. 43(16), pp. 3937–3940, 2018.

[213] J. M. Robinson, Y. Liu, and D. P. Shelton, "Development and characterization of a magneto-optical trap for rubidium," *Nevada State Undergraduate Research Journal*, vol. 1(1), p. 16, 2014.

[214] D. E. Sproles, *Laser Spectroscopy and Magneto-Optical Trapping of Rubidium Atoms*. PhD thesis, Stony Brook University, 2008.